UNIVERSITY OF
LIVERPOOL

Lattice Boltzmann Method for Simulating Shallow Free Surface Flows involving Wetting and Drying

Thesis submitted in accordance with the requirements of the University of Liverpool for the degree of Doctor in Philosophy

By

Siti Habibah Shafiai (BEng, MSc)

18 April 2011

Abstract

Turbulent open channel flow and wave run-up at the coastal are studied using the lattice Boltzmann method. A lattice Boltzmann model for nonlinear shallow water equations with turbulence modelling (LABSWE^{TM}), based on space-filtered Navier-Stokes equations with large eddy simulation and a subgrid-scale stress model for the unresolved scale stresses, is used to predict flow with eddy formation within complex channels. The effect of sidewall friction is also examined. Additionally, a lattice Boltzmann model for a moving shoreline is also developed. Here the lattice Boltzmann model is improved by incorporating two types of moving boundary techniques: thin film, and linear extrapolation. The study involves one- and two-dimensional long wave motions at a plane

beach, around a circular island, and within a parabolic shaped basin. In each case, the computational results are compared against available results from laboratory experiments, analytical solutions, and alternative numerical methods. The results demonstrate that the lattice Boltzmann model is capable of handling properly complex free surface flow phenomena.

Acknowledgement

To God, thanks for the strength that keep me standing and for the hope that keep me believing that this research would be possible.

To my supervisors Dr Jian Guo Zhou and Prof Richard Burrows, thanks for the supervision and support from the preliminary to the concluding level of the studies.

Also, a very much thank to my beloved husband Mohamad Abdullah Sani, daughter, parents and all family members who inspired, encouraged and fully supported me for every trials that comes during the studies.

Also to the MEWS and Engineering departmental colleagues who willingly helped during the research.

Publications

1. Zhou, J.G., Liu, H., Shafiai, S.H., Peng, Y. and Burrows, R. Lattice Boltzmann Method for Open Channel Flows. Proceedings of the Institution of Civil Engineers. *Engineering and Computational Mechanics* 2009 **163** (EM4):243-249. (Published).
2. Shafiai, S.H., Zhou, J.G. and Burrows, R. A lattice Boltzmann model for the solitary wave run-up. *Coastal Engineering* 2010 (Under review).
3. Shafiai, S.H. The analysis of moving shoreline method in 2D lattice Boltzmann model for the long wave resonance run-up in parabolic shaped basin. Oral presentation in the UK Young

Coastal Scientists and Engineers Conference 2011, Liverpool, 31 March 2011.

4. Brown, J.M., Chester, T., Beveridge, A.J., Shafiai, S.H., Murray, R.B., Smith, T.A.G., Bricheno, L.M., and Way, O. Briefing: Young Coastal Scientists and Engineers Conference 2011. Proceedings of the Institution of Civil Engineers. *Maritime Engineering* 2011 (Under review).

5. Shafiai, S.H., Zhou, J.G. and Burrows, R. A lattice Boltzmann model for 2D long wave run-up. *Coastal Engineering* 2010 (under review).

Table of Content

Abstract i

Acknowledgement iii

Publications iv

Table of Content vi

List of Figures xii

List of Tables xxii

List of Abbreviations and Symbols xxiv

Chapter 1 Introduction 1

1.1 Background 1

1.2 Historical Background of the LBM 8

1.3 Aims and Objectives 16

1.4 Outline of Thesis 17

Chapter 2 Governing Equations 19

2.0 Introduction 19

2.1 Navier-Stokes Equations 20

2.2 Shallow Water Equations 23

2.3 Space-filtered Navier-Stokes Equations for Turbulent Flows 37

2.4 Determination of the Eddy Viscosity 41

Chapter 3 Lattice Boltzmann Method 43

3.0 Introduction 43

3.1 Lattice Boltzmann Method for Shallow Water Flows 45

3.1.1 Lattice Boltzmann Equation 45

3.1.2 Lattice Pattern 48

3.1.3 Local Equilibrium Distribution Function: Shallow Water Flow Modelling 53

3.1.4 Macroscopic Properties 59

3.1.5 Recovery of Shallow-Water Equations 62

3.2 Lattice Boltzmann Method with Turbulence Modelling 66

3.2.1 Subgrid-scale Lattice Boltzmann Model for Turbulent Shallow Water Equations 67

3.2.2 Recovery of Turbulent Shallow Water Equations 71

3.3 Calculation of Force Terms 75

3.3.1 Centred Scheme 77

3.3.2 Discretization Errors 83

3.4 Continuum Boltzmann Equation 86

Chapter 4 Initial and Boundary Conditions 91

4.0 Introduction 91

4.1 Standard Bounce-back Scheme: No-slip Boundary 94

4.2 Modified Elastic-Collision Scheme 96

4.2.1 Slip Boundary Condition 98

4.2.2 Semi-slip Boundary Condition 106

4.3 Inflow and Outflow 107

4.4 Initial Condition 110

Chapter 5 Moving Boundary for Wave Run Up 111

5.0 Introduction 111

5.1 Treatment of the Moving Shoreline 115

5.1.1 Thin Film Technique 118

5.1.2 Linear Extrapolation Technique 120

Chapter 6 Stability, Errors, and Solution Procedures for LB Models 125

6.0 Introduction 125

6.1 Stability Conditions 127

6.2 Error Sources 129

6.3 Solution Procedures 132

6.3.1 Procedure for LABSWE 132

6.3.2 Procedure for LABSWE^{TM} 135

6.3.3 Lattice Boltzmann Model for Moving Shoreline 136

Chapter 7 Applications and Discussion 140

7.0 Introduction 140

7.1 LABSWE^{TM}: Study of Recirculating Flows 142

7.1.1 Flow in a Channel with Circular Cavity 143

7.1.1.1 Results 145

7.1.2 Flow in a Channel with Spur-dike 149

7.1.2.1 Results 150

7.1.3 Flow in a Single Expansion Channel 154

7.1.3.1 Results 156

7.1.4 Flow in a Double Expansion Channel 159

7.1.4.1 Results 161

7.1.5 Jet-Forced Symmetrical and Asymmetrical Flow in Circular Basins 163

7.1.5.1 Results 166

7.2 LABSWE^{TM}: Study of Sidewall Friction 171

7.2.1 The Effect of Sidewall Friction in a Rectangular Channel (Standard case) 173

7.2.2 The Effect of Sidewall Friction on Complex Flow and Channel Geometry 176

7.3 LABSWE^{TM}: Study of Moving Shoreline 185

7.3.1 1D of Wave Run-up Model: Solitary Wave on a Plane Beach 186

7.3.1.1 Results using thin film shoreline algorithm 188

7.3.1.2 Results using linear extrapolation shoreline algorithm 191

7.3.2 2D Solitary Wave Run-up around a Conical Island 197

7.3.2.1 Results using the thin film shoreline algorithm 200

7.3.2. 1 Results using the linear extrapolation shoreline algorithm 204

7.3.3 2D Long Wave Resonance in a Parabolic Basin 215

7.3.3.1 Results using the thin film shoreline algorithm 218

7.3.3.2 Results using the linear extrapolation shoreline algorithm 227

Chapter 8 Conclusions and Recommendations 238

8.0 Conclusions.....238

8.1 Recirculating Flow.....239

8.2 Sidewall Friction Effect 240

8.3 Wave Run-up and Moving Shoreline 242

8.4 Recommendations.....243

8.5 Final Remarks 245

Appendix A A proof of second-order accuracy for the stationary case $ui \equiv 0$ with source term or non-zero force term.....246

References.....254

List of Figures

Figure 1. 1 Illustration of 2-and 3-particle collisions. 11

Figure 1. 2 Streaming step: Particles from surrounding cells flow into given cells. 12

Figure 2. 1 Cartesian coordinate system: x, y represents a horizontal plane and z the vertical direction. 21

Figure 2. 2 The sketch of shallow water. 25

Figure 3. 1 The square lattice pattern with 5 and 9-velocity models. 49

Figure 3. 2 Hexagonal lattice pattern with 6 and 7-velocity models. 49

Figure 3. 3 The 9-velocity lattice pattern. 51

Figure 4. 1 An incoming particle towards the wall is bounced back into water. 95

Figure 4. 2 Elastic-collision scheme. 97

Figure 4. 3 Illustration of boundaries [107]. 100

Figure 4. 4 Sketch of boundary for $0^0 < \theta < \theta_0$. 101

Figure 4. 5 Sketch of boundaries for $\theta^0 < \theta \leq 90^0 - \theta_0$ 102

Figure 4. 6 Sketch of boundaries for $90^0 - \theta_0 < \theta \leq 90^0$ 103

Figure 4. 7 Sketch of boundaries. 105

Figure 4. 8 Sketch of inlet and outlet boundaries. 108

Figure 5. 1 Interface tracking of Lagrangian method. 113

Figure 5. 2 Interface tracking of Eulerian method. 114

Figure 5. 3 Illustration of thin film of fluid *hmin*. 119

Figure 5. 4 Run-up of 1D solitary wave in x-direction. Solid line denotes locations that are determined using the primitive equations, whereas dots are the extrapolated nodes 121

Figure 5.5 Illustration of a dry node D with eight wet surrounding points W_{1-8} in 2D lattices 123

Figure 5. 6 6-directions of wet nodes W extrapolation towards a dry node D. 124

Figure 6. 1 Flow chart for solution procedure in LBM..... 138

Figure 7. 1 The shape of open-channel with circular sidewall cavity in plan view. 144

Figure 7. 2 Velocity vectors within the open-channel with circular sidewall cavity 145

Figure 7. 3 Flow streamlines within the open-channel with circular sidewall cavity. 146

Figure 7. 4 Comparison of velocity components u at a-a cross section. 147

Figure 7. 5 Comparison of velocity components v at b-b cross section. 147

Figure 7. 6 Sketch of channel with spur-dike structure. 149

Figure 7. 7 Velocity vector around the spur-dike. 150

Figure 7. 8 Comparisons of water profiles along flow direction at transversal location of $y/b = 1$. 151

Figure 7. 9 Comparisons of water profiles along flow direction at transversal location of $y/b = 1.5$. 152

Figure 7. 10 Comparisons of water profiles along flow direction at transversal location of $y/b = 2$. 152

Figure 7. 11 Comparisons of water profiles along flow direction at transversal location of $y/b = 3$. 153

Figure 7. 12 Comparisons of water profiles along flow direction at transversal location of $y/b = 4$. 153

Figure 7. 13 The schematic diagram of the single expansion channel in plan view. 155

Figure 7. 14 Streamline contour for channel with sidewall expansion.. 156

Figure 7. 15 Velocity vectors for channel with sidewall expansion. 157

Figure 7. 16 The velocity component u at $x = 1.53m$ within the eddy zone. The circles indicate experimental data. 157

Figure 7. 17 The velocity component u at $x = 2.03m$ within the eddy zone. The circles indicate experimental data. 158

Figure 7. 18 The velocity component u at $x = 2.53m$ within the eddy zone. The circles indicate experimental data. 158

Figure 7. 19 The isometric diagram of the sudden expansion channel.. 160

Figure 7. 20 Comparison of predicted velocity component u across the channel with experimental measurements [169]..... 162

Figure 7. 21 The velocity vectors behind a one-sided channel expansion. 163

Figure 7. 22 Geometry for the jet-forced flow in the symmetrical circular basin. 164

Figure 7. 23 Geometry for the jet-forced flow in the asymmetrical circular basin. 165

Figure 7. 24 Steady state velocity vectors of jet-forced flow in the symmetrical circular basin. 167

Figure 7. 25 Steady state streamline contours of jet-forced flow in the symmetrical circular basin. 167

Figure 7. 26 Steady state velocity vectors of jet-forced flow in asymmetrical circular basin. 168

Figure 7. 27 Steady state streamline contours of jet-forced flow in asymmetrical circular basin. 168

Figure 7. 28 The velocity component u across mid-section of symmetrical circular basin. 169

Figure 7. 29 The velocity component u across mid-section of asymmetrical circular basin. 170

Figure 7. 30 Water surface elevation along a straight rectangular channel. Dashed-line indicates lattice Boltzmann model, whereas cross-symbols are experimental data [179]. 174

Figure 7. 31 Water surface elevation along a straight rectangular channel. Cross-symbols indicate experimental data by Lansford and Mitchell [179], the solid-line is lattice Boltzmann model and dashed-line for the numerical model by Molls et al. [55]. 175

Figure 7. 32 u-velocity profile across the single expansion channel (a) at an upstream location, (b) within the eddy zone and (c) at a downstream

location. The solid-lines indicate $C_f = 0$, space-lines are $C_f = 0.01$ and space-dot-lines are $C_f = 0.03$. 178

Figure 7. 33 u-velocity profile across the double expansion channel (a) at an upstream section, (b) within the eddy zone and (c) at a downstream section. The solid-lines indicate $C_f = 0$, space-lines are $C_f = 0.01$ and space-dot-lines are $C_f = 0.03$. 180

Figure 7. 34 u-velocity profiles across a channel with semi-circular sidewall cavity (a) at a upstream section, (b) within the eddy zone and (c) at downstream section. The solid-lines indicate $C_f = 0$, space-lines are $C_f = 0.01$ and space-dot-lines are $C_f = 0.03$ 183

Figure 7. 35 Definition sketch of solitary wave run up on a plane beach. 187

Figure 7. 36 Comparisons of computed and experimental water free surface profiles at $t^* = 25, 30, 35, 40, 45, 50, 55, 60, 65$ and 70. The solid lines represent numerical results; the symbols are experimental data [58] 189

Figure 7. 37 Comparisons of computed and experimental water free surface profiles at $t^* = 20, 26, 32, 38, 44, 50, 56$ and 62. The solid lines represent numerical results; the symbols are experimental data [58]. ... 190

Figure 7. 38 Comparisons of computed and experimental free surface profiles at $t^* = 25, 30, 35, 40, 45, 50, 55, 60, 65$ and 70. The solid lines represent numerical results; the symbols are experimental data [58]. ... 192

Figure 7. 39 Comparisons of computed and experimental free surface profiles at $t^* = 20, 26, 32, 38, 44, 50, 56$ and 62. The solid lines represent numerical results; the symbols are experimental data [58]. ... 193

Figure 7. 40 Comparisons of computed water free surface profile for nonbreaking wave condition obtained using the thin film and extrapolation techniques with experimental data at $t^* = 35, 50$ and 70. Symbols indicate experimental data [58].....195

Figure 7. 41 Comparisons of computed water free surface profiles for breaking wave condition obtained using the thin film and extrapolation techniques at $t^* = 38, 44$ and 62. Symbols indicate experimental data [58].....196

Figure 7. 42 Schematic diagram of the conical island: (a) plan views of the conical island and gauge locations; (b) side views of the island from A-A direction.....199

Figure 7. 43 Time history of solitary wave interaction with conical island for $H/h_0 = 0.045$ at 4 gauges. The solid line represents the numerical results. The crosses show experimental data [15].....200

Figure 7. 44 Time history of solitary wave interaction with conical island for $H/h_0 = 0.096$ at 4 gauges. The solid line represents the numerical results. The crosses show experimental data [15].....201

Figure 7. 45 Time history of solitary wave interaction with conical island for $H/h_0 = 0.181$ at 4 gauges. The solid line represents the numerical results. The crosses show experimental data [15].....201

Figure 7. 46 Maximum wave run-up around a conical island: a) $H/h_0 = 0.045$, b) $H/h_0 = 0.096$ and c) $H/h_0 = 0.181$. The circles depict experimental data [15]. The solid line represents the numerical results. 203

Figure 7. 47 Solitary wave interaction with a conical island: $H/h_0 = 0.045$ 205

Figure 7. 48 Solitary wave interaction with a conical island: $H/h_0 = 0.096$ 207

Figure 7. 49 Solitary wave interaction with a conical island: $H/h_0 = 0.181$ 208

Figure 7. 50 Time history of solitary wave interaction with conical island for $H/h_0 = 0.045$ at 4 gauges. The solid line represents the numerical results. The crosses show experimental data [15] 209

Figure 7. 51 Time history of solitary wave interaction with conical island for $H/h_0 = 0.096$ at 4 gauges. The solid line represents the numerical results. The crosses show experimental data [15] 210

Figure 7. 52 Time history of solitary wave interaction with conical island for $H/h_0 = 0.181$ at 4 gauges. The solid line represents the numerical results. The crosses show experimental data [15] 210

Figure 7. 53 Maximum wave run-up around the island: a) $H/h_0 = 0.045$, b) $H/h_0 = 0.096$ and c) $H/h_0 = 0.181$. The circles depict the experimental data [15]. The solid line represents the numerical results. 211

Figure 7. 54 Comparison of computed water level time histories based on the two moving shoreline techniques for $H/h_0 = 0.045$ at Gauge 9 and 22. Symbols indicate experimental data [15] 213

Figure 7. 55 Comparison of computed water level time histories based on the two moving shoreline techniques for $H/h_0 = 0.096$ at Gauge 9 and 22. Symbols indicate experimental data [15].....213

Figure 7. 56 Comparison of computed water level time histories based on the two moving shoreline techniques for $H/h_0 = 0.181$ at Gauge 9 and 22. Symbols indicate experimental data [15].....214

Figure 7. 57 The initial free surface profile in the parabolic shaped basin. 217

Figure 7. 58 Free surface profiles in parabolic basin at a) $t = 0$, and b) $t = 1/2T$. 219

Figure 7. 59 Free surface profiles in parabolic basin at a) $t = T$, and b) $t = T + 1/2T$.....220

Figure 7. 60 Free surface profiles in parabolic basin at a) $t = 2T$, and b) $t = 2T + 1/2T$. 221

Figure 7. 61 Free surface profiles in parabolic basin at a) $t = 3T$, and b) $t = 3T + 1/2T$. 222

Figure 7. 62 Free surface profiles in parabolic basin at a) $t = 4T$, and b) $t = 4T + 1/2T$. 223

Figure 7. 63 Visualisations of the simulated wave surface at $t = 0$ and $t = 1/2T$, marked without the mesh grids and with the mesh grids, respectively. (a) The wave surfaces in isometric view and (b) wave profile surface in x direction.....225

Figure 7. 64 3D visualisations of the computed free surfaces within the parabolic basin at (a) during the $1st$ cycle at $t = 0$ and $t = 1/2T$ and (b) during the $4th$ cycle at $t = 4T$ and t = $4T + 1/2T$. 226

Figure 7. 65 Free surface profiles in parabolic basin at a) $t =$ $0,$ and b) $t = 1/2T.$ 228

Figure 7. 66 Free surface profiles in parabolic basin at a) $t =$ $T,$ and b) $t = T + 1/2T.$ 229

Figure 7. 67 Free surface profiles in parabolic basin at a) $t =$ $2T,$ and b) $t = 2T + 1/2T.$ 230

Figure 7. 68 Free surface profiles in parabolic basin at a) $t =$ $3T,$ and b) $t = 3T + 1/2T.$ 231

Figure 7. 69 Free surface profiles in parabolic basin at a) $t =$ $4T,$ and b) $t = 4T + 1/2T.$ 232

Figure 7. 70 Comparison of computed water levels for both moving shoreline techniques at $t = T$ and t = $T + 1/2T$ sec. The dashed-line indicates the analytic solution [186]. 233

Figure 8. 1 Still water above an uneven bed. 246

List of Tables

Table 7. 1 The velocity errors for LABSWE™ compared to the experimental data. 148

Table 7. 2 The velocity errors of LABSWE™ model compared to the experimental data. 159

Table 7. 3 The velocity error for LABSWE™ compared to the numerical results for the symmetrical and asymmetrical circular basins. 170

Table 7. 4 Velocity values at upstream, eddy zone and downstream locations in the sudden expansion channel. 184

Table 7. 5 Water depth profile errors for thin film and linear extrapolation models applied to the non-breaking solitary case. 197

Table 7. 6 Water depth h at the middle of the basin obtained using analytical and for the thin film and the linear extrapolation models for $\Delta t = 0.001s$ and $\tau = 0.62$. 234

Table 7. 7 Water depth h at the middle of the basin obtained using analytical and the thin film and the linear extrapolation models for $\Delta t = 0.0005s$ and $\tau = 0.65$. 235

Table 7. 8 Relative error in water depth for the thin film model with $\Delta x = 0.01m$ and $0.005m$ at $\Delta t = 0.001s$ and $\tau = 0.62$ 236

Table 7. 9 Relative error in water depth for the thin film and the linear extrapolation models with $\Delta x = 0.005m, \Delta t = 0.0005s$ and $\tau = 0.65$. 236

List of Abbreviations and Symbols

Abbreviations

1D	One dimensional
2D	Two dimensional
3D	Three dimensional
BGK	Bhatnagar-Gross-Krook model
CA	Cellular automata
CFL	Courant Friedricks-Lewey
CFD	Computational fluid dynamic

FHP	Model designed by Frisch, Hasslacher and Pomeau
HPP	Model designed by Hardy, de Pazzis and Pomeau
LABSWE	The lattice Boltzmann model for nonlinear shallow water equations
LABSWE^{TM}	The lattice Boltzmann model for nonlinear shallow water equations with turbulence modelling
LBM	Lattice Boltzmann method
LES	Large eddy simulation
LGCA	Lattice gas cellular automata
N-S	Navier Stokes equations
REV	Reference element of volume
RMSE	Root mean-square error
SGS	Subgrid-scale stress model
PDE	Partial differential equations

Symbols

β	Beach slope	$Degree$
η	Free surface profile	m
ρ	Fluid density	kg/m^3

ρ_a	Air density	
ρ_w	Fluid density	
ρ_0	Constant density	
τ^*	Shear stress	N/m^2
τ_f	Wall shear stress vector	
τ_b	Bed shear stress	N/m^2
τ_w	Wind shear stress	N/m^2
τ	Single dimensionless relaxation time	
τ_e	Eddy relaxation time	
τ_t	Total relaxation time	
μ	Dynamic viscosity	$Pa.s$
ν	Kinematic viscosity	m^2/s
ν_e	Eddy viscosity	m^2/s
ν_t	Total viscosity	m^2/s
ξ	Particle velocity	m/s
γ	Acceleration	m/s^2
δ	Thickness of boundary layer	m
$\delta_{\alpha\beta}$	Kronecker delta function	
ϵ	Turbulent dissipation rate	m^2/s^3
Ω_α	Collision operator	
σ	Cauchy stress	Pa
Δt	Time step	s

Δx	Lattice size in x direction	m
Δy	Lattice size in y direction	m
∇	Gradient operator	
ω	Earth's rotation	Rad/s
ϕ	Earth's latitude	$Degree$
$\theta_1, \theta_2, \theta_3$	Momentum correction factor	
b	Spur-dike length normal to channel sidewall	m
C_b	Bed friction coefficient	
$\boldsymbol{c}_e$	Discrete velocity vector	
C_f	Sidewalls friction coefficient	
C_r	Courant number	
C_s	Smagorinsky constant	
C_w	Wind resistant coefficient	
C_z	Chézy coefficient	
d	Water depth	m
D	Dry node	
$\boldsymbol{e}_\alpha$	Velocity vector of particle in the α link	m
E_i	Corialis term in i direction	
E_R	Relative error	
f	Distribution function	m
f_w	Wishbach resistance coefficient	

f_x, f_y, f_z	Body forces per unit mass	N/kg
f_α	Particle distribution function in the α link	m
f'_α	The value of f_α before streaming	m
f^{eq}	Local equilibrium distribution function	m
F_i	External force term in i direction	N
Fr	Froude number	
g	Gravitational acceleration	m/s^2
$\tilde{G}$	Grid filter function	
h	Water depth	m
h_0	Still water depth	m
H	Solitary wave height	m
K_B	Boltzmann constant	
K_s	Nikuradse equivalent sand roughness	
Kn	Knudsen number	
ℓ	Characteristic length	
ℓ_s	Characteristic length scale	
L	Wave length	m
n	Manning roughness coefficient	
n_b	Bed Manning roughness coefficient	
N_x	Total lattice number	
p	Pressure	Pa
p_a	Atmospheric pressure	Pa

Q	Flow discharge	m^3/s
R	Height of wave run-up	m
R^*	Ideal gas constant	$J/Kmol$
R'	Hydraulic radius	m
R_e	Reynolds number	
S	Slope	
S_{ij}	Magnitude of the large scale strain-rate tensor	
t_c	Time between particle collisions	sec
T	Temperature	^oC
u	Flow velocity in x-direction	m/s
u_w	Wind velocity	m/s
U_0	Averaged flow velocity	m/s
v	Flow velocity in y-direction	m/s
V	Normalised fluid velocity	
w	Velocity in vertical direction	m/s
w_α	Weighting factor in i direction	
w_s	Free surface velocity in vertical direction	
w_b	Channel bed velocity in vertical direction	
W_0, W_1	Width of channel	m
W_{1-8}	Wet nodes	
x, y, z	Cartesian coordinates	

x_b	Solid nodes	
x_f	Fluid nodes	
z_b	Bed elevation above datum	m

Chapter 1 Introduction

1.1 Background

Shallow water flows are often found in rivers, channels, coastal areas, estuaries and harbours. An understanding of such flows plays a very important role in hydraulic and civil engineering. The flows are characterised by dominant horizontal features and often described with the shallow water equations. The equations have been applied by numerous researchers [1-6] in various fields of studies including ocean, hydraulic and coastal engineering. For example, tidal flows [7], fluctuations in coastal regions [8,9], tsunami propagation [10-16] and free

surface flows [1,17] have been studied using models based on the shallow water equations.

Many research works have been done to study the mathematical and numerical model development for hydraulics. For example, Harlow and Welch [18] proposed staggered grid for variable arrangement for free surface pressure calculation. Grubert [19] introduced procedure for two-dimensional (2D) shallow water flow computation. Later, a depth-averaged mathematical model for shallow water flows has been developed by McGuirk and Rodi [20]. It is only limited for a general situation due to small depth assumption in the model,

Several factors limit the numerical solution of the shallow water equations. One of the limits relates to the irregular topography data of shallow water regions [21]. In addition, the shallow water flows are subject to external forces such as the atmospheric pressure gradient, surface wind stress, tidal and Coriolis forces [4]. As the shallow water equations comprise coupled, non-linear partial differential equations, it is difficult to obtain an accurate solution for a system involving a complicated physical domain.

Many numerical methods have been used to discretise the shallow water equation. These include the finite difference method (FDM), the finite volume method (FVM) and the finite element method (FEM).

Abbott and Ionescu [22] provided solution for shallow water flow problems using the FDM. The solution is modified and extended into 2D depth-averaged flow by Falconer [23] who studied tidal problems for harbours. A semi-implicit form of FDM for 2D shallow water equations is proposed by Casulli [24]. For unsteady flow problem, Glaister [25] solved 2D unsteady shallow water equations using an approximate Riemann solver based on the FDM and operator splitting technique. Toro [26] proposed a treatment method for unsteady flow using ADI approach, which is a time and space-operator splitting technique to reduce 2D problems to one-dimensional (1D) for solution. Alcrudo and García-Navarro [27] improved Toro's method by redefining it on rectangular elements. Chippada et al. [28] constructed linear terms for the elevation variable. Aizinger and Dawson [29] proposed a Godunov-type method defined on triangular elements.

On the other hand, the lattice Boltzmann method (LBM) was originally created to model flows governed by the N-S equations [30-34]. It has become a well established numerical method with increasing applications in computational fluid dynamics [35-37]. The method can be considered as a class of kinetic theory approaches, as based on a special discrete form of the Boltzmann equation [38]. The ability of the LBM to recover macroscopic governing equations (such as the N-S equations, the shallow water equations, and the diffusion equation) is unique [4]. In LBM, a

simplified description modelled on the kinetic theory of gases is used instead of the nonlinear differential equations of macroscopic fluid dynamics [21]. The LBM commonly uses the Chapman-Enskog expansion (a perturbation expansion in time and space) to represent the hydrodynamic behaviour. This technique describes slowly varying solutions of kinetic equations. The local nature of particle interactions and the transport of particle information make LBM suitable for parallel computing, while the easy implementation of boundary conditions makes the method flexible to apply to complicated geometric [4]. Furthermore, LBM has become an alternative to conventional numerical methods like FDMs, FEMs, and FVMs in computational fluid dynamics.

A wide range of problems can be modelled using LBM. For example, LBM has been successfully used to study wind-driven ocean circulation [39,40] and atmospheric circulation with ideal boundary conditions [41].

Numerical experiments have shown that the LBM based on shallow water model produces accurate results for rapidly and gradually varied open channel flow problems [39,40,42-46].

In addition to the large scale vertical flow structure created by the presence of bed topographic features (e.g. island and headlands) and large man-made structures (e.g. groynes), turbulence is very important in shallow flows [4]. For example, turbulence greatly affects erosion in

waterways, leading to long-term change to the shape of the waterways. In addition to the need to include turbulent effects, numerical models should also take into account the effect of wall shear stress. It is well known that an understanding of the effect of friction force is important for applications in engineering fields such in the canal design, and the calculation of velocity distribution and sedimentation studies for open channels [47]. Friction affects flow characteristics like mean flows and turbulent motion [48]. Previous studies show that the majority of two dimensional (2D) depth-averaged numerical hydraulics models only take bed friction into consideration and overlook the sidewall friction factor. This is mainly due to the high proportional values between width and depth of channel for shallow water flow condition [49]. Only a few authors [50-54] applied sidewall friction in their numerical models. Molls et al. [55] have considered sidewall friction in a rectangular channel for depth-averaged flow numerical model by modifying the standard 2D friction slope equation. The modification involves distributing the sidewall friction across the channel. It works well for the relatively simple case of subcritical flow in a straight channel. Brufau [56] applied the proposed scheme to the simulation of dam break.

There are three zones that divide an ocean with respect to wave action; breaker zone, surf zone and swash zone. Beach run-up occurs when waves propagate up a beach slope into the swash zone [57]. Spontaneous

geophysical activities such as underwater earthquakes and landslides can generate a massive and disastrous wave run-up. This can cause an extensive flooding and loss of life [51].

Many experimental, analytical and numerical studies have been done to understand and explain the phenomena, e.g., experimental and numerical studies for solitary wave run-up on a plane beach [54,58,59], solitary wave run-up around a conical island [52,60] and tsunami run-up due to submarine earthquake [10,14-16,52,61], etc. Wave oscillation in a parabolic basin is another important test that has been widely studied for validation of a numerical scheme [62-68].

In a wave run-up model, an algorithm must be implemented to request the moving shoreline at the wet-dry front during wave motion run-up and down.

Typical moving boundary algorithm include the slot technique (also known as the Priessmann slot) [69], and the thin film technique [70,71], the minimum friction depth [72]. Such techniques are continually under improvement in order to increase their stability and accuracy. Another common technique is the extrapolation method proposed by Sielecki and Wurtele [73], Titov and Synolakis [51] and Lynett et al. [64]. The kinematics of the moving front is ignored in this technique [74].

Many studies based on conventional numerical methods have been developed for the simulation of wave run-up. For example, Titov and Synolakis [51] developed a variable-grid finite difference formulation model called VTCS-2. This model enables calculation of wave run-up without the need to apply any ad-hoc coefficients. Fuhrman and Madsen [52] produced a numerical analysis of wave run-up based on a high-order Boussinesq-type approach. A regression approach for the extrapolation scheme through the wet-dry boundary is used for the moving shoreline. Yamazaki et al. [53] suggested a depth-integrated non-hydrostatic formulation in their numerical model. The model is equivalent to the Boussinesq equations for weak dispersive waves. For 1D numerical analysis, Mahdavi and Talebbeydokhti [54] utilized the altered Monotone Upstream-centred Schemes for Conservation Laws (MUSCL) scheme in the Runge-Kutta method. It provides highly accurate numerical solutions for shocks, discontinuities, or large gradient problems [75]. Although there are many approaches in the conventional numerical method available for wave run-up, very limited attempts have been made with the LBM. Frandsen [76] proposed a BGK lattice Boltzmann model in simulating 1D tsunami wave run-up at a plane beach. Turbulence or bed friction is not taken into consideration.

The present study focuses on the lattice Boltzmann model for nonlinear shallow water equations with turbulence modelling (LABSWE^{TM}) [44],

which aims to further explore the behaviour of flow condition in complex channel geometries and find a solution for the wave run-up conundrum.

1.2 Historical Background of the LBM

Due to the fast development of computer technology, simple finite discrete space-time models such as cellular automata (CA), lattice gas cellular automata (LGCA), and LBM, have been developed.

CA was first introduced by Ulam, Neumann and Zuse [34]. Ulam [77] simulated the growth of calculation pattern by using CA in 1D and 2D. Neumann [78] proposed a self-reproducing cellular automaton, which was further implemented by Signorini [79]. Later, Zuse [80] published an application of CA using a monograph experiment. Several of Zuse's formulations contributed to the first LGCA model, namely HPP [34].

CA is an algorithmic entity that can be computed using dual arithmetic [81]. It occupies a position on a lattice point in space and interacts with its immediate neighbours. The capability of CA in solving complex systems is impressive [79,82-85]. A formal definition of CA is as follows [34]:

1. CA involves regular arrangements of single cells, each with the same kind of state.
2. Each cell holds a finite number of discrete states.
3. The states are updated simultaneously at separate time levels.
4. Update rules in space and time are uniform and deterministic.
5. Evolution rules for a cell depend on the collection cells which immediate neighbourhood.

It is essential to model physical properties that conserve mass and momentum, so that accurate predictions from the model can be obtained. However, CA does not generally maintain conservation of mass or momentum. Only a small subset of CA has conservation properties [34].

By contrast, LGCA obeys certain conservation laws [32,81,86]. The method preserves mass and momentum, and it is easier to construct models with desired macroscopic properties.

Frisch et al. [87] developed the first LGCA model, named FHP, which was used to simulate flows based on the 2D N-S equations. FHP model was constructed on an equilateral triangular lattice [81]. The six-speed directions on the lattice include Boolean variables. An exclusion principle is applied to describe the state of a cell (i.e. 0 and 1 indicating the presence and absence of the particles respectively). This exclusion

principle leads to the use of the Fermi-Dirac equilibrium distribution function.

A HPP lattice gas model for vector automata that based on a square grid was first described in 1973 by Hardy, Pomeau and de Pazzis [88]. However, this did not fulfil the requirement of rotational invariance, as evidenced by the square-shaped vortices produced by the HPP model. An FHP lattice gas model that fulfilled both requirements (i.e. the conservation of particle number and rotational invariance) was developed later on a hexagonal 2D lattice.

The improved LGCA equation involves streaming and collision steps:

$$n_\alpha(x + e_\alpha, t + 1) = n_\alpha(x, t) + \Omega_\alpha[n_\alpha(x, t)], \quad \alpha = 0,1, \dots, M, \qquad (1.1)$$

Where n_α is a Boolean variable; x is the distance in the x-direction of a Cartesian coordinate system; e_α is the velocity vector in the α^{th} link; t is time; Ω_α is the collision operator and M is the number of links.

At every time step, the streaming step moves the particles to the new node. During a collision, the particles interact at a node and change their velocity directions according to the lattice pattern. These two steps simulate advection and dispersion respectively for macroscopic phenomena in physics [89].

In the FHP model, only two types of collision are considered; two-body collisions involving two particles and three-body collisions involving three particles. Figure 1.1 illustrates 2- and 3-particle collisions.

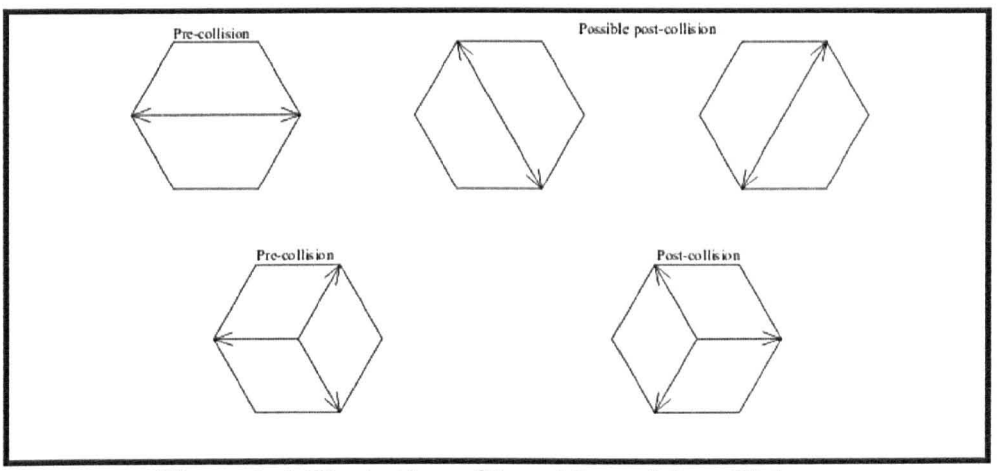

Figure 1. 1 Illustration of 2-and 3-particle collisions.

Often, simulations generated with a LGCA are very noisy due to its Boolean nature [90]. Also, the numerical procedure involves probabilities which reduce the efficiency of LGCA. This leads naturally to the use the Boltzmann equation.

The Boltzmann equation is derived from the LGCA to overcome its difficulties. It deals with a continuous distribution function, which solely involves distributions at a single node.

$$f_\alpha(x + e_\alpha, t + 1) = f_\alpha(x, t) + \Omega_\alpha[f_\alpha(x, t)], \quad \alpha = 0,1, \dots, M \qquad (1.2)$$

where f_α is the particle distribution function.

Hereafter, this distribution function propagates to the next neighbour in the collision process. According to Dreweke [91], during a single discrete time step, particles from each cell in the domain stream into their neighbouring cells according to the local velocity vector, as shown in Figure 1.2.

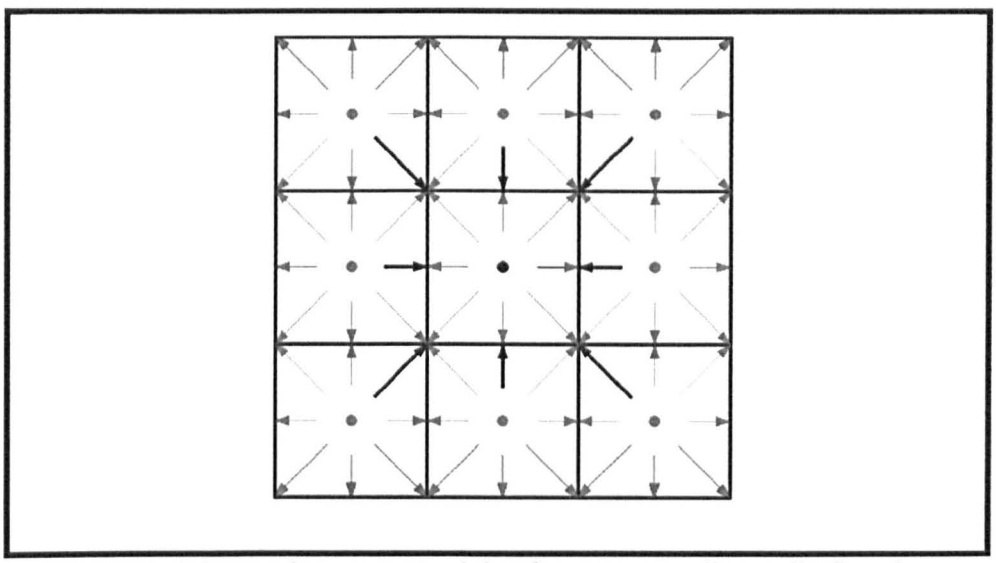

Figure 1. 2 Streaming step: Particles from surrounding cells flow into given cells.

In each neighbour cell, the particles collide with the other particles from the other surrounding cells. The results from these collisions are taken as the new particle distribution for the streaming process at the next discrete time step.

Based on the streaming and collision procedure, the Boltzmann equation can be written by neglecting the external forces as [91]:

$$\frac{\partial f}{\partial t} + \xi . \frac{\partial f}{\partial x} = Q(f, f), \tag{1.3}$$

where $Q(f, f)$ consists of a complex integrodifferential expression, which can be simplified by the Bhatnagar-Gross-Krook (BGK) model as follows:

$$Q(f, f) = -\frac{1}{\tau}[f - f^{eq}]. \tag{1.4}$$

By inserting equation (1.4) in (1.3), the Boltzmann equation with a single relaxation time approximation is obtained

$$\frac{\partial f}{\partial t} + \xi . \frac{\partial f}{\partial x} = -\frac{1}{\tau}[f - f^{eq}], \tag{1.5}$$

where ξ is the particle velocity, x is the site of the cell in the domain, τ is relaxation time, and t is time.

The Maxwell-Boltzmann distribution function f^{eq} is used to calculate the values of the particle distribution.

To solve the Boltzmann equation (1.5) numerically, a finite number of velocities $\mathbf{e}_\alpha$ in velocity space ξ are inserted into equation (1.5), which leads to:

$$\frac{\partial f_\alpha}{\partial t} + \mathbf{e}_\alpha . \frac{\partial f_\alpha}{\partial x} = -\frac{1}{\tau}[f_\alpha - f_\alpha{}^{eq}]. \tag{1.6}$$

For non-thermal fluids, Taylor series expansion is used to approximate the equilibrium functions in equation (1.6) leading to:

$$f_\alpha = \rho w_\alpha \left[1 + \frac{3}{e^2}\mathbf{e}_\alpha . u + \frac{9}{2e^4}(\mathbf{e}_\alpha . u)^2 - \frac{3}{2e^2}.u^2\right], \tag{1.7}$$

where $e = \Delta x/\Delta t$; w_α is a weighting factor, and $\mathbf{e}_\alpha$ is a discrete velocity vector. Equation (1.7) can be simplified by discretizing Δx and Δt, such that $e = 1$. Hence,

$$f_\alpha = \rho w_\alpha \left[1 + 3\mathbf{e}_\alpha . u + \frac{9}{2}(\mathbf{e}_\alpha . u)^2 - \frac{3}{2}.u^2\right] \tag{1.8}$$

is obtained. The fluid density $\rho(x,t)$ is calculated by adding up the particle distributions for each cell,

$$\rho(x,t) = \sum_\alpha f_\alpha (x,t). \tag{1.9}$$

The velocity of the domain can also be obtained by adding up the particle distributions with respect to the discrete velocities as follows:

$$\rho(x,t).u(x,t) = \sum_i \mathbf{e}_\alpha . f_\alpha (x,t). \tag{1.10}$$

Sterling and Chen [92] were the first to derive the lattice Boltzmann equation as a special discretization of the Boltzmann equation (1.3).

In the process of discretization, the Boltzmann equation (1.3) is nondimensionalized in terms of characteristic length scale ℓ, reference speed U, reference density n_r, and the time between particle collisions t_c,

$$\frac{\partial \hat{f}_\alpha}{\partial \hat{t}} + \hat{\mathbf{e}}_\alpha \hat{\nabla} \frac{\partial \hat{f}_\alpha}{\partial x} = -\frac{1}{\hat{\tau}\epsilon}\left(\hat{f}_\alpha - \hat{f}_\alpha^{\,eq}\right) \tag{1.11}$$

where $\hat{\mathbf{e}}_\alpha = \mathbf{e}_\alpha/U$, $\hat{\nabla} = \ell\nabla_\alpha, \hat{t} = t.U/\ell$, $\hat{\tau} = \tau/t_c$, $\hat{f}_\alpha = f_\alpha/n_r$, $\epsilon = t_c.U/\ell$ and $\Delta\hat{t} = \Delta t.U/\ell$. The gradient operator ∇_α is defined as $\nabla_\alpha = i\frac{\partial}{\partial x} + j\frac{\partial}{\partial y}$. Therefore, the discretization of equation (1.11) are as follows:

$$\frac{\hat{f}_\alpha(\hat{x}, \hat{t} + \Delta\hat{t}) - \hat{f}_\alpha(\hat{x}, \hat{t})}{\Delta\hat{t}} \tag{1.12}$$

$$+ \hat{e}_{\alpha x}\frac{\hat{f}_\alpha(\hat{x} + \Delta\hat{x}, \hat{t} + \Delta\hat{t}) - \hat{f}_\alpha(\hat{x}, \hat{t} + \Delta\hat{t})}{\Delta\hat{x}}$$

$$+ \hat{e}_{\alpha y}\frac{\hat{f}_\alpha(\hat{x} + \Delta\hat{y}, \hat{t} + \Delta\hat{t}) - \hat{f}_\alpha(\hat{x}, \hat{t} + \Delta\hat{t})}{\Delta\hat{y}}$$

$$+ \hat{e}_{\alpha z}\frac{\hat{f}_\alpha(\hat{x} + \Delta\hat{z}, \hat{t} + \Delta\hat{t}) - \hat{f}_\alpha(\hat{x}, \hat{t} + \Delta\hat{t})}{\Delta\hat{z}}$$

$$= -\frac{1}{\hat{\tau}\epsilon}\left(\hat{f}_\alpha - \hat{f}_\alpha^{\,eq}\right)$$

The process continues with dividing the lattice space by the time step $\frac{\Delta\hat{x}}{\Delta\hat{t}} = \hat{e}_{\alpha x}, \frac{\Delta\hat{y}}{\Delta\hat{t}} = \hat{e}_{\alpha y}$ and $\frac{\Delta\hat{z}}{\Delta\hat{t}} = \hat{e}_{\alpha z}$, where it becomes Lagrangian in behaviour:

$$\frac{\hat{f}_\alpha(\hat{x},\hat{t}+\Delta\hat{t})-\hat{f}_\alpha(\hat{x},\hat{t})}{\Delta\hat{t}} \tag{1. 13}$$

$$+\frac{\hat{f}_\alpha(\hat{x}+\hat{e}_\alpha\Delta\hat{t},\hat{t}+\Delta\hat{t})-\hat{f}_\alpha(\hat{x},\hat{t}+\Delta\hat{t})}{\Delta\hat{t}}$$

$$=\frac{\hat{f}_\alpha(\hat{x}+\hat{e}_\alpha\Delta\hat{t},\hat{t}+\Delta\hat{t})-\hat{f}_\alpha(\hat{x},\hat{t})}{\Delta\hat{t}}$$

$$=-\frac{1}{\hat{t}\epsilon}\left(\hat{f}_\alpha-\hat{f}_\alpha^{\,eq}\right),$$

where $\boldsymbol{e}_\alpha=\{e_{\alpha x},e_{\alpha y},e_{\alpha z}\}$. By cancelling the two terms on the left hand side of above equation (1.13) and assuming $\Delta t=t_c$, multiplying equation (1.13) by $\Delta\hat{t}$ and dropping all carets leads to the BGK lattice Boltzmann equation. This can explicitly be articulated as follows:

$$f_\alpha(x+\boldsymbol{e}_\alpha\Delta t,t+\Delta t)-f_\alpha(x+t)=-\frac{1}{\tau}\left(f_\alpha-f_\alpha^{eq}\right). \tag{1. 14}$$

1. 3 Aims and Objectives

The primary objective of this research work is to improve the LBM for complex flows in geometries. The LBM application includes different types of free surface flows and long wave run-up problems. Turbulent flow circumstances, specifically eddy formation and flow patterns in open channels, are considered. The effect of friction at channel sidewalls,

which is modelled using a semi-slip boundary condition along the channel walls, will also be examined. Two moving boundary techniques are coupled with LBM to predict the wave run-up phenomenon within inshore regions. Long wave motion analyses for one and two-dimensional problems are presented.

1.4 Outline of Thesis

Chapter 2 deals with the governing equations of fluid flow. It includes a brief introduction to the Navier-Stokes (N-S) equations. The theory of hydrodynamics related to shallow water equations in their conservative form (for depth-averaged properties of water flows with and without turbulence) is also reviewed.

In Chapter 3 describes, the details of the LBM for shallow water flow modelling with and without turbulence terms. The main characteristics of the lattice pattern and the type of local equilibrium distribution function that are commonly used in the method are also explained. The Chapman-Enskog procedure used to model the shallow water equations is explained in detail.

In Chapter 4, various types of boundary conditions are described for wall and solid objects (e.g. no-slip, slip, etc) and inflow and outflow boundaries for the LBM.

Chapter 5 deals with schemes for the moving shoreline phenomenon in the lattice Boltzmann model. Use of thin film and linear extrapolation techniques is investigated.

The stability, errors and solution procedures of the lattice Boltzmann models are explained in Chapter 6.

The lattice Boltzmann model test results are presented and discussed in Chapter 7. The predicted results are compared with available experimental and analytical data. The tests are divided into three main studies: a) recirculating flows, b) sidewall friction and c) moving shoreline.

Finally, the conclusions of the thesis are presented in Chapter 8, followed by suggestions for future research.

Chapter 2 Governing Equations

2.0 Introduction

The laws of conservation of mass and momentum are the most fundamental in physics. In a system that using the law conservation of momentum, the amount of momentum remains constant in it. It is neither created nor destroyed. It is only changed through the action of forces (Newton's laws of motion) [93].

Water flows obey the laws of conservation of mass and momentum. The continuity equation and the Navier-Stokes (N-S) equations are a general set of flow equations that are based on these laws of conservation. In this chapter, the governing equations, the N-S equations, and shallow water equations with and without turbulence terms are described.

2.1 Navier-Stokes Equations

The governing equations for incompressible flows are the three-dimensional (3D) continuity and N-S equations [89]. The continuity equation is derived from the law of conservation of mass. The N-S equations arise from applying Newton's second law to a fluid element, together with the assumption that the fluid stress is the sum of a distributing viscous term proportional to the gradient of velocity and a pressure term [89].

Assuming the fluid is Newtonian and incompressible, the governing equations in Cartesian coordinates (see Figure 2.1) are as follows:

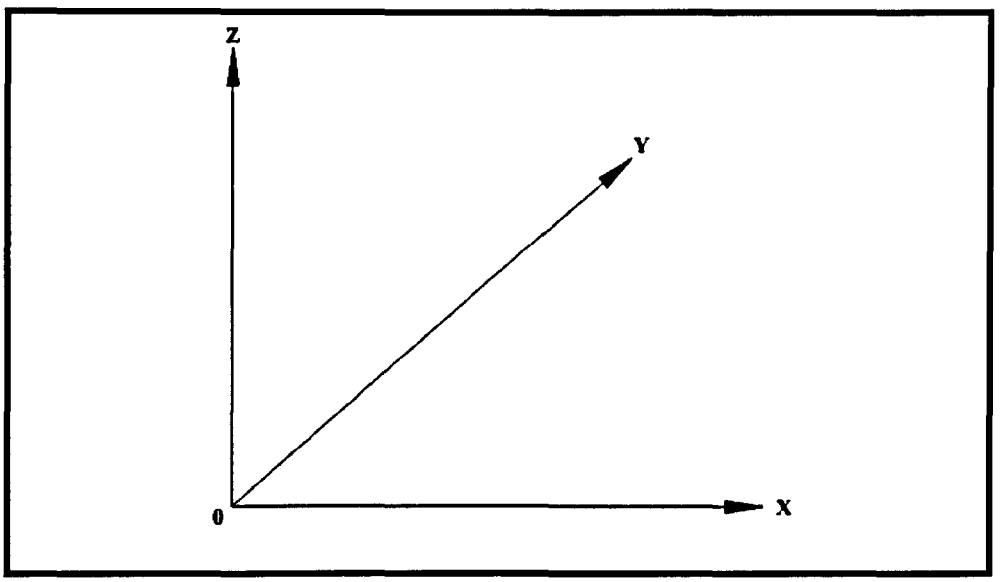

Figure 2. 1 Cartesian coordinate system: x, y represents a horizontal plane and z the vertical direction.

- Continuity equation:

$$\frac{\partial u}{\partial x}+\frac{\partial v}{\partial y}+\frac{\partial w}{\partial z}=0, \tag{2. 1}$$

- N-S equations in x, y and z components:

$$\frac{\partial u}{\partial t}+\frac{\partial uu}{\partial x}+\frac{\partial uv}{\partial y}+\frac{\partial uw}{\partial z} \tag{2. 2}$$

$$=-\frac{1}{\rho}\frac{\partial p}{\partial x}+\nu\left(\frac{\partial^2 u}{\partial x^2}+\frac{\partial^2 u}{\partial y^2}+\frac{\partial^2 u}{\partial z^2}\right)+f_x,$$

$$\frac{\partial v}{\partial t}+\frac{\partial uv}{\partial x}+\frac{\partial vv}{\partial y}+\frac{\partial wv}{\partial z} \tag{2.3}$$

$$=-\frac{1}{\rho}\frac{\partial p}{\partial y}+\nu\left(\frac{\partial^2 v}{\partial x^2}+\frac{\partial^2 v}{\partial y^2}+\frac{\partial^2 v}{\partial z^2}\right)+f_y,$$

$$\frac{\partial w}{\partial t}+\frac{\partial uw}{\partial x}+\frac{\partial vw}{\partial y}+\frac{\partial ww}{\partial z} \tag{2.4}$$

$$=-\frac{1}{\rho}\frac{\partial p}{\partial z}+\nu\left(\frac{\partial^2 w}{\partial x^2}+\frac{\partial^2 w}{\partial y^2}+\frac{\partial^2 w}{\partial z^2}\right)+f_z,$$

with u, v and w being the corresponding velocity components, f_x, f_y and f_z the body forces per unit mass in the particular direction, ρ the fluid density, t the time, ν the kinematic viscosity and p the pressure.

The left-hand sides of equations (2.2)–(2.4) are local and nonlinear advective acceleration terms. Even though exact solutions for certain specific flows have been found, the equations do not have a general analytical solution due to the presence of the nonlinear terms [94]. Meanwhile, the right-hand sides of the equations include pressure, gravitational or body and viscous force terms.

2.2 Shallow Water Equations

Water flows in rivers, channels, coastal areas, estuaries and harbours can be described and modelled with 3D or 2D shallow water equations. However, Stansby and Zhou [95] concluded that neither 3D nor 2D shallow water equations can predict the velocity in vertical direction accurately. Bearing this disadvantage in mind, the 2D shallow water equations are widely used as a mathematical model for shallow water flows [4], and as such, the current study also uses the 2D shallow water equations.

The 2D governing equations for shallow water flows can be derived from the general equations of continuity and the N-S equations (2.1) – (2.4). There are two body forces involved for water flows on the earth, which are gravity in the vertical direction and Coriolis acceleration in the horizontal plane [96]. They can be represented by equations (2.5) – (2.7) as follows [4]:

$$f_x = f_c v, \tag{2.5}$$

$$f_y = -f_c u, \tag{2.6}$$

$$f_z = -g, \tag{2.7}$$

where $g = 9.81\, m/s^2$ and $f_c = 2\omega \sin\phi$ are the gravitational acceleration and Coriolis parameter respectively. ϕ is the latitude of the

location on Earth and $\omega \approx 7.3 \times 10^{-5} rad/s$ is the Earth's rotational velocity. Accordingly, u and v are the velocity components in x and y directions.

In determining the continuity equation in depth-averaged cases, equation (2.1) is integrated over depth, based on Figure 2.2 as follows:

$$\int_{z_b}^{h+z_b} \left(\frac{\partial u}{\partial x} + \frac{\partial v}{\partial y} + \frac{\partial w}{\partial z}\right) dz = 0, \tag{2.8}$$

$$\int_{z_b}^{h+z_b} \frac{\partial u}{\partial x} dz + \int_{z_b}^{h+z_b} \frac{\partial v}{\partial x} dz + w_s - w_b = 0, \tag{2.9}$$

where w_s and w_b are the vertical velocities at the free surface and channel bed, respectively. h is the water depth and z_b is the bed elevation above the datum.

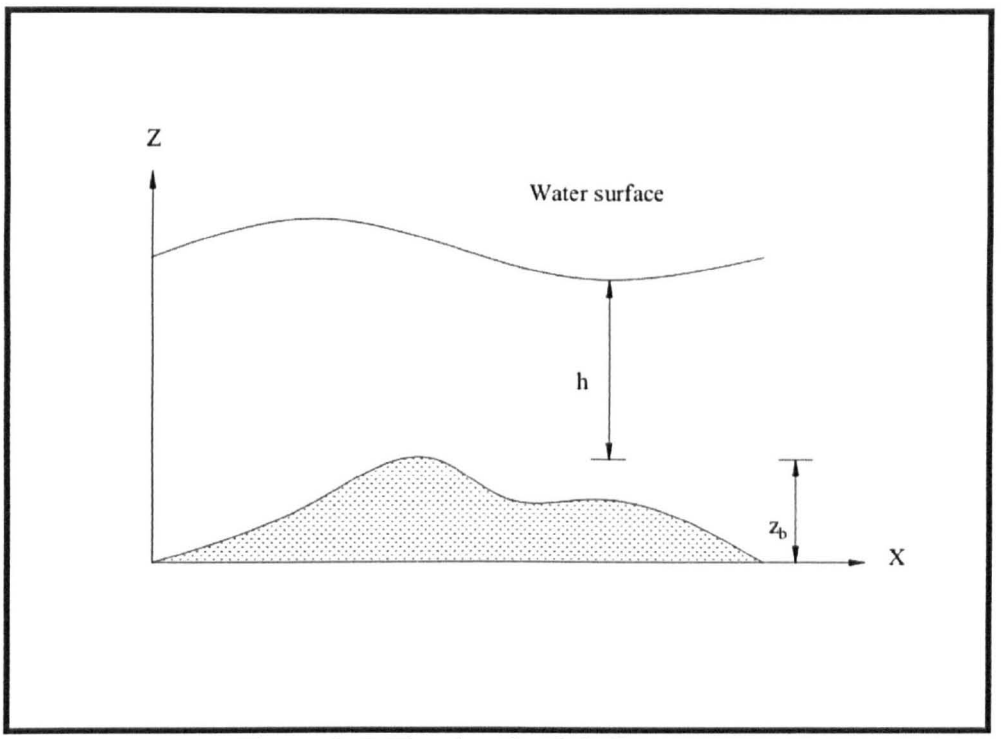

Figure 2. 2 The sketch of shallow water.

In the derivation, the first and second terms on the left hand side of equation (2.9) can be written according to Leibnitz's rule:

$$\int_{z_b}^{h+z_b} \frac{\partial u}{\partial x} dz = \frac{\partial}{\partial x} \int_{z_b}^{h+z_b} u dz - u_s \frac{\partial}{\partial x}(h + z_b) + u_b \frac{\partial z_b}{\partial x}, \tag{2. 10}$$

$$\int_{z_b}^{h+z_b} \frac{\partial v}{\partial y} dz = \frac{\partial}{\partial y} \int_{z_b}^{h+z_b} v dz - v_s \frac{\partial}{\partial y}(h + z_b) + v_b \frac{\partial z_b}{\partial y}. \tag{2. 11}$$

By inserting the equations (2.10) and (2.11) into (2.9) the following equation is obtained:

$$\frac{\partial}{\partial x}\int_{z_b}^{h+z_b} u dz + \frac{\partial}{\partial y}\int_{z_b}^{h+z_b} v dz \tag{2. 12}$$

$$+\left[w_s - u_s\frac{\partial}{\partial x}(h+z_b) - v_s\frac{\partial}{\partial y}(h+z_b)\right]$$

$$-\left(w_b - u_b\frac{\partial z_b}{\partial x} - v_b\frac{\partial z_b}{\partial y}\right) = 0.$$

The kinematic conditions at the free surface and channel bed are described respectively as follows:

$$w_s = \frac{\partial}{\partial t}(h+z_b) + u_s\frac{\partial}{\partial x}(h+z_b) + v_s\frac{\partial}{\partial y}(h+z_b), \tag{2. 13}$$

$$w_b = \frac{\partial z_b}{\partial t} + u_b\frac{\partial z_b}{\partial x} + v_b\frac{\partial z_b}{\partial y}. \tag{2. 14}$$

As a result, the continuity equation for shallow water flows for depth-averaged cases is obtained by insertion of equations (2.13) and (2.14) into (2.12),

$$\frac{\partial h}{\partial t} + \frac{\partial(h\bar{u})}{\partial x} + \frac{\partial(h\bar{v})}{\partial y} = 0, \tag{2. 15}$$

where $\bar{u}$ and $\bar{v}$ are depth-averaged velocity components defined as:

$$\bar{u} = \frac{1}{h}\int_{z_b}^{h+z_b} u dz, \tag{2. 16}$$

$$\bar{v} = \frac{1}{h}\int_{z_b}^{h+z_b} v dz, \tag{2. 17}$$

For the momentum equation in x-direction, equation (2.2) is integrated over the depth as follows:

$$\int_{z_b}^{h+z_b}\left[\frac{\partial u}{\partial t}+\frac{\partial(uu)}{\partial x}+\frac{\partial(vu)}{\partial y}+\frac{\partial(wu)}{\partial z}\right]dz \tag{2. 18}$$

$$= \int_{z_b}^{h+z_b} f_x v dz$$

$$+ \int_{z_b}^{h+z_b}\left[-\frac{1}{\rho}\frac{\partial p}{\partial x}+\nu\left(\frac{\partial^2 u}{\partial x^2}+\frac{\partial^2 u}{\partial y^2}+\frac{\partial^2 u}{\partial z^2}\right)\right]dz.$$

Based on the Leibnitz rule, the first three terms on the left hand side of equation (2.18) become

$$\int_{z_b}^{h+z_b}\frac{\partial u}{\partial t}dz = \frac{\partial}{\partial t}\int_{z_b}^{h+z_b} u dz - u_s\frac{\partial}{\partial t}(h+z_b)+u_b\frac{\partial z_b}{\partial t}, \tag{2. 19}$$

$$\int_{z_b}^{h+z_b}\frac{\partial uu}{\partial x}dz = \frac{\partial}{\partial x}\int_{z_b}^{h+z_b} uu dz - u_s u_s\frac{\partial}{\partial x}(h+z_b) \tag{2. 20}$$

$$+ u_b u_b\frac{\partial z_b}{\partial x},$$

and

$$\int_{z_b}^{h+z_b} \frac{\partial vu}{\partial y} dz = \frac{\partial}{\partial y} \int_{z_b}^{h+z_b} vudz - v_s u_s \frac{\partial}{\partial y}(h + z_b) + v_b u_b \frac{\partial z_b}{\partial y}. \quad (2.21)$$

The last term on the equation (2.18) can be integrated to give:

$$\int_{z_b}^{h+z_b} \frac{\partial wu}{\partial z} dz = w_s u_s - w_b u_b. \quad (2.22)$$

Equations (2.19) – (2.22) after rearranging yield:

$$\int_{z_b}^{h+z_b} \left[\frac{\partial u}{\partial t} + \frac{\partial (uu)}{\partial x} + \frac{\partial (vu)}{\partial y} + \frac{\partial (wu)}{\partial z}\right] dz \quad (2.23)$$

$$= \frac{\partial}{\partial t} \int_{z_b}^{h+z_b} udz + \frac{\partial}{\partial x} \int_{z_b}^{h+z_b} uudz + \frac{\partial}{\partial y} \int_{z_b}^{h+z_b} vudz + u_s \left[w_s - \frac{\partial}{\partial t}(h + z_b) - u_s \frac{\partial}{\partial x}(h + z_b) - v_s \frac{\partial}{\partial y}(h + z_b)\right] - u_b \left(w_b - \frac{\partial z_b}{\partial t} - u_b \frac{\partial z_b}{\partial x} - v_b \frac{\partial z_b}{\partial y}\right).$$

According to the kinematic conditions and depth-averaged velocity components of equations (2.13), (2.14) and (2.16) – (2.17) respectively, the above expression can be simplified to

$$\int_{z_b}^{h+z_b}\left[\frac{\partial u}{\partial t}+\frac{\partial(uu)}{\partial x}+\frac{\partial(vu)}{\partial y}+\frac{\partial(wu)}{\partial z}\right]dz \tag{2.24}$$

$$=\frac{\partial(\bar{u}h)}{\partial t}+\frac{\partial}{\partial x}\int_{z_b}^{h+z_b}uudz+\frac{\partial}{\partial y}\int_{z_b}^{h+z_b}vudz.$$

By considering the second mean value theorem for integrals, the second and third terms of the right hand side of equation (2.24) can be expressed as:

$$\int_{z_b}^{h+z_b}uudz=\breve{u}_1\int_{z_b}^{h+z_b}udz=\breve{u}_1h\bar{u}, \tag{2.25}$$

$$\int_{z_b}^{h+z_b}vudz=\breve{u}_2\int_{z_b}^{h+z_b}vdz=\breve{u}_2h\bar{v}. \tag{2.26}$$

Equations (2.25) and (2.26) are inserted into equation (2.24) by assuming $\breve{u}_1=\theta_1\bar{u}$ and $\breve{u}_2=\theta_2\bar{u}$. Hence, resulting in

$$\int_{z_b}^{h+z_b}\left[\frac{\partial u}{\partial t}+\frac{\partial(uu)}{\partial x}+\frac{\partial(vu)}{\partial y}+\frac{\partial(wu)}{\partial z}\right]dz \tag{2.27}$$

$$=\frac{\partial(h\bar{u})}{\partial t}+\frac{\partial(\theta_1h\bar{u}\bar{u})}{\partial x}+\frac{\partial(\theta_2h\bar{v}\bar{u})}{\partial y},$$

here, θ_1 and θ_2 are called the momentum correction factors. These can be described based on equation (2.25) and (2.26) as:

$$\theta_1 = \frac{1}{h\bar{u}\bar{u}} \int_{z_b}^{h+z_b} uudz, \tag{2.28}$$

$$\theta_2 = \frac{1}{h\bar{v}\bar{u}} \int_{z_b}^{h+z_b} vudz. \tag{2.29}$$

Equation (2.27) can be similarly expressed for the momentum equation in y direction (equation (2.3)). Thus, we obtain

$$\int_{z_b}^{h+z_b} \left[\frac{\partial v}{\partial t} + \frac{\partial (uv)}{\partial x} + \frac{\partial (vv)}{\partial y} + \frac{\partial (wv)}{\partial z}\right] dz \tag{2.30}$$

$$= \frac{\partial (h\bar{v})}{\partial t} + \frac{\partial (\theta_2 h\bar{u}\bar{v})}{\partial x} + \frac{\partial (\theta_3 h\bar{v}\bar{v})}{\partial y},$$

where the additional momentum correction factor θ_3 is defined as:

$$\theta_3 = \frac{1}{h\bar{v}\bar{v}} \int_{z_b}^{h+z_b} vvdz. \tag{2.31}$$

The reason that flow separation in the vertical direction is excluded in the 2D shallow water equations is related to the use of the second mean value theorem. This implies no change in the horizontal velocity components u and v over the water depth h at time t i.e., $u(x,y,z,t) \geq 0$ or $u(x,y,z,t) < 0$ is held from channel bed to free surface at the horizontal location (x,y), and so is $v(x,y,z,t)$.

In the momentum equation (2.18), the first term on the right hand side, Coriolis force, can be integrated as:

$$\int_{z_b}^{h+z_b} f_c v dz = f_c h \bar{v}. \tag{2.32}$$

Since the vertical acceleration in shallow water flows becomes unimportant compared with the horizontal effect [4], the momentum equation (2.2) – (2.4) in the vertical direction is reduced, with $w \approx 0$, to

$$\frac{\partial p}{\partial z} = -\rho g. \tag{2.33}$$

By integrating this, we obtain

$$p = -\rho g z + C, \tag{2.34}$$

where C is the integration constant. By assuming that the pressure at the free surface in equation (2.34) is atmospheric pressure p_a,

$$C = \rho g(h + z_b) + p_a. \tag{2.35}$$

Inserting equation (2.35) into (2.34) yields:

$$p = \rho g(h + z_b - z) + p_a. \tag{2.36}$$

In modelling hydraulic problems in a coastal, estuarine, etc, situation the atmospheric pressure p_a is always set as zero. This is due to the insignificant differences in atmospheric pressure at the water surface in practical situations [4]. Thus, equation (2.36) becomes a hydrostatic pressure approximation in shallow water flows such that:

$$p = \rho g(h + z_b - z). \tag{2.37}$$

Differentiating equation (2.37) with respect to x yields

$$\frac{\partial p}{\partial x} = \rho g \frac{\partial}{\partial x}(h + z_b). \tag{2.38}$$

The water depth h and the bed height z_b are not dependent on the vertical direction [4]. Hence, we obtain

$$\int_{z_b}^{h+z_b} \frac{\partial p}{\partial x} dz = \frac{h}{\rho} \frac{\partial p}{\partial x}. \tag{2.39}$$

Substituting (2.38) into (2.39) yields:

$$\int_{z_b}^{h+z_b} \frac{\partial p}{\partial x} dz = gh \frac{\partial}{\partial x}(h + z_b). \tag{2.40}$$

With the same procedure as above, the third and fourth terms on the right hand side of equation (2.18) can be expressed respectively as:

$$\int_{z_b}^{h+z_b} \nu \frac{\partial^2 u}{\partial x^2} dz \approx \nu \frac{\partial^2 (h\bar{u})}{\partial x \partial x}, \tag{2.41}$$

$$\int_{z_b}^{h+z_b} \nu \frac{\partial^2 u}{\partial y^2} dz \approx \nu \frac{\partial^2 (h\bar{u})}{\partial y \partial y}. \tag{2.42}$$

On the right hand side of equation (2.18), the last term can be derived as:

$$\int_{z_b}^{h+z_b} \nu \frac{\partial^2 u}{\partial z^2} dz = \left(\nu \frac{\partial u}{\partial z}\right)_s - \left(\nu \frac{\partial u}{\partial z}\right)_b. \tag{2.43}$$

The first and second terms on the right hand side of equation (2.43) can be approximated with the surface wind shear stress and the bed shear stress in x direction, respectively, as follows:

$$\left(\nu \frac{\partial u}{\partial z}\right)_s = \frac{\tau_{wx}}{\rho}, \tag{2.44}$$

$$\left(\nu \frac{\partial u}{\partial z}\right)_b = \frac{\tau_{bx}}{\rho}. \tag{2.45}$$

Thus, equation (2.43) becomes

$$\int_{z_b}^{h+z_b} \nu \frac{\partial^2 u}{\partial z^2} dz = \frac{\tau_{wx}}{\rho} - \frac{\tau_{bx}}{\rho}. \tag{2.46}$$

Insertion of equations (2.27), (2.32), (2.40) – (2.42) and (2.46) into (2.18) leads to the following momentum equation for shallow water flow in the x-direction.

$$\frac{\partial(h\bar{u})}{\partial t}+\frac{\partial(\theta_1 h\bar{u}\bar{u})}{\partial x}+\frac{\partial(\theta_2 h\bar{v}\bar{u})}{\partial y} \tag{2.47}$$

$$=-g\frac{\partial}{\partial x}\left(\frac{h^2}{2}\right)+\nu\frac{\partial^2(h\bar{u})}{\partial x\partial x}+\nu\frac{\partial^2(h\bar{u})}{\partial y\partial y}$$

$$-gh\frac{\partial z_b}{\partial x}+f_c h\bar{v}+\frac{\tau_{wx}}{\rho}-\frac{\tau_{bx}}{\rho}.$$

A similar derivation can be applied in the y-direction, leading to the y-momentum equation for shallow water flow,

$$\frac{\partial(h\bar{v})}{\partial t}+\frac{\partial(\theta_2 h\bar{u}\bar{v})}{\partial x}+\frac{\partial(\theta_3 h\bar{v}\bar{v})}{\partial y} \tag{2.48}$$

$$=-g\frac{\partial}{\partial y}\left(\frac{h^2}{2}\right)+\nu\frac{\partial^2(h\bar{v})}{\partial x\partial x}+\nu\frac{\partial^2(hv)}{\partial y\partial y}$$

$$-gh\frac{\partial z_b}{\partial y}+f_c h\bar{u}+\frac{\tau_{wy}}{\rho}-\frac{\tau_{by}}{\rho}.$$

The momentum correction factors θ_1, θ_2 and θ_3 can be determined by equations (2.28), (2.29) and (2.31) if velocity profiles for u and v are known. However, this may be difficult for flows involving circulation, or flows in complex geometry channels, for which no valid velocity profile is available [4]. Therefore, these momentum correction factors are frequently assumed to be equal to one in numerical analogues for shallow water flows. This has been found to provide a good approximation in most situations [20,97,98]. Using θ_1, θ_2 and $\theta_3 = 1$, equations (2.47) and (2.48) lead to

$$\frac{\partial(h\bar{u})}{\partial t}+\frac{\partial(h\bar{u}\bar{u})}{\partial x}+\frac{\partial(h\bar{v}\bar{u})}{\partial y} \tag{2.49}$$

$$=-g\frac{\partial}{\partial x}\left(\frac{h^2}{2}\right)+\nu\frac{\partial^2(h\bar{u})}{\partial x\partial x}+\nu\frac{\partial^2(h\bar{u})}{\partial y\partial y}$$

$$-gh\frac{\partial z_b}{\partial x}+f_c h\bar{v}+\frac{\tau_{wx}}{\rho}-\frac{\tau_{bx}}{\rho}.$$

$$\frac{\partial(h\bar{v})}{\partial t}+\frac{\partial(h\bar{u}\bar{v})}{\partial x}+\frac{\partial(h\bar{v}\bar{v})}{\partial y} \tag{2.50}$$

$$=-g\frac{\partial}{\partial y}\left(\frac{h^2}{2}\right)+\nu\frac{\partial^2(h\bar{v})}{\partial x\partial x}+\nu\frac{\partial^2(hv)}{\partial y\partial y}$$

$$-gh\frac{\partial z_b}{\partial y}+f_c h\bar{u}+\frac{\tau_{wy}}{\rho}-\frac{\tau_{by}}{\rho}.$$

Hence, the continuity equation (2.15) and momentum equations (2.49) and (2.50) after dropping the overbars can be expressed in a tensor form as:

$$\frac{\partial h}{\partial t}+\frac{\partial(hu_j)}{\partial x_j}=0, \tag{2.51}$$

$$\frac{\partial(hu_i)}{\partial t}+\frac{\partial(hu_iu_j)}{\partial x_j}=-g\frac{\partial}{\partial x_i}\left(\frac{h^2}{2}\right)+\nu\frac{\partial^2(hu_i)}{\partial x_j x_j}+F_i, \tag{2.52}$$

where the force term F_i is defined as:

$$F_i=-gh\frac{\partial z_b}{\partial x_i}+\frac{\tau_{wi}}{\rho}-\frac{\tau_{bi}}{\rho}+E_i, \tag{2.53}$$

and the Coriolis term E_i is given by:

$$E_i = \begin{cases} f_c hv, & i = x, \\ -f_c hu, & i = y. \end{cases} \quad (2.54)$$

The bed shear stress τ_{bi} in the i direction can be determined by the depth-averaged velocities as:

$$\tau_{bi} = \rho C_b u_i \sqrt{u_j u_j}, \quad (2.55)$$

where the bed friction coefficient, C_b, which may be either constant or estimated based on the Chézy coefficient, C_z and the Manning equation, respectively as follows:

$$C_b = \frac{g}{C_z^2}, \quad (2.56)$$

$$C_b = \frac{g n_b^2}{h^{1/3}}. \quad (2.57)$$

Here, the Chézy coefficient can also be calculated as $C_z = h^{1/6}/n_b$, where n_b is the bed Manning coefficient, or by the Colebrook-White equation as follows [99]:

$$C_z = -\sqrt{32g} log_{10}\left(\frac{K_s}{14.8h} + \frac{1.255\nu\, C_z}{4\sqrt{2g}h\sqrt{u_i u_i}}\right), \quad (2.58)$$

where, K_s is the Nikuradse equivalent sand roughness. The wind shear stress τ_{wi} is frequently expressed as:

$$\tau_{wi} = \rho_a C_w u_{wi} \sqrt{u_{wj} u_{wj}}, \tag{2. 59}$$

where ρ_a is the air density, C_w is the wind resistance coefficient and u_{wi} is the wind velocity component in the direction i.

2.3 Space-filtered Navier-Stokes Equations for Turbulent Flows

Generally, water flows in rivers, estuaries, coasts, open channels, etc, are mostly turbulent. There are two approaches based on the modified N-S equations that are used to determine the turbulent features in numerical models [4]. The first is the time-averaged N-S equation, or Reynolds equation together with k-ε turbulence model. The second is known as the space-filtered N-S equations with the large eddy simulation (LES) and a subgrid-scale stress (SGS) model for the unresolved scale stress.

According to Piomelli [100], only the large, energy-containing scales are resolved in the LES, whereas the small subgrid scales whose effect appears through a residual stress term are not modelled. The modelling of subgrid scales (which is responsible for only a fraction of the momentum and energy transport) is easier than the modelling of all scales of motion

required in Reynolds equations. Moreover, subgrid scale modelling requires less computational effort than the direct numerical simulation of the N-S equations [4].

Better results are usually obtained using the N-S equations with LES [44]. The solutions are more accurate and the detailed characteristics of turbulent flows such as the fluctuation of a physical quantity. LES has been successfully applied to the study of various transitional and turbulent flows [4,100].

In LES, the flow variables are decomposed into a large-scale component and a subgrid-scale component. The large-scale component (denoted by a tilde) is defined by the filtering operation as [100]:

$$\tilde{f}(x) = \int_D \tilde{G}(x, \acute{x}) f(\acute{x}) d\acute{x}, \tag{2. 60}$$

where the integral is extended over the single lattice D, and $\tilde{G}$ is the grid filter function.

The filtered N-S and the continuity equations, which describe the evolution of the large, energy-carrying eddies, can be expressed by applying the filtering operation to the incompressible N-S equation (2.52) and continuity equation (2.51) to yield [4,100,101]:

$$\frac{\partial \tilde{u}_i}{\partial t} + \frac{\partial(\tilde{u}_i \tilde{u}_j)}{\partial x_j} = f_i - \frac{1}{\rho}\frac{\partial(p)}{\partial x_i} + \nu \frac{\partial^2(\tilde{u}_i)}{\partial x_j \partial x_j} - \frac{\partial \tau_{ij}}{\partial x_j}, \tag{2. 61}$$

$$\frac{\partial \tilde{u}_j}{\partial x_j} = 0, \tag{2. 62}$$

where $\tilde{u}_i$ is the space-filtered velocity component in the *i* direction,

$$\tilde{u}_i(x,y,z,t) = \iiint_{\Delta x \Delta y \Delta z} u(x,y,z,t)\tilde{G}(x,y,z,\acute{x},\acute{y},\acute{z})d\acute{x}d\acute{y}d\acute{z}. \tag{2. 63}$$

τ_{ij} n the above expression (2.61) is called the SGS which reflects the effects of the unresolved scales with the resolved scale, i.e.

$$\tau_{ij} = \widetilde{u_i u_j} - \tilde{u}_i \tilde{u}_j, \tag{2. 64}$$

which must be modelled. Hence, the SGS with an SGS eddy viscosity that corresponds to the Boussinesq assumption for turbulent flows can be expressed as:

$$\tau_{ij} = -\nu_e \left(\frac{\partial \tilde{u}_i}{\partial x_j} + \frac{\partial \tilde{u}_j}{\partial x_i}\right). \tag{2. 65}$$

The new momentum equation based on the SGS method is obtained by substituting (2.65) into (2.61), as follows:

$$\frac{\partial \tilde{u}_i}{\partial t} + \frac{\partial(\tilde{u}_i \tilde{u}_j)}{\partial x_j} = f_i - \frac{1}{\rho}\frac{\partial p}{\partial x_i} + (\nu + \nu_e)\frac{\partial^2(\tilde{u}_i)}{\partial x_j \partial x_j}, \tag{2. 66}$$

in which the eddy viscosity is defined as:

$$\nu_e = (C_s \ell_s)^2 \sqrt{S_{ij} S_{ij}}, \tag{2. 67}$$

where C_s is the Smagorinsky constant; ℓ_s is the characteristic length scale and S_{ij} is the magnitude of the large scale strain-rate tensor,

$$S_{ij} = \frac{1}{2}\left(\frac{\partial \tilde{u}_i}{\partial x_j} + \frac{\partial \tilde{u}_j}{\partial x_i}\right). \tag{2. 68}$$

The modified continuity and N-S equations are applicable to turbulent flows. In practice, the resolved large-scale fields are numerically solved and the effect of unresolved scale eddies is modelled with an SGS model. By application of the SGS model to the LBM, it is expected to that accurate solutions will be produced turbulent flows. This is due to the grid size, with the mesh size in the LBM being much smaller than that required by a traditional computational method for fluid flows. Hence, the finer grid size will lead to fewer unresolved scale eddies [4]. The modelling of SGS for LES in the LBM for shallow water flows is described in detail in the next section.

2.4 Determination of the Eddy Viscosity

The SGS model is used for modelling flow turbulence as indicated in the previous section. To include the turbulence effects, the shallow water equations (2.60) and (2.61) need to be modified accordingly as [4]:

$$\frac{\partial h}{\partial t}+\frac{\partial(h\tilde{u}_j)}{\partial x_j}=0, \tag{2.69}$$

$$\frac{\partial(h\tilde{u}_i)}{\partial t}+\frac{\partial(h\tilde{u}_i\tilde{u}_j)}{\partial x_j}=-g\frac{\partial}{\partial x_i}\left(\frac{h^2}{2}\right)+(\nu+\nu_e)\frac{\partial^2(h\tilde{u}_i)}{\partial x_j\partial x_j}+F_i. \tag{2.70}$$

The use of depth-averaged space-filtered velocity components differentiates the above equations from equations (2.51) and (2.52), where the eddy viscosity ν_e is defined by:

$$-\nu_e=\frac{\tau_{ij}}{\left(\frac{\partial\tilde{u}_i}{\partial x_j}+\frac{\partial\tilde{u}_j}{\partial x_i}\right)}. \tag{2.71}$$

The eddy viscosity in (2.71) retains the same form as equation (2.67), such that

$$\nu_e=(C_s\ell_s)^2\sqrt{S_{ij}S_{ij}}. \tag{2.72}$$

Instead of using equation (2.68), S_{ij} is replaced with

$$S_{ij} = \frac{1}{2h}\left(\frac{\partial(h\tilde{u}_i)}{\partial x_j} + \frac{\partial(h\tilde{u}_j)}{\partial x_i}\right). \tag{2.73}$$

The depth-averaged subgrid-scale stress τ_{ij} with eddy viscosity is calculated from:

$$\tau_{ij} = -2h\nu_e S_{ij}. \tag{2.74}$$

The force term F_i in equation (2.70) is defined by equation (2.53). For convenience, the tildes of u_j in the continuity and momentum equations (2.69) and (2.70) are dropped, resulting in the same form of general shallow water equations. But it should be remembered that the corresponding symbols represent the space-filtered variables:

$$\frac{\partial h}{\partial t} + \frac{\partial(hu_j)}{\partial x_j} = 0, \tag{2.75}$$

$$\frac{\partial(hu_i)}{\partial t} + \frac{\partial(hu_i u_j)}{\partial x_j} = -g\frac{\partial}{\partial x_i}\left(\frac{h^2}{2}\right) + (\nu + \nu_e)\frac{\partial^2(hu_i)}{\partial x_j \partial x_j} + F_i. \tag{2.76}$$

Chapter 3 Lattice Boltzmann Method

3.0 Introduction

The LBM is a class of computational fluid dynamics (CFD) methods for fluid simulation. Specifically for the numerical simulation of physical phenomena, LBM serves as an alternative to classical solutions of partial differential equations (PDE) [4,38,88,102]. The main field of application is fluid dynamics and it solves the incompressible N-S equation [81,102].

The strength of the LBM lies in its ability to easily represent complex physical phenomena, ranging from multiphase flows to fluids with chemical reactions [4]. As the method is based on a molecular description of a fluid, knowledge of microscopic physics can be directly used to formulate an adequate numerical model [32,103]. The three unique features of the LBM include the linear convection operator, the simple equation for pressure calculation, and the minimal set of velocities in phase space [32].

The main topic of this thesis is the modelling of flows in shallow water regions using the LBM. This is now described, including the derivation of the lattice Boltzmann equation with the lattice pattern and the local equilibrium distribution function. The modelling of terms such as those related to flow turbulence is also taken into consideration, and is followed by the modelling of the force term in the LBM.

3.1 Lattice Boltzmann Method for Shallow Water Flows

A LBM has been successfully used to study shock waves [42,43], multiphase flows [30,104], and turbulent flows [31,36]. The LBM based shallow water model has produced accurate results for rapidly and gradually varied open channel flow problems [39,40,42-46].

However, a robust numerical method that can dependably and precisely solve the shallow water equations over variable topography in extensive conditions is required. Therefore, Zhou [44] proposed a lattice Boltzmann model for shallow water flows considering the flow turbulence by using the LABSWE^{TM}. A centred scheme for the force term is applied in the lattice Boltzmann equation and this will be elaborated in section 3.31.

3.1.1 Lattice Boltzmann Equation

In lattice Boltzmann theory [4], the streaming and collision steps are the main two steps that make up the LBM. In the streaming step, particles that move towards their nearest neighbours at their own velocities and their directions are governed by:

$$f_\alpha(x + e_\alpha \Delta t, t + \Delta t) = \acute{f}_\alpha(x,t) + \frac{\Delta t}{N_\alpha e^2} e_{\alpha i} F_i(x,t), \tag{3.1}$$

where f_α is the particle distribution function; $\acute{f}_\alpha$ is the value of f_α before the streaming; e_α is the velocity vector of a particle in the α link; $e = \Delta x/\Delta t$, where Δx and Δt is the lattice size and time step respectively; N_α is a constant decided by the lattice pattern as:

$$N_\alpha = \frac{1}{e^2}\sum_\alpha e_{\alpha x} e_{\alpha x} = \frac{1}{e^2}\sum_\alpha e_{\alpha y} e_{\alpha y} \tag{3.2}$$

Meanwhile, in the collision step, the particles arrive and interact with one another and change their velocities and directions according to the rules of scattering, denoted by:

$$\acute{f}_\alpha(x,t) = f_\alpha(x,t) + \Omega_\alpha[f(x,t)], \tag{3.3}$$

where Ω_α is the collision operator that controls the speed of change in f_α during collision.

The collision operator Ω_α is a matrix and can be obtained from kinetic theory. However, due to the complexity of the analytic solutions, Higuera and Jimenez [105] proposed a fundamentally important idea of simplifying the collision operator. They linearized the collision operator around its local equilibrium state. This collision operator Ω_α is then

expanded in terms of its equilibrium value. Referring to Chen [106], the operator is as follows:

$$\Omega_\alpha(f) = \Omega_\alpha(f^{eq}) + \frac{\partial \Omega_\alpha(f^{eq})}{\partial f_\beta}\left(f_\beta - f_\beta^{eq}\right) + O\left[\left(f_\beta - f_\beta^{eq}\right)^2\right], \tag{3.4}$$

where f^{eq} is the local equilibrium distribution function.

By neglecting the higher-order terms in equation (3.4) and implying that $\Omega_\alpha(f^{eq}) \approx 0$, a linearized collision operator (equation (3.5)) is obtained:

$$\Omega_\alpha(f) \approx -\frac{\partial \Omega_\alpha(f^{eq})}{\partial f_\beta}\left(f_\beta - f_\beta^{eq}\right). \tag{3.5}$$

By assuming $f_\beta \to f_\beta^{eq}$, and the local particle distribution relaxes to an equilibrium state at a single rate τ [4,51,52] (3.5) yields

$$\frac{\partial \Omega_\alpha(f^{eq})}{\partial f_\beta} = -\frac{1}{\tau}\delta_{\alpha\beta}, \tag{3.6}$$

where $\delta_{\alpha\beta}$ is the Kronecker delta function:

$$\delta_{\alpha\beta} = \begin{cases} 0 & \alpha \neq \beta, \\ 1 & \alpha = \beta. \end{cases} \tag{3.7}$$

Hence, equation (3.5) can be rewritten as:

$$\Omega_\alpha(f) = -\frac{1}{\tau}\delta_{\alpha\beta}(f_\alpha - f_\alpha^{eq}) = -\frac{1}{\tau}\delta_{\alpha\beta}\left(f_\beta - f_\beta^{eq}\right). \tag{3.8}$$

Equation (3.8) results in the lattice BGK collision operator:

$$\Omega_\alpha(f) = -\frac{1}{\tau}(f_\alpha - f_\alpha^{eq}), \tag{3.9}$$

where τ is so-called single relaxation time. By substituting the collision operator (3.9) into (3.3), the most popular lattice Boltzmann equation or the so-called single relaxation time lattice Boltzmann equation can be expressed as follows [4]:

$$f_\alpha(\boldsymbol{x} + \boldsymbol{e}_\alpha \Delta t, t + \Delta t) - f_\alpha(\boldsymbol{x}, t) \tag{3.10}$$
$$= -\frac{1}{\tau}(f_\alpha - f_\alpha^{eq}) + \frac{\Delta t}{N_\alpha e^2} e_{\alpha i} F_i.$$

3.1.2 Lattice Pattern

There are two main functions for the lattice application in the LBM. It is used numerically for representing grid points and determining the motion of a particle.

In 2D modelling, square and hexagonal lattices are commonly used. The square lattice can have 4, 5, 8 and 9-velocity models. Meanwhile, the hexagonal lattice can have 6 and 7-velocity models (see Figures 3.1 and 3.2), where for each of these patterns, the particle speed can vary at each node of the lattice.

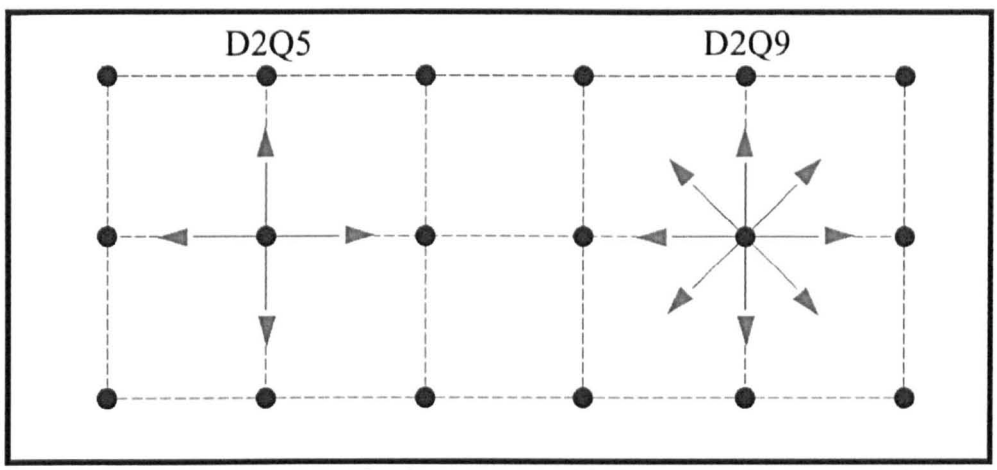

Figure 3. 1 The square lattice pattern with 5 and 9-velocity models.

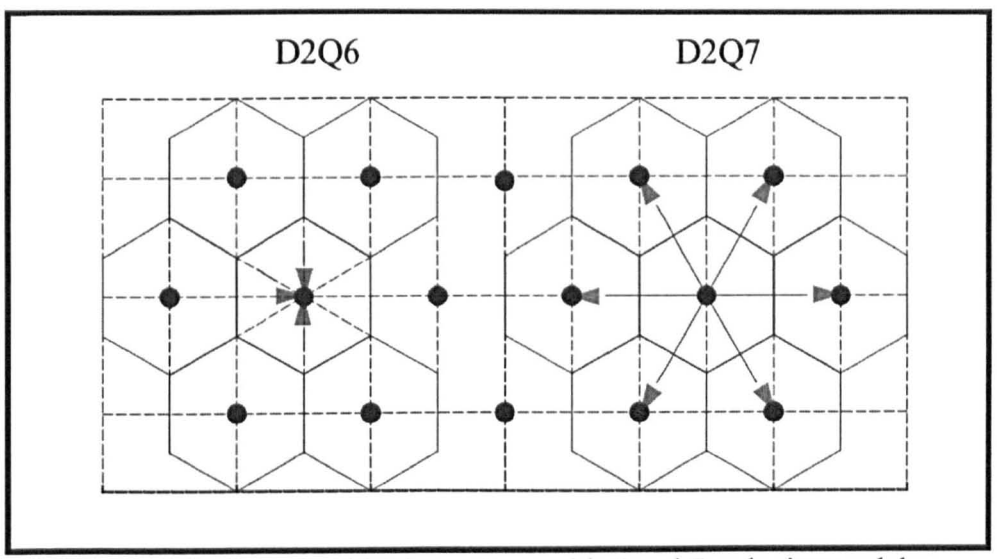

Figure 3. 2 Hexagonal lattice pattern with 6 and 7-velocity models.

All these models follow the same naming scheme DXQY, where X indicates the number of dimensions of the lattice model and Y implies the number of discrete velocities in the model [91] e.g., D2Q9 specifies a 2D lattice model with nine velocity directions.

Nevertheless, not all of these models have sufficient lattice symmetry, which is the most important requirement for recovery of the correct flow equations [87]. The 9-velocity square lattice and 7-speed hexagonal lattice provide satisfactory performance in numerical simulations as indicated by theoretical and numerical analyses [4]. These lattices are widely used in the LBM.

The square lattice makes it easier in terms of boundary implementation [107]. The use of square lattice pattern in the LBM is also supported by the fact that it usually gives more accurate results than that based on the hexagonal lattice [108]. Thus, the 9-velocity square lattice is preferred in practice.

Particle movement in the 9-velocity square lattice begins with each particle moving on a lattice unit at its velocity along one of the eight links specified 1-8, while zero is denoted as a resting particle with zero speed as Figure 3.3.

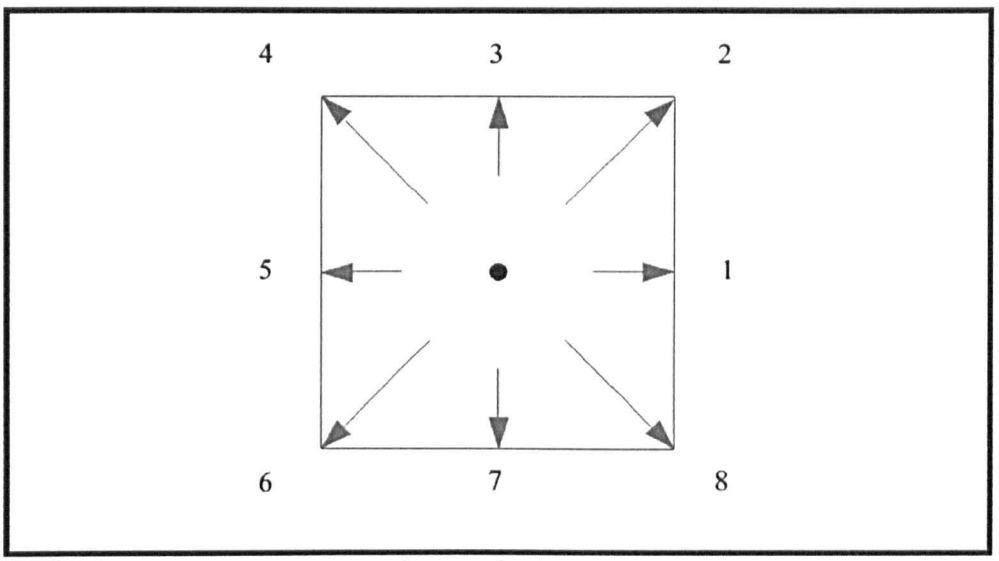

Figure 3. 3 The 9-velocity lattice pattern.

According to this lattice, the velocity vector of particles can be defined as:

$$\boldsymbol{e}_{\alpha} = \begin{cases} (0,0) & \alpha = 0, \\ e\left[cos\dfrac{(\alpha-1)\pi}{4}, sin\dfrac{(\alpha-1)\pi}{4}\right] & \alpha = 1,3,5,7, \\ \sqrt{2}e\left[cos\dfrac{(\alpha-1)\pi}{4}, sin\dfrac{(\alpha-1)\pi}{4}\right] & \alpha = 2,4,6,8. \end{cases} \quad (3.\ 11)$$

The basic features of the 9-velocity square lattice are follows [4]:

$$\sum_{\alpha} e_{\alpha i} = \sum_{\alpha} e_{\alpha i} e_{\alpha j} e_{\alpha k} = 0, \tag{3.12}$$

$$\sum_{\alpha} e_{\alpha i} e_{\alpha j} = 6e^2 \delta_{ij}, \tag{3.13}$$

$$\sum_{\alpha} e_{\alpha i} e_{\alpha j} e_{\alpha k} e_{\alpha l} = 4e^4 \left(\delta_{ij}\delta_{kl} + \delta_{ik}\delta_{jl} + \delta_{il}\delta_{jk}\right) - 6e^4 \Delta_{ijkl}, \tag{3.14}$$

where

$$\Delta_{ijkl} = \begin{cases} 1, & i = j = k = l, \\ 0, & otherwise. \end{cases} \tag{3.15}$$

Substitution of equation (3.11) into (3.2) yields:

$$N_{\alpha} = \frac{1}{e^2} \sum_{\alpha} e_{\alpha x} e_{\alpha x} = \frac{1}{e^2} \sum_{\alpha} e_{\alpha y} e_{\alpha y} = 6. \tag{3.16}$$

Insertion of (3.16) into (3.10) leads to the most common form of the lattice Boltzmann model used for simulating shallow water flows:

$$f_{\alpha}(\boldsymbol{x} + \boldsymbol{e}_{\alpha}\Delta t, t + \Delta t) - f_{\alpha}(\boldsymbol{x}, t) \tag{3.17}$$

$$= -\frac{1}{\tau}\left(f_{\alpha} - f_{\alpha}^{eq}\right) + \frac{\Delta t}{6e^2} \boldsymbol{e}_{\alpha i} F_i.$$

3.1.3 Local Equilibrium Distribution Function: Shallow Water Flow Modelling

A suitable equilibrium distribution function needs to be chosen for the LBM, as it plays an important role in deciding the flow equations to be solved by the lattice Boltzmann equation (3.17) [4].

Maxwellian distributions usually expanded as Taylor series in macroscopic velocity to second order have become the functions of choice in LGCA models [4]. By using the same approach, the Maxwell-Boltzmann function can be used to solve the lattice Boltzmann equation. However, this can only be used to recover the N-S equation, and are not particularly apply to the shallow water equations. Therefore, in order to recover the shallow water condition, the so-called Ansatz method is used [82].

An equilibrium distribution function can be expressed by using the Ansatz method as a power series in macroscopic velocity such as [4]:

$$f_\alpha^{eq} = A_\alpha + B_\alpha e_{\alpha i} u_i + C_\alpha e_{\alpha i} e_{\alpha j} u_i u_j + D_\alpha u_i u_i. \qquad (3.18)$$

The above general approach is used herein, as it is known to provide satisfactory solutions of various flow problems [4,31,109].

In terms of symmetry, the equilibrium distribution function (3.18) is the same as in the lattice shown in Figure 3.3, and is expressed as:

$$A_1 = A_3 = A_5 = A_7 = \bar{A}, \tag{3.19}$$

$$A_2 = A_4 = A_6 = A_8 = \tilde{A}, \tag{3.20}$$

Similar results are also obtained for B_α, C_α and D_α. Thus, for convenience, the equilibrium distribution function can be written as:

$$f_\alpha^{eq} \tag{3.21}$$

$$= \begin{cases} A_0 + D_0 u_i u_i, & \alpha = 0, \\ \bar{A} + \bar{B} e_{\alpha i} u_i + \bar{C} e_{\alpha i} e_{\alpha j} u_i u_j + \bar{D} u_i u_i, & \alpha = 1,3,5,7, \\ \tilde{A} + \tilde{B} e_{\alpha i} u_i + \tilde{C} e_{\alpha i} e_{\alpha j} u_i u_j + \tilde{D} u_i u_i, & \alpha = 2,4,6,8. \end{cases}$$

The unknown coefficients in the above equation (3.21) can be determined, based on constraints of the equilibrium distribution function that obey the mass and momentum conservation laws. Therefore, for the shallow water equation, three conditions have to be satisfied:

$$\sum_{\alpha} f_{\alpha}^{eq}(\boldsymbol{x},t) = h\,(\boldsymbol{x},t), \tag{3.22}$$

$$\sum_{\alpha} e_{\alpha i} f_{\alpha}^{eq}(\boldsymbol{x},t) = h\,(\boldsymbol{x},t) u_i(\boldsymbol{x},t), \tag{3.23}$$

$$\sum_{\alpha} e_{\alpha i} e_{\alpha j} f_{\alpha}^{eq}(\boldsymbol{x},t) \tag{3.24}$$

$$= \frac{1}{2} g h^2(\boldsymbol{x},t)\delta_{ij} + h(\boldsymbol{x},t) u_i(\boldsymbol{x},t) u_j(\boldsymbol{x},t).$$

Insertion of equation (3.21) into (3.22) yields:

$$A_0 + D_0 u_i u_i + 4\bar{A} + \sum_{\alpha=1,3,5,7} \bar{B} e_{\alpha i} u_i + \sum_{\alpha=1,3,5,7} \bar{C} e_{\alpha i} e_{\alpha j} u_i u_j \tag{3.25}$$

$$+ 4\bar{D} u_i u_i + 4\tilde{A} + \sum_{\alpha=2,4,6,8} \tilde{B} e_{\alpha i} u_i$$

$$+ \sum_{\alpha=2,4,6,8} \tilde{C} e_{\alpha i} e_{\alpha j} u_i u_j + 4\tilde{D} u_i u_i = h.$$

By substituting (3.25) into (3.11) and correlating h and $u_i u_i$, the following expressions are obtained:

$$A_0 + 4\bar{A} + 4\tilde{A} = h, \tag{3.26}$$

and

$$D_0 + 2e^2\bar{C} + 4e^2\tilde{C} + 4\bar{D} + 4\tilde{D} = 0. \tag{3.27}$$

Insertion of (3.21) into (3.23) yields:

$$A_0 e_{\alpha i} + D_0 e_{\alpha i} u_j u_j \tag{3.28}$$

$$+ \sum_{\alpha=1,3,5,7} (\bar{A} e_{\alpha i} + \bar{B} e_{\alpha i} e_{\alpha j} u_j$$

$$+ \bar{C} e_{\alpha i} e_{\alpha j} e_{\alpha k} u_j u_k + \bar{D} e_{\alpha i} u_j u_j)$$

$$+ \sum_{\alpha=2,4,6,8} (\tilde{A} e_{\alpha i} + \tilde{B} e_{\alpha i} e_{\alpha j} u_j$$

$$+ \tilde{C} e_{\alpha i} e_{\alpha j} e_{\alpha k} u_j u_k + \tilde{D} e_{\alpha i} u_j u_j) = h u_i,$$

from which we obtain:

$$2e^2 \bar{B} + 4e^2 \tilde{B} = h. \tag{3.29}$$

Substitution of (3.21) into (3.24) gives below:

$$\sum_{\alpha=1,3,5,7} (\bar{A} e_{\alpha i} e_{\alpha j} + \bar{B} e_{\alpha i} e_{\alpha j} e_{\alpha k} u_k + \bar{C} e_{\alpha i} e_{\alpha j} e_{\alpha k} e_{\alpha l} u_k u_l \tag{3.30}$$

$$+ \bar{D} e_{\alpha i} e_{\alpha j} u_k u_k)$$

$$+ \sum_{\alpha=2,4,6,8} (\tilde{A} e_{\alpha i} e_{\alpha j} + \tilde{B} e_{\alpha i} e_{\alpha j} e_{\alpha k} u_k$$

$$+ \tilde{C} e_{\alpha i} e_{\alpha j} e_{\alpha k} e_{\alpha l} u_k u_l + \tilde{D} e_{\alpha i} e_{\alpha j} u_k u_k)$$

$$= \frac{1}{2} g h^2 \delta_{ij} + h u_i u_j.$$

Equation (3.30) can be simplified using equation (3.11), yielding:

$$2\bar{A}e^2\delta_{ij} + 2\bar{C}e^4u_iu_i + 2\bar{D}e^2u_iu_i + 4\tilde{A}e^2\delta_{ij} + 8\tilde{C}e^4u_iu_j \quad (3.31)$$

$$+ 4\tilde{C}e^4u_iu_i + 4\tilde{D}e^2u_iu_i = \frac{1}{2}gh^2\delta_{ij} + hu_iu_j,$$

from which:

$$2\bar{A}e^2 + 4\tilde{A}e^2 = \frac{1}{2}gh^2, \quad (3.32)$$

$$8e^4\tilde{C} = h, \quad (3.33)$$

$$2e^4\bar{C} = h, \quad (3.34)$$

and

$$2\bar{D}e^2 + 4\tilde{D}e^2 + 4\tilde{C}e^4 = 0. \quad (3.35)$$

Combining (3.33) and (3.34) gives:

$$\bar{C} = 4\tilde{C}. \quad (3.36)$$

Based on the symmetrical lattice that has been shown in equation (3.36), three additional relations can also be assumed as:

$$\bar{A} = 4\tilde{A}. \quad (3.37)$$

$$\bar{B} = 4\tilde{B}. \quad (3.38)$$

and

$$\bar{D} = 4\tilde{D}. \quad (3.39)$$

The unknown coefficient is determined by solving equations (3.26), (3.27), (3.28) and (3.32) – (3.39). Hence,

$$A_0 = h - \frac{5gh^2}{6e^2}, \quad D_0 = -\frac{2h}{3e^2}, \tag{3.40}$$

$$\bar{A} = \frac{gh^2}{6e^2}, \quad \bar{B} = \frac{h}{3e^2}, \quad \bar{C} = \frac{h}{2e^4}, \quad \bar{D} = -\frac{h}{6e^2}, \tag{3.41}$$

$$\tilde{A} = \frac{gh^2}{24e^2}, \quad \tilde{B} = \frac{h}{12e^2}, \quad \tilde{C} = \frac{h}{8e^4}, \quad \tilde{D} = -\frac{h}{24e^2}, \tag{3.42}$$

These coefficients (equations (3.40) – (3.42)) are then inserted into equation (3.21), which leads to the following local equilibrium distribution function:

$$f_\alpha^{eq} \tag{3.43}$$

$$= \begin{cases} h - \frac{5gh^2}{6e^2} - \frac{2h}{3e^2} u_i u_i, & \alpha = 0, \\ \frac{gh^2}{6e^2} + \frac{h}{3e^2} e_{\alpha i} u_i + \frac{h}{2e^4} e_{\alpha i} e_{\alpha j} u_i u_j - \frac{h}{6e^2} u_i u_i, & \alpha = 1,3,5,7, \\ \frac{gh^2}{24e^2} + \frac{h}{12e^2} e_{\alpha i} u_i + \frac{h}{8e^4} e_{\alpha i} e_{\alpha j} u_i u_j - \frac{h}{24e^2} u_i u_i, & \alpha = 2,4,6,8. \end{cases}$$

This local equilibrium distribution function is then used in the lattice Boltzmann equation (3.17) for solving the shallow water equations (2.51) and (2.52).

3.1.4 Macroscopic Properties

A few more steps are required to solve the shallow water equations (2.51) and (2.52). The main tasks are to determine physical quantities such as the water depth h and the velocity components. Zhou [4] carried out a microscopic examination of the lattice Boltzmann equation (3.17) by taking the sum of the zeroth moment of the distribution function in equation (3.17) over the lattice velocities as follows:

$$\sum_{\alpha}[f_{\alpha}(\boldsymbol{x}+\boldsymbol{e}_{\alpha}\Delta t, t+\Delta t)-f_{\alpha}(\boldsymbol{x},t)] \tag{3.44}$$

$$=-\frac{1}{\tau}\sum_{\alpha}(f_{\alpha}-f_{\alpha}^{eq})+\frac{\Delta t}{6e^{2}}\sum_{\alpha}e_{\alpha i}F_{i}.$$

With reference to equation (3.11), it can be found that $\sum_{\alpha} e_{\alpha i}F_i = 0$ may be assumed (based on the symmetrical lattice system in the velocity vectors), which leads to:

$$\sum_{\alpha}[f_{\alpha}(\boldsymbol{x}+\boldsymbol{e}_{\alpha}\Delta t, t+\Delta t)-f_{\alpha}(\boldsymbol{x},t)]=-\frac{1}{\tau}\sum_{\alpha}(f_{\alpha}-f_{\alpha}^{eq}). \tag{3.45}$$

The process of examining the microscopic properties in the lattice Boltzmann equation is continued by considering the conservative properties such as cumulative mass and momentum. Therefore, the summations of the microdynamic mass and momentum, which are conserved, are used. Based on the mass conservation identity (the

continuity equation (3.46) with microdynamic variables), substitution of equation (3.45) into (3.46) leads to:

$$\sum_{\alpha} f_{\alpha}(\boldsymbol{x} + \boldsymbol{e}_{\alpha}\Delta t, t + \Delta t) \equiv \sum_{\alpha} f_{\alpha}(\boldsymbol{x}, t), \tag{3.46}$$

$$\sum_{\alpha} f_{\alpha}(\boldsymbol{x}, t) = \sum_{\alpha} f_{\alpha}^{eq}(\boldsymbol{x}, t). \tag{3.47}$$

According to the (3.22), the expression (3.47) in fact defines a physical quantity, the water depth h, given by:

$$h(\boldsymbol{x}, t) = \sum_{\alpha} f_{\alpha}(\boldsymbol{x}, t). \tag{3.48}$$

Therefore, in order to obtain the expression for the velocity, the sum of the first moment of the distribution function (3.17) over the lattice velocities can be rearranged as follows:

$$\sum_{\alpha} e_{\alpha i}[f_{\alpha}(\boldsymbol{x} + \boldsymbol{e}_{\alpha}\Delta t, t + \Delta t) - f_{\alpha}(\boldsymbol{x}, t)] \tag{3.49}$$

$$= -\frac{1}{\tau}\sum_{\alpha} e_{\alpha i}(f_{\alpha} - f_{\alpha}^{eq}) + \frac{\Delta t}{6e^2}\sum_{\alpha} e_{\alpha i}e_{\alpha j}F_i.$$

$$\sum_{\alpha} e_{\alpha i}[f_{\alpha}(\boldsymbol{x}+\boldsymbol{e}_{\alpha}\Delta t, t+\Delta t)-f_{\alpha}(\boldsymbol{x},t)] \tag{3.50}$$

$$= \Delta t F_i - \frac{1}{\tau}\sum_{\alpha} e_{\alpha i}(f_{\alpha}-f_{\alpha}^{eq}).$$

Equation (3.50) reflects the evolution of cumulative momentum in the distribution function [4]. According to Newton's second law, force is the time rate of change of the momentum [110], hence, the momentum equation with the microdynamic variables can be presented as:

$$\sum_{\alpha} e_{\alpha i}[f_{\alpha}(\boldsymbol{x}+\boldsymbol{e}_{\alpha}\Delta t, t+\Delta t)-f_{\alpha}(\boldsymbol{x},t)] \equiv \Delta t F_i. \tag{3.51}$$

Substitution of (3.51) into (3.50) yields:

$$\sum_{\alpha} e_{\alpha i} f_{\alpha}(\boldsymbol{x},t) = \sum_{\alpha} e_{\alpha i} f_{\alpha}^{eq}(\boldsymbol{x},t). \tag{3.52}$$

Referring to equation (3.23), the term on the right hand side of equation (3.52) leads to a physical variable called velocity u_i given by:

$$u_i(\boldsymbol{x},t) = \frac{1}{h(\boldsymbol{x},t)}\sum_{\alpha} e_{\alpha i} f_{\alpha}(\boldsymbol{x},t). \tag{3.53}$$

The physical variables such as water depth h and velocity u_i are then obtained whilst at the same time preserving the two identities (3.46) and (3.51) which reflect conservative properties such as cumulative mass and momentum.

3.1.5 Recovery of Shallow-Water Equations

The Chapman-Enskog method is an analytic procedure to recover macroscopic equations. It is an important technique for generating approximate solutions to one-body kinetic equations. Originally formulated, it consists of a gradient expansion about a local-equilibrium state [111]. In the current study, it is applied to the lattice Boltzmann equation (3.17) to prove that the depth h and velocity u_i calculated from equations (3.48) and (3.53) are the solution to the shallow water equations (2.51) and (2.52).

The process starts by assuming Δt is small and equal to ε, [4]

$$\Delta t = \varepsilon. \tag{3.54}$$

The lattice Boltzmann equation (3.17) is then rearranged as:

$$f_\alpha(\boldsymbol{x} + \boldsymbol{e}_\alpha\varepsilon, t + \varepsilon) - f_\alpha(\boldsymbol{x}, t) = -\frac{1}{\tau}(f_\alpha - f_\alpha^{eq}) + \frac{\varepsilon}{6e^2}e_{\alpha i}F_i. \tag{3.55}$$

A Taylor expansion procedure is then applied to the first term on the left hand side of the above equation in time and space around the point $(\boldsymbol{x}, t)$, which yields:

$$\varepsilon\left(\frac{\partial}{\partial t}+e_{\alpha j}\frac{\partial}{\partial x_j}\right)f_\alpha+\frac{1}{2}\varepsilon^2\left(\frac{\partial}{\partial t}+e_{\alpha j}\frac{\partial}{\partial x_j}\right)^2 f_\alpha+O(\varepsilon^3) \tag{3.56}$$

$$=-\frac{1}{\tau}(f_\alpha-f_\alpha^0)+\frac{\varepsilon}{6e^2}e_{\alpha i}F_i.$$

Moreover, the Taylor expansion, f_α can also be expanded around f_α^0, where $(f_\alpha^0=f_\alpha^{eq})$, such that

$$f_\alpha=f_\alpha^0+\varepsilon f_\alpha^1+\varepsilon^2 f_\alpha^2+O(\varepsilon^3), \tag{3.57}$$

Ignoring order ε^3 and higher terms, (3.56) to order ε is defined as:

$$\left(\frac{\partial}{\partial t}+e_{\alpha j}\frac{\partial}{\partial x_j}\right)f_\alpha^0=-\frac{1}{\tau}(f_\alpha^1)+\frac{1}{6e^2}e_{\alpha i}F_i. \tag{3.58}$$

Meanwhile, the equation (3.56) to order ε^2 is defined as:

$$\left(\frac{\partial}{\partial t}+e_{\alpha j}\frac{\partial}{\partial x_j}\right)f_\alpha^1+\frac{1}{2}\left(\frac{\partial}{\partial t}+e_{\alpha j}\frac{\partial}{\partial x_j}\right)^2 f_\alpha^0=-\frac{1}{\tau}(f_\alpha^2). \tag{3.59}$$

Substitution of (3.58) into (3.59) yields:

$$\left(1-\frac{1}{2\tau}\right)\left(\frac{\partial}{\partial t}+e_{\alpha j}\frac{\partial}{\partial x_j}\right)f_\alpha^1 \tag{3.60}$$

$$=-\frac{1}{\tau}(f_\alpha^2)-\frac{1}{2}\left(\frac{\partial}{\partial t}+e_{\alpha j}\frac{\partial}{\partial x_j}\right)\left(\frac{1}{6e^2}e_{\alpha k}F_k\right).$$

Then, taking $\sum[(3.58)+\varepsilon\times(3.60)]$, leads to:

$$\frac{\partial}{\partial t}\left(\sum_{\alpha} f_{\alpha}^{0}\right)+\frac{\partial}{\partial x_{j}}\left(\sum_{\alpha} e_{\alpha j} f_{\alpha}^{0}\right) \tag{3.61}$$

$$=-\varepsilon \frac{1}{12e^{2}} \frac{\partial}{\partial x_{j}}\left(\sum_{\alpha} e_{\alpha j} e_{\alpha k} F_{k}\right).$$

If the first-order accuracy for the force term is applied in (3.61), then the evaluation of other terms in the same equation using equation (3.11) and (3.43) will result in:

$$\frac{\partial h}{\partial t}+\frac{\partial\left(h u_{j}\right)}{\partial x_{j}}=0, \tag{3.62}$$

which is the continuity equation (2.51) for shallow water flows. By considering $\sum e_{\alpha i}[(3.58)+\varepsilon \times(3.60)]$,

$$\frac{\partial}{\partial t}\left(\sum_{\alpha} e_{\alpha i} f_{\alpha}^{0}\right)+\frac{\partial}{\partial x_{j}}\left(\sum_{\alpha} e_{\alpha i} e_{\alpha j} f_{\alpha}^{0}\right) \tag{3.63}$$

$$+\varepsilon\left(1-\frac{1}{2\tau}\right) \frac{\partial}{\partial x_{j}}\left(\sum_{\alpha} e_{\alpha i} e_{\alpha j} f_{\alpha}^{1}\right)$$

$$=F_{j} \delta_{i j}$$

$$-\varepsilon \frac{1}{2} \sum_{\alpha} e_{\alpha i}\left(\frac{\partial}{\partial t}+e_{\alpha j} \frac{\partial}{\partial x_{j}}\right)\left(\frac{1}{6e^{2}} e_{\alpha j} F_{j}\right).$$

Again, using the first-order accuracy for the force term in the above equation (3.63), the evaluation of the other terms in the same equation by (3.11) and (3.43) results in:

$$\frac{\partial hu_i}{\partial t} + \frac{\partial (hu_i u_j)}{\partial x_j} = -g \frac{\partial}{\partial x_i}\left(\frac{h^2}{2}\right) - \frac{\partial}{\partial x_j} \Lambda_{ij} + F_i, \tag{3.64}$$

where

$$\Lambda_{ij} = \frac{\varepsilon}{2\tau}(2\tau - 1) \sum_{\alpha} e_{\alpha i} e_{\alpha j} f_{\alpha}^{1}. \tag{3.65}$$

Considering equations (3.58), (3.11) and (3.43), the following expression is obtained:

$$\Lambda_{ij} \approx -\nu \left[\frac{\partial hu_i}{\partial x_j} + \frac{\partial (hu_j)}{\partial x_i}\right]. \tag{3.66}$$

Insertion of (3.66) into (3.64) yields the following momentum equation (2.52) for shallow water flow:

$$\frac{\partial hu_i}{\partial t} + \frac{\partial (hu_i u_j)}{\partial x_j} = -g \frac{\partial}{\partial x_i}\left(\frac{h^2}{2}\right) + \nu \frac{\partial^2 (hu_i)}{\partial x_j \partial x_j} + F_i, \tag{3.67}$$

where the kinematic viscosity ν and the force term F_i are defined respectively as follows:

$$\nu = \frac{e^2 \Delta t}{6}(2\tau - 1). \tag{3.68}$$

and

$$F_i = -gh\frac{\partial z_b}{\partial x_i} + \frac{\tau_{wi} - \tau_{bi}}{\rho} + E_i. \tag{3.69}$$

The foregoing proof of derivation in terms of force for the shallow water equation recovery can be classified as first-order accurate [4]. In order to achieve second-order accuracy, an application of the appropriate expression for force (i.e. the centred scheme for the recovered macroscopic continuity and momentum equations) needs to be evaluated, and this will be discussed later in this chapter.

3.2 Lattice Boltzmann Method with Turbulence Modelling

Turbulence is characterised by chaotic property changes in a gas or fluid. This includes rapid changes of momentum convection, pressure and velocity in space and time [112]. The coexistence of the chaotic has made turbulence modelling one of the most challenging and unpredictable problems in science and engineering [38,113,114]. Nevertheless,

turbulence modelling and prediction is of primary importance in understanding many flow processes in practice.

The LBM for turbulent shallow water flows [44] is described in this section. Use of the Smagorinsky SGS model in the LES leads to the simple lattice Boltzmann turbulent flow model.

3.2.1 Subgrid-scale Lattice Boltzmann Model for Turbulent Shallow Water Equations

SGS modelling refers to the representation of important small-scale physical processes that occur at length-scales that cannot be sufficiently determined on a computational mesh [115]. In LES of turbulence, SGS modelling is used to demonstrate the effects of unresolved small-scale fluid motions (i.e. small eddies, swirls, vortices, etc.) in the equations governing the large scale motions that are resolved in computer models [100].

Hou et al. [116] proposed a basic concept underpinning the lattice Boltzmann SGS model, where the appearance of eddy viscosity in the momentum equation (2.70) can be related to the relaxation time via

equation (3.68) to solve the shallow water equations (2.69) and (2.70). Zhou [4] illustrated a new lattice Boltzmann equation in his model by redefining the relaxation time based on the SGS model, as follows:

$$\tau_t = \tau + \tau_e, \tag{3.70}$$

where, use of a total relaxation time (such as (3.70)) that contains the eddy relaxation time τ_e, yields a total viscosity

$$\nu_t = \nu + \nu_e, \tag{3.71}$$

hence leading to a new lattice Boltzmann equation with a total relaxation time τ_t:

$$f_\alpha(\boldsymbol{x} + \boldsymbol{e}_\alpha \Delta t, t + \Delta t) - f_\alpha(\boldsymbol{x}, t) \tag{3.72}$$
$$= -\frac{1}{\tau_t}(f_\alpha - f_\alpha^{eq}) + \frac{\Delta t}{6e^2} e_{\alpha i} F_i.$$

In order to determine the total relaxation time τ_t, the strain-rate tensor S_{ij} is resolved in terms of the distribution function so as to remain consistent with lattice gas dynamics [4]. Since the strain-rate tensor S_{ij} is related to the non-equilibrium momentum fluctuation tensor (using Chapman-Enskog analysis), this provides an easy and efficient way to calculate S_{ij} as follows:

$$S_{ij} = -\frac{3}{2e^2 h\tau_t \Delta t}\sum_{\alpha} e_{\alpha i} e_{\alpha j}\left(f_\alpha - f_\alpha^{eq}\right). \tag{3.73}$$

By assuming τ_t and ν_t satisfy (3.68), this leads to:

$$\tau_t = \frac{1}{2} + \frac{3\,\nu_t}{e^2 \Delta t}. \tag{3.74}$$

Inserting (3.70) and (3.71) into (3.74) yields:

$$\tau_t + \tau = \frac{1}{2} + \frac{3(\nu + \nu_e)}{e^2 \Delta t}, \tag{3.75}$$

which can be simplified according to (3.68) to give:

$$\tau_e = \frac{3\,\nu_e}{e^2 \Delta t}. \tag{3.76}$$

The eddy viscosity ν_e in (3.76) is then replaced by that in (2.72) as follows:

$$\tau_e = \frac{3}{e^2 \Delta t}(C_s \ell_s)^2 \sqrt{S_{ij} S_{ij}}. \tag{3.77}$$

Substitution of the strain-rate tensor S_{ij} given by (3.73) into (3.77) gives:

$$\tau_e = \frac{3}{e^2 \Delta t}(C_s \ell_s)^2 \frac{3}{2e^2 h\tau_t \Delta t}\sqrt{\Pi_{ij}\Pi_{ij}}, \tag{3.78}$$

where

$$\Pi_{ij} = \sum_{\alpha} e_{\alpha i}\, e_{\alpha j}(f_\alpha - f_\alpha^{eq}). \tag{3.79}$$

By replacing the characteristic length scale $\ell_s = \Delta x$ in (3.78) with (3.70) related to the total relaxation time, gives:

$$\tau_e = \frac{9}{2}\frac{{C_s}^2}{e^2 h(\tau_e + \tau)}\sqrt{\Pi_{ij}\Pi_{ij}}. \tag{3.80}$$

Alternatively, the eddy relaxation time can be determined from:

$$\tau_e = \frac{-\tau + \sqrt{\tau^2 + \left(\frac{18{C_s}^2}{e^2 h}\right)\sqrt{\Pi_{ij}\Pi_{ij}}}}{2}, \tag{3.81}$$

leading to the total relaxation time τ_t :

$$\tau_t = \frac{\tau + \sqrt{\tau^2 + \left(\frac{18{C_s}^2}{e^2 h}\right)\sqrt{\Pi_{ij}\Pi_{ij}}}}{2}. \tag{3.82}$$

3.2.2 Recovery of Turbulent Shallow Water Equations

In this section, the lattice Boltzmann equation with turbulence (3.72), as described in the previous section, is proved to be a solution to the macroscopic equation (2.69) and (2.70) using the Chapman-Enskog expansion. Under the usual considerations, by assuming $\Delta t = \varepsilon$, equation (3.72) can be written as follows:

$$f_\alpha(x + e_\alpha\varepsilon, t + \varepsilon) - f_\alpha(x,t) = -\frac{1}{\tau_t}\left(f_\alpha - f_\alpha^{eq}\right) + \frac{\varepsilon}{6e^2}e_{\alpha j}F_j. \tag{3.83}$$

The first term on the left-hand side in the above equation is expanded using a Taylor expansion in time and space as:

$$\varepsilon\left(\frac{\partial}{\partial t} + e_{\alpha j}\frac{\partial}{\partial x_j}\right)f_\alpha + \frac{1}{2}\varepsilon^2\left(\frac{\partial}{\partial t} + e_{\alpha j}\frac{\partial}{\partial x_j}\right)^2 f_\alpha + O(\varepsilon^3) \tag{3.84}$$

$$= -\frac{1}{\tau_t}(f_\alpha - f_\alpha^0) + \frac{\varepsilon}{6e^2}e_{\alpha j}F_j.$$

Then f_α can also be expanded around f_α^0 , where ($f_\alpha^0 = f_\alpha^{eq}$), giving:

$$f_\alpha = f_\alpha^0 + \varepsilon f_\alpha^1 + \varepsilon^2 f_\alpha^2 + O(\varepsilon^3), \tag{3.85}$$

where (3.84) to order ε is defined as:

$$\left(\frac{\partial}{\partial t}+e_{\alpha j}\frac{\partial}{\partial x_j}\right)f_\alpha^0=-\frac{1}{\tau_t}(f_\alpha^1)+\frac{1}{6e^2}e_{\alpha j}F_j. \tag{3.86}$$

And (3.84) to order ε^2 is defined as:

$$\left(\frac{\partial}{\partial t}+e_{\alpha j}\frac{\partial}{\partial x_j}\right)f_\alpha^1+\frac{1}{2}\left(\frac{\partial}{\partial t}+e_{\alpha j}\frac{\partial}{\partial x_j}\right)^2 f_\alpha^0=-\frac{1}{\tau_t}(f_\alpha^2). \tag{3.87}$$

Substitution of (3.86) into (3.87) yields:

$$\left(1-\frac{1}{2\tau_t}\right)\left(\frac{\partial}{\partial t}+e_{\alpha j}\frac{\partial}{\partial x_j}\right)f_\alpha^1 \tag{3.88}$$

$$=-\frac{1}{\tau_t}(f_\alpha^2)-\frac{1}{2}\left(\frac{\partial}{\partial t}+e_{\alpha j}\frac{\partial}{\partial x_j}\right)\left(\frac{1}{6e^2}e_{\alpha k}F_k\right).$$

Then, by taking $\sum[(3.86)+\varepsilon\times(3.88)]$, gives

$$\frac{\partial}{\partial t}\left(\sum_\alpha f_\alpha^0\right)+\frac{\partial}{\partial x_j}\left(\sum_\alpha e_{\alpha j}f_\alpha^0\right) \tag{3.89}$$

$$=-\varepsilon\frac{1}{12e^2}\frac{\partial}{\partial x_j}\left(\sum_\alpha e_{\alpha j}e_{\alpha k}F_k\right).$$

By applying first-order accuracy to the force term, evaluation of the other terms in (3.89) using (3.11) and (3.43) will result in the continuity equation (2.69) for shallow water flows:

$$\frac{\partial h}{\partial t}+\frac{\partial(hu_j)}{\partial x_j}=0, \tag{3.90}$$

From $\sum e_{\alpha i}[(3.86)+\varepsilon\times(3.88)]$,

$$\begin{aligned}\frac{\partial}{\partial t}\left(\sum_\alpha e_{\alpha i}f_\alpha^0\right)+\frac{\partial}{\partial x_j}\left(\sum_\alpha e_{\alpha i}e_{\alpha j}f_\alpha^0\right)&\\ +\varepsilon\left(1-\frac{1}{2\tau_t}\right)\frac{\partial}{\partial x_j}\left(\sum_\alpha e_{\alpha i}e_{\alpha j}f_\alpha^1\right)&\\ =F_j\delta_{ij}&\\ -\varepsilon\frac{1}{2}\sum_\alpha e_{\alpha i}\left(\frac{\partial}{\partial t}+e_{\alpha j}\frac{\partial}{\partial x_j}\right)\left(\frac{1}{6e^2}e_{\alpha j}F_j\right).&\end{aligned} \tag{3.91}$$

Similarly, using first-order accuracy for the force term in (3.91), the evaluation of the other terms in the equation by using (3.43) will result in:

$$\frac{\partial hu_i}{\partial t}+\frac{\partial(hu_iu_j)}{\partial x_j}=-g\frac{\partial}{\partial x_i}\left(\frac{h^2}{2}\right)-\frac{\partial}{\partial x_j}\Lambda_{ij}+F_i, \tag{3.92}$$

where

$$\Lambda_{ij}=\frac{\varepsilon}{2\tau_t}(2\tau_t-1)\sum_\alpha e_{\alpha i}e_{\alpha j}f_\alpha^1. \tag{3.93}$$

Consideration of equations (3.86), and (3.43), yields:

$$\Lambda_{ij} \approx -\frac{\varepsilon}{6} e^2 (2\tau_t - 1) \left[\frac{\partial h u_i}{\partial x_j} + \frac{\partial (h u_j)}{\partial x_i} \right]. \tag{3.94}$$

Insertion of (3.94) into (3.92) yields the following expression for the shallow water momentum equation:

$$\frac{\partial h u_i}{\partial t} + \frac{\partial (h u_i u_j)}{\partial x_j} = -g \frac{\partial}{\partial x_i} \left(\frac{h^2}{2} \right) + \nu_t \frac{\partial^2 (h u_i)}{\partial x_j \partial x_j} + F_i, \tag{3.95}$$

where the total kinematic viscosity ν_t is defined by:

$$\nu_t = \frac{e^2 \Delta t}{6} (2\tau_t - 1). \tag{3.96}$$

Replacing the (3.96) with (3.68), (3.70), (3.71) and (3.76), yields:

$$\nu_t = \nu_e + \nu. \tag{3.97}$$

Therefore, insertion of (3.97) into (3.95) yields the momentum equation (2.70). The derivation is continued for the strain-rate tensor S_{ij}, which is obtained by combining equations (3.93) and (3.94):

$$\frac{1}{2h} \left[\frac{\partial h u_i}{\partial x_j} + \frac{\partial (h u_j)}{\partial x_i} \right] = -\frac{3}{2 e^2 h \tau_t} \sum_{\alpha} e_{\alpha i} e_{\alpha j} f_{\alpha}^1. \tag{3.98}$$

Based on (3.85), the following expression is obtained:

$$f_\alpha^1 = \frac{(f_\alpha - f_\alpha^0)}{\varepsilon} + O(\varepsilon) \approx \frac{(f_\alpha - f_\alpha^0)}{\varepsilon}. \quad (3.99)$$

By referring to the definition of the strain-rate tensor, S_{ij} in equation (3.69) and to the assumptions made, $f_\alpha^0 = f_\alpha^{eq}$ and $\Delta t = \varepsilon$, the strain-rate tensor (see equation (3.73)) in the form of distribution function is obtained by substituting equation (3.99) into (3.98).

3.3 Calculation of Force Terms

Water flows in rivers, coastal, estuaries etc are subject to different forces such as gravity, Coriolis and bed slope [4]. Determination of these forces plays an important role in obtaining accurate predictions of such flows. Despite the fact that these forces may affect the results, most studies reported in the literature are restricted to the standard lattice Boltzmann equation without consideration of such forces [34].

Investigation to include a force in the lattice Boltzmann equation commenced in the late 1990s when. Martys et al. [117] derived the forcing term in Hermite polynomials based on the continuum Boltzmann BGK equation for use in lattice Boltzmann models. The method has been

used in porous media studies by Hayashi [118]. Buick and Greated [119] considered the inclusion of gravity force in a lattice Boltzmann scheme using a composite method, and proposed four methods by which to include a body force:

1. Method 1: Introduces gravity by incorporating an additional term in the equilibrium distribution function. An altered pressure term is produced.
2. Method 2: Introduces gravity into the lattice Boltzmann model by taking into account the equilibrium distribution function to be a function of an 'equilibrium velocity'. It is described as the sum of the lattice Boltzmann velocity.
3. Method 3: Introduces gravity by adding a term to the collision function.
4. Method 4: Introduces gravity by considering the equilibrium distribution to be a function of an altered velocity and by adding an additional term to the collision operator. It is a combination of methods 2 and 3.

Using a less direct approach, Guo et al. [120] proposed incorporating the force term into the local equilibrium distribution function. A straightforward way for estimating a force was proposed by Zhou [44,107] who successfully demonstrated the direct integration of wind shear stress and bed slope into the streaming step in the lattice Boltzmann

equation. Zhou's method is also believed to have the flexibility to allow for additional forces. This technique has recently been enhanced by using a centred scheme to derive the force term and hence obtain improved accuracy [4]. The enhanced scheme is used in the current studies.

3.3.1 Centred Scheme

Theoretically, there are three schemes to represent a force F_i [4]: 1) a basic scheme, where force is measured at the lattice points, 2) a second-order scheme, where the force term takes the averaged value of the two values at the lattice point and its neighbouring lattice point, respectively, and 3) a centred scheme, where the force is considered to act at the mid-point between the lattice point and its neighbouring lattice point. These schemes can be expressed as follows:

- Basic scheme

$$F_i = F_i(\boldsymbol{x}, t). \tag{3.100}$$

- Second-order scheme

$$F_i = \frac{1}{2}[F_i(\boldsymbol{x}, t) + F_i(\boldsymbol{x} + \boldsymbol{e}_\alpha \Delta t, t + \Delta t)], \tag{3. 101}$$

or for the parallel process, equation (3.101) can be expressed as:

$$F_i = \frac{1}{2}[F_i(\boldsymbol{x}, t) + F_i(\boldsymbol{x} + \boldsymbol{e}_\alpha \Delta t, t)]. \tag{3. 102}$$

- Centred scheme

$$F_i = F_i\left(\boldsymbol{x} + \frac{1}{2}\boldsymbol{e}_\alpha \Delta t, t + \frac{1}{2}\Delta t\right), \tag{3. 103}$$

or for the parallel process, equation (3.103) can be expressed as the following semi-implicit form:

$$F_i = F_i\left(\boldsymbol{x} + \frac{1}{2}\boldsymbol{e}_\alpha \Delta t, t\right). \tag{3. 104}$$

The Chapman-Enskog procedure is used to analyze the character of these schemes, by assuming Δt is small and equal to ε. Insertion of centred scheme force terms into the lattice Boltzmann equation (3.17) leads to:

$$f_\alpha(\boldsymbol{x}+\boldsymbol{e}_\alpha\varepsilon, t+\varepsilon) - f_\alpha(\boldsymbol{x}, t) \tag{3.105}$$

$$= -\frac{1}{\tau}(f_\alpha - f_\alpha^{eq})$$

$$+\frac{\varepsilon}{6e^2} e_{\alpha i} F_i\left(\boldsymbol{x}+\frac{1}{2}\boldsymbol{e}_\alpha\varepsilon, t+\frac{1}{2}\varepsilon\right).$$

Taking the Taylor expansion of the first term on the left hand side and the force term on the right hand side of the above equation in time and space around the point $(\boldsymbol{x}, t)$, respectively yields:

$$f_\alpha(\boldsymbol{x}+\boldsymbol{e}_\alpha\varepsilon, t+\varepsilon) \tag{3.106}$$

$$= f_\alpha(\boldsymbol{x}, t) + \varepsilon\left(\frac{\partial}{\partial t} + e_{\alpha j}\frac{\partial}{\partial x_j}\right) f_\alpha$$

$$+\frac{1}{2}\varepsilon^2\left(\frac{\partial}{\partial t} + e_{\alpha j}\frac{\partial}{\partial x_j}\right)^2 f_\alpha + O(\varepsilon^3).$$

$$F_i\left(\boldsymbol{x}+\frac{1}{2}\boldsymbol{e}_\alpha\varepsilon, t+\frac{1}{2}\varepsilon\right) \tag{3.107}$$

$$= F_i(\boldsymbol{x}, t) + \frac{1}{2}\varepsilon\left(\frac{\partial}{\partial t} + e_{\alpha j}\frac{\partial}{\partial x_j}\right) F_i(\boldsymbol{x}, t)$$

$$+ O(\varepsilon).$$

Substitution of equations (3.106) and (3.107) into (3.105) leads to:

$$\varepsilon\left(\frac{\partial}{\partial t}+e_{\alpha j}\frac{\partial}{\partial x_j}\right)f_\alpha+\frac{1}{2}\varepsilon^2\left(\frac{\partial}{\partial t}+e_{\alpha j}\frac{\partial}{\partial x_j}\right)^2 f_\alpha \tag{3.108}$$

$$=-\frac{1}{\tau}\left(f_\alpha-f_\alpha^{(0)}\right)+\frac{\varepsilon}{6e^2}e_{\alpha i}F_i$$

$$+\frac{\varepsilon^2}{12e^2}\left(\frac{\partial}{\partial t}+e_{\alpha j}\frac{\partial}{\partial x_j}\right)e_{\alpha i}F_i+O(\varepsilon^2).$$

Expanding f_α around $f_\alpha^{(0)}$ yields:

$$f_\alpha=f_\alpha^{(0)}+\varepsilon f_\alpha^{(1)}+\varepsilon^2 f_\alpha^{(2)}+O(\varepsilon^3), \tag{3.109}$$

where $f_\alpha^{(0)}=f_\alpha^{(eq)}$, and so equation (3.108) to order ε may be expressed as:

$$\left(\frac{\partial}{\partial t}+e_{\alpha j}\frac{\partial}{\partial x_j}\right)f_\alpha^{(0)}=-\frac{1}{\tau}f_\alpha^{(1)}+\frac{1}{6e^2}e_{\alpha i}F_i, \tag{3.110}$$

and to order ε^2 given:

$$\left(\frac{\partial}{\partial t}+e_{\alpha j}\frac{\partial}{\partial x_j}\right)f_\alpha^{(1)}+\frac{1}{2}\left(\frac{\partial}{\partial t}+e_{\alpha j}\frac{\partial}{\partial x_j}\right)^2 f_\alpha^{(0)} \tag{3.111}$$

$$=-\frac{1}{\tau}f_\alpha^{(2)}+\frac{1}{12e^2}\left(\frac{\partial}{\partial t}+e_{\alpha j}\frac{\partial}{\partial x_j}\right)e_{\alpha i}F_i.$$

Insertion of equation (3.110) into (3.111) yields:

$$\left(1-\frac{1}{2\tau}\right)\left(\frac{\partial}{\partial t}+e_{\alpha j}\frac{\partial}{\partial x_j}\right)f_\alpha^{(1)}=-\frac{1}{\tau}f_\alpha^{(2)}. \tag{3.112}$$

Taking $\sum[(3.110)+\varepsilon\times(3.112)]$,

$$\frac{\partial}{\partial t}\left(\sum_\alpha f_\alpha^{(0)}\right)+\frac{\partial}{\partial x_j}\left(\sum_\alpha e_{\alpha j}f_\alpha^{(0)}\right)=0, \tag{3.113}$$

where the second-order accurate continuity equation (2.51) is obtained by evaluating the terms in (3.113).

Taking the sum of $\sum e_{\alpha i}[(3.110)+\varepsilon\times(3.112)]$ yields:

$$\frac{\partial}{\partial t}\left(\sum_\alpha e_{\alpha i}f_\alpha^{(0)}\right)+\frac{\partial}{\partial x_j}\left(\sum_\alpha e_{\alpha i}e_{\alpha j}f_\alpha^{(0)}\right) \tag{3.114}$$

$$+\varepsilon\left(1-\frac{1}{2\tau}\right)\frac{\partial}{\partial x_j}\left(\sum_\alpha e_{\alpha i}e_{\alpha j}f_\alpha^{(1)}\right)=F_i.$$

By simplifying the above equation with (3.43), we obtain:

$$\frac{\partial hu_i}{\partial t}+\frac{\partial\left(hu_iu_j\right)}{\partial x_j}=-g\frac{\partial}{\partial x_i}\left(\frac{h^2}{2}\right)-\frac{\partial}{\partial x_j}\Lambda_{ij}+F_i, \tag{3.115}$$

where

$$\Lambda_{ij} = \frac{\varepsilon}{2\tau}(2\tau - 1)\sum_{\alpha} e_{\alpha i} e_{\alpha j} f_{\alpha}^{1}. \tag{3.116}$$

Considering equations (3.43) and (3.110), yields the expression:

$$\Lambda_{ij} \approx -\frac{e^2 \varepsilon}{6}(2\tau - 1)\left[\frac{\partial h u_i}{\partial x_j} + \frac{\partial (h u_j)}{\partial x_i}\right]. \tag{3.117}$$

The substitution of (3.117) into (3.115) results in the momentum equation (2.52), which is second-order accurate.

Zhou [4] highlighted that a second order accurate force term in the lattice Boltzmann equation (3.17) can be generated through equation (3.101) obtained using the same Chapman-Enskog expansion. However, second order accuracy is not achievable for the basic scheme force terms (equation (3.100)), which provide only first-order accuracy. Therefore, Zhou concluded that the centred scheme is the correct choice for determining the force in the lattice Boltzmann equation (3.17). The advantage is due to the capability of the centred scheme in representing the action of forces on the particle during streaming. Incorporation of force into the streaming step reproduces the essential physics required to achieve accurate solutions. A proof of the centred scheme satisfying a necessary property of the numerical scheme is given in Appendix A.

3.3.2 Discretization Errors

As discussed in the previous section, the centred scheme satisfies the numerical scheme property to second order accuracy, which leads to consistency of accuracy for the lattice Boltzmann equation. In terms of satisfaction of the numerical scheme, the second order accuracy of the basic force scheme can also be proven in the same manner as given in Appendix A. Therefore, analysis of the discretization errors for both the basic (equation (3.100)) and the second-order (equation (3.101)) schemes is described here.

Firstly, a Taylor expansion of the force terms [4] in the basic scheme (3.100) gives:

$$F_i = F_i(\boldsymbol{x},t) = F_i\left(\boldsymbol{x} + \frac{1}{2}\boldsymbol{e}_\alpha \Delta t, t\right) - \frac{\Delta t}{2} e_{\alpha j} \frac{\partial F_i(\xi_0, t)}{\partial x_j}, \tag{3.118}$$

where $\boldsymbol{x} < \xi_0 < \left(\boldsymbol{x} + \frac{1}{2}\boldsymbol{e}_\alpha \Delta t\right)$. Since $e_{\alpha j} \sim e$ and $e\Delta t = \Delta x$, equation (3.118) can be written as:

$$F_i = F_i(\boldsymbol{x},t) = F_i\left(\boldsymbol{x} + \frac{1}{2}\boldsymbol{e}_\alpha \Delta t, t\right) + O(\Delta x). \tag{3.119}$$

Secondly, a Taylor expansion of the force terms in the second-order scheme (equation (3.101)) leads to:

$$F_i = \frac{1}{2}[F_i(\boldsymbol{x},t) + F_i(\boldsymbol{x}+\boldsymbol{e}_\alpha\Delta t,t)] \tag{3.120}$$

$$= F_i\left(\boldsymbol{x}+\frac{1}{2}\boldsymbol{e}_\alpha\Delta t,t\right)$$

$$+\frac{\Delta t}{4}e_{\alpha j}\left[\frac{\partial F_i(\xi_2,t)}{\partial x_j}-\frac{\partial F_i(\xi_1,t)}{\partial x_j}\right].$$

where $\boldsymbol{x} < \xi_1 < \left(\boldsymbol{x}+\frac{1}{2}\boldsymbol{e}_\alpha\Delta t\right)$and $\left(\boldsymbol{x}+\frac{1}{2}\boldsymbol{e}_\alpha\Delta t\right) < \xi_2 < (\boldsymbol{x}+\boldsymbol{e}_\alpha\Delta t)$.

If

$$\frac{\partial F_i(\xi_1,t)}{\partial x_j} \neq \frac{\partial F_i(\xi_2,t)}{\partial x_j}, \tag{3.121}$$

equation (3.120) can then be written as:

$$F_i = \frac{1}{2}[F_i(\boldsymbol{x},t) + F_i(\boldsymbol{x}+\boldsymbol{e}_\alpha\Delta t,t)] \tag{3.122}$$

$$= F_i\left(\boldsymbol{x}+\frac{1}{2}\boldsymbol{e}_\alpha\Delta t,t\right) + O(\Delta x).$$

Analysis of the discretization errors is made by applying these schemes to simple types of force, i.e. constant force, linearly varying force, etc.

Firstly, consider a constant force F_i such that:

$$\frac{\partial F_i}{\partial x_j} = 0. \tag{3. 123}$$

Substitution of (3.103) and (3.105) into the 3.123) then reduces to the centred scheme, indicating that there are no discretization errors.

Secondly, consider the linearly varying force F_i, such that:

$$\frac{\partial F_i}{\partial x_j} = C_0, \tag{3. 124}$$

where C_0 is constant. Substitution of (3.124) into (3.118) yields:

$$F_i = F_i(x,t) = F_i\left(x + \frac{1}{2}e_\alpha \Delta t, t\right) - \frac{\Delta t}{2} e_{\alpha j} C_0 . \tag{3. 125}$$

By taking $e_{\alpha j} \sim e$ and $e\Delta t = \Delta x$, equation (3.125) can be written as:

$$F_i = F_i(x,t) = F_i\left(x + \frac{1}{2}e_\alpha \Delta t, t\right) - \frac{C_0 \Delta x}{2}. \tag{3. 126}$$

Inserting equation (3.124) into (3.120) leads to:

$$F_i = \frac{1}{2}[F_i(x,t) + F_i(x + e_\alpha \Delta t, t)] = F_i\left(x + \frac{1}{2}e_\alpha \Delta t, t\right). \tag{3. 127}$$

Equation (3.126) indicates that there is discretization error in the basic scheme of the order of $O(C_0 \Delta x/2)$. Whereas, no discretization error for the second-order scheme is evident in equation (3.127). The right hand side is merely the centred scheme [4].

If the force is a non-linear function, the basic scheme and the second-order scheme will have discretization errors in the order of $O(\Delta x)$ (see equations (3.119) and (3.122)). In fact, more complex representations of force will also produce additional discretization errors [89]. The above analysis implies that the centred scheme is preferable in determining force in the lattice Boltzmann model in order to obtain accurate solutions.

3.4 Continuum Boltzmann Equation

In general, fluids are composed of molecules that collide with one another and solid objects. The continuum assumption, however, considers fluids to be continuous [93,121].

The continuum Boltzmann equation is the continuity form of the Boltzmann equation explained in section (1.5). The main characteristic of the continuum Boltzmann equation is the Knudsen number which is used to assess the extent to which the approximation of continuity can be made [38,121]. For an ideal gas, the Knudsen number gives:

$$Kn = \frac{k_B T}{\sqrt{2}\pi\sigma^2 pL}, \tag{3. 128}$$

where, k_B is the Boltzmann constant; T is the thermodynamic temperature; σ is the particle hard shell diameter; p is the total pressure and L is the representative physical length scale.

According to the continuum concept, the lattice Boltzmann equation can also be obtained from this type of equation [4,122,123]. Derivation of the lattice Boltzmann equation (3.17) through the continuum Boltzmann equation is explained in [4].

The first simple kinetic model, known as the Boltzmann BGK equation, is [124]

$$\frac{\partial f}{\partial t} + \boldsymbol{e}.\nabla f = -\frac{1}{\lambda}(f - f^{eq}). \tag{3. 129}$$

where $f = f(\boldsymbol{x}, \boldsymbol{e}, t)$ is the single-particle distribution in continuum phase space $(\boldsymbol{x}, \boldsymbol{e})$, $\boldsymbol{e}$ is the particle velocity, $\nabla = \bar{\imath}\frac{\partial}{\partial x} + \bar{\jmath}\frac{\partial}{\partial y}$ is the gradient operator and λ is a relaxation time. The Maxwell-Boltzmann equilibrium distribution function f^{eq} is:

$$f^{eq} = \frac{\rho}{(2\pi/3)^{\frac{D}{2}}} exp\left[-\frac{3}{2}(\boldsymbol{e} - \boldsymbol{V})^2\right], \tag{3.130}$$

which D is the spatial dimension; the particle velocity $\boldsymbol{e}$ and fluid velocity $\boldsymbol{V}$ are normalized by $\sqrt{3\bar{R}T}$, where $\bar{R}$ is the ideal gas constant and T is the temperature. The fluid density and velocity are calculated in terms of the distribution function as:

$$\rho \boldsymbol{V} = \int \boldsymbol{e} f d\boldsymbol{e}. \tag{3.131}$$

If the fluid velocity $\boldsymbol{V}$ is smaller than the non-dimensional speed of sound $U_s = 1/\sqrt{3}$, the equilibrium distribution function given by equation (3.130) can be expanded in the following form up to second-order [125]:

$$f^{eq} = \frac{\rho}{(2\pi/3)^{\frac{D}{2}}} exp\left(-\frac{3}{2}(\boldsymbol{e})^2\right)\left[1 + 3(\boldsymbol{e}.\boldsymbol{V}) + \frac{9}{2}(\boldsymbol{e}.\boldsymbol{V})^2 - \frac{3}{2}\boldsymbol{V}.\boldsymbol{V}\right]. \tag{3.132}$$

For discrete model development, a limited number of particle velocities i.e. $\boldsymbol{e}_\alpha(\alpha = 1, \ldots, M)$ are used [4], and the distribution functions at these velocities are:

$$f_\alpha(\boldsymbol{x},t) = f(\boldsymbol{x},\boldsymbol{e}_\alpha,t), \tag{3.133}$$

and

$$f_\alpha^{eq}(\boldsymbol{x},t) = f^{eq}(\boldsymbol{x},\boldsymbol{e}_\alpha,t), \tag{3.134}$$

which also satisfy equation (3.129)

$$\frac{\partial f_\alpha}{\partial t} + \boldsymbol{e}_\alpha.\nabla f_\alpha = -\frac{1}{\lambda}(f_\alpha - f_\alpha^{eq}). \tag{3.135}$$

Equation (3.135) is the lattice Boltzmann equation in Lagrangian form, which describes the change in the distribution function along its direction of motion from one point in the lattice to a neighbouring point. The Lagrangian time derivative (the left hand side of equation (3.135)) can be expressed as:

$$\frac{\partial f_\alpha}{\partial t} + \boldsymbol{e}_\alpha.\nabla f_\alpha = \frac{Df_\alpha}{Dt}, \tag{3.136}$$

where

$$\frac{Df_\alpha}{Dt} = \frac{f_\alpha(\boldsymbol{x},\boldsymbol{e}_\alpha\Delta t, t+\Delta t) - f_\alpha(\boldsymbol{x},t)}{\Delta t}. \tag{3.137}$$

Substitution of (3.137) into (3.135) yields the standard lattice Boltzmann equation:

$$f_\alpha(\boldsymbol{x}+\boldsymbol{e}_\alpha\Delta t, t+\Delta t)-f_\alpha(\boldsymbol{x},t)=-\frac{1}{\tau}\left(f_\alpha-f_\alpha^{eq}\right). \tag{3.138}$$

$\tau=\lambda/\Delta t$ is so-called single dimensionless relaxation time.

Chapter 4 Initial and Boundary Conditions

4.0 Introduction

Proper choice of boundary conditions is important in solving the governing equation encountered numerical fluid dynamics. In many cases, the choice of boundary conditions can strongly influence the accuracy of the algorithm [108,126,127].

Succi [38] categorised two classes of boundary conditions in fluid dynamics as e.g., a) boundary conditions for simple cases and b) boundary conditions for complex cases. Brief descriptions of these types of boundaries are given as follows (detailed explanations can be found in [38]):

1. Boundary conditions for simple fluid dynamic cases

    - Periodic: The domain becomes folded along the direction of the periodic boundary conditions pair. Because the flow region consists of same modules, the flow pattern repeats itself module after module using this type of boundary condition.
    - No-slip: Simple boundary conditions that are based on the bounce-back scheme. The incoming particles at a wall node are reflected back to the original fluid nodes.
    - Slip: Similar to the no-slip boundary condition, except that the particles are reflected in a mirror-like fashion instead of being bounced-back [38].
    - Open inlet/outlet: Open boundary conditions are applied at fluid inlets and outlets. Setting up the distribution function of the particle normal to the boundary with the zero gradients is a common technique [4].

2. Boundary conditions for the complicated fluid dynamics cases

    - Staircasing: A sort of lattice polymer for non-aligned solid boundaries, the cutting boundary is replaced with a zig-zagging contour lying entirely on the grid. Relevant to flows in porous media.
    - Extrapolation: Second-order accurate schemes whereby the method places the wall at boundary nodes and lets the nodes undergo the same collisional step as the fluid nodes.
    - Surface elements (surfels) dynamics: A boundary that acts as flux scattering elements receiving incoming fluxes from the flow and reorganizing a corresponding set of fluxes at the surface [128].

All of these boundary conditions are commonly applied in CFD. Besides, more advanced work on boundary conditions has been undertaken by Zhou et al. [129], Yu [130] and Liu et al. [131]. This includes multi-block lattice design in the simulation of fluid flows.

Zhou [107] introduced a general elastic-collision scheme for slip and semi-slip boundary conditions to deal with water flows in arbitrary complex geometries. This is explained in detail in this chapter, which also covers the standard bounce-back scheme for no-slip boundary

condition and the inlet and outlet boundaries. Initial conditions are also discussed at the end of this chapter.

4.1 Standard Bounce-back Scheme: No-slip Boundary

The standard bounce-back scheme is derived from the LGCA boundary conditions that are simple and widely used in implementing wall boundary conditions [38,102]. The post-collision distribution function in the lattice Boltzmann equation (3.17) coming from a solid node $\boldsymbol{x}_b$ to a water node $\boldsymbol{x}_f$ is not known during the streaming step. The bounce-back scheme is utilized to complete the unknown distribution function in the lattice Boltzmann equation [132]. In other words, the distribution function from the incoming particle $f_\alpha(\boldsymbol{x}_f, t)$ towards the wall boundary is bounced back into the water (see Figure 4.1) [4,38].

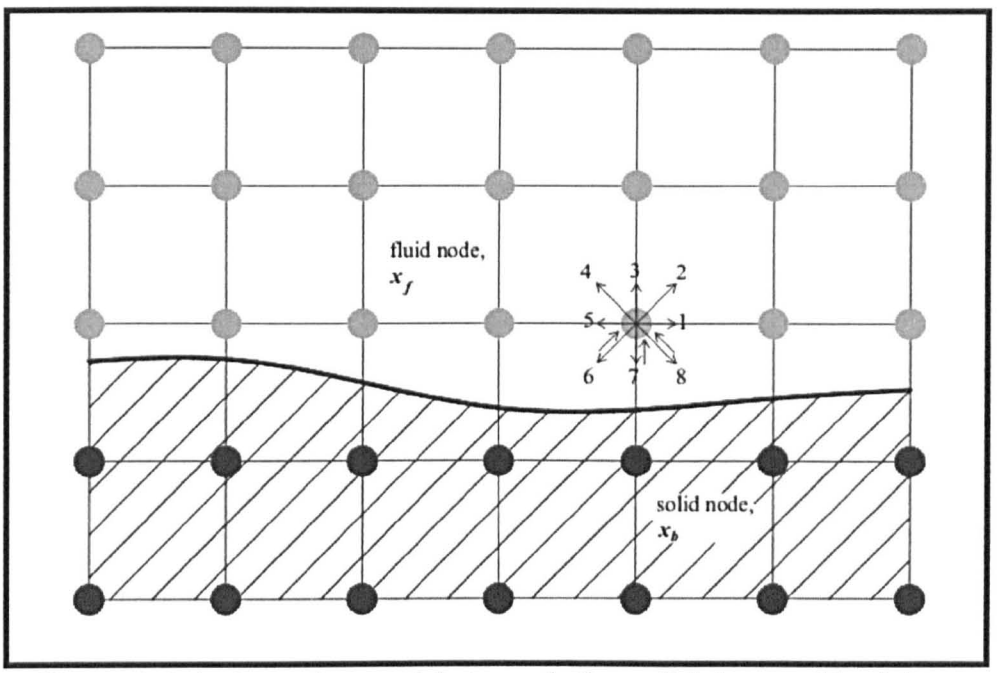

Figure 4. 1 An incoming particle towards the wall is bounced back into water.

For a stationary wall, the bounce-back scheme is equivalent to setting the distribution function as follows [132]:

$$f_4(\boldsymbol{x}_f, t) = f_8(\boldsymbol{x}_b, t), \tag{4. 1}$$

$$f_3(\boldsymbol{x}_f, t) = f_7(\boldsymbol{x}_b, t), \tag{4. 2}$$

$$f_2(\boldsymbol{x}_f, t) = f_6(\boldsymbol{x}_b, t). \tag{4. 3}$$

The zero momentum of the particle close to the solid wall is summed from the above equations leading to no-slip boundary conditions. The no-slip boundary condition is first-order accurate [133]. In order to achieve second-order accuracy, the wall needs to be placed in the middle of the

lattice nodes, e.g. $x = 1/2$ with additional approximation of staircase boundary scheme treatment [106,134].

4.2 Modified Elastic-Collision Scheme

Elastic-collision is one of the standard schemes for a wall boundary condition in lattice gas dynamics [4]. The principle of the method is similar to the bounce-back scheme, except the sum of the particle momentum normal to the solid wall is zero, which leads to a slip boundary condition for a plane solid wall.

As it is a simple method, the elastic-collision scheme has become the most popular method for simulating fluid flows in the LBM [4,106,126]. Here a particle directed towards the boundary is reflected back into the water according to the pattern of directions shown in Figure 4.2.

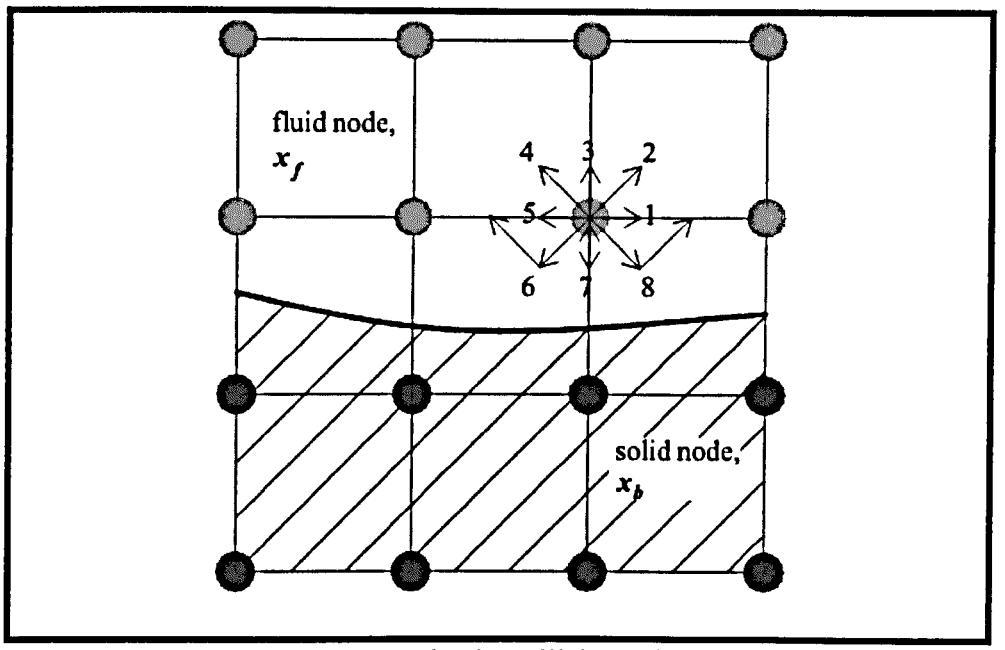

Figure 4. 2 Elastic-collision scheme.

The unknown particle distribution function after streaming is:

$$f_2(x_f, t) = f_8(x_b, t), \tag{4. 4}$$

$$f_3(x_f, t) = f_7(x_b, t), \tag{4. 5}$$

$$f_4(x_f, t) = f_6(x_b, t). \tag{4. 6}$$

Unfortunately, the scheme is not feasible for modelling water flows in complex geometries [4]. In order to obtain the solution to the boundary condition for complex geometry, Zhou [107] proposed a modified elastic-collision scheme to achieve slip and semi-slip boundary conditions. A detailed explanation of this treatment is discussed in the next section.

4.2.1 Slip Boundary Condition

In explaining the treatment of the slip boundary condition for arbitrary complex geometry, it is necessary to represent the boundaries as follows,

- LC: Lattice cell
- LN: Lattice node
- BN: Boundary node
- BC: Boundary cell

To get a better understanding, an illustration of the boundaries is shown in Figure 4.3, where the boundary representation is as follows:

1. Lattice cell (LC) is the control volume created around each LN, the boundaries delineated by straight-lines placed midway between each LNs.
2. The solid boundary shape is represented with a bold line. It divides the LNs into water and solid.
3. Boundary node (BN) is defined based on a water node with at least one neighbouring solid node. The fluid's LC is then called a boundary cell (BC).
4. Four types of BNs are categorized based on the positions of the solid nodes:

    - Type I: $0^0 < \theta \leq 90^0$

- Type II: $90^0 < \theta \leq 180^0$
- Type III: $180^0 < \theta \leq 270^0$
- Type IV: $270^0 < \theta \leq 360^0$

5. A variable C_{ij} is then used to indicate the characteristics of LNs. It is taken to be the node that represents water when $C_{ij} = 0$, a slip boundary when $C_{ij} = 0.5$ and solid when $C_{ij} = 1$.
6. Three subtypes are defined for each of the four BNs (see Step 4) based on the characteristic angle θ_0:

   - $0^0 < \theta \leq \theta_0$
   - $\theta_0 < \theta \leq (90^0 - \theta_0)$
   - $(90^0 - \theta_0) < \theta \leq 90^0$

   where the characteristic angle θ_0 is between 0^0 and 45^0.

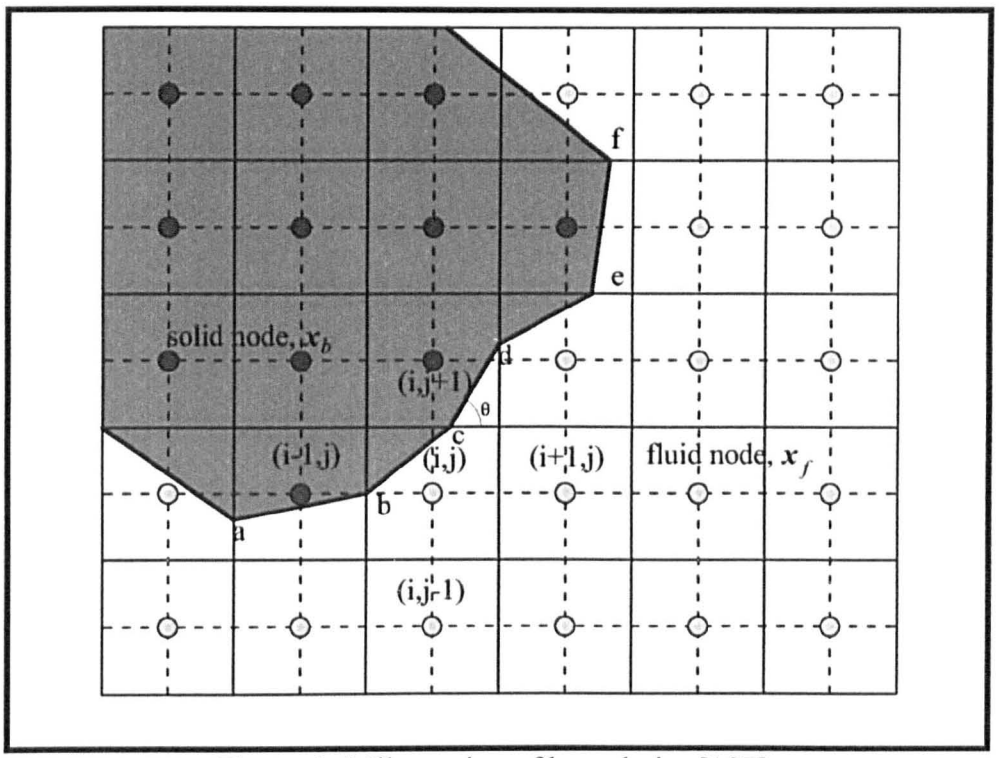

Figure 4. 3 Illustration of boundaries [107].

A detailed description is given of the slip boundary condition treatment for a Type I BN. The remaining BN types can be formulated in the same manner.

In Type I condition (see Figure 4.4), BN is $0^0 < \theta \leq \theta_0$ and the solid boundary line $x - y$ is treated as a horizontal line.

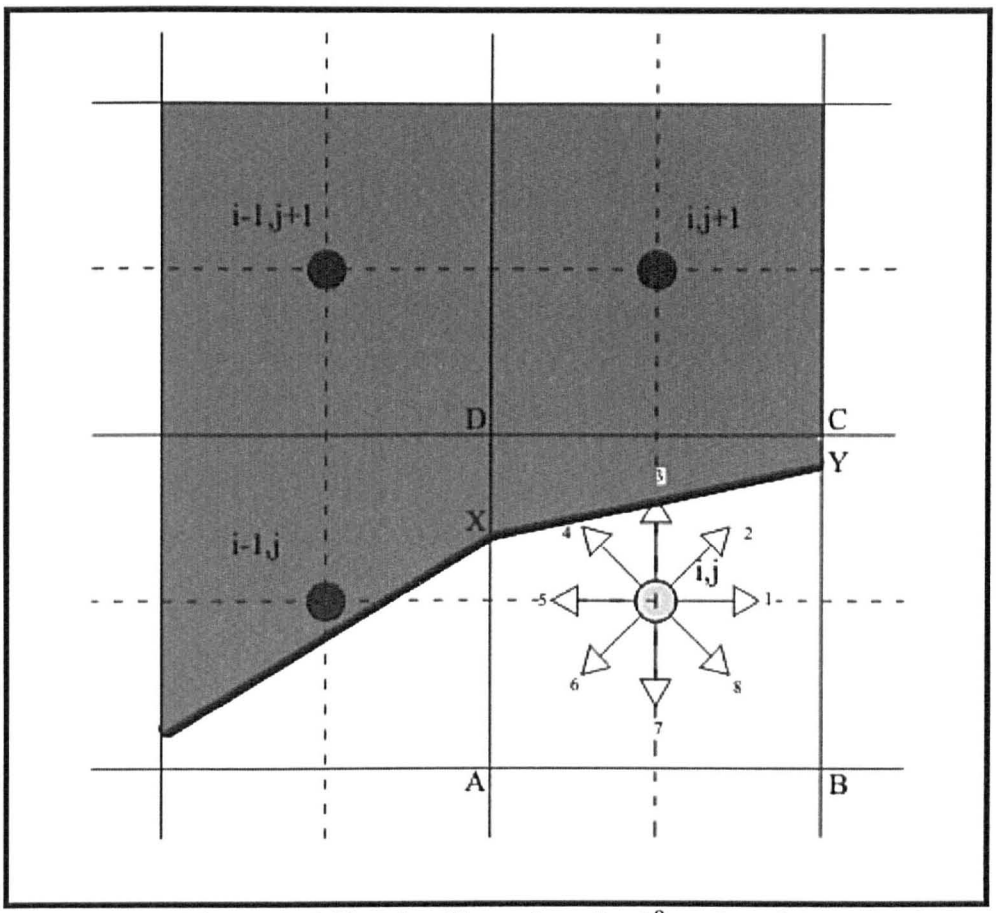

Figure 4. 4 Sketch of boundary for $0^0 < \theta < \theta_0$.

After streaming, the unknown distribution function is:

$$f_7(\boldsymbol{x}_f, t) = f_3(\boldsymbol{x}_b, t), \tag{4. 7}$$

$$f_6(\boldsymbol{x}_f, t) = f_4(\boldsymbol{x}_b, t), \tag{4. 8}$$

$$f_8(\boldsymbol{x}_f, t) = f_2(\boldsymbol{x}_b, t), \tag{4. 9 }$$

with the characteristics of LNs C_{ij} is equal to 1 (solid node) for $C_{i,j+1}$ and $C_{i-1,j+1}$.

For BN $\theta_0 < \theta \leq (90^0 - \theta_0)$ (see Figure 4.5), the solid boundary line $x - y$ is treated as a line with $\theta = 45^0$.

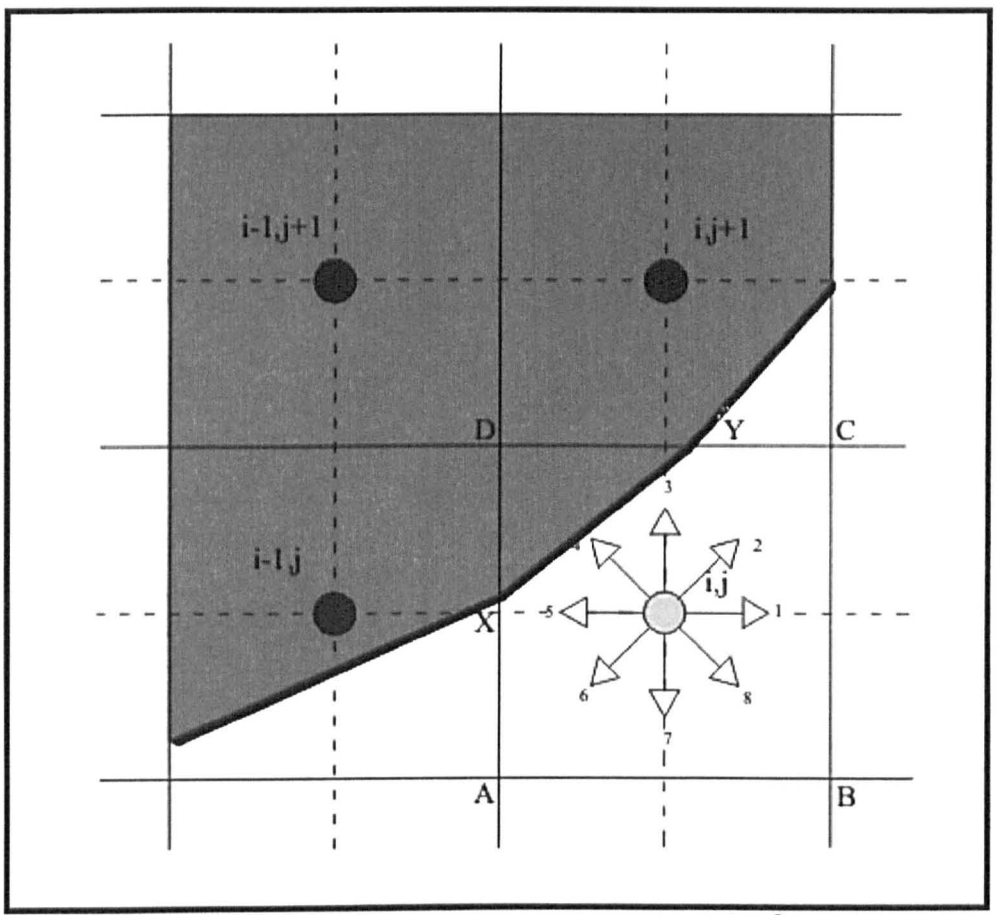

Figure 4. 5 Sketch of boundaries for $\theta_0 < \theta \leq (90^0 - \theta_0)$.

The unknown distribution functions f_8, f_1 and f_7 after streaming are specified by:

$$f_8(\boldsymbol{x}_f, t) = f_4(\boldsymbol{x}_b, t), \tag{4. 10}$$

$$f_7(\boldsymbol{x}_f, t) = f_5(\boldsymbol{x}_b, t), \tag{4. 11}$$

$$f_1(\boldsymbol{x}_f, t) = f_3(\boldsymbol{x}_b, t), \tag{4. 12}$$

where in this condition, the characteristics of LNs C_{ij} is equal to 1 for $C_{i,j+1}$ and $C_{i-1,j}$.

Meanwhile, for BN $(90^0 - \theta_0) < \theta \leq 90^0$ as in Figure 4.6, the solid boundary line $x - y$ is treated as a vertical line.

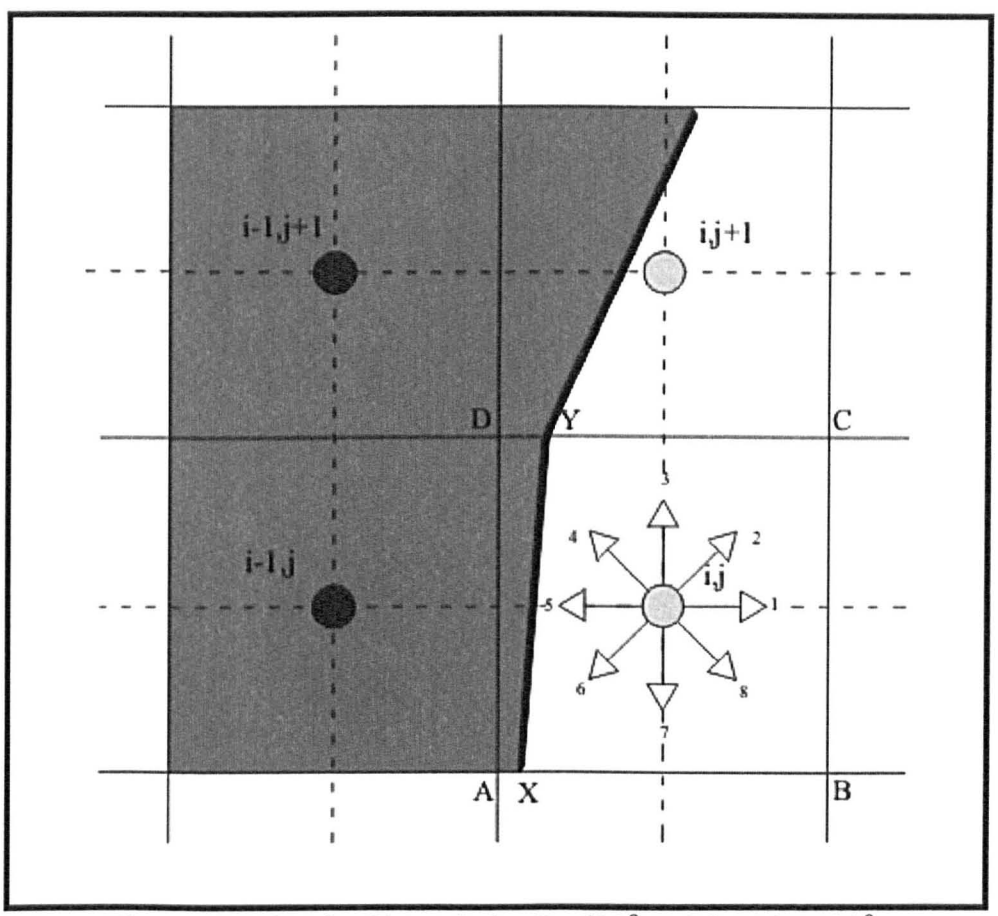

Figure 4. 6 Sketch of boundaries for $(90^0 - \theta_0) < \theta \leq 90^0$.

Therefore, the unknown distribution functions after streaming are obtained by:

$$f_1(x_f, t) = f_5(x_b, t), \tag{4. 13}$$

$$f_8(x_f, t) = f_6(x_b, t), \tag{4. 14}$$

$$f_2(x_f, t) = f_4(x_b, t), \tag{4. 15}$$

where the characteristics of LNs C_{ij} is equal to 1 for $C_{i-1,j}$ and $C_{i-1,j+1}$.

Besides the subtype conditions described above, if only one solid node exists on the left top corner of a BN (see Figure 4.7), and no matter what the slope θ of the interface is, there is only one unknown distribution function f_8 that can be stated as:

$$f_8(x_f, t) = f_4(x_b, t). \tag{4. 16}$$

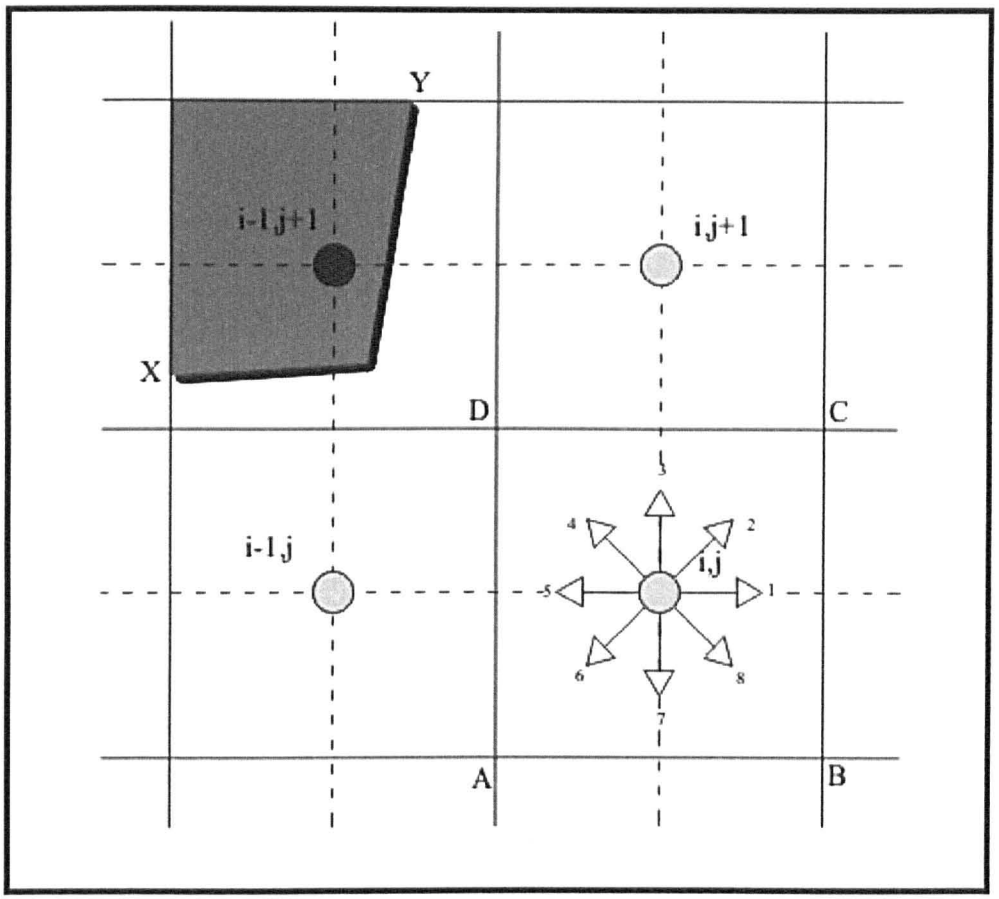

Figure 4. 7 Sketch of boundaries.

Zhou [107] highlighted the advantages of the modified elastic-collision scheme when applied in the range of the characteristic angle $15^0 \leq \theta_0 \leq 30^0$. Detailed explanations of this can be found in [107], in which $\theta_0 = 20^0$ is a highly recommended value for practical computations.

4.2.2 Semi-slip Boundary Condition

When water flows over a stationary surface such as the bed of a river or the wall of a channel, the water touching the surface is brought to rest by the shear stress [38,135]. Water particles partly bounce back into the main stream and partly move along the surface subject to friction force. There is no motion normal to the surface; only a thin film of water moves tangentially along it, for which a combination of no-slip and slip boundary conditions provides the best estimate.

Zhou [136] suggested that it is necessary to consider the effect of wall shear stress in order to achieve a semi-slip boundary condition. The wall shear stress vector $\boldsymbol{\tau}_f$ due to wall friction can be expressed,

$$\boldsymbol{\tau}_f = -\rho\nu\frac{\partial \boldsymbol{V}_\tau}{\partial n^*} = -\rho C_f|\boldsymbol{V}_\tau|\boldsymbol{V}_\tau, \tag{4. 17}$$

where $\boldsymbol{V}_\tau$ is the velocity vector parallel to the wall; n^* is the outward coordinate normal to the wall; and C_f is the friction factor at the wall. The wall friction factor C_f may be estimated with the Manning roughness n_f by:

$$C_f = \frac{gn_f^2}{h^{1/3}}. \tag{4. 18}$$

The velocity vector normal to the wall tends to be zero if the slip boundary condition is applied at the boundary node. Thus,

$$V_\tau \approx V. \tag{4.19}$$

Substitution of equation (4.19) into (4.17) gives the tensor form of wall shear stress:

$$\tau_{fi} = -\rho C_f u_i \sqrt{u_j u_j}. \tag{4.20}$$

Hence, a semi-slip boundary condition can be used at the boundary node by adding the wall shear stress τ_{fi} into the force term F_i in the lattice Boltzmann equation (3.17) together with the slip boundary condition.

4.3 Inflow and Outflow

To obtain realistic simulation results, appropriate inlet and outlet boundary conditions are required, which work as constraints to ensure consistency with the surrounding flow conditions. In fact, dependent flow variables (such as velocity and water depth) at the boundary have to reflect correctly the actual situation.

In conventional numerical methods, it is common to assign a given velocity profile at the inlet while imposing a given water depth at the outlet [38]. In LBM, the zero gradients technique for these physical

variables in the computational analysis has been proven to give satisfactory results [4].

The zero gradient technique can be applied to the unknown distribution function f_1, f_2, f_8 and f_4, f_5, f_6 at the inlet and outlet boundary (see Figure 4.8), respectively, as follows:

$$f_\alpha(1,j) = f_\alpha(2,j), \alpha = 1,2,8. \tag{4. 21}$$

$$f_\alpha(N_x,j) = f_\alpha(N_x - 1,j), \alpha = 4,5,6, \tag{4. 22}$$

with N_x is the total lattice number along x.

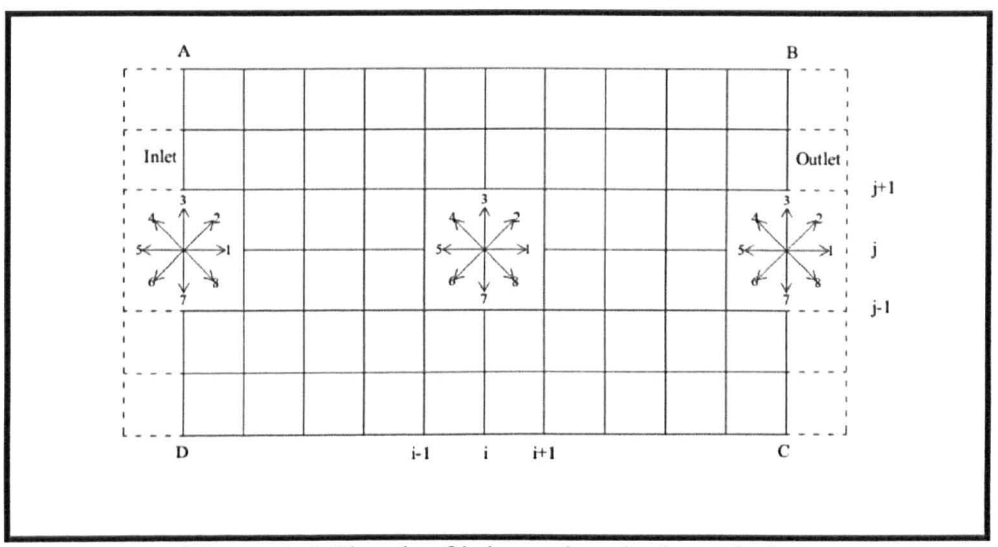

Figure 4. 8 Sketch of inlet and outlet boundaries.

In addition, the unknown distribution functions at the inlet can also be obtained with the method proposed by Zou and He [127]. In this method, the velocity of the flow and the water depth should be known beforehand.

Substituting f_α into equation (3.48) and (3.53), one can obtain three equations:

$$f_1 + f_2 + f_8 + f_3 + f_4 + f_5 + f_6 + f_7 + f_9 = h, \tag{4.23}$$

$$e(f_1 + f_2 + f_8) - e(f_4 + f_5 + f_6) = hu, \tag{4.24}$$

$$e(f_2 + f_4) - e(f_6 + f_8) + ef_3 + ef_7 = hv. \tag{4.25}$$

By assuming $v = 0$ in the above equations (4.23) – (4.25), the solution for the unknown distribution functions f_1, f_2, f_8 at the inlet boundary are

$$f_1 = f_5 + \frac{2hu}{3e}, \tag{4.26}$$

$$f_2 = \frac{hu}{6e} + f_6 + \frac{f_7 - f_3}{2}, \tag{4.27}$$

$$f_8 = \frac{hu}{6e} + f_4 + \frac{f_3 - f_7}{2}. \tag{4.28}$$

In a similar way, the unknown f_4, f_5, f_6 for the outlet boundary can be obtained as:

$$f_5 = f_1 + \frac{2hu}{3e}, \tag{4.29}$$

$$f_4 = -\frac{hu}{6e} + f_8 + \frac{f_7 - f_3}{2}, \tag{4.30}$$

$$f_6 = -\frac{hu}{6e} + f_2 + \frac{f_3 - f_7}{2}. \tag{4.31}$$

4.4 Initial Condition

The unsteady flow of water in channels, the run up and run down of waves at a beach, and the rise and fall of tidal sea levels represent dynamical systems. A dynamical system is a concept in mathematics, where a fixed rule describes the time dependence of a point in a geometrical space [137]. The behaviour of a dynamic system is dependent upon the initial conditions [138].

In LBM, there are two ways to specify an initial condition [4]: a) set random values between 0 and 1 for the distribution function f_α and b) choose the local equilibrium function f_α^{eq} as an initial condition for f_α i.e. $f_\alpha^{eq} = f_\alpha$.

In steady flow analysis, there is no difference between solutions obtained with these two initial conditions. However, in terms of efficiency and accuracy, the second method is preferred. This relates to the fact that the determination of a macroscopic quantity is much easier than the microscopic [4].

Chapter 5 Moving Boundary for Wave Run Up

5.0 Introduction

Flows with moving boundaries occur in many practical cases such as sediment transport in coastal areas [139], a moving valley glacier in isothermal shallow ice [140], heat transfer due to solidification or melting [141], etc. Most of these flows involve physical boundaries as a part of the numerical solution procedures [142].

In civil engineering, moving boundaries are normally found in wave overtopping, run-up, etc. Moving boundaries have been studied in detail by several researchers including Pontillo et al. [143], Sierra et al. [144], Tuan et al. [145], Hu et al. [72] and Dodd [70]. Long wave run up such as a tsunami subject to wave propagation over the beach is another type of problem worthy of study, and has attracted a great deal of research interest in recent years [53,54,61,64,70,76]. In practice, it is challenging to develop satisfactory computational techniques to treat a system with a moving boundary [74].

To date, a number of techniques exist to treat moving boundary problems. Shyy [74] identifies three main categories:

a) Moving-grid (Lagrangian) methods,

b) Fixed-grid (Eulerian) methods and

c) Combined Lagrangian-Eulerian methods.

Lagrangian methods utilize the interface tracking procedure. In these methods, interfacial conditions are implemented whereby the grid system is continuously updated to match the movement of interface (see Figure 5.1). The fluxes are estimated from the neighbouring computational cell in the calculation.

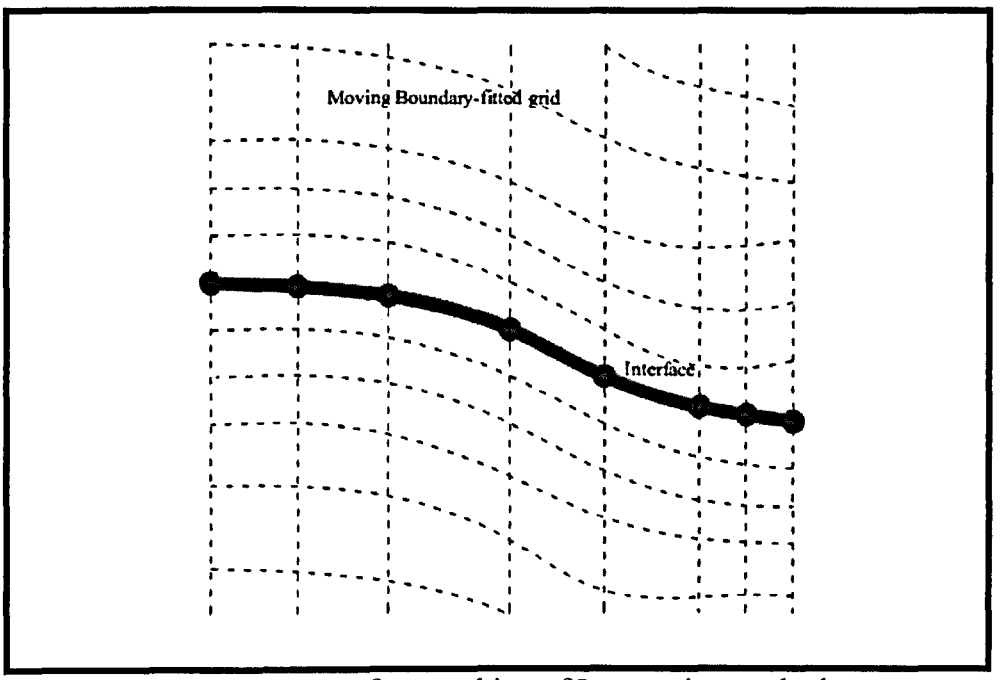

Figure 5. 1 Interface tracking of Lagrangian method.

In the Eulerian methods, the interfacial conditions are incorporated into the flow equations (see Figure 5.2). The interface profile is not explicitly tracked, but estimated after the computation is updated at every time step [74].

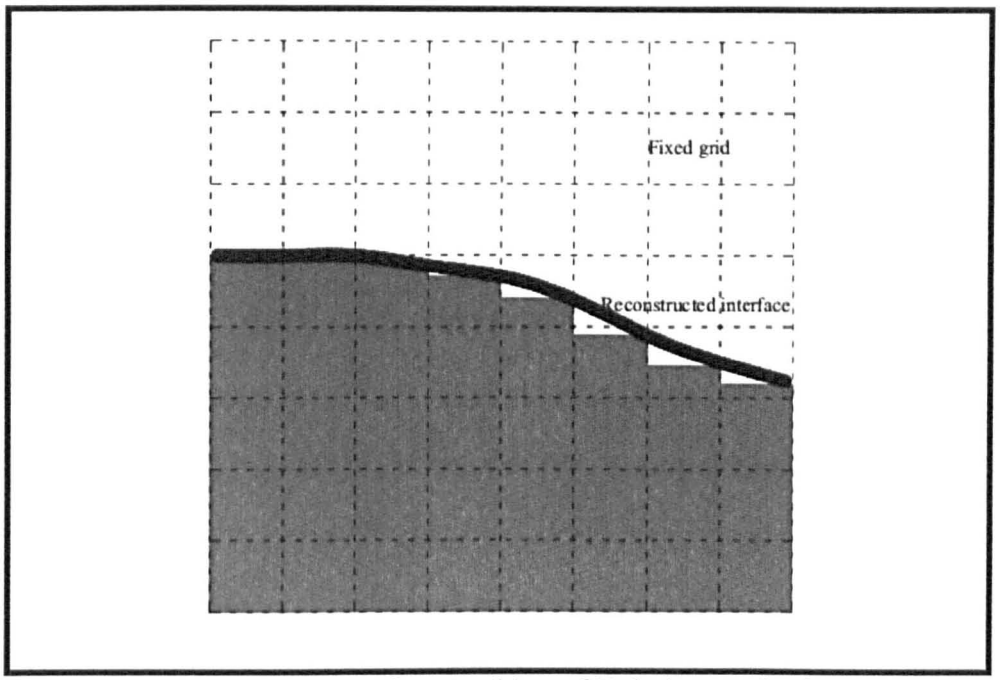

Figure 5. 2 Interface tracking of Eulerian method.

In the combined Lagrangian-Eulerian method, the interface is advected in a Lagrangian framework, whereas the mass, momentum, and energy conservation equations are solved on a fixed (Eulerian) grid.

Each of these methods has its own strengths and weaknesses. Shyy [74] highlighted that it is less natural to express the moving boundaries in an Eulerian method than in a Lagrangian method, where computation is done at fixed grid elements as they move in time through space. However, the moving boundaries are handled naturally in Lagrangian methods, but perform poorly in flows exhibiting strong shearing and vorticity motion.

In the current study, Eulerian based techniques that are used for moving shoreline boundaries are utilized in the lattice Boltzmann model in treating wave run-up at a beach.

5.1 Treatment of the Moving Shoreline

Moving shoreline is a term used for locating the wetting and drying of wave motion (run-up and down). It can be analyzed numerically using an appropriate moving boundary approach. It is coupled with the conventional numerical method in modelling a wave run-up model.

Several different approaches have been developed and improved for simulating wave run-ups. The earliest of the moving shoreline methods was developed by Preissmann [69], who proposed the use of a very simple slot technique. It allows the open channel flow equations to imitate pressure flow equations for an enclosed cross section [146]. In particular, the slot geometry (or so called Preissmann slot) is assigned in the dry domain to allow the water surface to rise to the hydraulic gradeline within the slot. Madsen et al. [147] proposed a porous cells technique, in which a diffusion-style assumption is introduced to smooth the progressive inundation of the cell.

Subsequently, Dodd [70] and Oey [71] assigned a thin film of fluid in the dry cells such that the primitive equations in these cells can be solved together with other points (wet cells).

Hu et al. [72] additionally proposed a minimum friction depth that is used to overcome the instability caused by the effect of minimum water depth by considering the friction factor at bed channel. In this technique, the minimum friction depth is used to calculate an equivalent friction loss when the water depth is shallower than the minimum friction depth.

One popular technique of simple extrapolation from within the local flow domain to the location of the moving front is proposed by Sielecki and Wurtele [73], Titov and Synolakis [51] and Lynett et al. [64]. This approach additionally ignores the kinematics of the moving front [74].

All these moving shoreline techniques are successfully implemented in wave run-up simulation studies [10,14,16,17,21,26,29,148,149] . Indeed, there are many types of conventional numerical models that have been developed and improved upon these techniques. For example, Titov and Synolakis [51] developed a variable-grid finite difference formulation model called VTCS-2. This model is capable of calculating the wave run-up without applying any ad-hoc coefficients.

Fuhrman and Madsen [52] further studied and modelled wave run-up. They produced a numerical analysis of wave run-up based on a high-

order Boussinesq-type method. A regression approach for the extrapolation scheme through the wet-dry boundary was introduced.

Meanwhile, Yamazaki et al. [53] suggested a depth-integrated non-hydrostatic formulation in their numerical model, which is equivalent to the Boussinesq equations for weak dispersive waves.

Mahdavi and Talebbeydokhti [54] developed a model based on the Runge-Kutta method. The model analyzed 1D wave run-up by utilizing the altered MUSCL (Monotone Upstream-centred Schemes for Conservation Laws) scheme, which provides highly accurate numerical solutions to shocks, discontinuities and large gradient problems [75].

Although there are many models developed for wave run-up using conventional numerical methods, very limited attempts have been made for the LBM. In 2008, Frandsen [76] proposed a lattice Boltzmann model for wave run-up and simulated 1D tsunami wave run-up on a plane beach with the standard BGK LBM without flow turbulence.

Implementation of the moving shoreline boundary for wave run-up is employed in the present lattice Boltzmann study. The thin film and linear extrapolation moving shoreline techniques are applied in an Eulerian frame and presented in this chapter.

5.1.1 Thin Film Technique

Thin film algorithms are simple; the cell is assumed to be dry only when the water depth h within the cell is below a minimum water depth h_{min}, otherwise, the cell is assumed to be wet (i.e., the technique deals with cells that are either completely wet, or dry but retain a small minimum depth of water [61]).

Consequently, a wet cell becomes dry if there is excessive flow divergence from that cell, and a dry cell becomes wet if there is sufficient convergence. The divergences and convergences of the flows depend on pressure gradients and surface friction across the cells interfaces [71]. Detailed explanations of these can be obtained by referring to Hu et al. [72] and Oey [71].

In the technique, a thin layer of fluid h_{min} is first defined throughout the domain (see Figure 5.3).

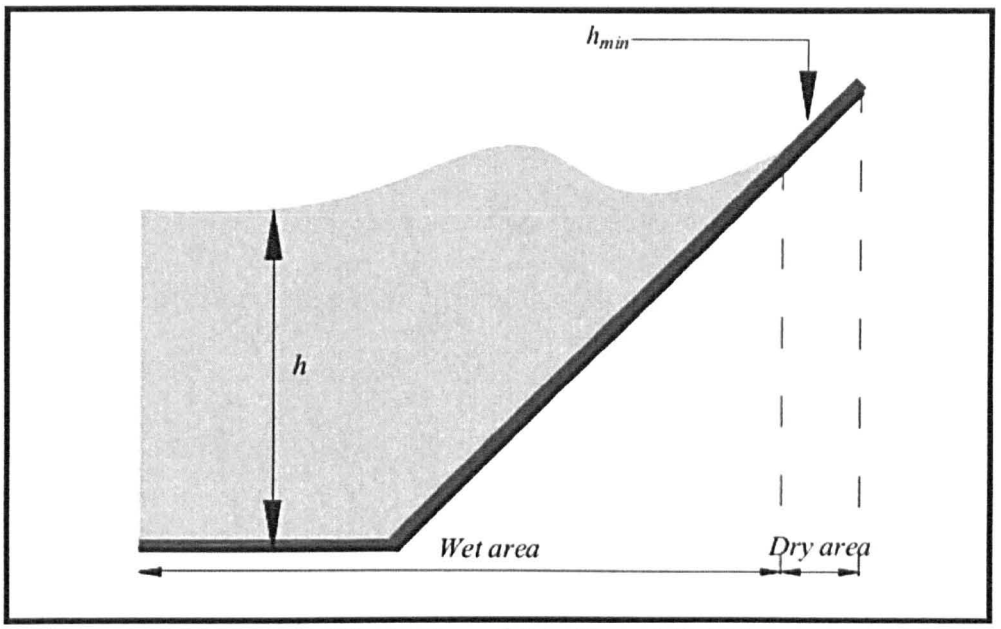

Figure 5. 3 Illustration of thin film of fluid h_{min}.

The cell is assumed to be dry only when the water depth h within the cell is below h_{min}. Otherwise, the cell is wet. In this technique, the lattice Boltzmann equation (3.17) is used to calculate the new water depth h within all cells. However, for a dry cell where $h \leq h_{min}$, the water depth h and flow velocity are set to h_{min} and zero, respectively.

At each time step during the calculation, the water depths h at the cell's interfaces are checked and the velocity u is set to zero if the water depth drops below or equal to the minimum water depth h_{min}, i.e. $u_i = 0$ for $h \leq h_{min}$.

The lattice Boltzmann equation (3.17) is simultaneously applied with the thin film technique to model wave run-up phenomena.

5.1.2 Linear Extrapolation Technique

Another simple technique is a linear extrapolation. In this technique, the cells are extrapolated from within the local flow domain to the new location of the moving front. Sielecki and Wurtele [73] were first to propose the idea of extrapolating nodes between shoreline boundaries. This was followed by Kowalik [10] who used a leapfrog scheme in approximating the non-linear shallow water equations. The model was developed by taking into consideration the 1D and nonbreaking problems of wave run-up.

Lynett et al. [64] began with a search for a scheme that allows the wet-dry boundary to exist at any location that is not restricted to a node on a fixed grid. They developed an extrapolation technique for 1D and 2D wet-dry problems. This technique allows the wet-dry boundary to exist in between the nodal points as shown in Figure 5.4.

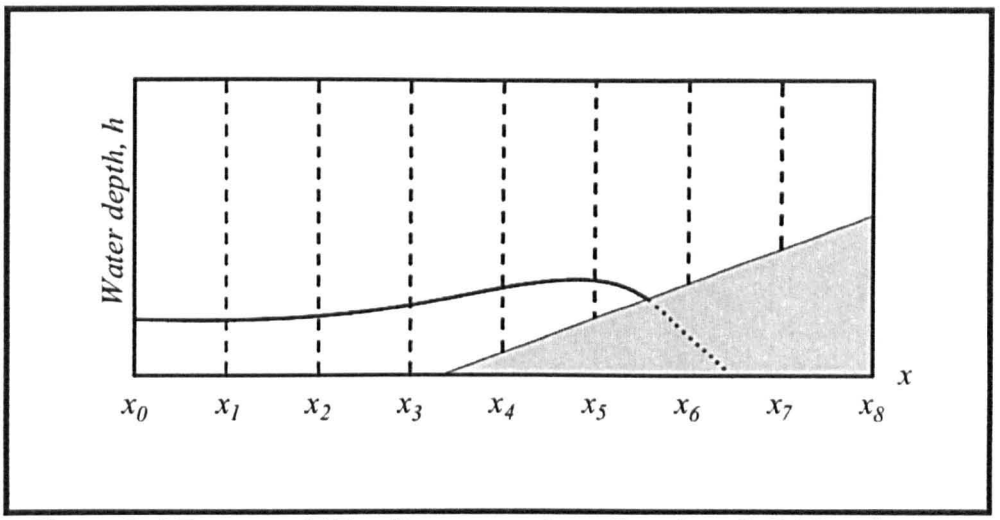

Figure 5. 4 Run-up of 1D solitary wave in x-direction. Solid line denotes locations that are determined using the primitive equations, whereas dots are the extrapolated nodes.

As depicted in the Figure 5.4, an extrapolation performed for a 1D solitary wave propagating on a 1:20 beach slope. The solid line shows the free surface locations that are determined using the primary equations. Meanwhile, the dots show the linear extrapolated points.

The extrapolation algorithm first involves dividing the node into dry and wet cells. The criteria for wet and dry conditions are based on the water depth h at a cell. A dry area is defined as the water depth h at the cells within the region containing the minimum water depth h_{min}. In these cells, the flow velocity and water depth are set to zero and h_{min} , respectively.

In implementing the technique for the run-up simulation process, a thin layer of fluid h_{min} is defined throughout the domain. The process is then followed by calculating the new water depth h via the lattice Boltzmann equation (3.17) at a node, as long as its water depth h is above the set minimum value h_{min} i.e. $h > h_{min}$. Otherwise, the flow variables at the node with $h \leq h_{min}$ are extrapolated.

The scheme is straightforward to be applied to the 1D problem, where by using the two wet points nearest to the wet-dry boundary, a linear extrapolation in the dry region is performed (see Figure 5.4). For 2D problems, the procedure is more complicated. The process of extrapolation in the 2D problem starts with the illustration as shown in Figure 5.5, in which, the dry node D is pictured to have 8 neighbour points of wet nodes W_{1-8}.

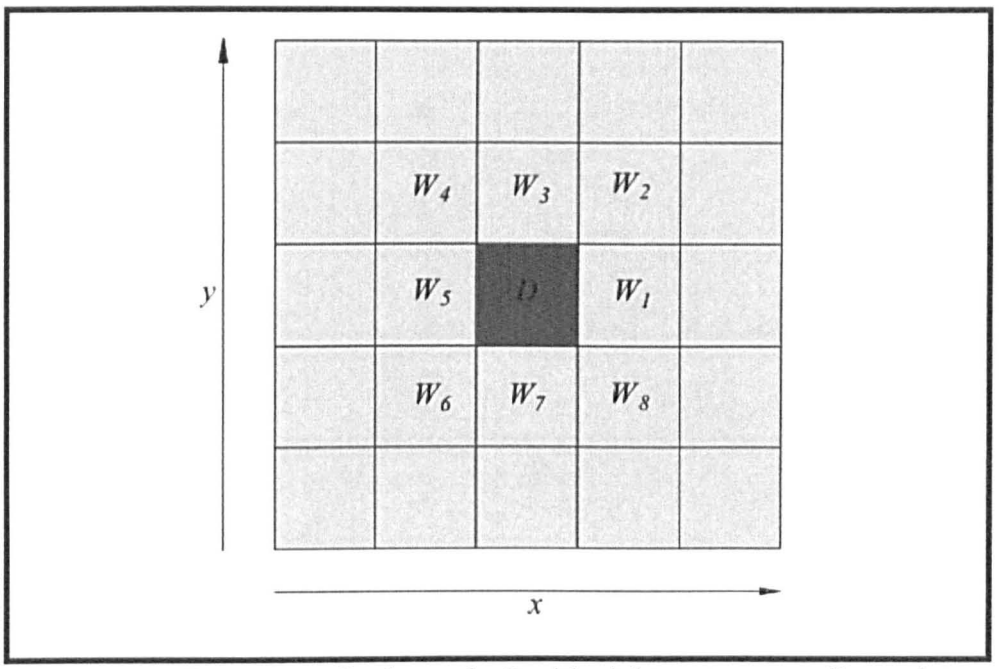

Figure 5.5 Illustration of a dry node D with eight wet surrounding points W_{1-8} in 2D lattices.

In this case, each of the dry nodes is checked for its surrounding eight nodes, each of which is wet. 1D linear extrapolation is used to estimate the free surface at the dry node. In other word, each of the nearest wet nodes W_{1-8} is extrapolated according to the directions shown in Figure 5.6, and the extrapolated values at the dry node D from the wet nodes are then taken as the averaged from. $(\sum W_1 + W_2 + \cdots W_8)/8$. This procedure is then repeated for the second layer of dry nodes

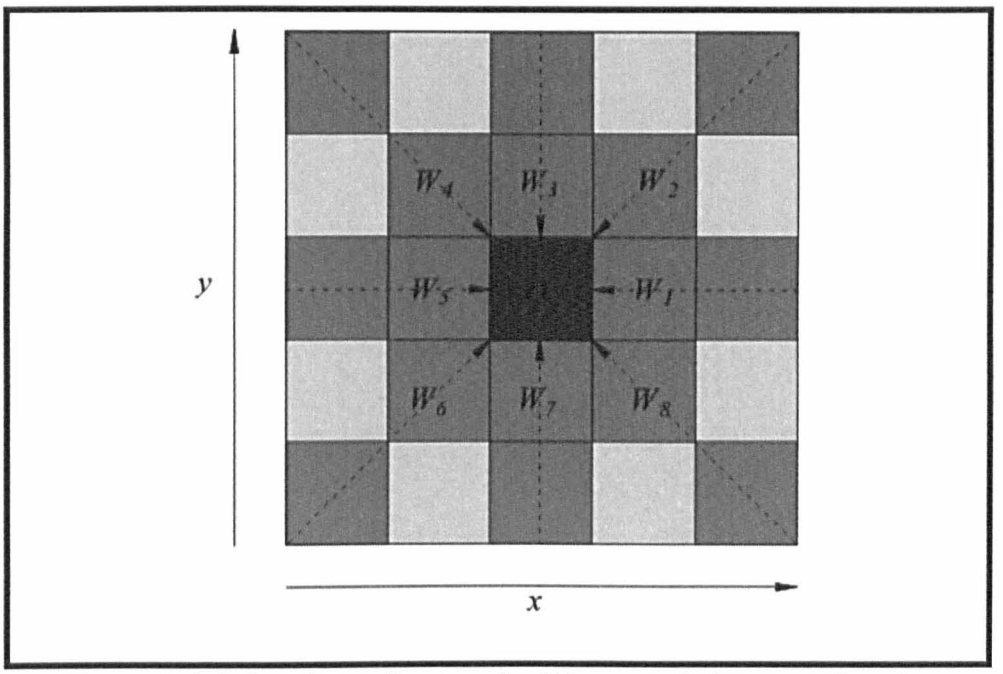

Figure 5. 6 6-directions of wet nodes W extrapolation towards a dry node D.

Chapter 6 Stability, Errors, and Solution Procedures for LB Models

6.0 Introduction

Errors in numerical methods are a common problem. Without special care, errors may cause the numerical system to become unstable.

However, through detailed analysis, cumulative errors (that could cause instability) can be avoided or reduced.

Linear and nonlinear stability analyses can be undertaken for uniform flows [34]. The Fourier method of John von Neumann is a standard stability analysis applicable to nonlinear systems or full-space problems [34,150]. It has been applied by Sterling and Chen [92] in analyzing the stability of the LBM. Cao et al. [151] stated that the use of semi-implicit schemes might be an option for improving LBM stability. The unknown density and momentum in the local equilibrium function can easily be obtained through moment equations. It obviates the solution of a tridiagonal matrix.

In LBM, the instability problem encountered is due to the discrete form of the lattice Boltzmann equation [4]. Although some preliminary work exists, the stability of the LBM has not been well-understood [33,92,152]. In fact, there are several aspects that need to be taken into account.

This chapter describes the particular stability factors needed in shallow flow lattice Boltzmann models such as LABSWE and LABSWE^{TM}. In addition, the source of errors for the models is discussed. This is followed by a solution procedure for: LABSWE and LABSWE^{TM}, and a wave run-up lattice Boltzmann model.

6.1 Stability Conditions

Theoretically, the stability conditions are not generally known for LBM, and may be different for different problems. For the shallow water flows models, LABSWE and LABSWE™, Zhou [4] simplifies the stability aspect to four basic criteria. These criteria are summarized, according to the physical water flow properties when solving the lattice Boltzmann equation (3.17), as follows:

Firstly, as dispersion is a common feature of water flows [92], kinematic viscosity (see equation (3.68)) must be a positive value; i.e.

$$\nu = \frac{e^2 \Delta t}{6}(2\tau - 1) > 0. \tag{6. 1}$$

It can be deduced from above, that the relaxation time τ :

$$\tau > \frac{1}{2}. \tag{6. 2}$$

Secondly, the lattice Boltzmann equation (3.17) often encounters numerical instability for high Reynolds number flows [151], in such case, time step and spatial step must satisfy the Courant Friedricks-Lewey (CFL) [153] condition for a stable solution to be achieved. Therefore, in order to make the lattice Boltzmann equation (3.17) consistent with the

CFL conditions, the Courant number C_r of the scheme should be smaller than unity,

$$C_r = \sqrt{u_j u_j}\frac{\Delta t}{\Delta x} < 1. \tag{6. 3}$$

In other words, the magnitude of the resultant velocity must be smaller than the speed calculated from the lattice size divided by the time step; i.e.

$$\sqrt{u_j u_j} < \frac{\Delta x}{\Delta t} = e. \tag{6. 4}$$

Thirdly, the wave speed in shallow water should also be less than the maximum speed e that the lattice can support; i.e.

$$\sqrt{gh} < e. \tag{6. 5}$$

Finally, as the lattice Boltzmann is limited to low speed flows [4], subcritical shallow water flow is assumed, and so:

$$F_r = \frac{\sqrt{u_j u_j}}{\sqrt{gh}} < 1. \tag{6. 6}$$

These four stability criteria must be met when applying the LABSWE and LABSWE^{TM}. It should be noted that, there are other advanced techniques for analysing stability [91,150,154,155] that could be used to improve further the stability of the current model.

6.2 Error Sources

Like other numerical schemes, the LBM has associated errors. Four common sources are [82,106,108,156-158]:

1) The finite size effect (grid convergence),

2) The boundary condition,

3) Round-off errors, and

4) Truncation errors.

- **Finite Size Effect (Grid convergence)**

The finite size effect is a significant source of error in the LBM [131]. The limited number of grid points in the computational lattice is known to affect the simulation results.

This type of error affects utilization of the lattice spacing. In other words, suitable lattice spacing needs to be determined to obtain accurate simulation results. In fact, in order to make the model stable, the largest possible size of lattice spacing is applied.

However, it can vary from one problem to another i.e., a very big lattice may be needed for the percolation threshold in porous media simulations even if they contain very small pores [156]. Nevertheless, a refined and non-uniform grid would improve the solution. Also, the error may be reduced by avoiding the use of very small values for the relaxation parameter in the simulation.

- **Boundary condition**

Errors can also appear due to the boundary conditions. Application of an unsuitable boundary could produce unphysical errors to propagate in the calculation.

The bounce-back scheme for no-slip boundary conditions is first-order accurate. For problems involving simple geometries, the bounce-back scheme can readily generate accurate solutions. However, the bounce-back scheme is not recommended for complex geometrical shapes such as curved objects. To solve such complex geometry problems, other boundary schemes including the elastic-collision scheme for slip and semi-slip boundary conditions should be applied. These are achieved through specialised treatments, as described in Chapter 4.

- **Round-off Errors**

Round-off errors arise due to the approximation values of numbers that have been evaluated by a computer (e.g., instead of 1/3, the number is limited to six decimal points 0.333333 in single precision on a computer) [159]. Consequently, the accuracy of the model will decrease, and this may cause the model to be invalid. Nevertheless, round-off errors can be reduced by choosing double precision.

- **Truncation Errors**

A truncation error is defined as the error caused by truncating terms in the mathematical procedure [159]. In order to reduce this error, the concept of a relative approximate error has normally been used to determine how many terms need to be considered.

In the lattice Boltzmann model for shallow water flows, higher order terms are neglected in deriving the shallow water equations when generating a second-order accurate model (see Section 3.1.5). Consequently, truncation errors may be brought in the model due to the omitted terms.

These errors have been identified as major factors affecting the LBM accuracy [89]. In addition, there are several other sources that might

influence the accuracy of the method such as the effect of Mach number, the finite-difference error, spatial-rounding and staircase errors, which are not described in the thesis. Explanations of this stability are given by Llewellin [160].

6.3 Solution Procedures

The LBM consists of simple arithmetic calculations that generate solutions of a governing partial differential equation. Moreover, LABSWE and LABSWE^{TM} solely involve explicit calculations, which make programming easy and efficient [4]. The detailed solution procedure for lattice Boltzmann models of shallow water flows is next described.

6.3.1 Procedure for LABSWE

In LABSWE, the solution procedure contains six main steps:

- **Set initial values of h, u and v.**

h, u and v, are the water depth and velocity components, respectively. In practice, these values are gathered from experimental information, or analytical solutions, or numerical data in published literature, or else assumed. The variables are used in the local equilibrium function (3.43) for the process of solving the lattice Boltzmann equation (3.17).

- **Calculate local equilibrium function f^{eq}.**

  f^{eq} is determined by equation (3.43) with the flow parameters h, u and v. The local equilibrium function is then used as the initial value for the distribution function f_α i.e., $f_\alpha = f_\alpha^{eq}$.

- **Calculate f_α at both collision and streaming steps from the lattice Boltzmann equation (3.17) with the relaxation time τ**

$$f_\alpha(\boldsymbol{x} + \boldsymbol{e}_\alpha \Delta t, t + \Delta t) = f_\alpha(\boldsymbol{x}, t) - \frac{1}{\tau}\left(f_\alpha - f_\alpha^{eq}\right) + \frac{\Delta t}{6e^2}\boldsymbol{e}_{\alpha i} F_i. \quad (6.7)$$

  Since no turbulence is considered, only a single relaxation time $\tau > 0.5$ is required, which satisfies stability.

The process of obtaining the new distribution function f_α on the left hand side of equation (6.7) consists of a force term calculation. Here, force terms caused by wind, bed and sidewall friction are evaluated using the third term in the right hand side of equation (6.7) as follows:

$$F_i = -gh\frac{\partial z_b}{\partial x_i} + \frac{\tau_{wi}}{\rho} - \frac{\tau_{bi}}{\rho} + \frac{\tau_{fi}}{\rho} \tag{6.8}$$

The wind, bed and sidewall shear stresses in (6.8) are determined from equations (2.59), (2.55) and (4.18), respectively.

- **Implement boundary conditions**

  Suitable boundary conditions are applied to calculating unknown f_α at all boundaries.

- **Update h, u and v**

  The water depth and velocities h, u and v, respectively, are then updated according to equation (3.48) and (3.53), respectively.

- **Return to Step 2 for next time step**

  The above process is continued until the required results are obtained.

6.3.2 Procedure for LABSWE™

In LABSWE™, a subgrid-scale stress (SGS) model is used as indicated in Section 3.2.1 for turbulent shallow water flows. The difference between LABSWE and LABSWE™ is that in the former, a single relaxation time is used while in the latter, the total relaxation time τ_t is used in the lattice Boltzmann equation,

$$f_\alpha(\boldsymbol{x} + \boldsymbol{e}_\alpha \Delta t, t + \Delta t) = f_\alpha - \frac{1}{\tau_t}\left(f_\alpha - f_\alpha^{eq}\right) + \frac{\Delta t}{6e^2}\boldsymbol{e}_{\alpha i}F_i. \tag{6.9}$$

The total relaxation time τ_t in the equation (6.9) is calculated using equation (3.82). In the present study, the Smagorinsky value C_s is in the range from $0.1 - 0.4$ when dealing with turbulent flows.

The solution procedure for LABSWE™ follows the six steps given for LABSWE in the previous section, except for the addition of a new step and a change in the third step according to this, respectively,

- **Calculate τ_t from equation (3.82), if LES model is used.**
- **Calculate f_α from equation (6.9) with the total relaxation time τ_t.**

6.3.3 Lattice Boltzmann Model for Moving Shoreline

A lattice Boltzmann model for a moving shoreline in the study has been developed for predicting wave run-up at a beach. In the model computation, the usual numerical calculations are implemented at a node with a water depth of $h > h_{min}$, and all other cells than considered with the thin film or linear extrapolation moving shoreline algorithms. In general, the difference between both moving shoreline techniques depends on the dry node conditions. In the thin film technique, the water depth h and flow velocity at a dry node are set to h_{min} and zero, respectively. Meanwhile, for the extrapolation technique, the water depth and velocity at the dry node are extrapolated.

The solution procedure for the model follows the steps given in the previous section (6.3.1), except that a new step is added after the water depth h and velocities u, v are updated as follows:

- **Update h, u and v**
- **Implementing moving boundary conditions**

The solution procedures for the three models are depicted in the flow chart shown in Figure 6.1,

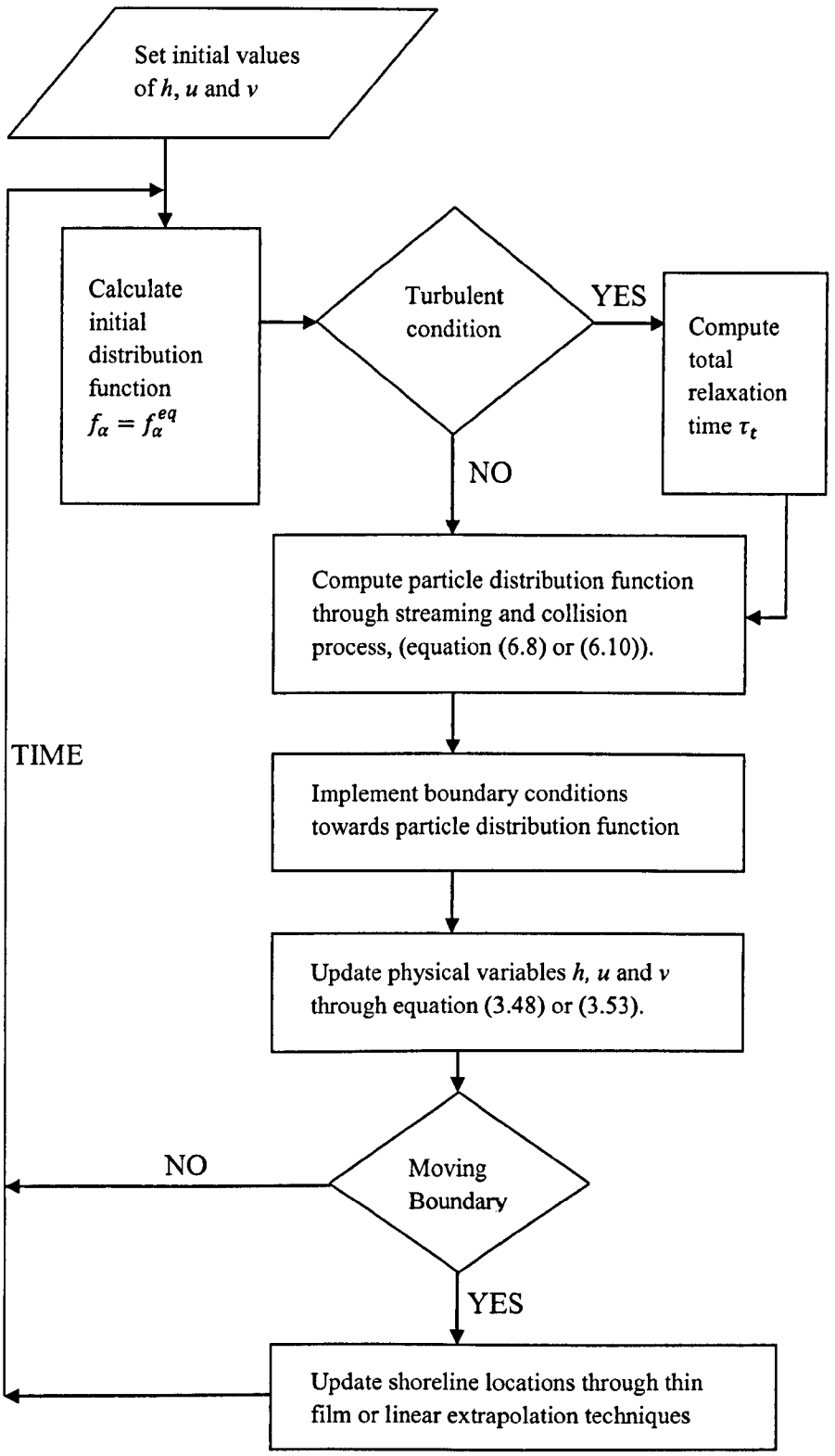

Figure 6. 1 Flow chart for solution procedure in LBM.

The LBM solution method in Figure 6.1 is simple and flexible, and can be implemented for complex fluid flows. In order to validate the capability of the model in predicting shallow flows, several benchmark applications of the model are presented in Chapter 7.

Chapter 7 Applications and Discussion

7.0 Introduction

Natural phenomena of free surface shallow water flows include tides, bores, wave run-up at beach, and tsunami propagation. Extreme free surface flows, such as floods can be hazardous to life and damage property. It is therefore essential that a shallow flow model can demonstrably provide accurate prediction of such natural phenomena.

In this chapter, the LBM model is applied to several water flow problems in order to assess accuracy and performance. For this purpose, the test cases are divided into three main groups that are classified as follows:

- Study of recirculating flows: Five typical problems in shallow water flows with different channel geometries are simulated with LABSWE^{TM}. For validation, the results are compared with available experimental, analytical and numerical data.
- Study of sidewall friction: LABSWE^{TM} with the semi-slip boundary condition is examined. The effect of wall friction in turbulent flows is studied. Several different values of wall friction coefficient are applied and discussed.
- Study of moving shoreline: The shoreline tracking capability of wave run-up model is studied. 1D and 2D problems are tested for validation. Results generated by two different moving shoreline algorithms are compared and discussed.

In all computations, the relative error E_R in the velocities between two time steps is determined from:

$$E_R = \sum_{n=1}^{Lx \times Ly} \frac{\sqrt{\left(u_n(t+\Delta t) - u_n(t)\right)^2 + \left(v_n(t+\Delta t) - v_n(t)\right)^2}}{Lx \times Ly} \qquad (7.1)$$

where Lx and Ly are the total number of nodes in the x and y directions within the computational domain, respectively. Full convergence is assumed to have been achieved when $E_R \geq 1 \times 10^{-8}$.

7.1 LABSWE™: Study of Recirculating Flows

In this section, LABSWE™ (for turbulent flow in complicated channel geometries) is validated by examining five shallow water flow problems:

a) Turbulent flow within a channel with a circular cavity,

b) Flow within an open-channel with a spur-dike,

c) Turbulent flow within a single expansion open-channel,

d) Turbulent flow within a double expansion open-channel,

e) Turbulent jet-forced flow in symmetrical and asymmetrical circular basins.

7.1.1 Flow in a Channel with Circular Cavity

Rivers and streams can become pathways that accelerate the delivery of silt causing lake sedimentation [161]. In practice, the fluvial flow pattern plays an important role in the process of erosion and entrainment.

Thus, as a test case, the flow in a channel with a circular cavity is simulated by LABSWE^{TM} to demonstrate the ability of the model in simulating the effect of turbulent flow in a river attached to a lake (a case involving complicated geometry). The model predictions are compared against simulation results obtained from a finite-difference model for unsteady flow proposed by Kuipers and Vreugdenhil [97].

The rectangular channel is $1.89m$ wide and $18.9m$ long. A $3.15m$ radius circular sidewall cavity is located on the right side of the channel in Figure 7.1.

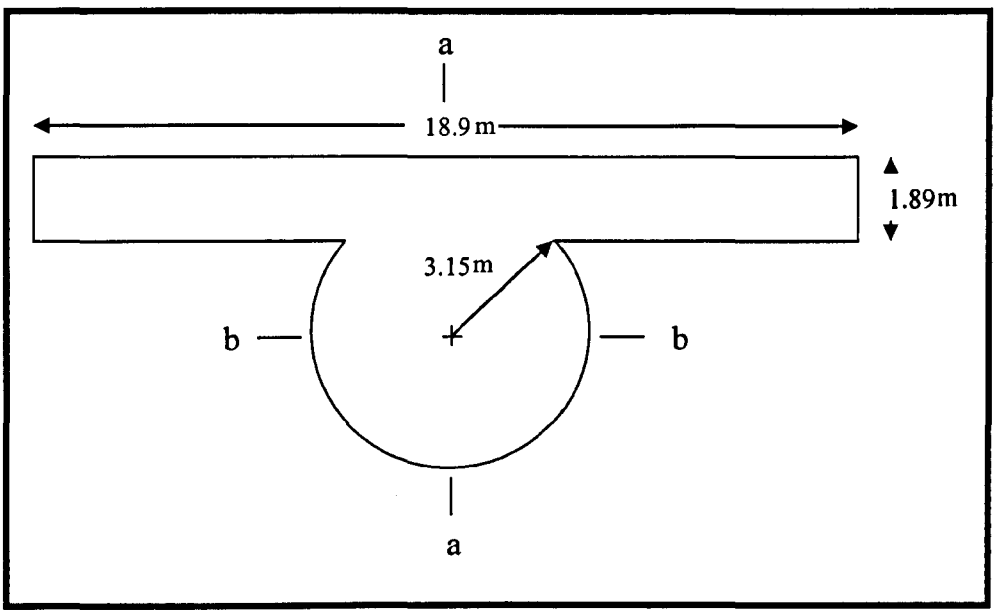

Figure 7. 1 The shape of open-channel with circular sidewall cavity in plan view.

Throughout the computation, flow velocity components of $u = 0.25m/s$ and $v = 0m/s$ and water depth $h = 0.25m$ are imposed at the inflow and outflow boundaries respectively of the channel.

A 190×70 lattice with grid space of $\Delta x = 0.1m$ is used. A semi-slip boundary condition with surface roughness coefficient $C_f = 0.0045$ is utilized at the solid walls. The relaxation time $\tau = 0.6$ and the Smagorinsky constant $C_s = 0.3$ are applied. A time step $\Delta t = 0.03s$ satisfies the stability criteria and hence is used in the model.

7.1.1.1 Results

Initially, the simulation was carried out by applying semi-slip boundary conditions for the solid wall. However, the velocity streamlines within the circular cavity slightly diverged due to the implementation of the semi-slip boundary condition. In order to overcome this problem, no-slip boundary condition was applied with relaxation time $\tau = 0.6$. For the no-slip condition, steady state was reached after the 10000^{th} iteration with $E_R = 5.24 \times 10^{-9}$. The model generated fully convergence flow velocity vectors and streamlines in the cavity, as illustrated in Figures 7.2 and 7.3, respectively.

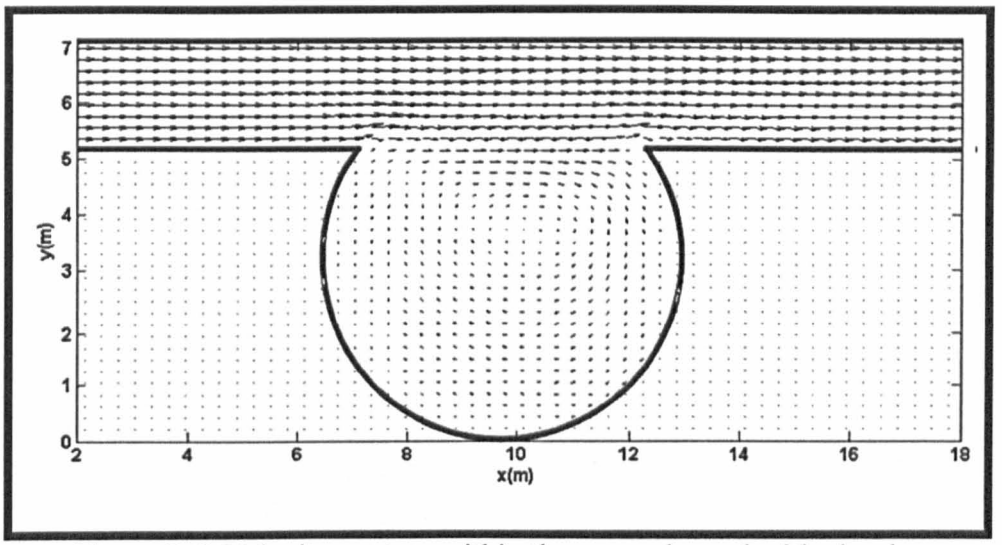

Figure 7. 2 Velocity vectors within the open-channel with circular sidewall cavity

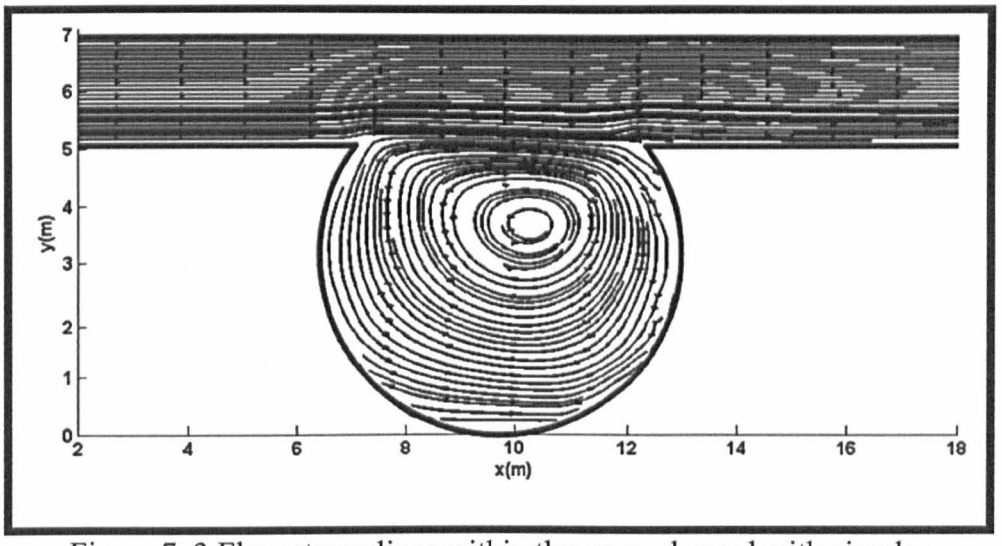

Figure 7. 3 Flow streamlines within the open-channel with circular sidewall cavity.

For validation, the u and v velocity components along $a-a$ and $b-b$ cross sections (see Figure 7.1), are compared against the alternative numerical and experimental results [97] in Figures 7.4 and 7.5.

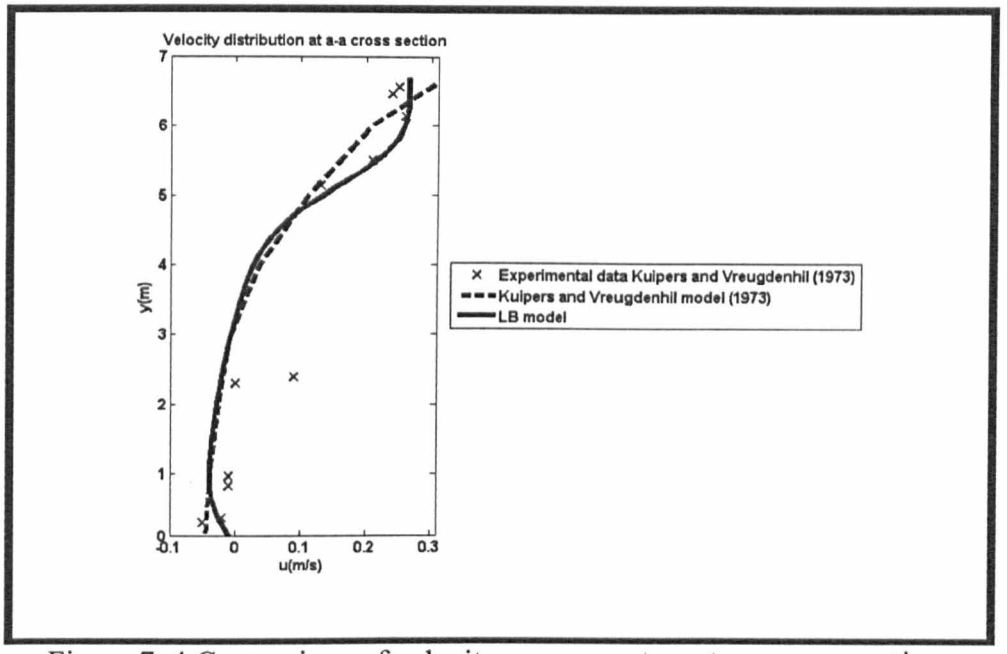

Figure 7. 4 Comparison of velocity components u at a-a cross section.

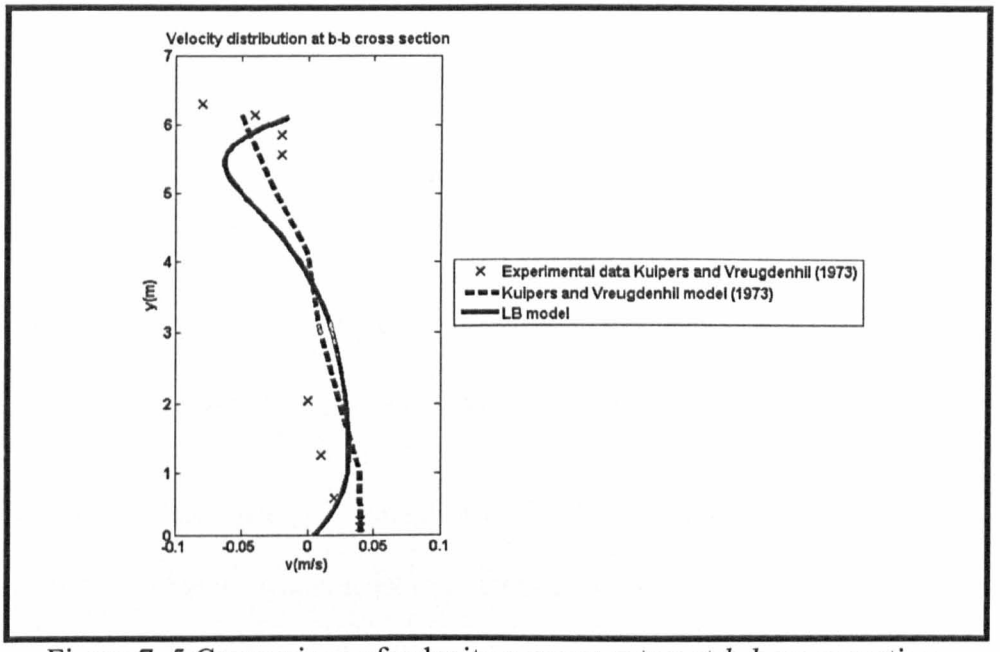

Figure 7. 5 Comparison of velocity components v at b-b cross section.

The comparison shows that the present model generates better agreement than the results from the alternative finite difference model [97] with the

experimental data [97], except for the velocity component v in Figure 7.5, which is slightly under predicted near the wall of the circular cavity.

Analysis of the relative error for velocity values u along the $a-a$ cross section was estimated by comparing the experimental data and the predictions by lattice Boltzmann models with no-slip and semi-slip wall boundary conditions. The results obtained are listed in Table 7. 1.

	LABSWE™ Error
No-slip boundary condition	0.0215
Semi-slip boundary condition	0.0237

Table 7. 1 The velocity errors for LABSWE™ compared to the experimental data.

For the semi-slip boundary condition, the error is 0.0237. For a no-slip boundary condition, the error reduces slightly to 0.0215. There is no significant difference of accuracy between both boundaries. Generally, this test proves the sufficiency of the semi-slip boundary condition in solving a shallow flow problem involving a complex geometry.

From the above analysis, the present model performs better than Kuipers and Vreugdenhill's solver in predicting flow recirculation in a sidewall cavity expansion.

7.1.2 Flow in a Channel with Spur-dike

A spur-dike is a river training structure such that one end is adjacent to the riverbank and the other end projects into the main flow [162]. It is commonly used for redirecting the flow of water in a river. However, the presence of a spur-dike can cause flow separation and recirculation around the structure. This in turn leads to the phenomenon of scouring in the river [163]. Therefore, LABSWE^{TM} is used to predict flow pattern around a spur-dike, which herein is taken to be a thin structure.

Nawachukwu [103] investigated this problem experimentally and conducted tests in a straight rectangular channel flume 37m long and 0.9m wide. A 3mm thick and 152mm long spur-dike projected above the surface of the water. The layout is illustrated in Figure 7.6.

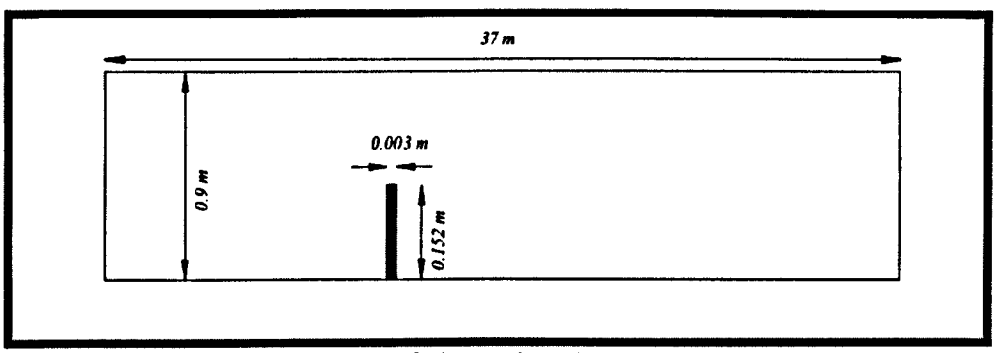

Figure 7. 6 Sketch of channel with spur-dike structure.

A 900×90 square lattice is applied with $\Delta t = 0.005\, s$, $\Delta x = 0.01\, m$ and $\tau = 0.62$. For laminar flow condition, the Smagorinsky constant $C_s = 0$ is used. At the upstream inflow boundary, the velocity

components are set to $u = 0.253\, m/s$ and $v = 0\, m/s$. At the downstream outlet, the velocity components are extrapolated and the water depth is set to $h = 0.189\, m$.

7.1.2.1 Results

Two types of wall boundary conditions are used in solving the spur-dike problem. At the spur-dike structure, a no-slip boundary condition is applied, while at the channel walls, a slip boundary condition is utilized.

The flow reached steady state after the 20000 iterations, with $E_R = 2.03 \times 10^{-9}$. Figure 7.7 show the predicted steady state velocity field.

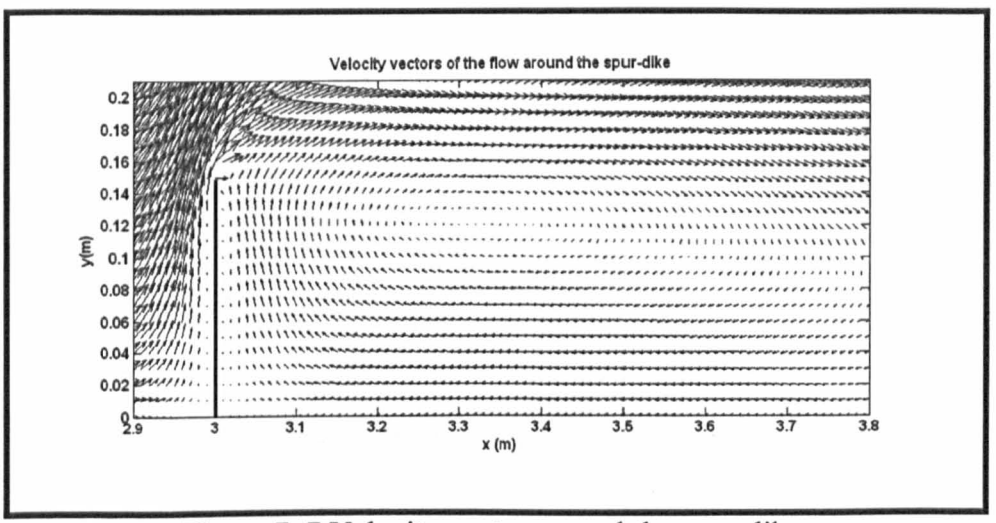

Figure 7. 7 Velocity vector around the spur-dike.

The velocity vectors are largest as the flow accelerates past the spur-dike are a large recirculation eddy that is clearly seen after the spur.

The numerical results have further been compared with experimental data [103] at different transversal locations for non-dimensionalized velocity (dividing through by the inlet value of $u_0 = 0.253\, m/s$) along flow direction in Figures 7.8 - 7.12. In these figures, b indicates as spur-dike length.

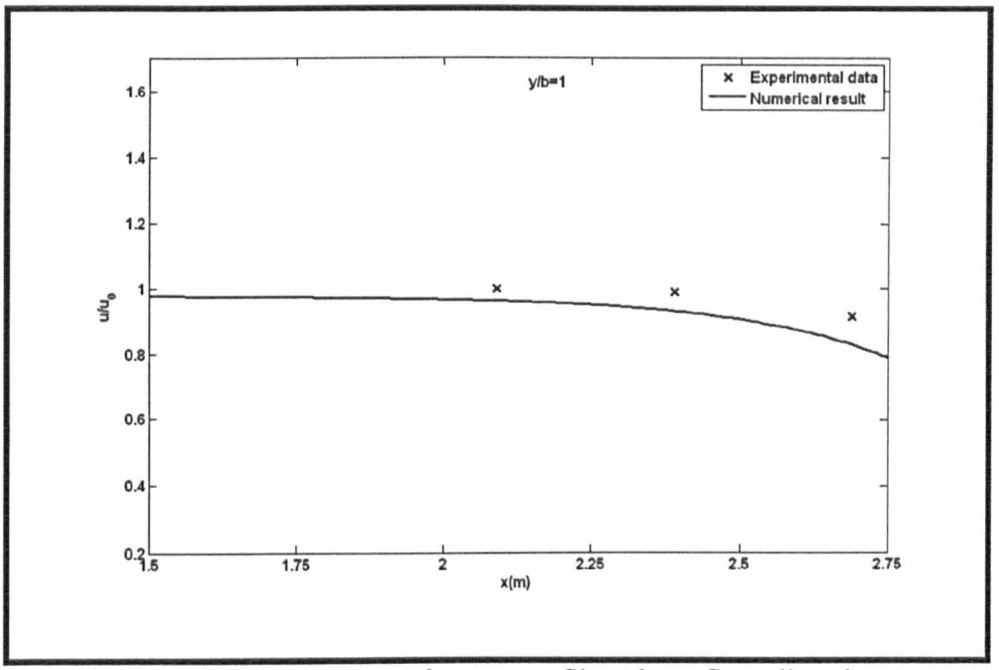

Figure 7. 8 Comparisons of water profiles along flow direction at transversal location of $y/b = 1$.

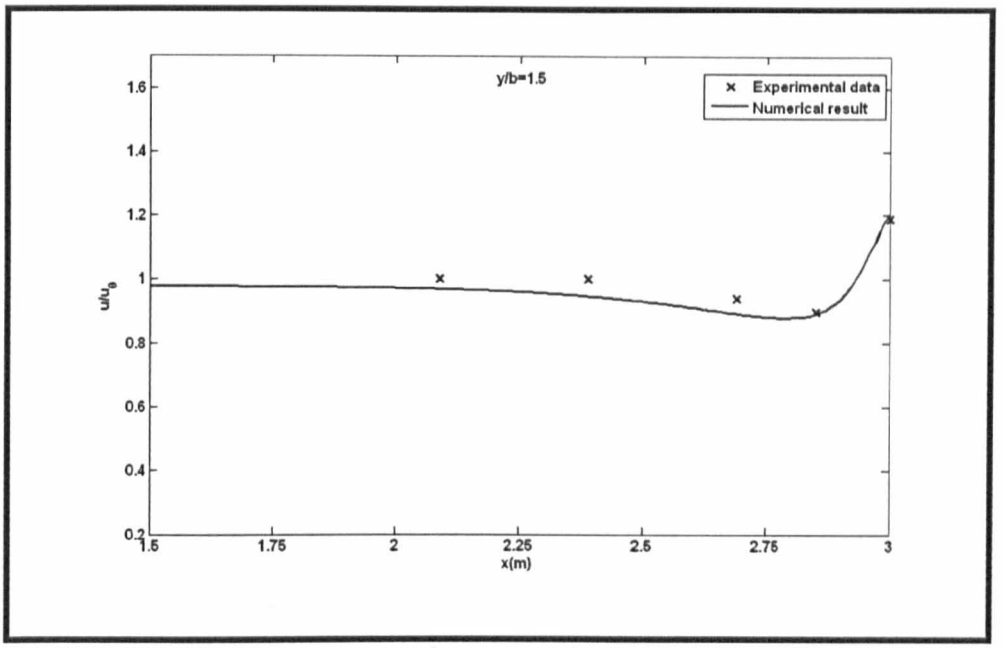

Figure 7. 9 Comparisons of water profiles along flow direction at transversal location of $y/b = 1.5$.

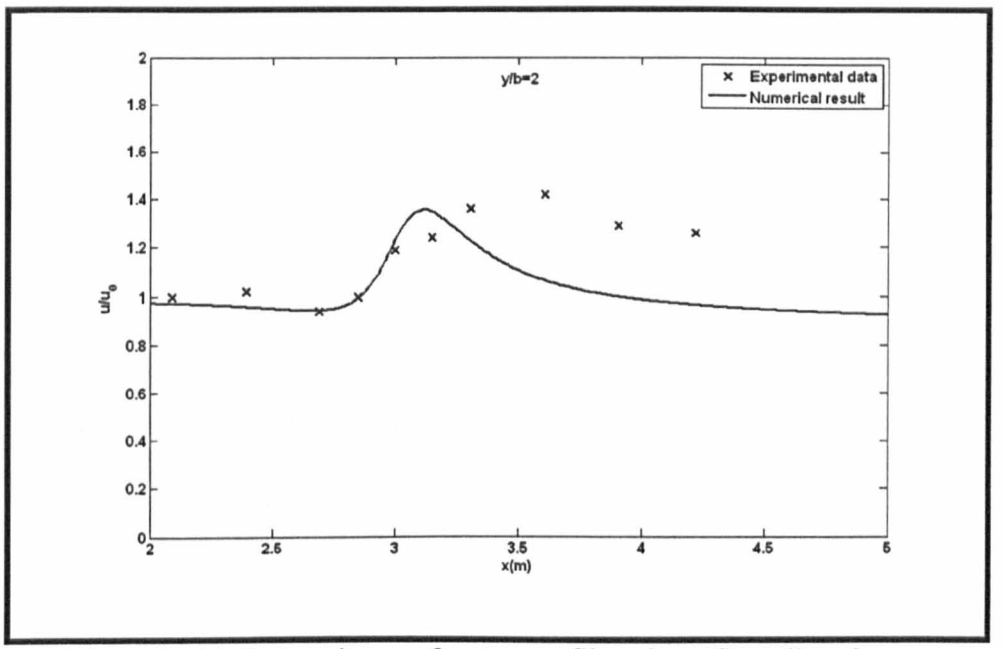

Figure 7. 10 Comparisons of water profiles along flow direction at transversal location of $y/b = 2$.

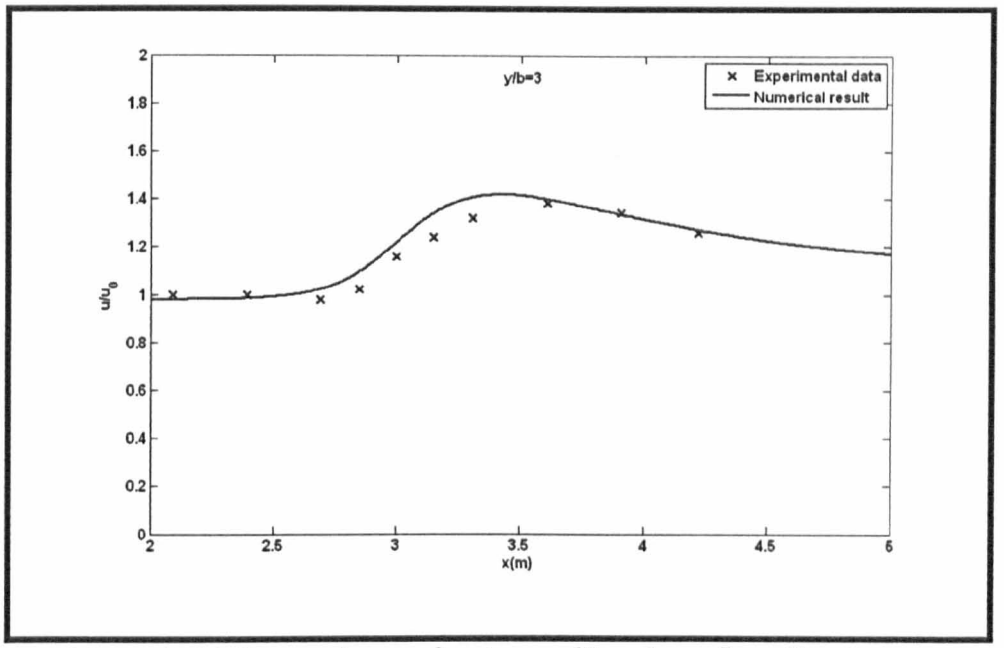

Figure 7. 11 Comparisons of water profiles along flow direction at transversal location of $y/b = 3$.

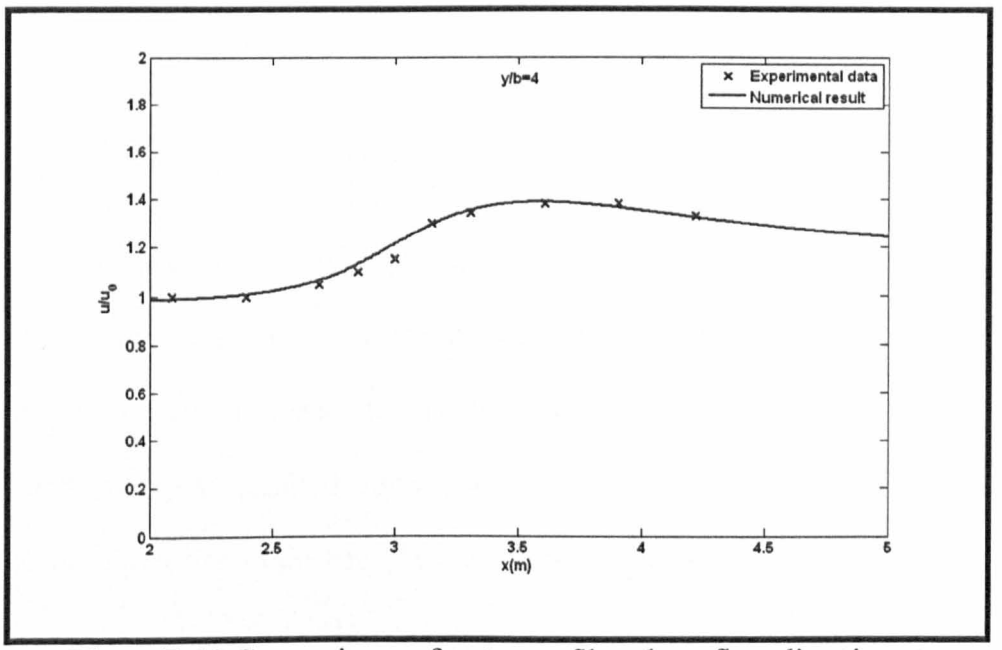

Figure 7. 12 Comparisons of water profiles along flow direction at transversal location of $y/b = 4$.

The agreement is satisfactory for all locations, except for $y/b = 2$, where the computed results under predict the experimental data downstream of the spur. However, it is possible that the experimental data may be erroneous specifically in this region (as indicated by similar results from other numerical comparisons done by others [162,164]).

7.1.3 Flow in a Single Expansion Channel

Expansion or separation in an open-channel is common in hydraulic and environmental engineering. Hydraulic structures such as spillways, chutes and flood relief canals use this approach to allow water to be diverted from the main channel [165].

Flow in an open-channel with a single expansion is one of the cases used to investigate the flow circulation pattern caused by viscous effects and by turbulence. The way turbulence is modelled can lead to different circulation patterns and lengths [166]. Turbulence plays a significant role in the simulation of the eddy flow in the recirculation circulating zone.

The performance of a k-ε turbulence model discretised using a finite volume method in simulating flow in a channel with a single expansion

has been studied by Fe et al. [166]. The model predicted remarkably accurate flow circulation compared to the experimental data [167]. The same test is used to evaluate the ability of LABSWE^{TM} in simulating flow circulation.

The channel consists of a single $0.297\ m$ wide expansion on the right hand side of a channel whose inlet is with $0.206\ m$ wide, as shown in Figure 7.13. The upstream flow discharge is $Q = 20.21 l/s$ and the downstream water depth is $h = 24.2m$.

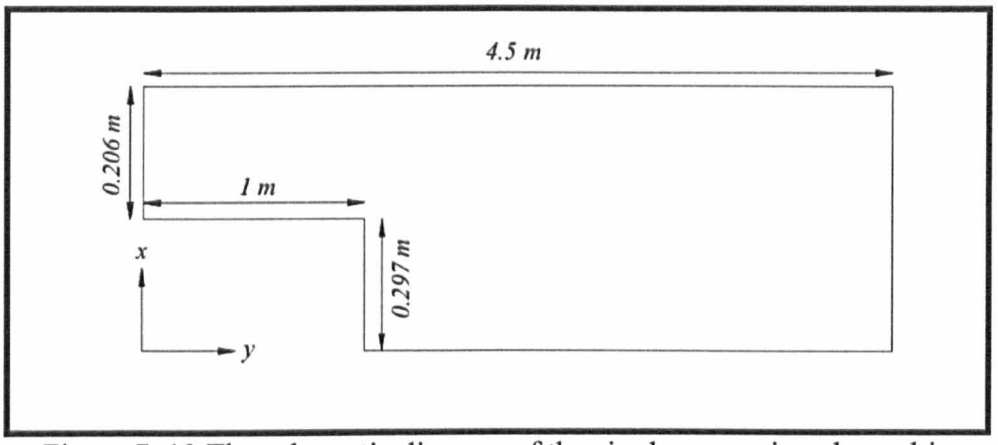

Figure 7. 13 The schematic diagram of the single expansion channel in plan view.

The computational grid consists of 150×17 lattices of spacing $\Delta x = \Delta y = 0.03\ m$ covering the overall $4.5\ m$ length and $0.503\ m$ width of the shallow channel. To include turbulence, the Smagorinsky constant $C_s \neq 0$ is used. The wall friction coefficient is $C_f = 0.03$ with associated

Manning value $n = 0.01$ (for the glass surface). The time step $\Delta t = 0.005s$ and the relaxation time $\tau = 0.53$ satisfies the stability criteria.

7.1.3.1 Results

The steady state condition is reached after the 10000 iteration. However, although the eddy after the channel expansion is reproduced, the circulation length is too short. The most accurate streamline pattern giving the best fit to the circulation length is obtained using $C_s = 0.25$ and $\tau = 0.53$, with an associated error of $E_R = 3.16 \times 10^{-7}$. The simulation provides very satisfactory results for streamlines and velocity vectors as illustrated in Figures 7.14 and 7.15, respectively.

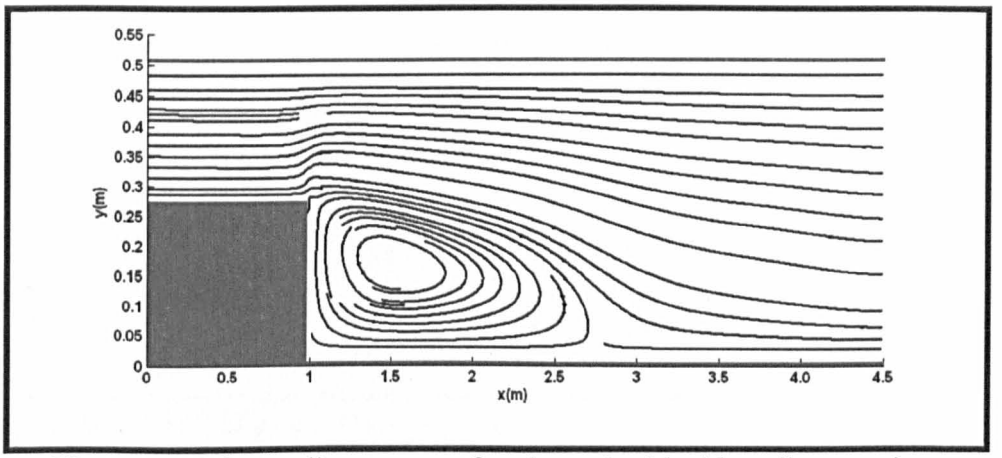

Figure 7. 14 Streamline contour for channel with sidewall expansion.

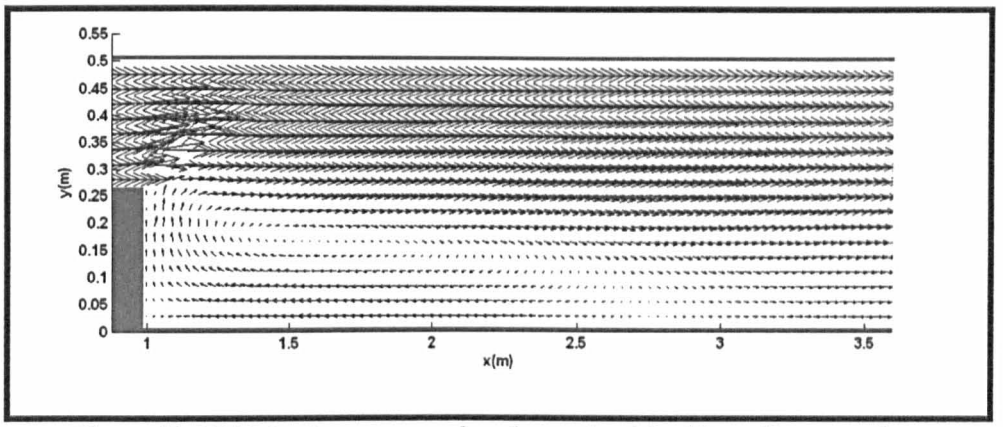

Figure 7. 15 Velocity vectors for channel with sidewall expansion.

In order to validate the model, numerical results have been plotted for the velocity component u at three different locations along the x-direction within the eddy zone. They are compared with the experimental data [167] and the k-ε simulation results [166] in Figures 7.16 – 7.18.

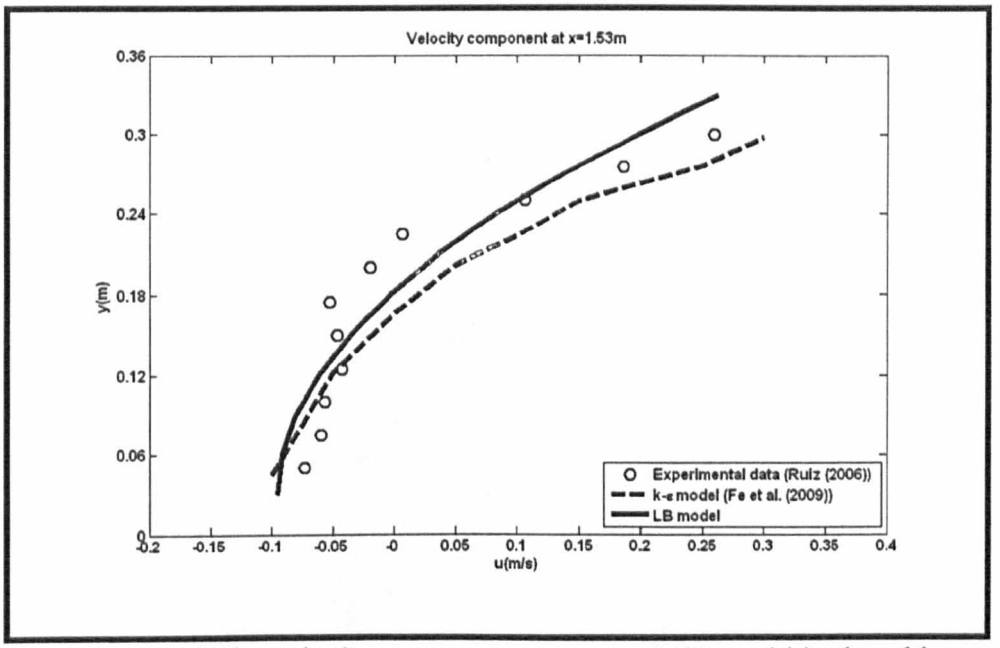

Figure 7. 16 The velocity component u at $x = 1.53m$ within the eddy zone. The circles indicate experimental data.

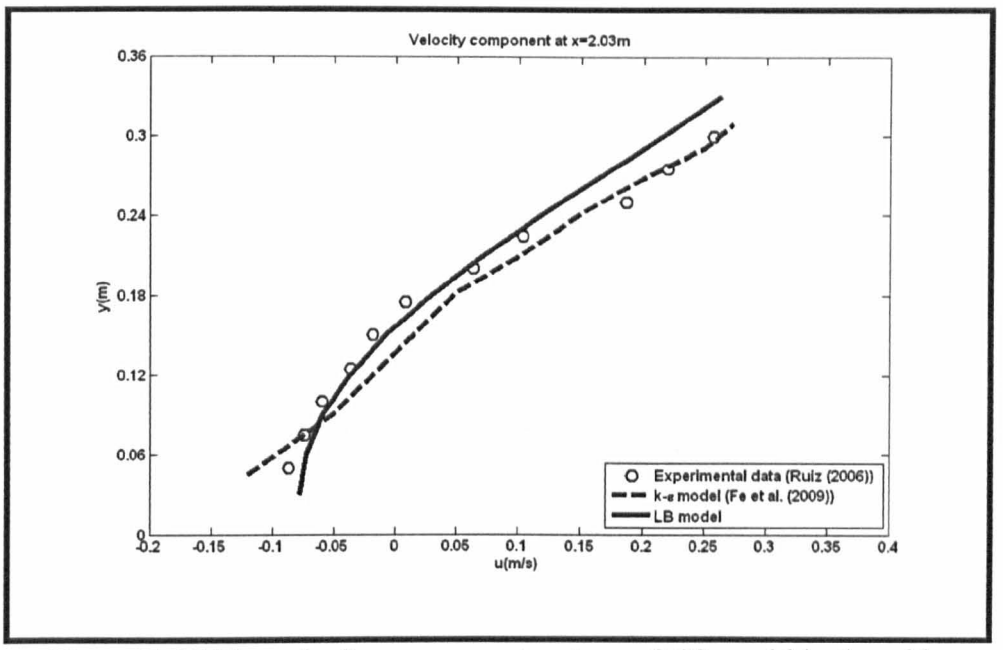

Figure 7. 17 The velocity component u at $x = 2.03m$ within the eddy zone. The circles indicate experimental data.

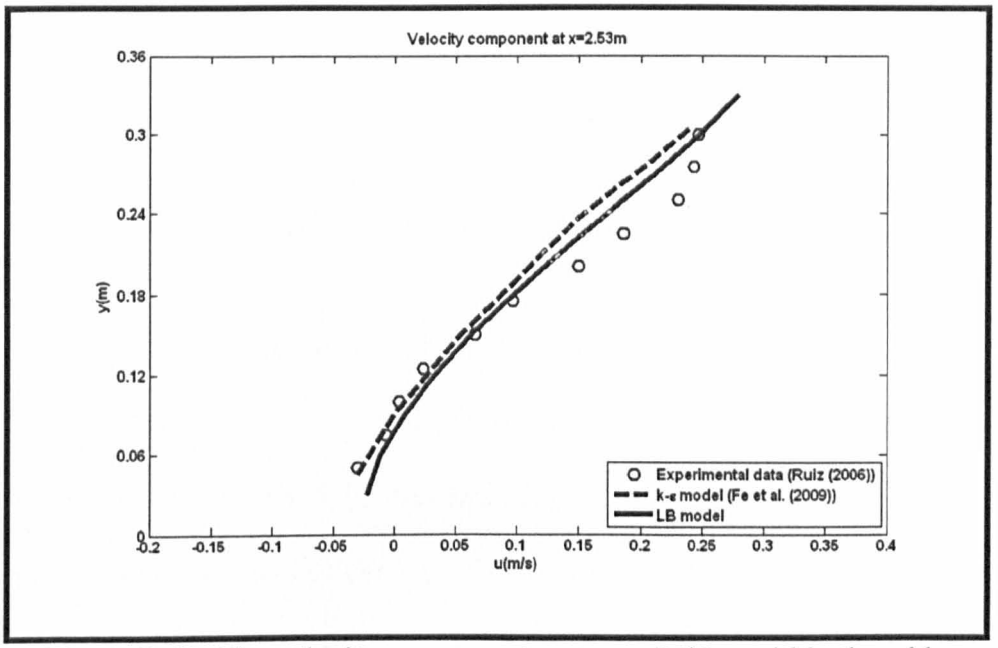

Figure 7. 18 The velocity component u at $x = 2.53m$ within the eddy zone. The circles indicate experimental data.

The predicted velocity profiles at $x = 1.53m, 2.05m$ and $2.53m$ are in very good agreement with the corresponding experimental profiles. Table 7.2 lists the relative error for velocity values u between the experimental data and the lattice Boltzmann model results. It can be seen that reasonable agreement has been achieved with most errors smaller than 5%.

Position x(m)	LABSWE^{TM} Error
1.53	0.0295
2.03	0.0096
2.53	0.0179

Table 7. 2 The velocity errors of LABSWE^{TM} model compared to the experimental data.

7.1.4 Flow in a Double Expansion Channel

A double expansion channel is a common hydraulic structure. It can be used to control flow rates in rivers and dams [168], and is often an essential feature of a dam structure. Using a double expansion channel, the water in the main catchment of a dam can be diverted to several other channels downstream [168].

Moss et al. [169] conducted experimental tests for flow through a double expansion channel. Later, Chapman and Kuo [170] used the k-ε method to model the same flow. With some modifications and ad-hoc corrections, the results generated by Chapman and Kuo's model were shown to be in agreement with the experimental data. The same case is repeated here in order to verify the capability of the LBM.

In this section, the channel geometry is similar to the former case (see Section 7.1.3). Instead of a single expansion, it consists of double expansions in width. The channel aspect ratio is $1.45 = 1 + W_1/W_0$, and is illustrated in Figure 7.19 [169,170], where $W_0 = 20m$ and $W_1 = 9m$ with a channel slope of 0.0005.

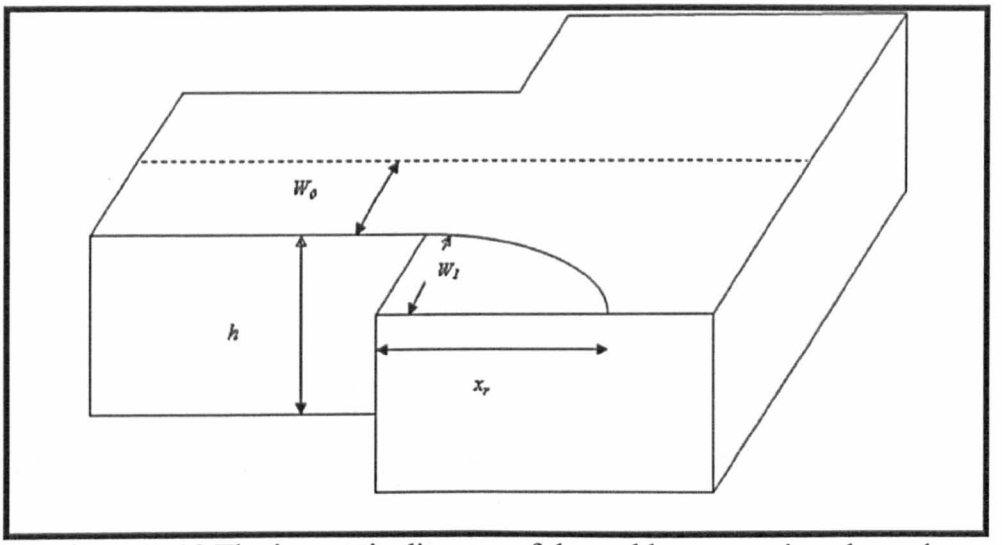

Figure 7. 19 The isometric diagram of the sudden expansion channel.

For computation, the domain consists of 100×40 lattices with grid spacing $\Delta x = \Delta y = 0.05m$ and time step $\Delta t = 0.025s$. The inlet velocity

component $u_0 = 2.35m/s$ and downstream water depth $h = 1.524m$ are imposed throughout the simulation. A semi-slip boundary condition is used. The wall friction coefficient $C_f = 0.0045$ is applied along the channel sidewalls. For the bed friction effect, $C_b = 0.0045$ is included.

7.1.4.1 Results

The strong the turbulence intensity, the longer the circulation length. From the previous analysis done by Moss et al. [169], the inlet channel width with aspect ratio of 1.45 suggests that the circulation length should be in the range of $40.5m - 45m$ in the prototype.

In an attempt to fit the model predictions to the required length of circulating flow, the simulation was tested for several combinations of relaxation time τ and Smagorinsky constant C_s. Relaxation times τ in the range of $0.53 - 0.55$ were used together with $0.1 - 0.4$ of C_s for the model simulation. As a result, $C_s = 0.4$ and $\tau = 0.55$, were found to give the best match to the required circulation length. Steady state results are reached after the 6500^{th} iteration, with $E_R = 6.516 \times 10^{-6}$. The simulation results are plotted as in Figures 7.20 and 7.21.

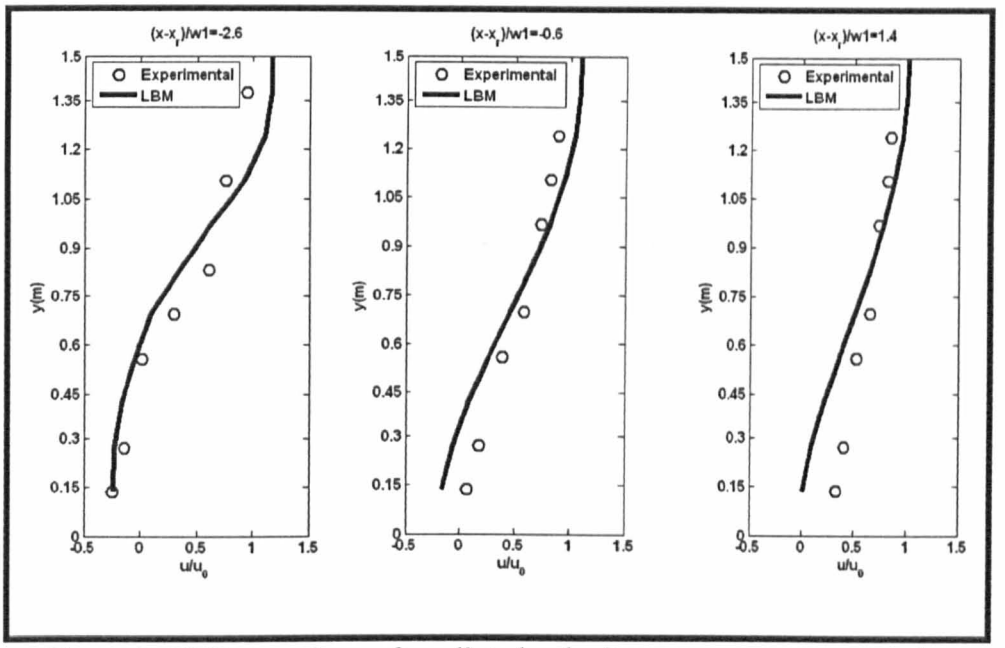

Figure 7. 20 Comparison of predicted velocity component u across the channel with experimental measurements [169].

Figure 7.20 compares the LBM model predictions against experimental data obtained by Moss et al. [169] for the transverse profile of the velocity component u (across the recirculation zone) at three different streamwise locations along the channel. As depicted in the figure, the predictions demonstrate close good agreement with the experimental data.

The simulated velocity vector field is symmetric, and so is plotted over half the channel in Figure 7.21. The model formed well-developed circulating flows behind the step. The predicted value of circulation length in the simulation is approximately $44.5m$, which agrees well with the experimental measurements.

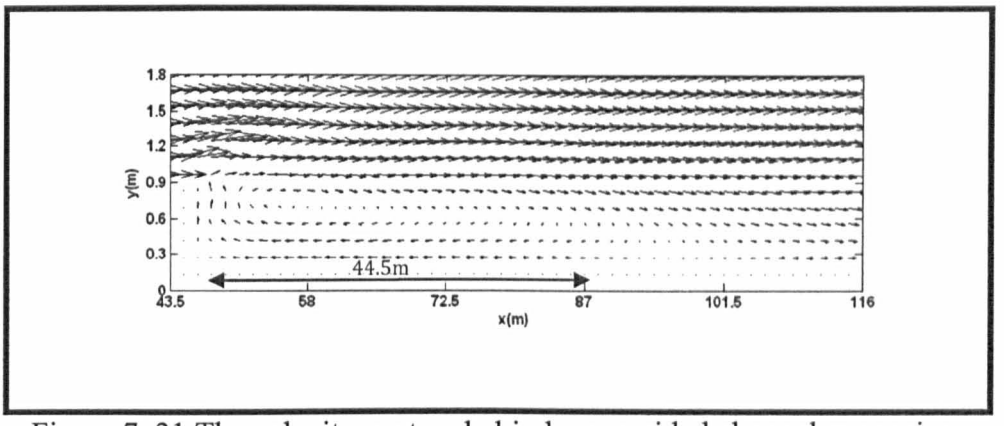

Figure 7. 21 The velocity vectors behind a one-sided channel expansion.

The above comparison verifies the use of the proper relaxation time and Smagorinsky constant in simulating flow circulation and the velocity fields using the lattice Boltzmann model.

7.1.5 Jet-Forced Symmetrical and Asymmetrical Flow in Circular Basins

In civil and environmental engineering, jet-forced flows are commonly found in ponds and reservoirs for treating waste water. In fact, the jet-forced flows facilitate better mixing of chemicals for treatment.

In computational fluid dynamics, modelling jet-forced flow in circular channels is a challenging task. This is due to the complexity of the boundary geometry of the circular shaped channel. Nevertheless, several

authors have considered this problem [63,171-176], which involved the use of common conventional numerical methods such as Godunov-type finite volume method and finite element method.

Overall, two essential hydraulic systems are observed that can affect the fluid transport in the jet-forced hydraulic structure [177]: a) the inlet jet and b) the circulating flow. Hence, these systems will be simulated in the current study by using the LABSWE^{TM} in testing the capability of the model.

The dimensions and flow parameters for the symmetrical and asymmetrical circular basins are shown as in Figures 7.22 and 7.23 [176].

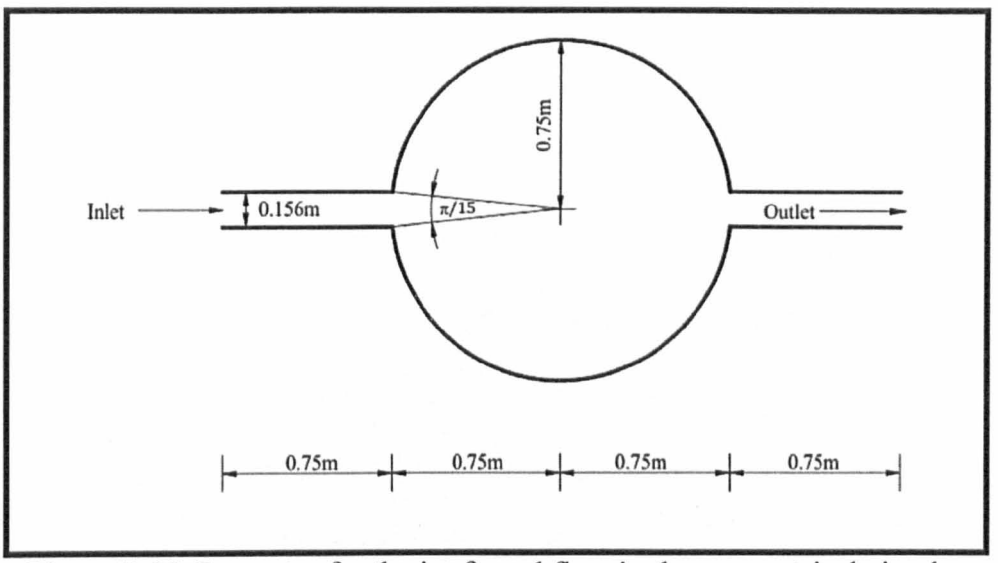

Figure 7. 22 Geometry for the jet-forced flow in the symmetrical circular basin.

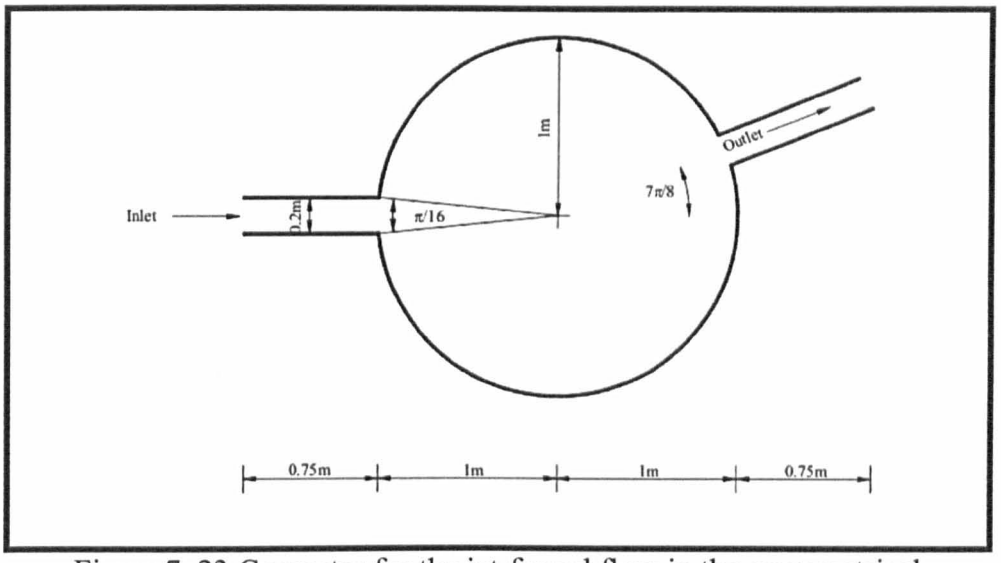

Figure 7. 23 Geometry for the jet-forced flow in the asymmetrical circular basin.

For computation of flow in the symmetrical circular basin, the radius of the basin is $r = 0.75m$ with inlet and outlet openings at an angle of $\pi/15\ rad$. The domain consists of 250×125 lattices with grid spacing $\Delta x = \Delta y = 0.012m$, and the time step $\Delta t = 0.006s$. For boundary conditions, the velocity component $u = 0.1m/s$ and $v = 0m/s$, respectively, and water depth $h = 0.1m$ are used at the upstream of the channel. Meanwhile, the water depth $h = 0.1m$ and the velocity components $u = 0.1m/s$ and $v = 0m/s$ are set at the downstream. At solid walls, a no slip boundary condition for complex shape [107] is applied.

For simulation of flow in the asymmetrical circular basin, the initial, inflow and outflow boundary conditions are repeated from the

symmetrical circular basin problem, except for the radius of the basin $R = 1m$ and the opening angle $\pi/16\ rad$ for the inlet and outlet of the channel. In this problem, the outlet position is separated by $7\pi/8rad$ from the inlet. 280×160 lattice with grid spacing $\Delta x = \Delta y = 0.0125m$ and time step $\Delta t = 0.00625s$ are utilized in the model.

7.1.5.1 Results

The steady state condition for both problems is reached at 10000^{th} iteration, with $E_R = 1.60 \times 10^{-8}$ and $E_R = 1.54 \times 10^{-7}$ for symmetrical and asymmetrical channels, respectively. In order to obtain accurate results, a number of Smagorinsky values have been tested. The best streamline with the required circulation length and pattern are obtained using $\tau = 0.55$ and $C_s = 0.25$. The velocity vectors of eddy and well-developed circulation flows in the symmetrical and asymmetrical channels are plotted in Figures 7.24 – 7.27.

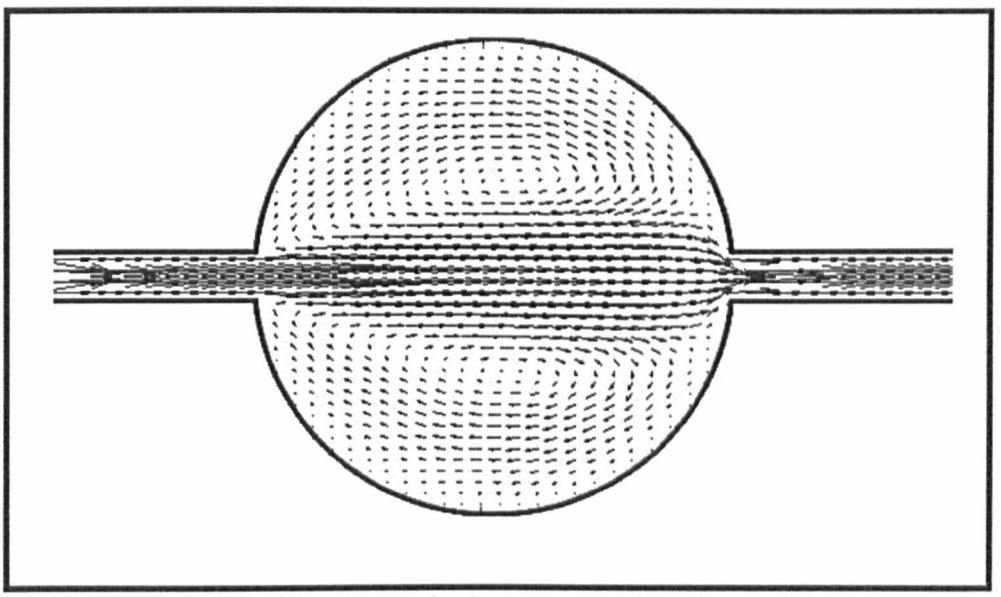

Figure 7. 24 Steady state velocity vectors of jet-forced flow in the symmetrical circular basin.

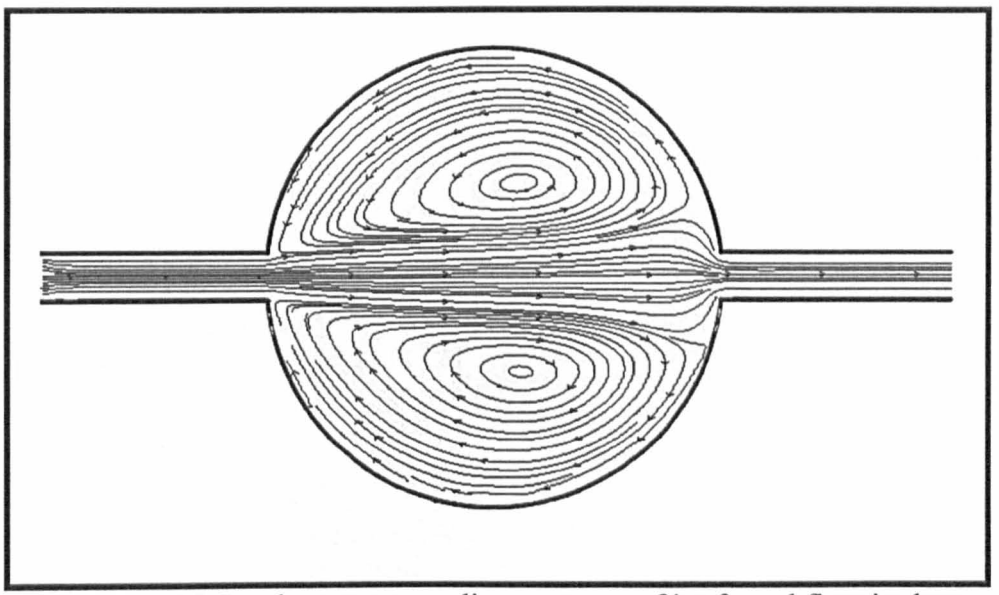

Figure 7. 25 Steady state streamline contours of jet-forced flow in the symmetrical circular basin.

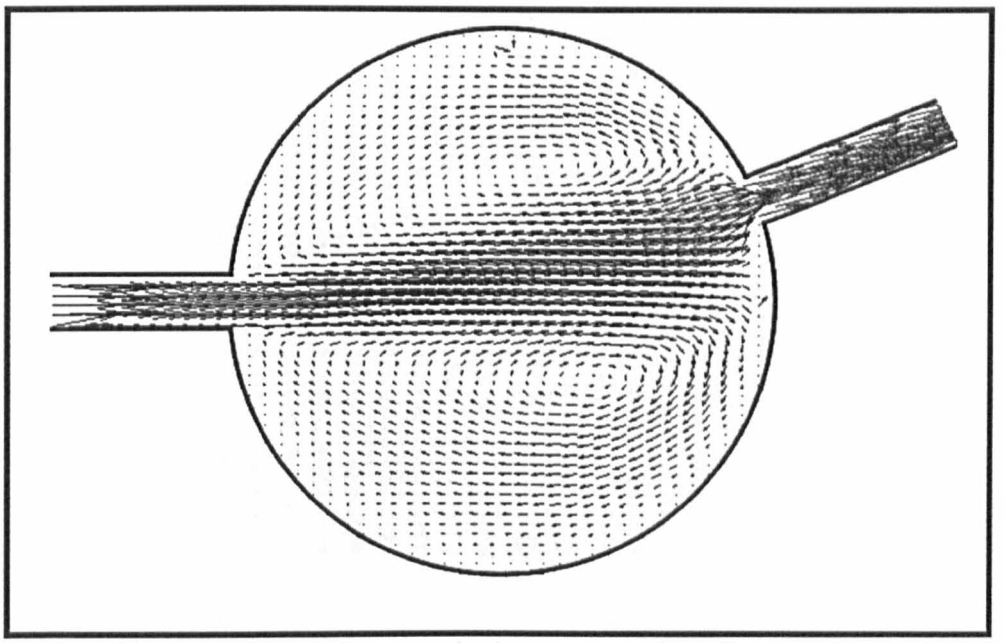

Figure 7. 26 Steady state velocity vectors of jet-forced flow in asymmetrical circular basin.

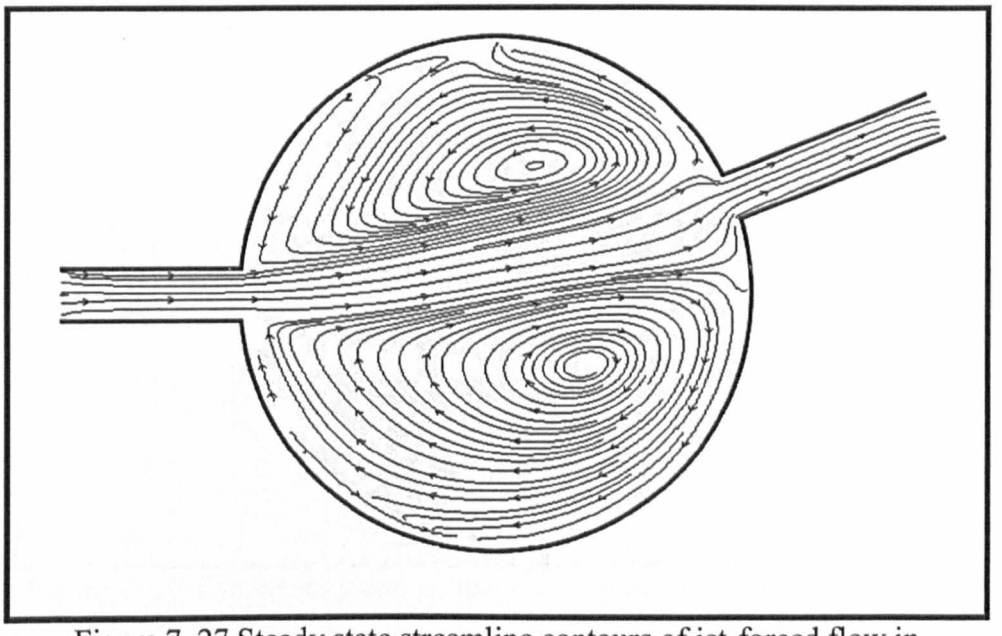

Figure 7. 27 Steady state streamline contours of jet-forced flow in asymmetrical circular basin.

Comparison of the circulation patterns revealed that there is a close agreement between the present predictions and alternative numerical results obtained by [63,174-176]. However, there is small spurious velocities occurred near to the left hand side of the channel (see Figure 7.26). It is caused from the use of square lattice pattern in representing circular shape. Despite of the discrepancies, the use of curve boundary condition [131] and multi block [130] treatments can be applied in future to overcome this situation. To verify the model further, the velocity component u profile across the mid-section of both types of channels is plotted in Figure 7.28 and 7.29.

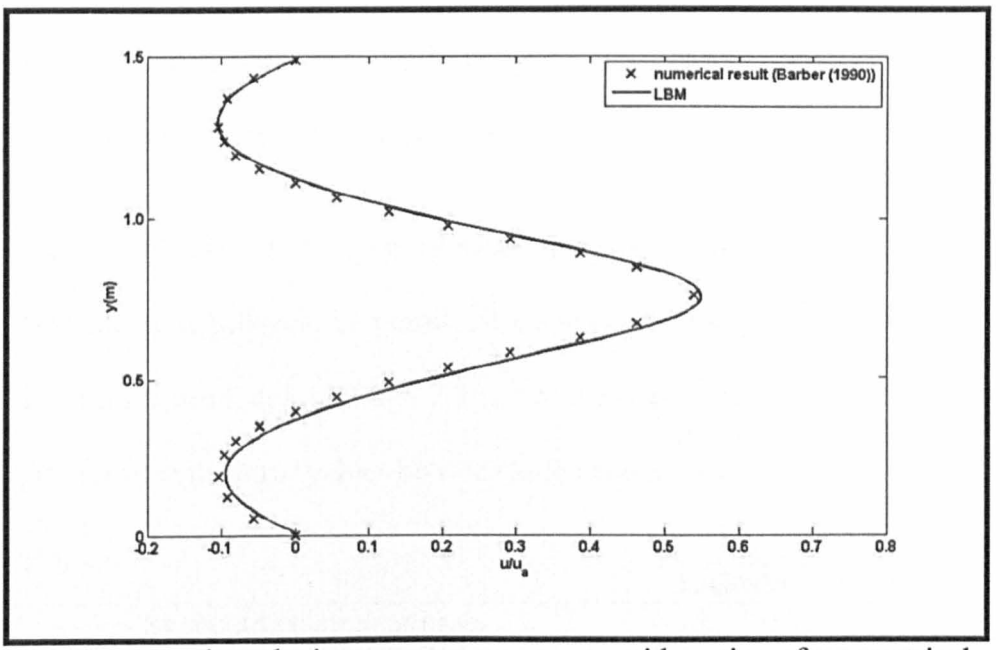

Figure 7. 28 The velocity component u across mid-section of symmetrical circular basin.

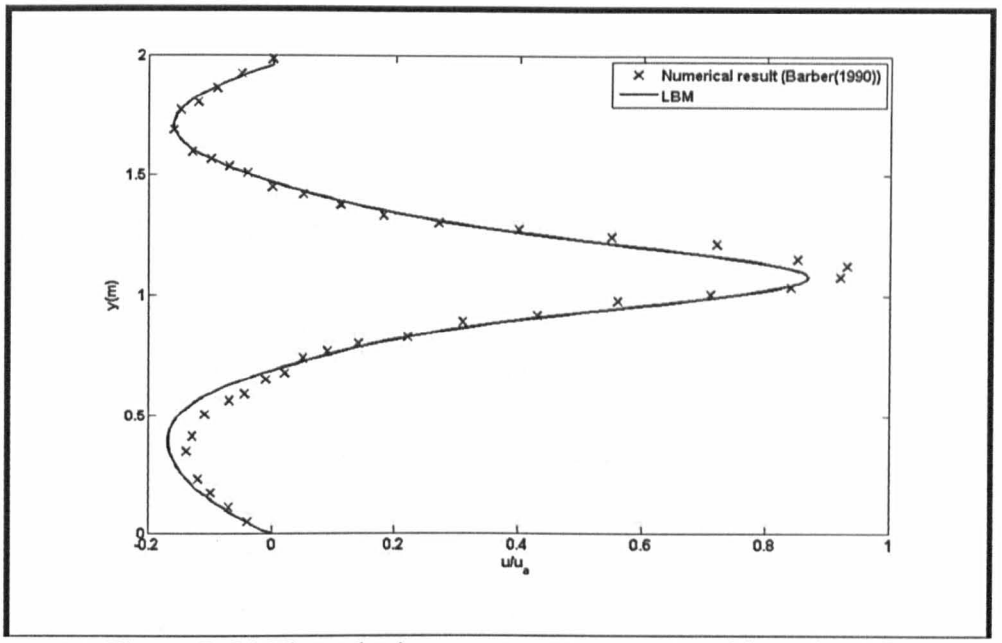

Figure 7. 29 The velocity component *u* across mid-section of asymmetrical circular basin.

The LBM and the boundary-fitted primitive variable scheme results are in good agreement especially in the recirculation zones.

Analysis of relative error for velocity profile across mid-section of both type channels between the numerical results and LABSWE^{TM} was done. The results are listed in Table 7.3 indicating that there is no significant difference in the error values between both results.

	LABSWE^{TM} Error
Symmetrical circular basin	0.0109
Asymmetrical circular basin	0.0273

Table 7. 3 The velocity error for LABSWE^{TM} compared to the numerical results for the symmetrical and asymmetrical circular basins.

7.2 LABSWE™: Study of Sidewall Friction

Knowledge of the friction force is important in many open-channel engineering applications such as in the design of canals, and in sedimentation studies [47]. This affects not only physical variables including the mean flow velocity and turbulence intensity motion [48]. Neglect of friction in a numerical model will of course lead to inaccurate results.

The friction factor for bottom and sidewalls has to be determined correctly, as wrong assumptions on friction will lead to the inaccurate computation of results. It is well known (see e.g., Zhou [4]) that the boundary layer near a solid boundary has large velocity gradient in a turbulent flow due to wall friction (bottom and sides). Turbulent flow cannot be correctly modelled without taking into account the effect of wall shear stress. In fact, wall friction increases the drag coefficient of the mean velocity profile [178].

However, most 2D depth-averaged numerical hydraulics models consider only bed friction and neglect sidewall friction. This is because of the high aspect ratio between width and depth of channel for many shallow water flow condition [49]. Only a few studies [50-54] have employed sidewall friction in the numerical models.

Molls et al. [55] have taken into account sidewall friction in a rectangular channel for a depth-averaged flow numerical model by modifying the standard 2D friction slope equation. The modification involves distributing the sidewall friction across the channel. It works well for the relatively simple case of subcritical flow in a straight channel. This has been confirmed by Brufau [56], in the simulation of dam break.

Therefore, in the lattice Boltzmann model LABSWE^{TM} used in the current study to predict the turbulence phenomenon in complex flows, the semi-slip boundary condition is used to reflect the friction from sidewalls.

A numerical study of wall friction effect for the velocity distribution of turbulent flow across the channel as included herein, through a standard hydraulic problem [55] and three different hydraulic problems that have been introduced previously: a) flow within a single expansion channel, b) flow within a double expansion channel, and c) flow within a channel with circular cavity.

The experiments were conducted with and without the wall friction coefficient C_f. For the sidewall friction analysis, three different values of wall friction coefficient: a) $C_f = 0$, b) $C_f = 0.01$, and c) $C_f = 0.03$ are used together with the semi-slip boundary condition. The predicted

velocity profile across the channel is compared at three different cross sections including upstream, eddy zone, and downstream locations.

In the present study, all the parameters and channel dimensions for the cases are the same as adopted previously in Sections (7.1.1), (7.1.3) and (7.1.4), except for the double expansion channel case, where the width of the channel is reduced to 0.5:1 for computational efficiency.

7.2.1 The Effect of Sidewall Friction in a Rectangular Channel (Standard case)

As a preliminary test, a simulation is made of the numerical experiment undertaken by Molls et al. [55]. The computational results are then compared with the experimental data [179].

The laboratory channel was 91.4m long and 1.52m wide, of rectangular section, made of concrete with a bed slope of 0.003. The channel bottom and sides were roughened with galvanised steel wire mesh.

For the lattice Boltzmann computation, 914×15 square lattices are used. The time step, grid space and relaxation time are $\Delta t = 0.025s$, $\Delta x = 0.1m$ and $\tau = 0.8$, respectively. At the upstream inlet of the channel, the

flow is set to $Q = 0.226m^3/s$. Meanwhile, the downstream outlet water depth is set to $h = 0.319m$. For a laminar flow, the Smagorinsky value $C_s = 0$ is used. To take into account friction in the computation, a semi-slip boundary condition is employed along the channel sidewall with Manning's value $n = 0.019$.

At the 10000^{th} iteration, steady state results are obtained. They are compared with experimental data and plotted in Figure 7.30. The figure shows that the lattice Boltzmann model provides predicted velocity profile in good agreement with the experiment data.

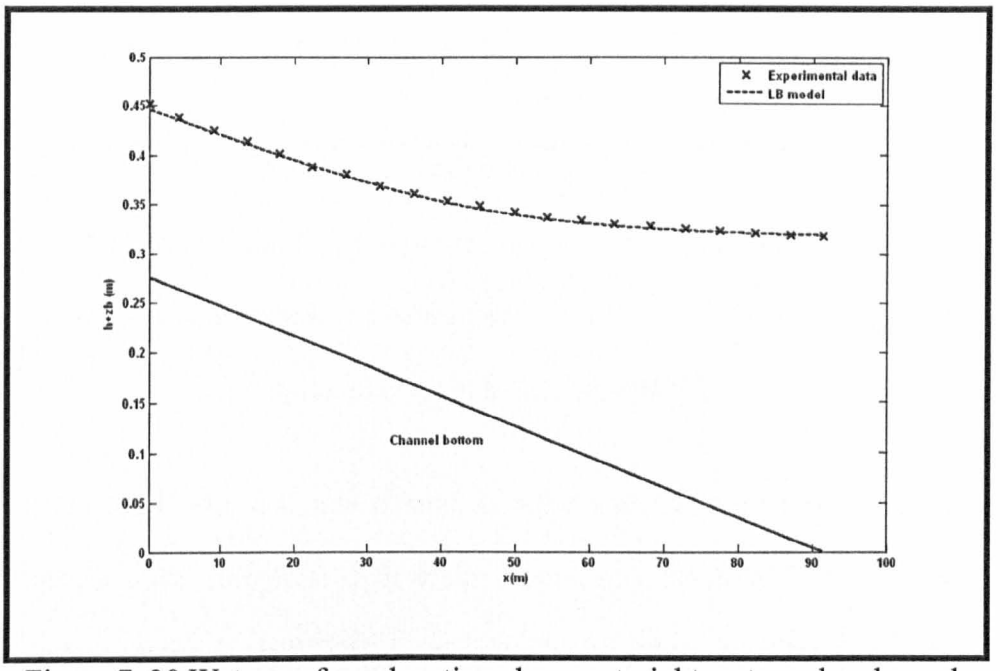

Figure 7. 30 Water surface elevation along a straight rectangular channel. Dashed-line indicates lattice Boltzmann model, whereas cross-symbols are experimental data [179].

The lattice Boltzmann model is also compared with the model proposed by Molls et al. [55] based on the leapfrog scheme. The results show only a slight difference between them (see Figure 7.31).

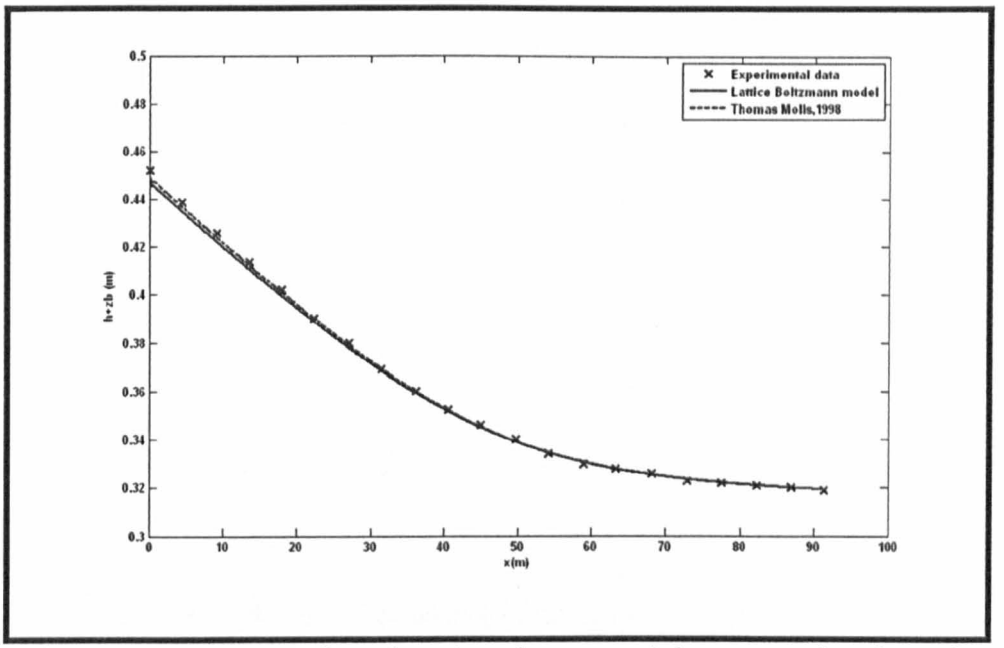

Figure 7. 31 Water surface elevation along a straight rectangular channel. Cross-symbols indicate experimental data by Lansford and Mitchell [179], the solid-line is lattice Boltzmann model and dashed-line for the numerical model by Molls et al. [55].

From the highly accurate results shown above, further tests are carried out for more complicated flow situations using LABSWE^{TM}. While the ability of the LABSWE^{TM} is examined, the effect of sidewall friction within the complex channel geometry problems is also explored.

7.2.2 The Effect of Sidewall Friction on Complex Flow and Channel Geometry

Through the results presented previously in section 7.2.1, the capability of the model in predicting the effect of friction on the sidewall surfaces is achieved. The model is then tested for more cases that include different flow characteristics and channel geometries, purposely to determine the effect of sidewall friction on complicated flows.

Firstly, the effect of sidewall friction is tested in the channel with a single expansion (see section (7.1.3)). The domain consists of 150×17 lattices with grid spacing $\Delta x = \Delta y = 0.03m$, time step $\Delta t = 0.005s$ and relaxation time $\tau = 0.53$. For channel dimensions and flow characteristic, the previous values mentioned in Sec 7.1.3 are used. These include an inflow discharge $Q = 20.21l/s$ and outflow water depth $h = 24.2m$.

The model simulated ran until the 10000^{th} iteration, when the water flow became fully steady. The profile of the velocity distribution across the channel u is plotted in Figure 7.32 for three different locations: a) upstream, $x = 0.45m$, b) within the eddy zone, $x = 1.95m$ and c) downstream, $x = 4.4m$.

(a)

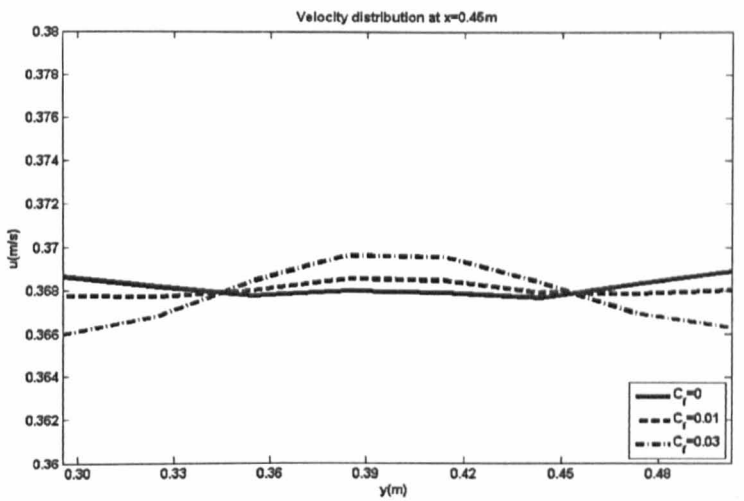
Velocity distribution at x=0.45m
u(m/s)
y(m)
0.38
0.378
0.376
0.374
0.372
0.37
0.368
0.366
0.364
0.362
0.36
0.30
0.33
0.36
0.39
0.42
0.45
0.48
C_f=0
C_f=0.01
C_f=0.03

(b)

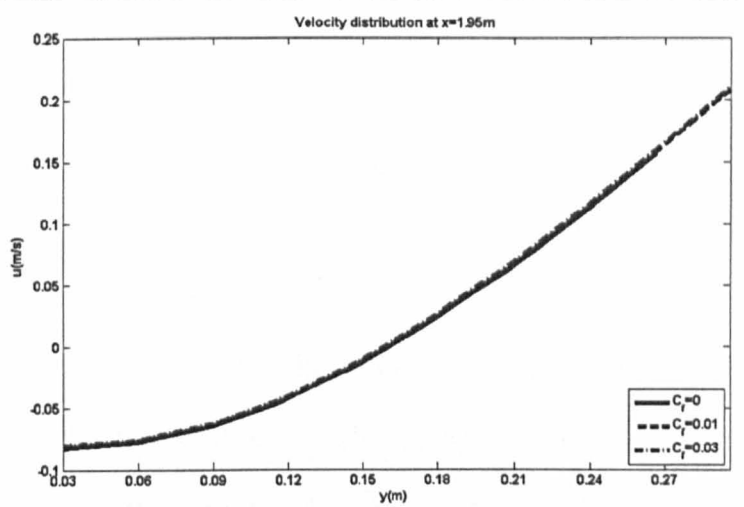
Velocity distribution at x=1.95m
u(m/s)
y(m)
0.25
0.2
0.15
0.1
0.05
0
-0.05
-0.1
0.03
0.06
0.09
0.12
0.15
0.18
0.21
0.24
0.27
C_f=0
C_f=0.01
C_f=0.03

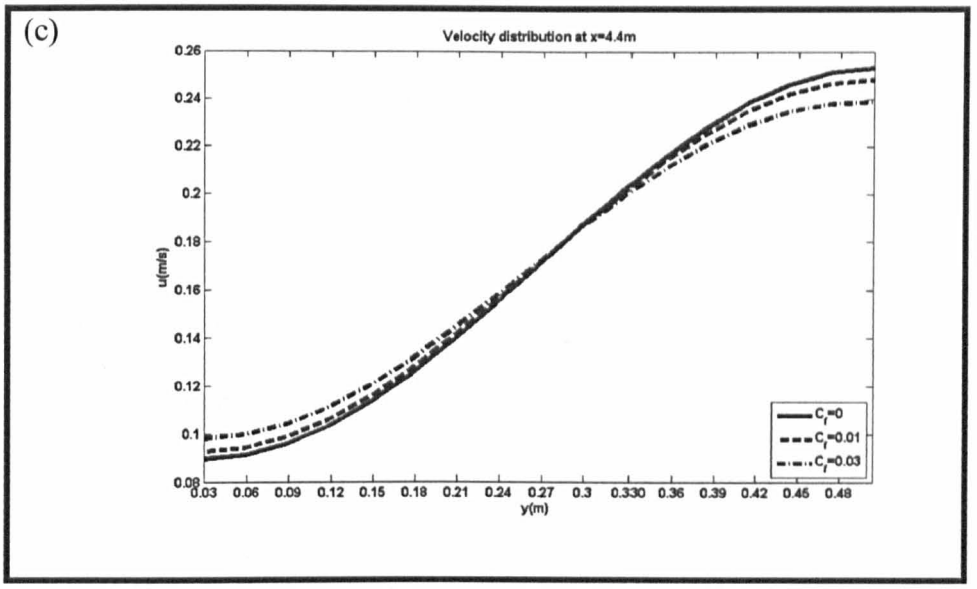

Figure 7. 32 u-velocity profile across the single expansion channel (a) at an upstream location, (b) within the eddy zone and (c) at a downstream location. The solid-lines indicate $C_f = 0$, dashed-lines are $C_f = 0.01$ and dash-dot-lines are $C_f = 0.03$.

The effect of the shear stress at the sidewalls of the channel can be seen clearly at the upstream location. The higher the value used for the friction, the greater the reduction in velocity. As depicted in Figure 7.32 (a), u reduces near the wall and increases in the middle of the channel due to the effect of friction. However, no significant effect of the shear stress can be seen in Figure 7.32(b) within the eddy zone due to the strong turbulence intensity. At the downstream location, the effect of unsymmetrical shear stress on the profile of the velocity is shown. The velocity component u at the left hand side of the channel in Figure 7.32

(c) is quite different to that obtained at the upstream location. In this situation, the velocity is clearly affected by the motion of the eddy.

Secondly, the effect of sidewall friction is tested on flow in a channel with double expansions (see section (7.1.4)). The width of the channel is reduced by a ratio of 1:0.5, where the original channel was as very wide. The computational domain consists of 100×40 lattices with grid spacing of $\Delta x = \Delta y = 0.05m$ and time step $\Delta t = 0.025s$. The inflow velocity component is $u_0 = 2.35m/s$ and downstream water depth is $h = 1.524m$. The effect of sidewall friction is examined at three different locations: a) upstream, $x = 21.75m$, b) within the eddy zone, $x = 50.75m$ and c) downstream, $x = 142m$. Figure 7.33 plots the results.

(a)

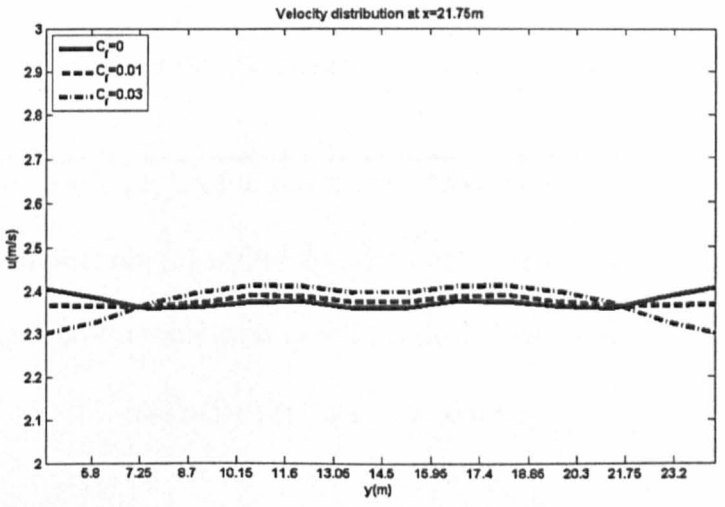

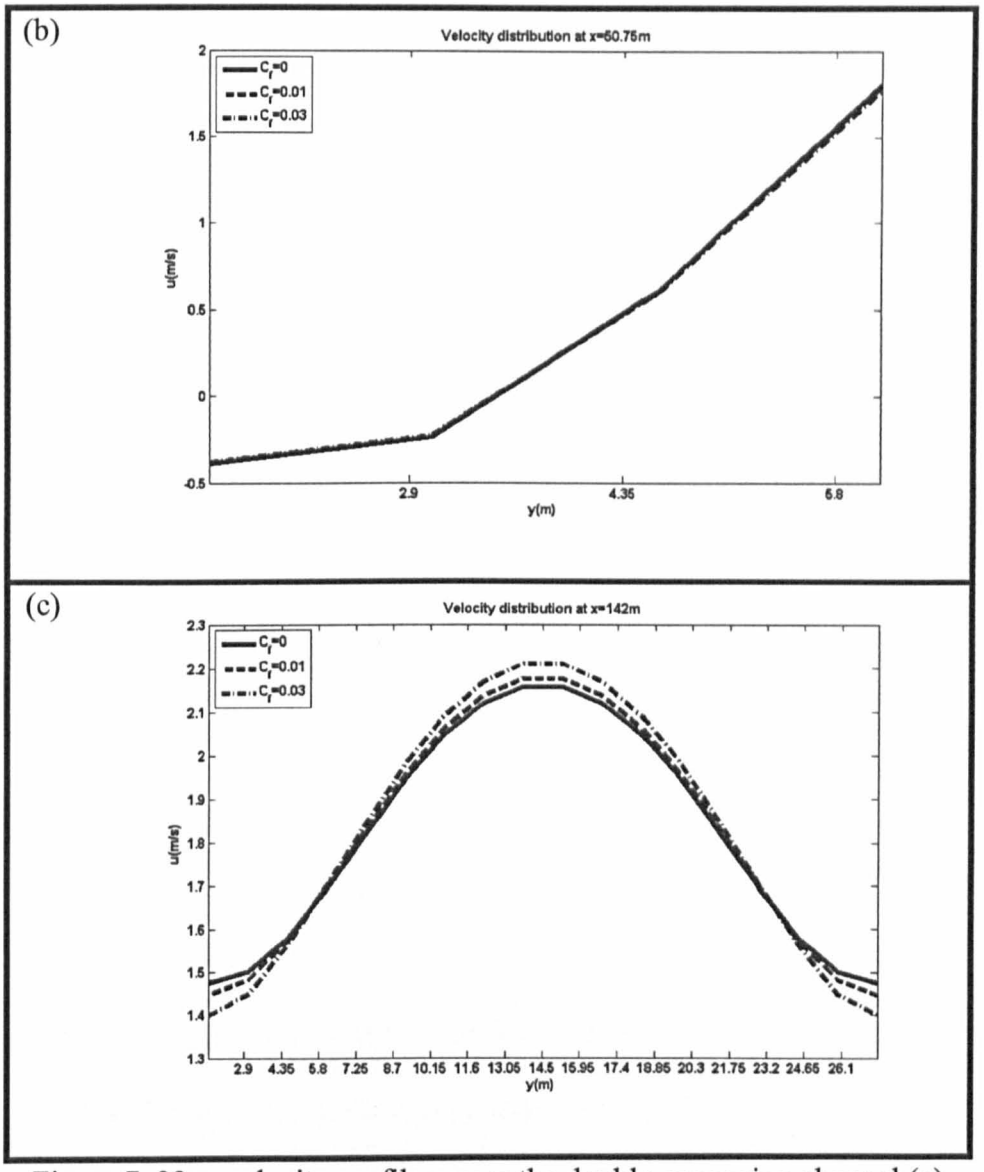

Figure 7. 33 u-velocity profile across the double expansion channel (a) at an upstream section, (b) within the eddy zone and (c) at a downstream section. The solid-lines indicate $C_f = 0$, dashed-lines are $C_f = 0.01$ and dash-dot-lines are $C_f = 0.03$.

Figure 7.33 (a) shows the effect of the shear stress at the sidewalls of the channel at an upstream section, where the reduced values of u result from

the choice of friction coefficient. However, the shape of the velocity profile at the middle is slightly flattened. This is caused by the width of the channel. The effects of sidewall friction shown in the figure are acceptable, where it is far from the strong turbulence located at the back of the one-sided channel expansion. In the eddy zone (see Figure 7.33 (b)), there is no noticeable effect of the shear stress. For the u-velocity component distribution at the downstream section, the velocity profile reduces near to the wall but increases at the middle of the channel (see Figure 7.33 (c)).

Lastly, a test is carried out on the effect of friction on a complicated flow domain for the open-channel with a semi-circular sidewall cavity (see section (7.1.1)). The computational domain consists of 190×70 lattices with grid space of $\Delta x = 0.1$ and time step $\Delta t = 0.03s$ with relaxation time $\tau = 0.6$. Flow velocity components of $u = 0.25m/s$ and $v = 0m/s$ are imposed at the inflow boundary. The water depth $h = 0.25m$ is specified at the outflow boundary. Simulation results are obtained after the 10000^{th} iteration. Figure 7.34 plots the steady state u-velocity profiles at three different locations: a) upstream, $x = 1.6m$, b) within the eddy zone, $x = 9.5m$ and c) downstream, $x = 18m$.

(a)

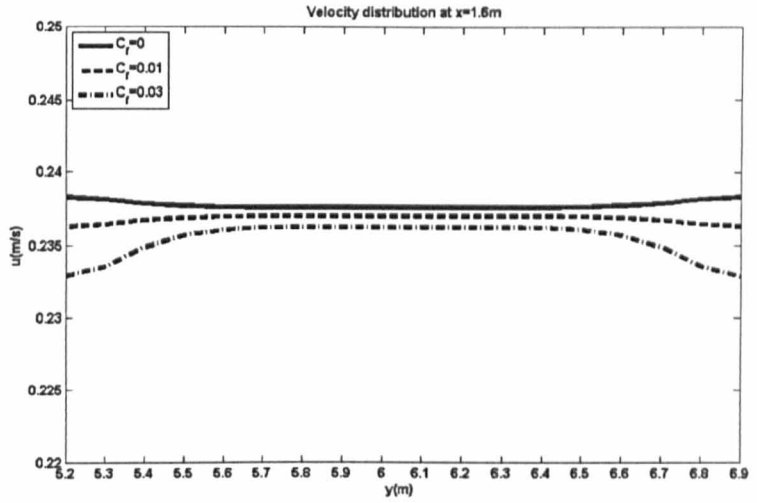
Velocity distribution at x=1.6m
C_f=0
C_f=0.01
C_f=0.03
u(m/s)
y(m)
0.25
0.245
0.24
0.235
0.23
0.225
0.22
5.2
5.3
5.4
5.5
5.6
5.7
5.8
5.9
6
6.1
6.2
6.3
6.4
6.5
6.6
6.7
6.8
6.9

(b)

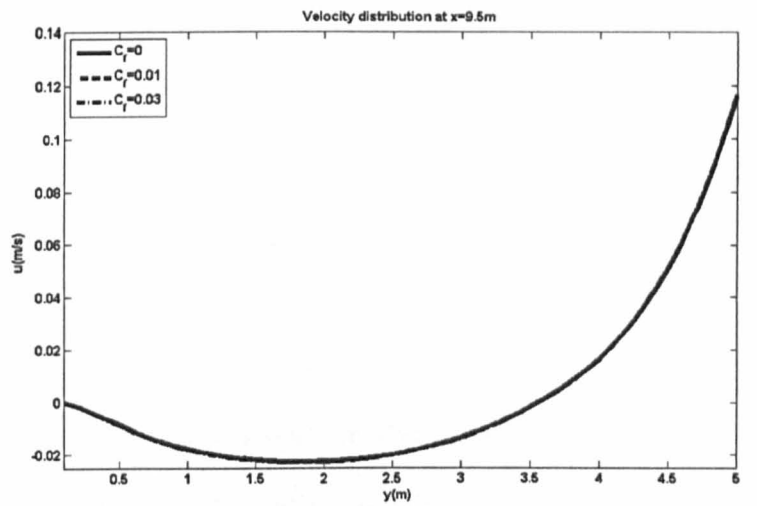
Velocity distribution at x=9.5m
C_f=0
C_f=0.01
C_f=0.03
u(m/s)
y(m)
0.14
0.12
0.1
0.08
0.06
0.04
0.02
0
-0.02
0.5
1
1.5
2
2.5
3
3.5
4
4.5
5

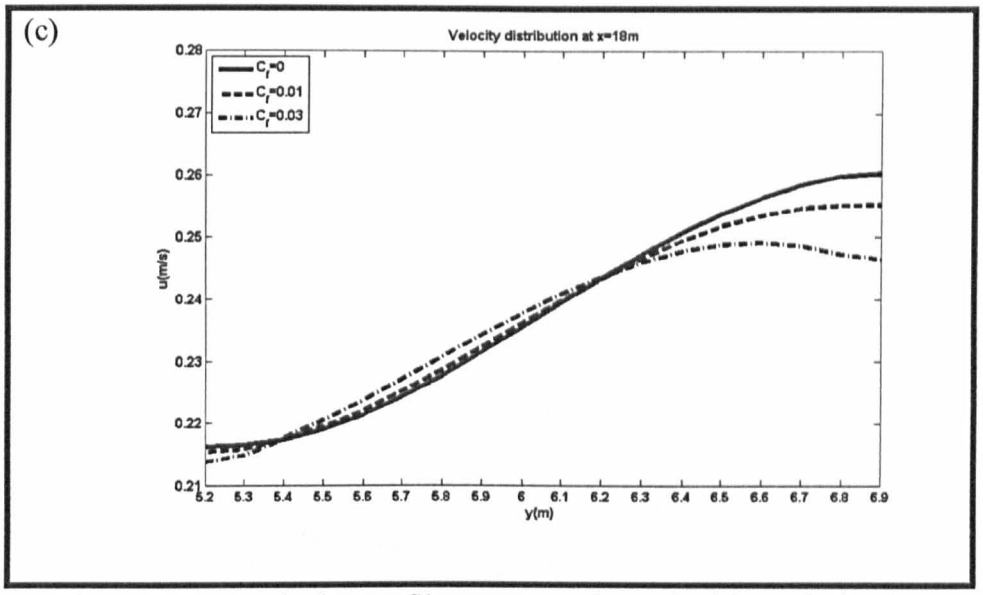

Figure 7. 34 u-velocity profiles across a channel with semi-circular sidewall cavity (a) at a upstream section, (b) within the eddy zone and (c) at downstream section. The solid-lines indicate $C_f = 0$, dashed-lines are $C_f = 0.01$ and dash-dot-lines are $C_f = 0.03$.

The effect of the sidewall friction on the u-velocity profile can be seen clearly in Figure 7.34 (a). However, due to the fact that the channel is very wide, the velocity distribution u at the upstream location becomes flattened.

Similar to the previous analysis figure (see Figure 7.34 (b)), the use of sidewall friction has no significant effect on the velocity within the eddy zone. However, due to eddying motions within the circular cavity, the u-velocity profile at the left hand side of the channel in the Figure 7.34 (c) shows an unsymmetrical profile.

Wall friction analyses have been conducted for turbulent flow in three different channel geometries. In order to study the influence of wall friction coefficients used in the simulations, the velocity values nearest to the wall are compared at the upstream, eddy zone and downstream sections of the sudden expansion channel. The results obtained are listed in Table 7.4.

	Velocity component u (m/s)		
Friction coefficient	**Upstream** $x = 21.75m$	**In eddy** $x = 50.75m$	**Downstream** $x = 142m$
$C_f = 0$	2.4001	-0.4788	1.4783
$C_f = 0.01$	2.3569	-0.4737	1.4675
$C_f = 0.03$	2.2823	-0.4644	1.3984

Table 7. 4 Velocity values at upstream, eddy zone and downstream locations in the sudden expansion channel.

As indicated in Table 7.4, the use of higher wall friction coefficient values C_f affects the velocity profile at the downstream and upstream locations, significantly rather than in the eddy. Hence, it is necessary to include the wall friction effect in a model simulation to obtain more realistic results.

7.3 LABSWE™: Study of Moving Shoreline

Wetting and drying is a familiar feature of flows in shallow coastal zones and also in embayment and inlets [61,71]. However, with extreme tides, wetting and drying processes could affect local navigation routes. The impact can also be seen in local flow recirculation and contaminant transport [61]. Thus, the study of wave run-up is essential.

As described previously in Chapter 5, a moving shoreline algorithm is used for locating the wet-dry front in the swash zone, and hence determining wave run-up at a beach.

In this section, LABSWE™ is used with a moving shoreline boundary to validate wave run-up for: a) solitary wave run-up at a plane beach, b) solitary wave run-up around a conical island and c) wave run-up in a parabolic shaped basin. Two types of wave conditions are considered; nonbreaking and breaking. However, for the breaking wave condition, only spilling breaking waves is studied. For validation, the numerical simulation results are compared with available experimental, analytical and numerical data.

7.3.1 1D of Wave Run-up Model: Solitary Wave on a Plane Beach

Spontaneous geophysical activities such as underwater earthquakes and landslides cause massive displacement of oceanic water leading to the generation of tsunami, which are known to cause extensive flood and loss of life [51]. Important aspects of such disastrous waves can be studied by simulating a solitary wave [54,58,180].

A detailed experimental study of solitary wave run-up on a plane beach has been undertaken by Synolakis [180] who considered the run-up of nonbreaking and breaking solitary waves. Synolakis's data have been used by a number of researchers [59], [64], [53] and [54] in validating their models. In the present study, two types of incident wave conditions are considered i.e., $H/h_0 = 0.0185$ and $H/h_0 = 0.04$ with a beach slope 1: 19.85, where H is the solitary wave height, h_0 is the still water level, β is the beach slope, L is the wavelength and R is the run-up height measured above still water level (Figure 7.35).

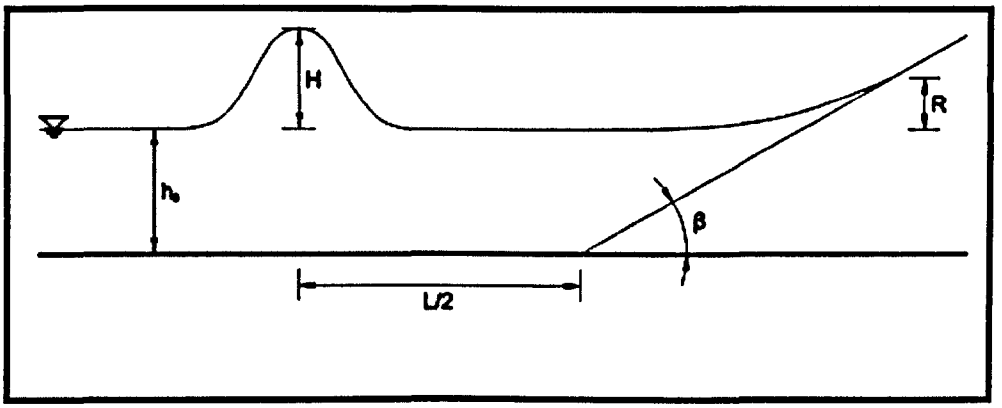

Figure 7. 35 Definition sketch of solitary wave run up on a plane beach.

The wave height of the solitary wave at $t = 0$ with initial wave crest located at half wavelength from the toe of the beach X may be defined:

$$\eta(x,0) = H\,sech\left[\sqrt{\frac{3H}{4h_0^3}}(x-X)\right], \tag{7.2}$$

and the flow velocity is given by

$$u(x,0) = -\eta(x,0)\left[\sqrt{\frac{g}{h_0}}\right]. \tag{7.3}$$

For all numerical computations, $\Delta x = 0.05m$, $\tau = 1$ and $\Delta t = 0.01s$. The non-dimensional time is defined as:

$$t^* = t\left[\sqrt{\frac{g}{h_0}}\right]. \tag{7.4}$$

Bed friction with Manning's coefficient $n = 0.01$ is included, to best fit the numerical results to Synolakis's data [181].

7.3.1.1 Results using thin film shoreline algorithm

First, a lattice Boltzmann model undertaken is simulated with the thin film shoreline algorithm. In this analysis, a thin film of fluid $h_{min} = 0.003m$ is prescribed to treat the wet-dry interface. Simulations are carried out for two incident wave heights, $H/h_0 = 0.0185$ and $H/h_0 = 0.04$, at different time levels. To evaluate the accuracy of the model, wave profiles at fixed times of the computed data are compared with experimental results [180].

Figure 7.36 shows the results for nonbreaking solitary waves of incident wave height $H/h_0 = 0.0185$ running up the beach of slope 1: 19.85 for non-dimensional time i.e., $t^* = 25$ until $t^* = 70$.

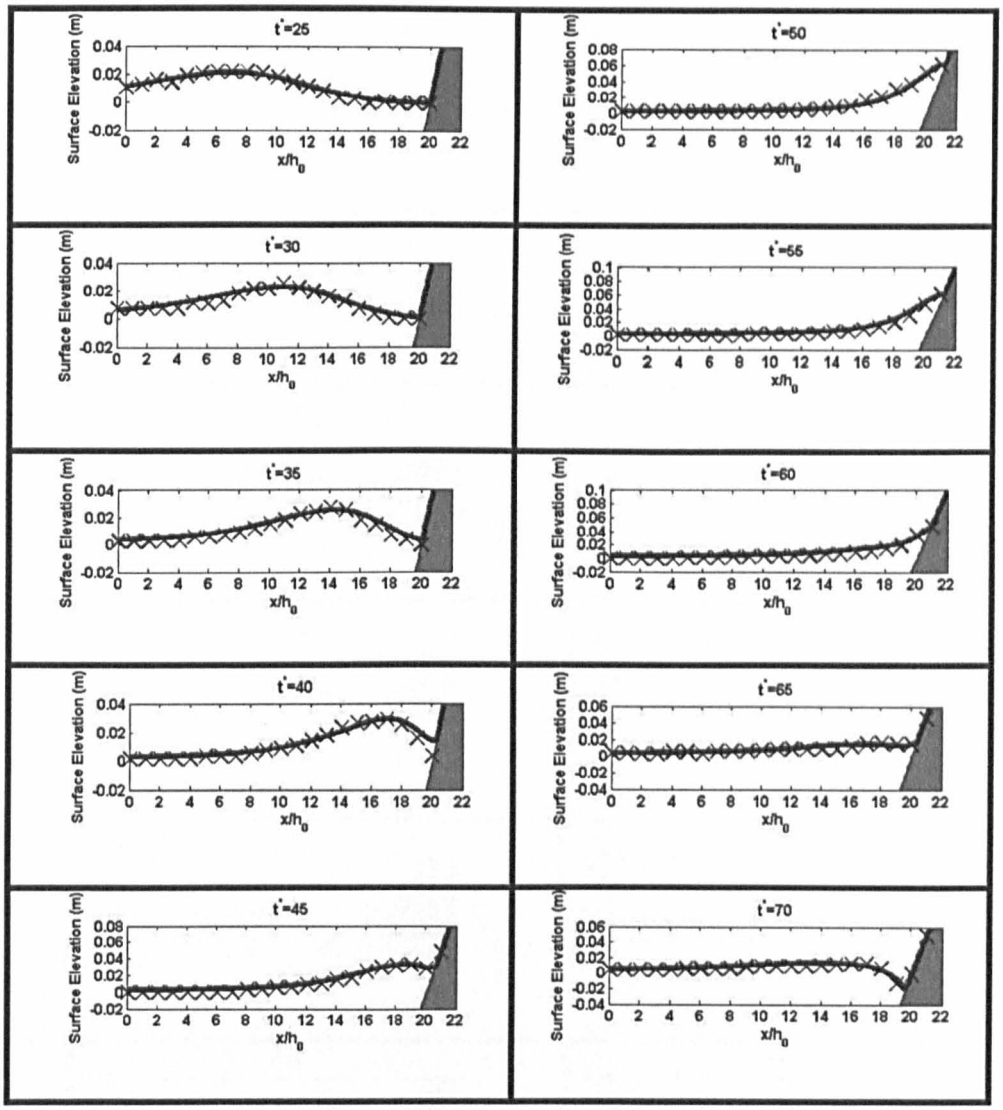

Figure 7. 36 Comparisons of computed and experimental water free surface profiles at $t^* = 25, 30, 35, 40, 45, 50, 55, 60, 65$ and 70. The solid lines represent numerical results; the symbols are experimental data [58].

As depicted in Figure 7.36, the wave profiles are well predicted. There is no significant difference between the profiles, except for the small

disagreement in numerical water levels close to the shore at $t^* = 40$, which are slightly over predicted.

Figure 7.37 shows the development of a breaking wave with incident wave height $H/h_0 = 0.04$.

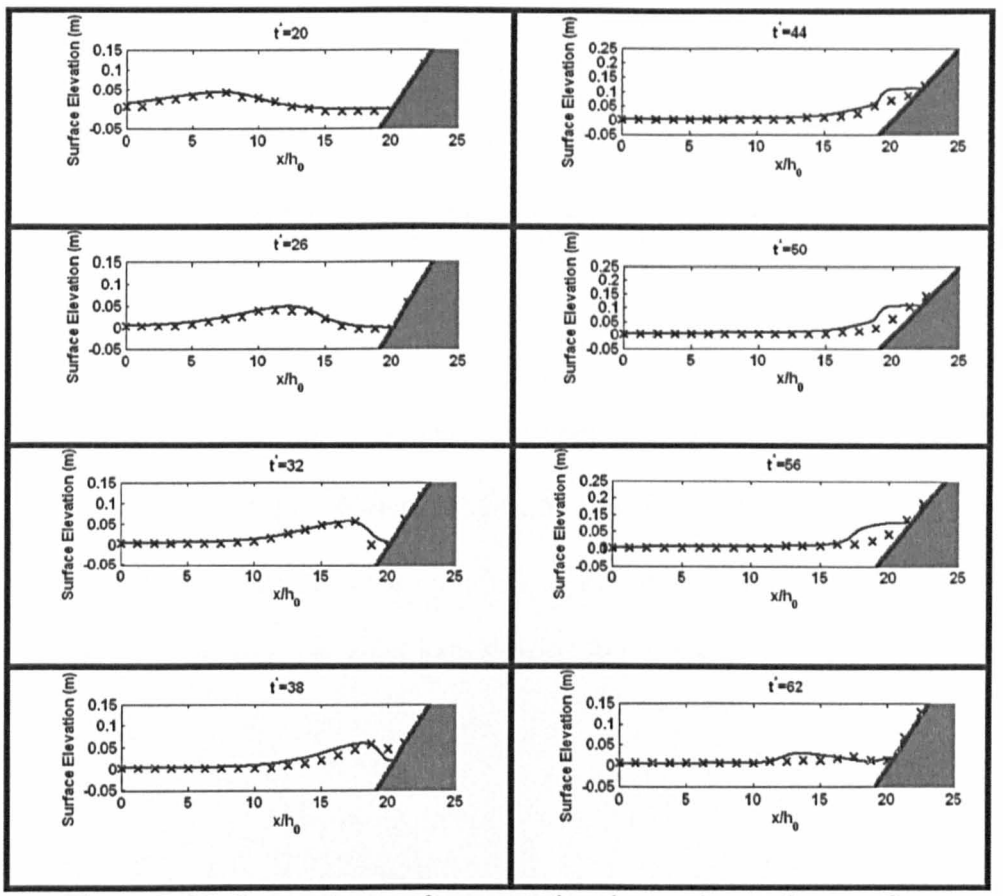

Figure 7. 37 Comparisons of computed and experimental water free surface profiles at $t^* = 20, 26, 32, 38, 44, 50, 56$ and 62. The solid lines represent numerical results; the symbols are experimental data [58].

As illustrated in the figure, the simulated wave motions from $t^* = 20$ to $t^* = 32$ are in good agreement with the experimental data. However,

at $t^* = 38$ and 44, the very front of water profile does not matched properly, and the discrepancy continues until $t^* = 62$. From the experimental data, the water should continue to run-up at $t* = 50$ before running down at $t^* = 56$.

7.3.1.2 Results using linear extrapolation shoreline algorithm

The 1D wave run-up simulation is next undertaken using a linear extrapolation moving shoreline algorithm [64]. Figure 7.38 shows the computed wave profile for a nonbreaking wave with $H/h_0 = 0.0185$ at different times, and compared with Synolakis's experimental data.

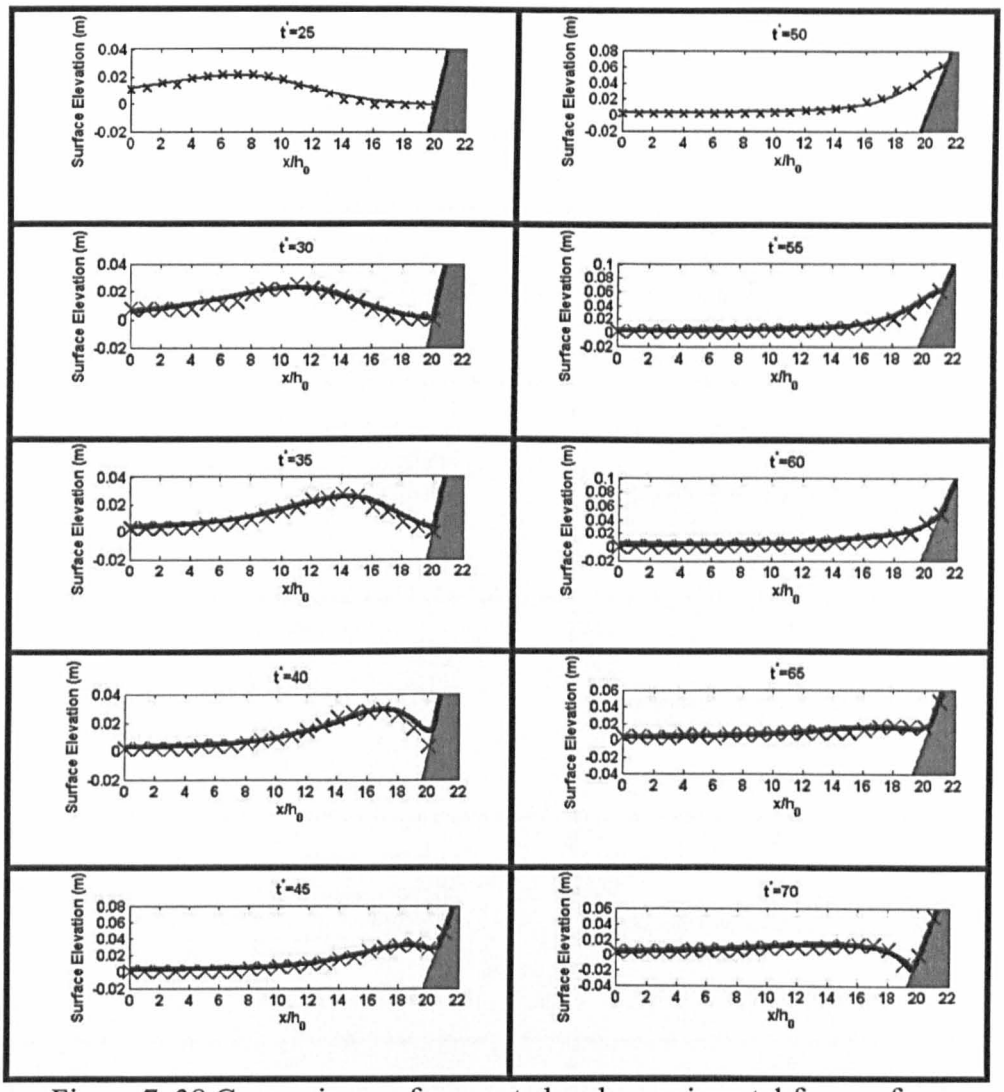

Figure 7. 38 Comparisons of computed and experimental free surface profiles at $t^* = 25, 30, 35, 40, 45, 50, 55, 60, 65$ and 70. The solid lines represent numerical results; the symbols are experimental data [58].

As depicted in the figure, the wave propagates up the sloping beach from $t^* = 25$ to $t^* = 45$ and accelerates down the beach from $t^* = 50$ to $t^* = 70$. However, a small disagreement between the numerical result and experimental data can be found at $t^* = 40$, where the numerical

result near the shoreline is slightly over predicted. Overall, the wave profile is well predicted.

Figure 7.39 presents a comparison of numerical and experimental breaking solitary wave run-up with incident wave height $H/h_0 = 0.04$.

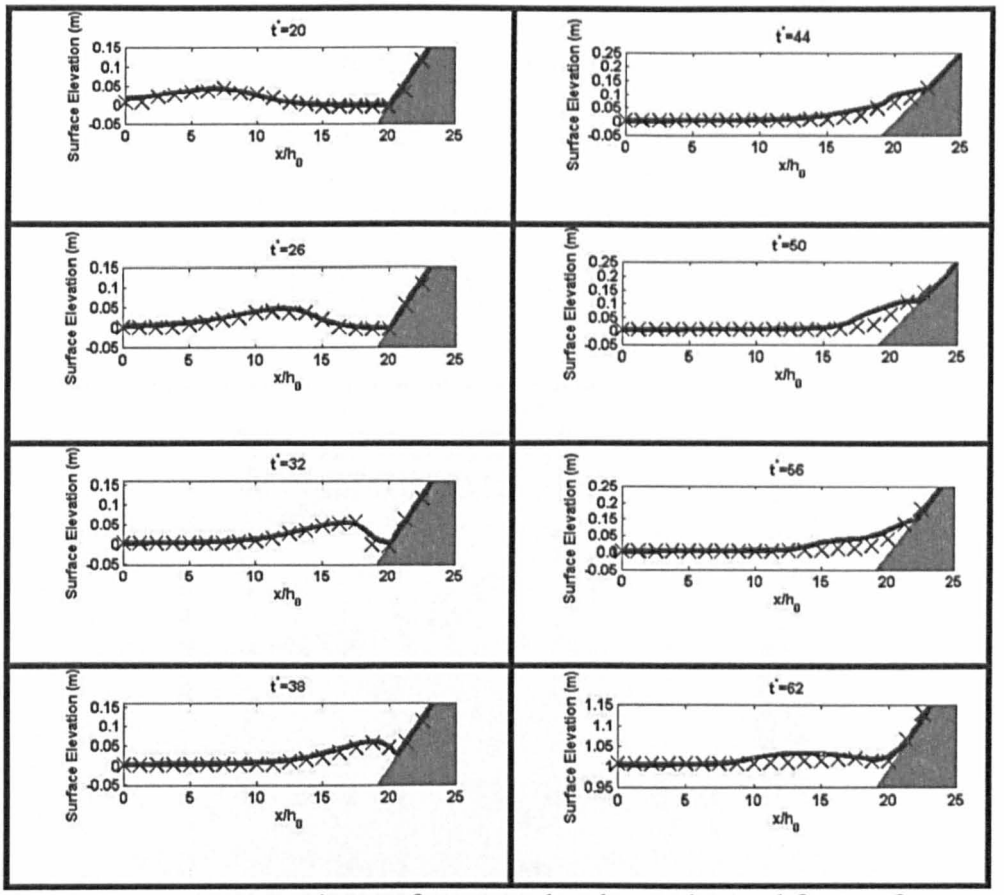

Figure 7. 39 Comparisons of computed and experimental free surface profiles at $t^* = 20, 26, 32, 38, 44, 50, 56$ and 62. The solid lines represent numerical results; the symbols are experimental data [58].

As illustrated in Figure 7.39, wave run-up at the sloping beach can be seen from $t^* = 20$ to $t^* = 38$. The maximum run-up level is reached at

about $t^* = 44$, after which the run-down process take place as the water drains back down the beach slope. Small discrepancies are seen at $t^* = 44$ and beyond. The breaking numerical results are slightly over predicted.

In order to evaluate the accuracy of the moving shoreline applications, the computed wave profiles are plotted for both moving shoreline techniques against experimental data. For nonbreaking wave conditions i.e., $H/h_0 = 0.0185$, the comparison of the various wave profiles at $t^* = 35, 50$ and 70 is plotted in Figure 7.40.

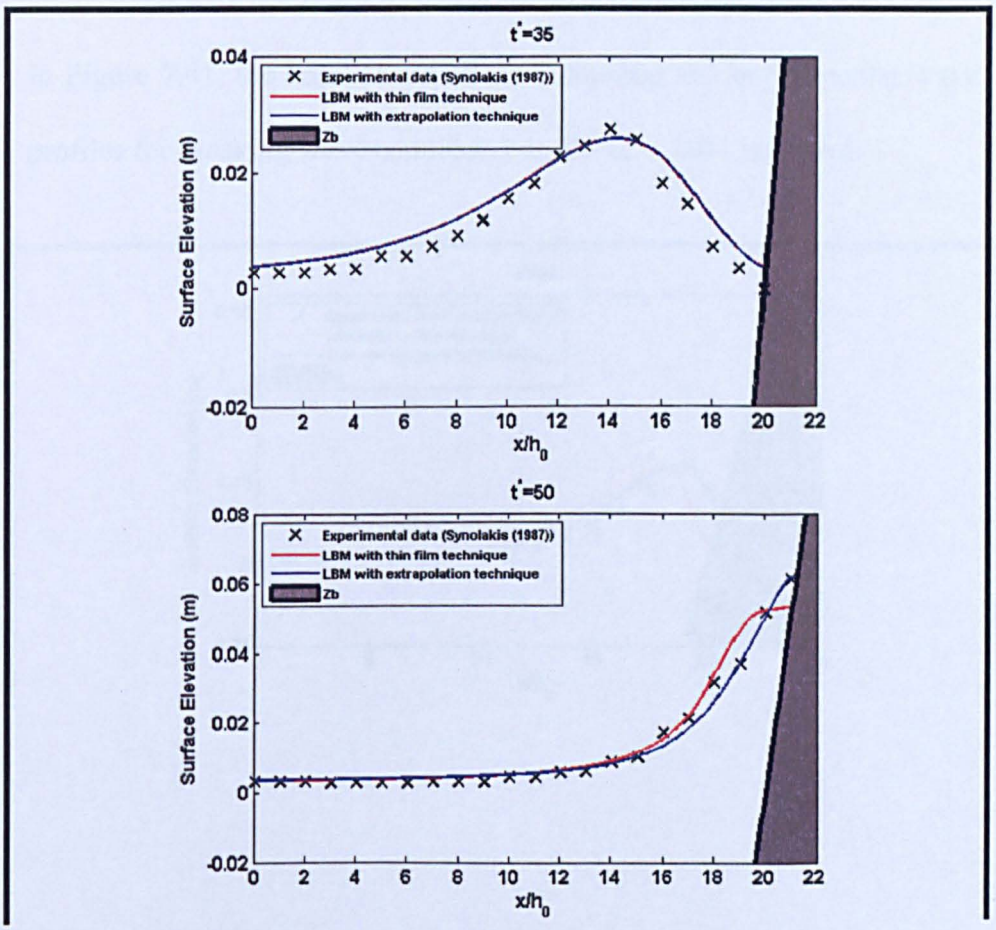

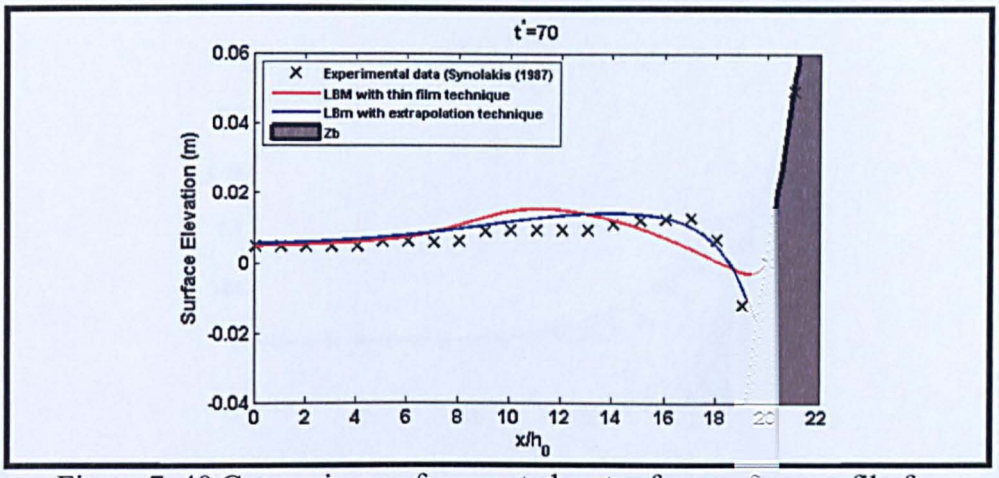

Figure 7. 40 Comparisons of computed water free surface profile for nonbreaking wave condition obtained using the thin film and extrapolation techniques with experimental data at $t^* = 35, 50$ and 70. Symbols indicate experimental data [58].

In Figure 7.41, the comparison of the computed and experimental wave profiles for breaking wave condition i.e., $H/h_0 = 0.04$ is shown.

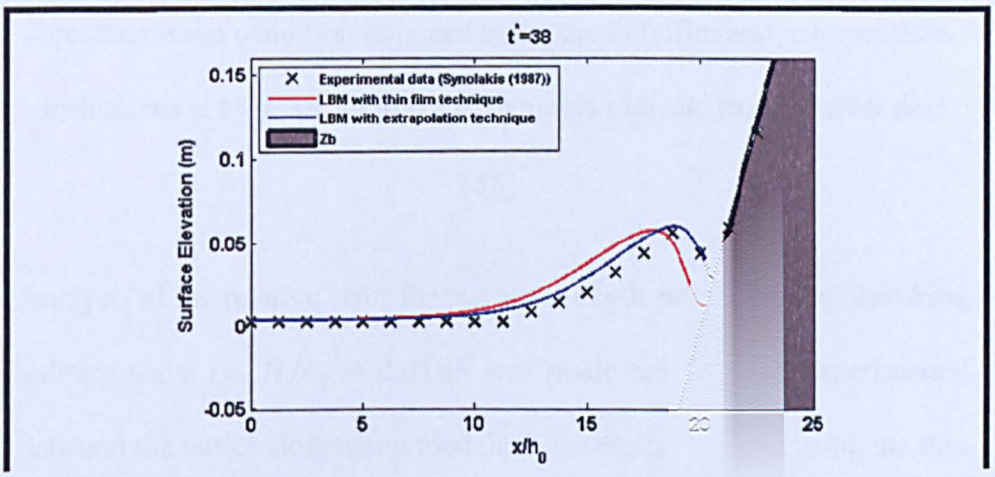

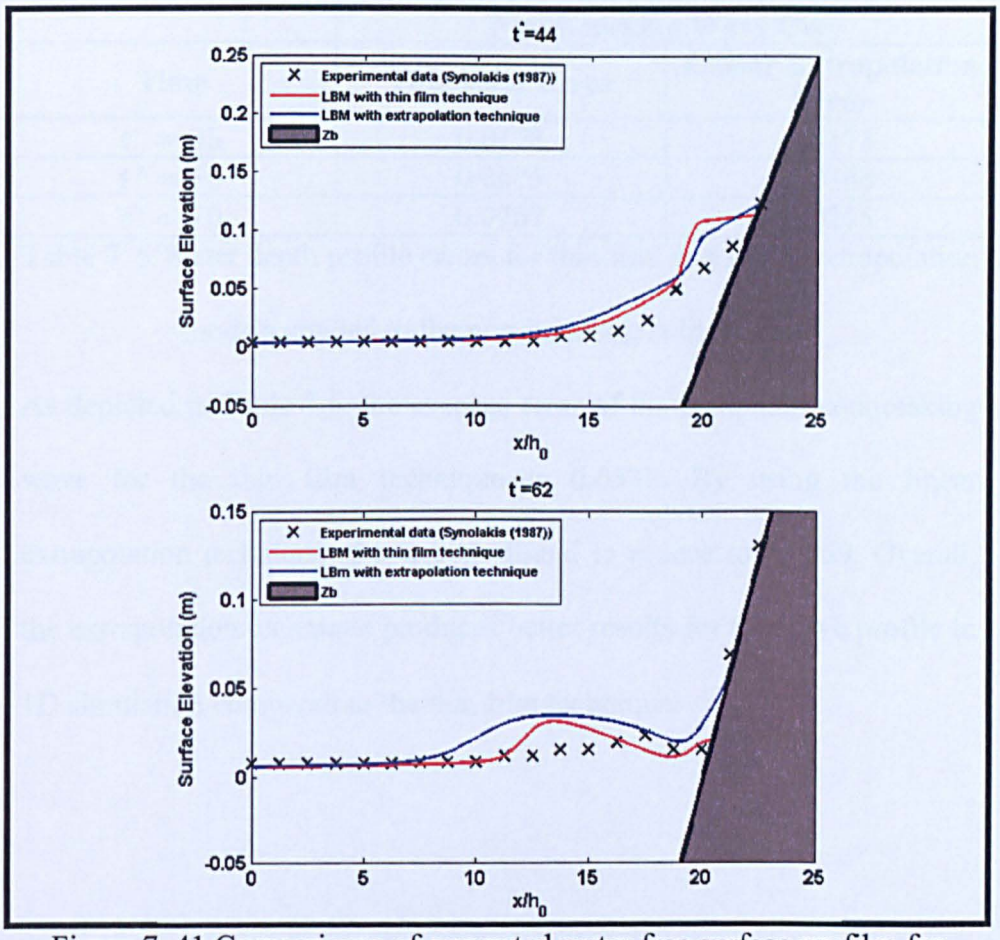

Figure 7. 41 Comparisons of computed water free surface profiles for breaking wave condition obtained using the thin film and extrapolation techniques at $t^* = 38, 44$ and 62. Symbols indicate experimental data [58].

Analysis of the relative error for the water depth profile of a nonbreaking solitary wave i.e., $H/h_0 = 0.0185$ was made between the experimental data and the lattice Boltzmann models. The results obtained using the thin film and linear extrapolation models are listed in Table 7.5.

	Non-breaking Wave Case	
Time	**Thin Film Error**	**Linear Extrapolation Error**
$t^* = 35$	0.0173	0.0173
$t^* = 50$	0.0675	0.0368
$t^* = 70$	0.0767	0.0265

Table 7. 5 Water depth profile errors for thin film and linear extrapolation models applied to the non-breaking solitary case.

As depicted in Table 7.5, the average error of the computed nonbreaking wave for the thin film technique is 0.0538. By using the linear extrapolation technique, the error is found to reduce to 0.0269. Overall, the extrapolation technique produces better results for the wave profile in 1D simulation compared to the thin film technique.

7.3.2 2D Solitary Wave Run-up around a Conical Island

At least 1640 people on islands around the Pacific Ocean were killed by large tsunamis in the years 1992 to 1994 [11-13]. These tsunamis badly damaged the small villages on nearby islands. The behaviour of these tsunamis, therefore, initiated many experimental and theoretical studies [10-16,52,61].

It is common to model a solitary wave in studying tsunami phenomenon. The solitary wave represents some of the important features of tsunamis well. Notwithstanding the complex spectrum of frequencies actually present in tsunamis, this solitary wave enables realistic analysis in the laboratory [15]. This has motivated the use of the solitary wave by many researchers [52,54,58,59,182,183].

Therefore, by using the lattice Boltzmann model for wave run-up, the behaviour of the solitary wave run-up around a conical island is studied here.

A series of laboratory experiments to investigate the solitary wave run-up around a conical island with water depth $h = 0.32m$ and $0.42m$ was reported by Briggs et al. [15]. Three different solitary waves with three incident wave heights: $H/h_0 = 0.05, 0.1$ and 0.2 were investigated. In the experiment, the length and width of the basin were $25m$ and $30m$, respectively. An island of conical frustum with $0.625m$ height and $1:4$ side of slope was placed at the centre of the basin with base and crest diameter of $7.2m$ and $2.2m$, respectively. Figure 7.42 shows a schematic diagram of the conical island used in the experiment and the gauge locations for time series of surface elevation. The symbol ▲ shows the locations of Gauges $6, 9, 22$ and 16.

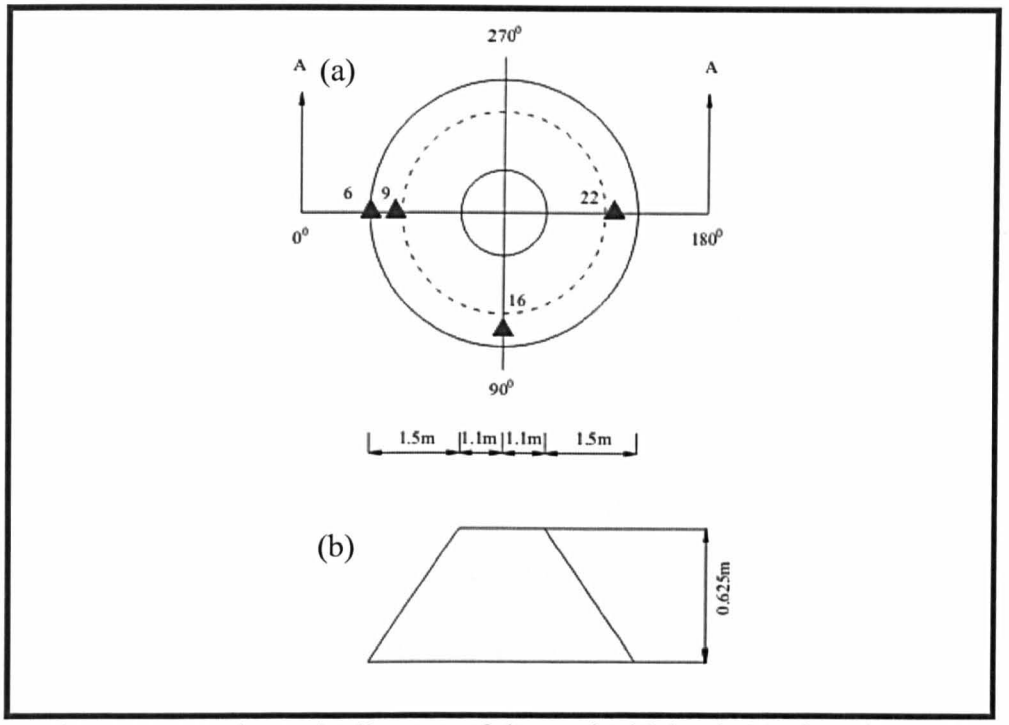

Figure 7. 42 Schematic diagram of the conical island: (a) plan views of the conical island and gauge locations; (b) side views of the island from A-A direction.

In the present study, experimental results [15] for $h = 0.32m$ and $H/h_0 = 0.045, 0.096$ and 0.181 are used to validate the model.

The computational setup consists of $250x300$ square lattices, $\Delta x = \Delta y = 0.1m, \Delta t = 0.01s$ and $\tau = 1$. For a smooth concrete surface, Manning's $n = 0.016$ coefficient is used.

7.3.2.1 Results using the thin film shoreline algorithm

The thin film concept applied in the 2D model is exactly same to that used in 1D. A thin layer of fluid $h_{min} = 0.001m$ is applied throughout the domain.

Numerical-experimental time series comparisons of solitary wave profiles for three types of incident wave height (i.e., $H/h_0 = 0.045, 0.096$ and 0.181) at four different gauges locations are shown in Figures 7.43 – 7.45. The gauge number is shown immediately above each subplot.

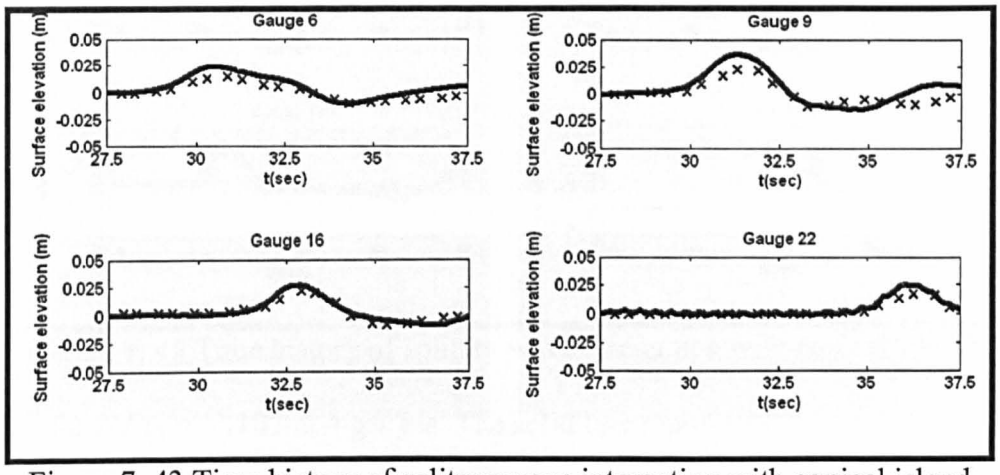

Figure 7. 43 Time history of solitary wave interaction with conical island for $H/h_0 = 0.045$ at 4 gauges. The solid line represents the numerical results. The crosses show experimental data [15].

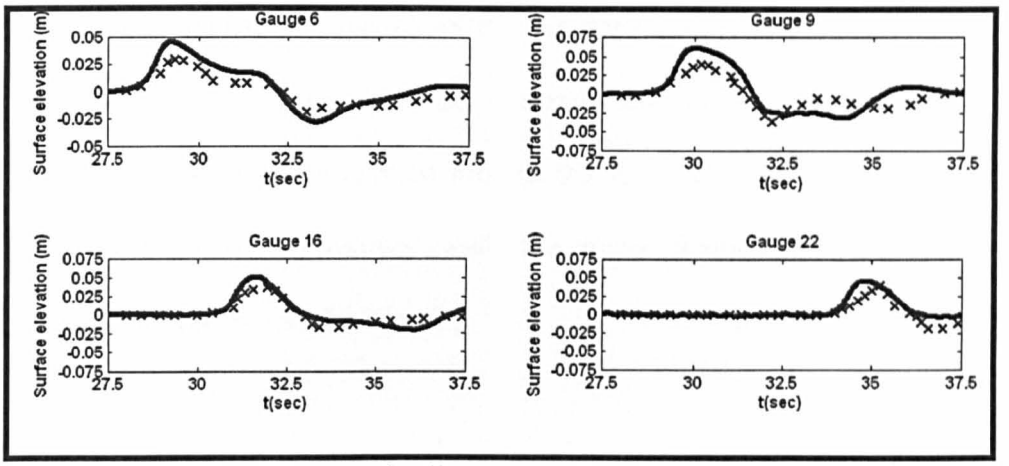

Figure 7. 44 Time history of solitary wave interaction with conical island for $H/h_0 = 0.096$ at 4 gauges. The solid line represents the numerical results. The crosses show experimental data [15].

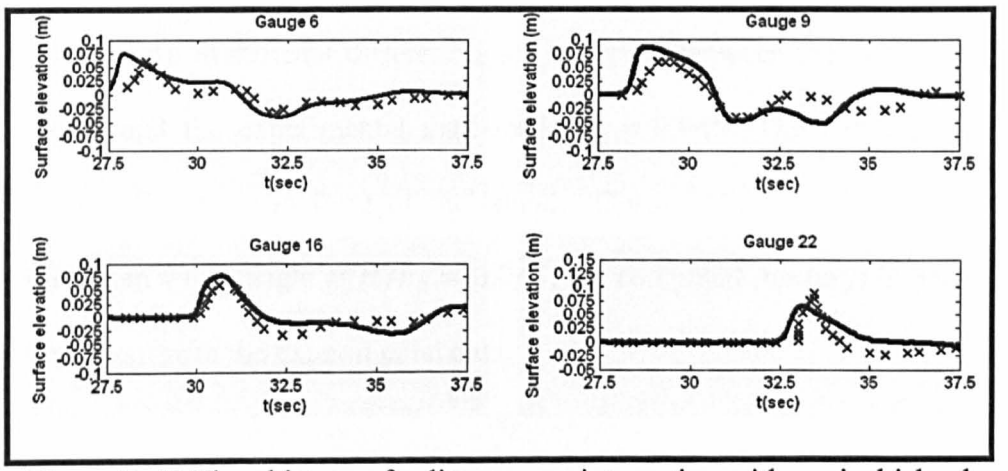

Figure 7. 45 Time history of solitary wave interaction with conical island for $H/h_0 = 0.181$ at 4 gauges. The solid line represents the numerical results. The crosses show experimental data [15].

The comparisons show that the computed wave imitates the incident wave very well. In front of the island, wave gauges 6 and 9 show a primary wave followed by a depression wave. Note that the depression

wave also appears in the experimental data [183]. However, in the computed results, these vary from the experimental profiles because no boundary absorption is applied around the modelled area. Overall, the thin film model reproduces well the main features of the wave transformation around the island.

In Figure 7.46, maximum run-up heights around the island are presented for different incident wave heights. The angle is measured clockwise around the island from the incoming wave direction. For the cases where incident wave height $H/h_0 = 0.096$ and 0.181, the predicted and measured maximum run-up heights are almost the same (see Figure 7.46 (b) and (c)). Significant differences are observed between the numerical results and the experimental data for $H/h_0 = 0.045$. The result over-predicts the wave in front of the island. Despite the discrepancies of maximum wave height at $H/h_0 = 0.045$, the computed run-up is in good agreement with the experimental data.

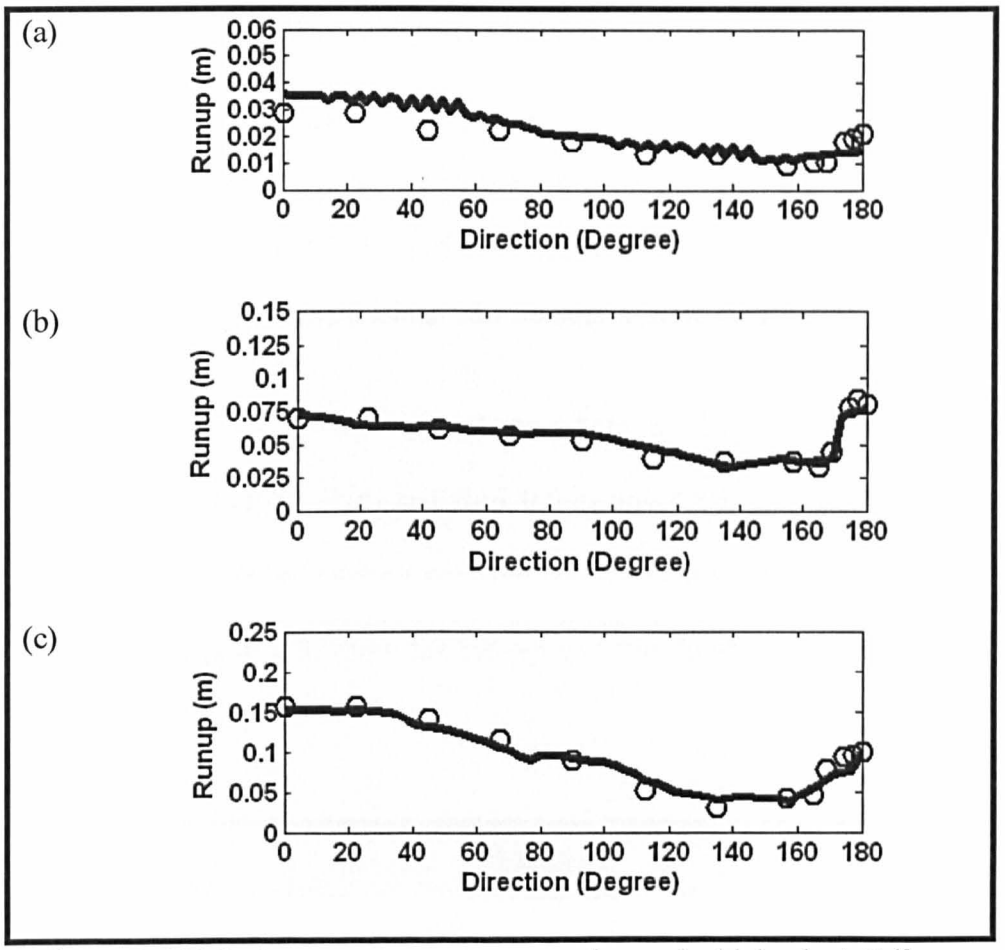

Figure 7. 46 Maximum wave run-up around a conical island: a) $H/h_0 = 0.045$, b) $H/h_0 = 0.096$ and c) $H/h_0 = 0.181$. The circles depict experimental data [15]. The solid line represents the numerical results.

7.3.2. 1 Results using the linear extrapolation shoreline algorithm

A 2D scheme proposed by Lynett et al. [64] is applied to locate the shoreline around a conical island (for details, refer to Chapter 5).

Figures 7.47–7.49 provide typical snapshots of the wave surface for incident wave heights $H/h_0 = 0.045, 0.096$ and 0.181 at different times of a solitary wave interacting with the conical island. The snapshots are presented purposely to show the run-up and run-down phenomenon in a better way.

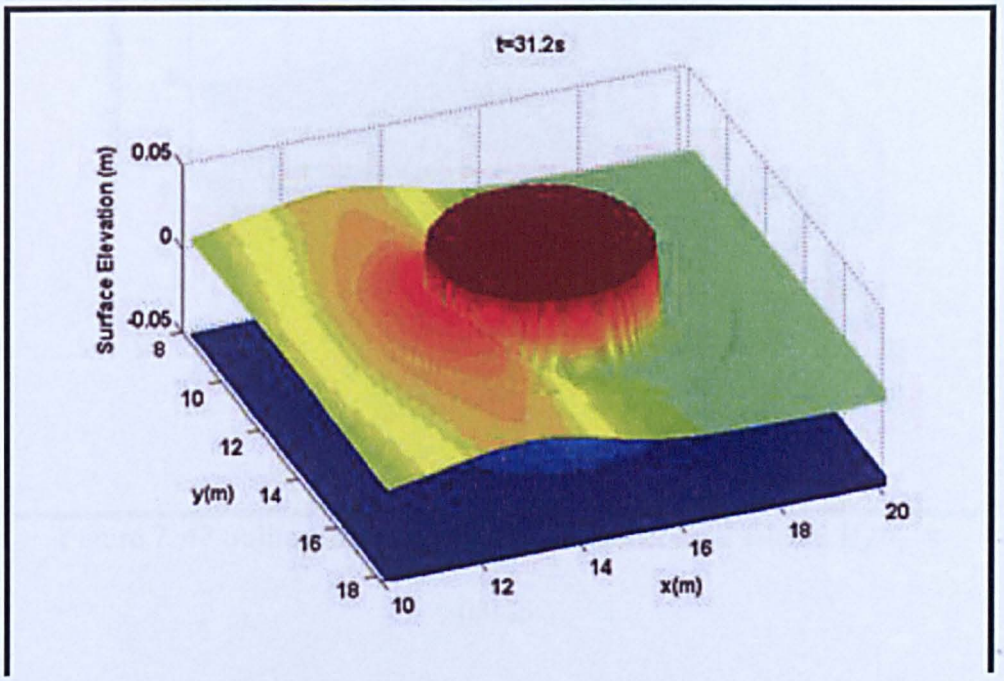

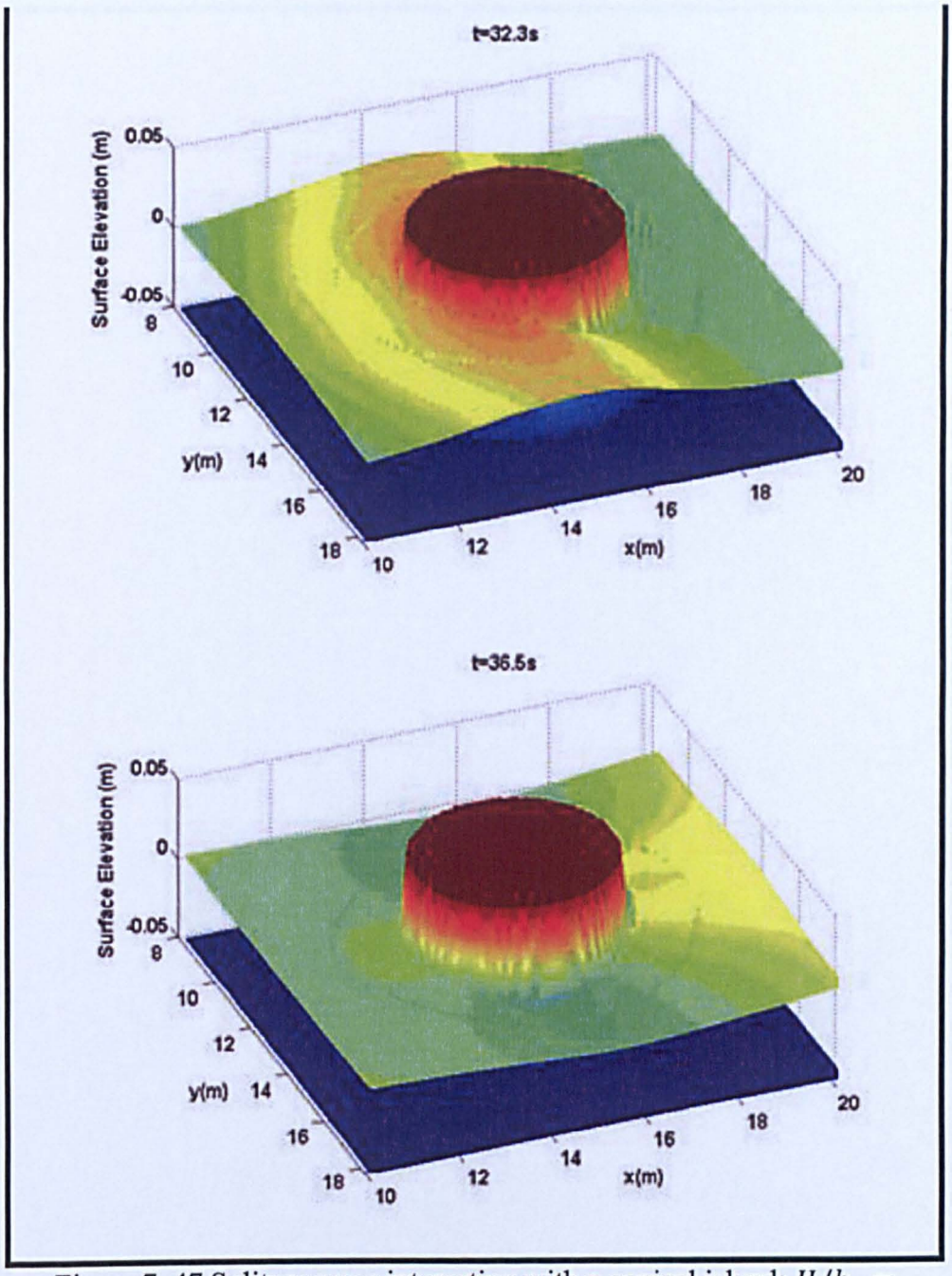

Figure 7. 47 Solitary wave interaction with a conical island: $H/h_0 =$ 0.045.

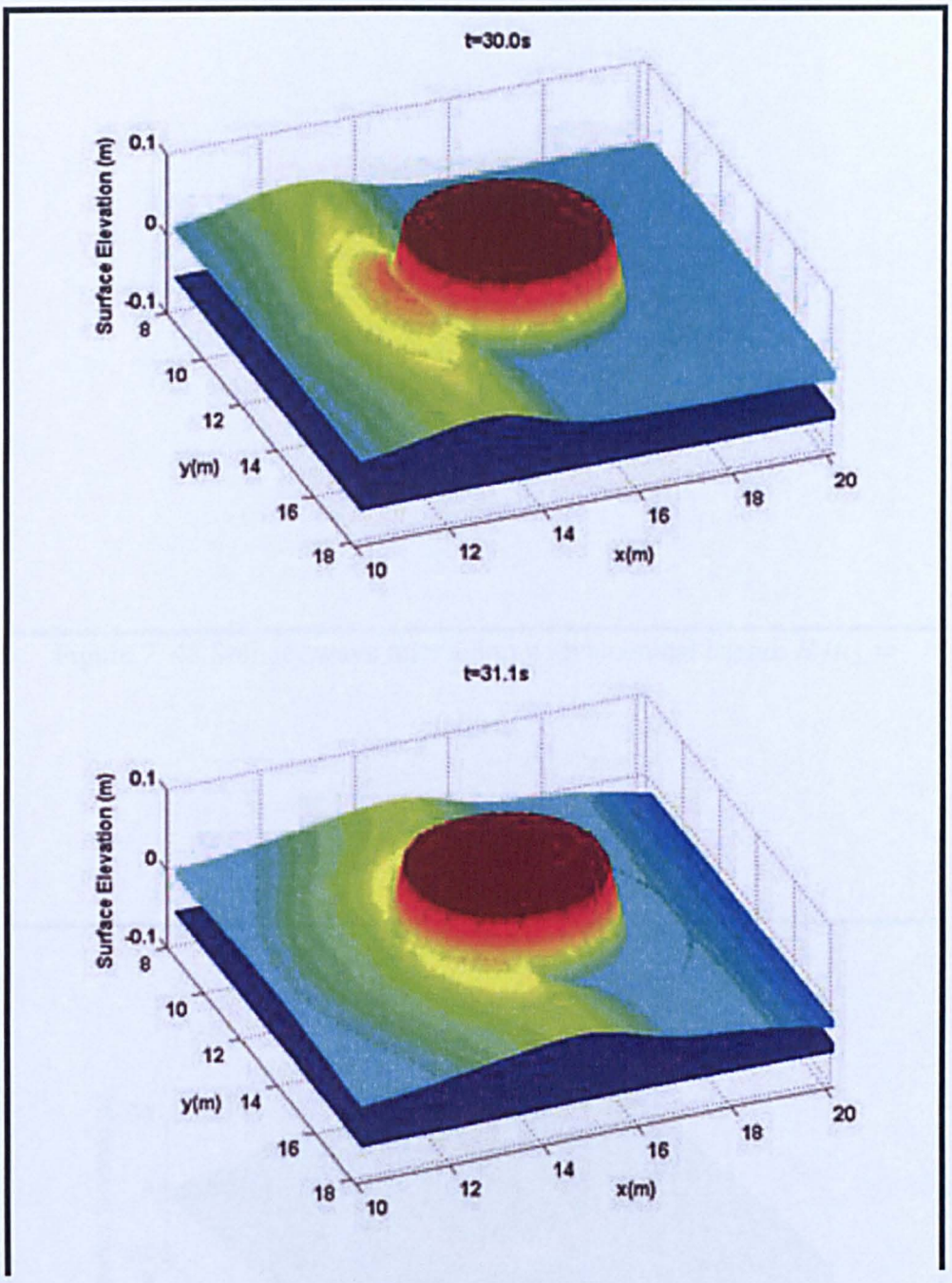
t=30.0s
Surface Elevation (m)
0.1
0
-0.1
8
10
12
y(m) 14
16
18
10
12
14
16
18
20
x(m)
t=31.1s
Surface Elevation (m)
0.1
0
-0.1
8
10
12
y(m) 14
16
18
10
12
14
16
18
20
x(m)

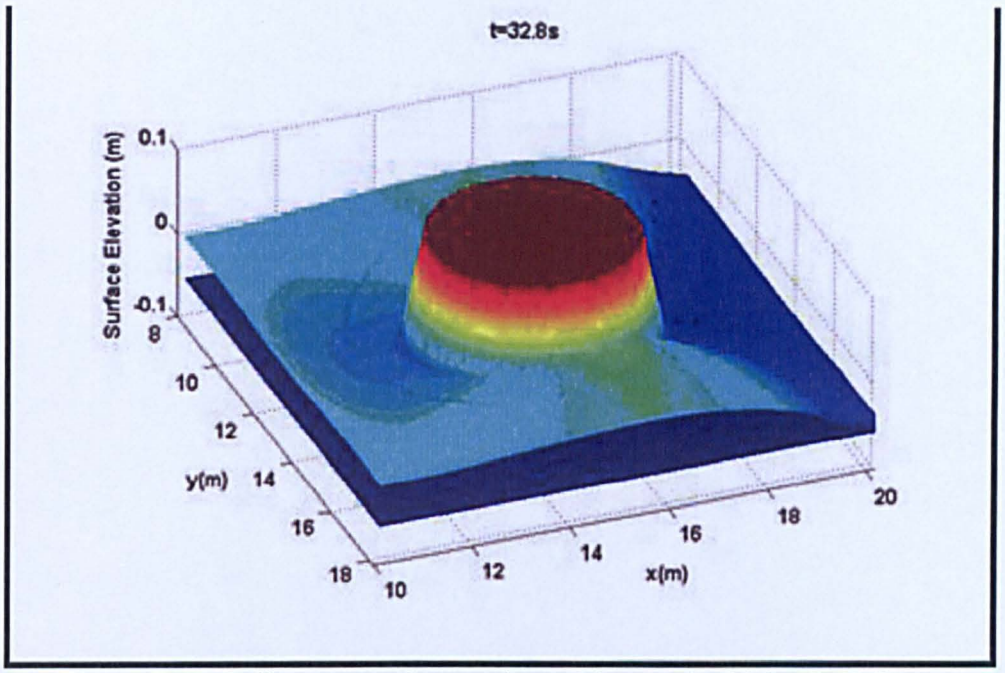

Figure 7. 48 Solitary wave interaction with a conical island: $H/h_0 =$ 0.096.

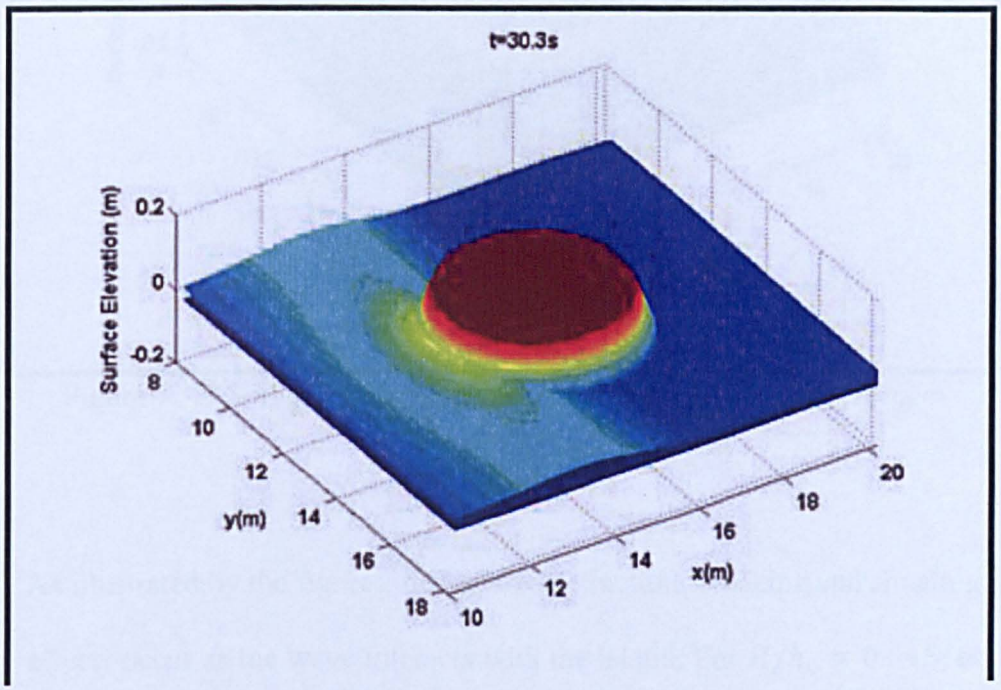

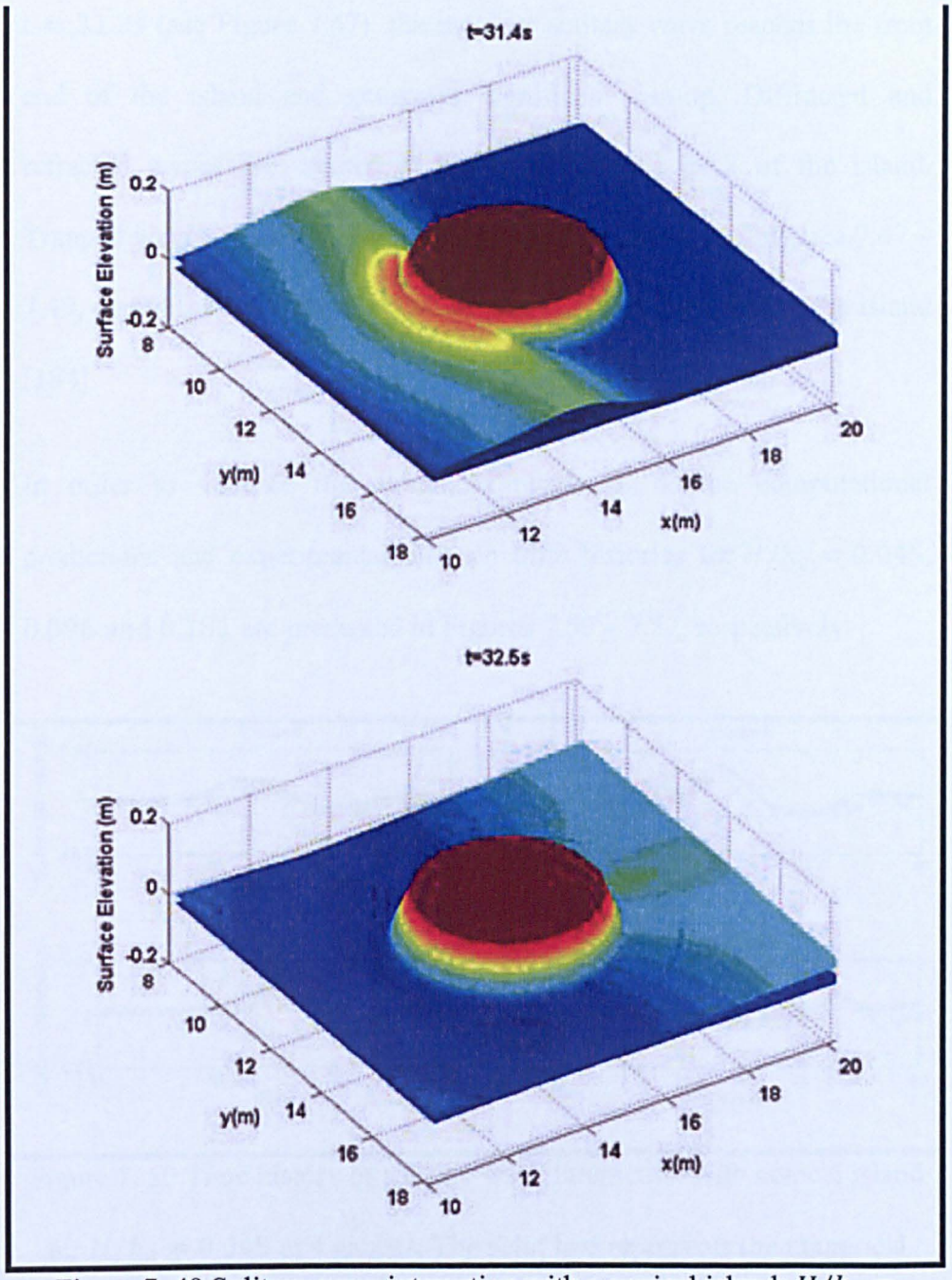

Figure 7. 49 Solitary wave interaction with a conical island: $H/h_0 = 0.181$.

As illustrated by the figures, diffraction, refraction, breaking and shoaling effects occur as the wave interacts with the island. For $H/h_0 = 0.045$, at

$t = 31.2s$ (see Figure 7.47), the incident solitary wave reaches the front end of the island and generates significant run-up. Diffracted and refracted waves are created at the front and the back of the island. Trapped waves can be discerned in the right hand plots of Figures 7.47 – 7.49, due to the solitary wave that breaks along the backside of the island [184].

In order to validate the model, comparisons of the computational predictions and experimental data on time histories for $H/h_0 = 0.045$, 0.096 and 0.181 are presented in Figures 7.50 – 7.52, respectively.

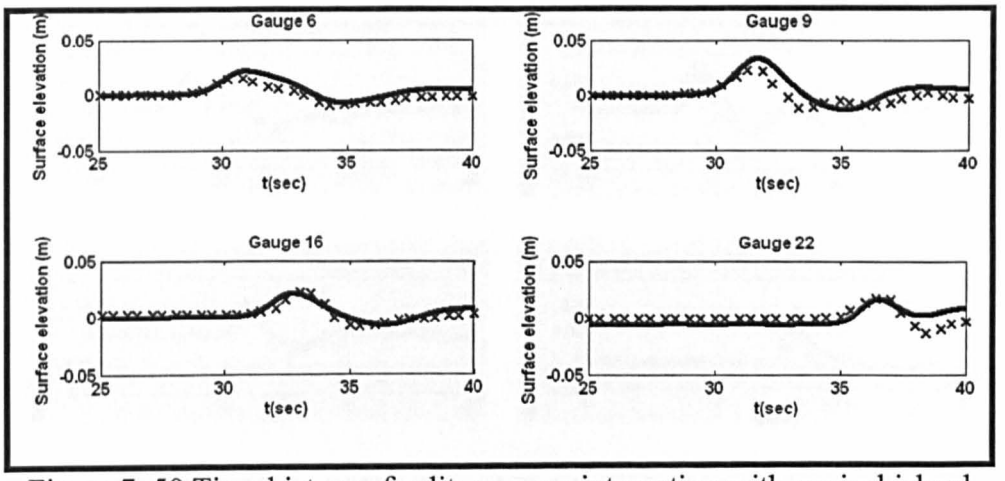

Figure 7. 50 Time history of solitary wave interaction with conical island for $H/h_0 = 0.045$ at 4 gauges. The solid line represents the numerical results. The crosses show experimental data [15].

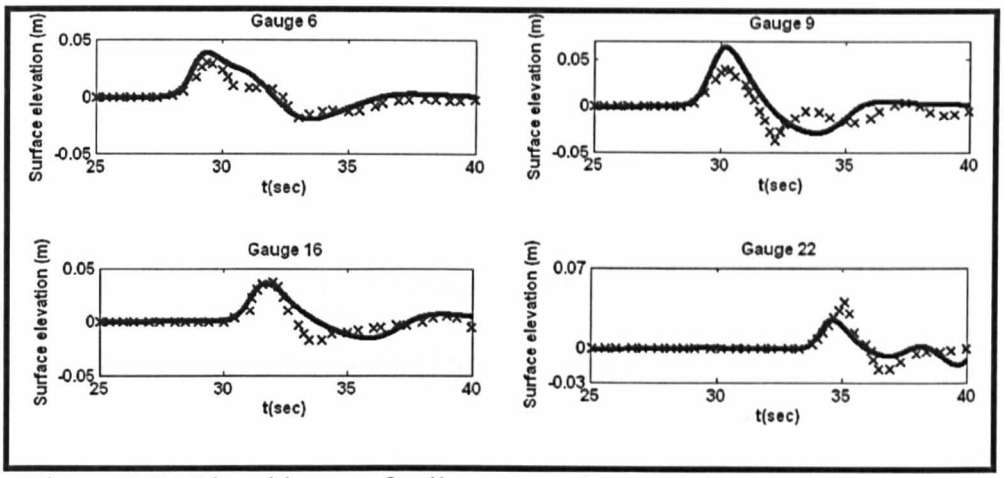

Figure 7. 51 Time history of solitary wave interaction with conical island for $H/h_0 = 0.096$ at 4 gauges. The solid line represents the numerical results. The crosses show experimental data [15].

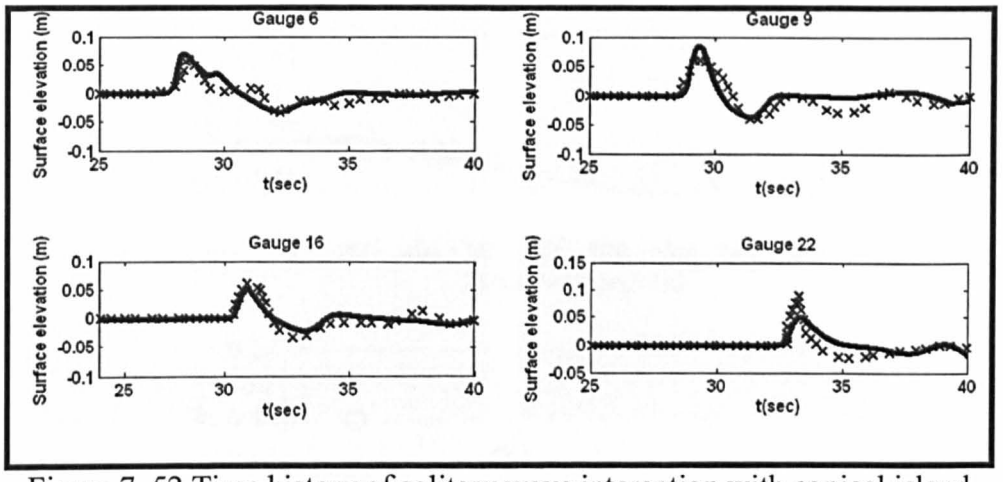

Figure 7. 52 Time history of solitary wave interaction with conical island for $H/h_0 = 0.181$ at 4 gauges. The solid line represents the numerical results. The crosses show experimental data [15].

For all comparisons, the main features of wave transformation are predicted quite well, except for the secondary depression waves. The numerical results show less of a depression following the main wave than

in the experiments. This is clearly seen in Figure 7.51. Nevertheless, this deviation is consistent with other run-up model tests [184].

Figure 7.53 presents a comparison between computed and experimented results for maximum wave run-up height around the island for incident wave heights $H/h_0 = 0.045, 0.096$ and 0.181.

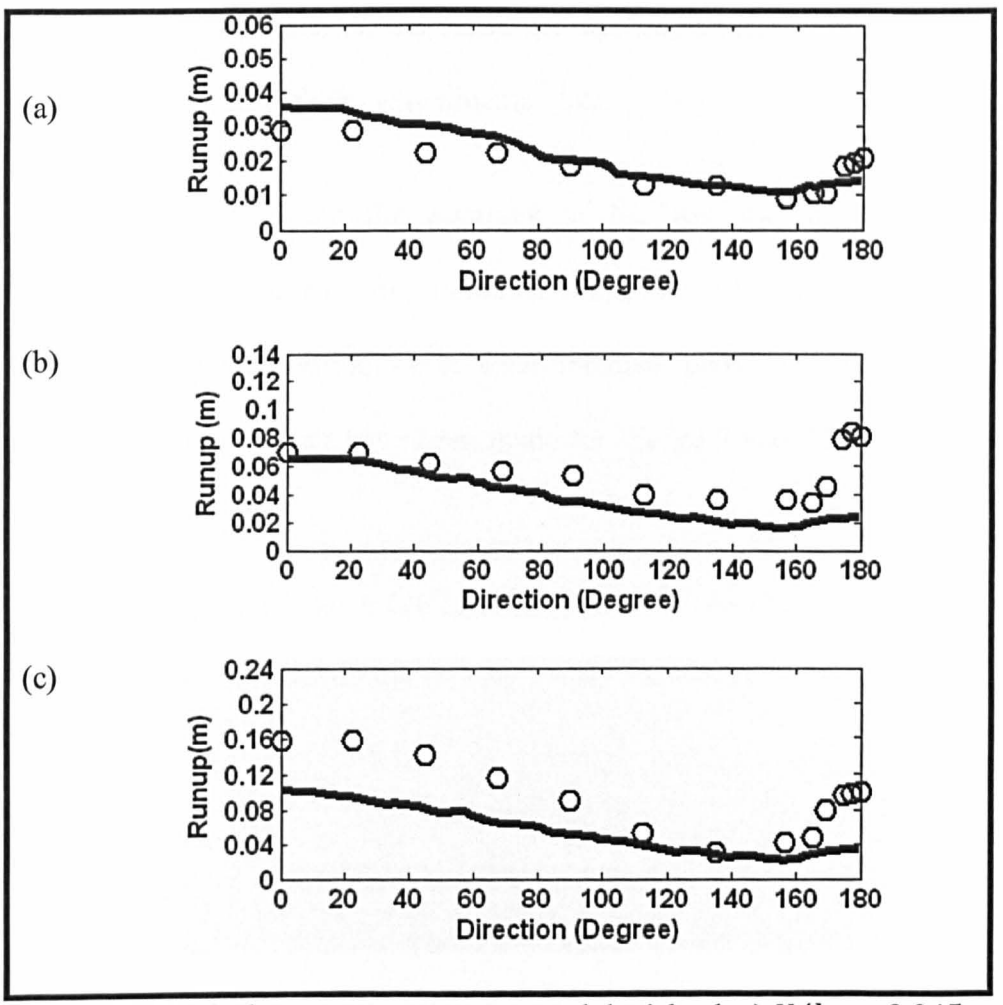

Figure 7. 53 Maximum wave run-up around the island: a) $H/h_0 = 0.045$, b) $H/h_0 = 0.096$ and c) $H/h_0 = 0.181$. The circles depict the experimental data [15]. The solid line represents the numerical results.

For the maximum run-up height results depicted in Figure 7.53, the computed results show a good agreement with the experiments, except for $H/h_0 = 0.181$, where, the numerical results give under prediction from angle 0^0 to 110^0. As the depth-averaged shallow water equation is utilized in the model, it is incapable of predicting the breaking wave accurately. In fact, the results agreed with the previous analyses [183]. Despite the discrepancies, the linear extrapolation run-up model is in overall agreement with the experimental data.

In order to investigate the accuracy of the two moving shoreline techniques, comparisons of computed wave time histories for both moving shoreline techniques at each incident wave height $H/h_0 = 0.045, 0.096$ and 0.181 have been made for Gauge 9 and 22 in Figures 7.54 – 7.56.

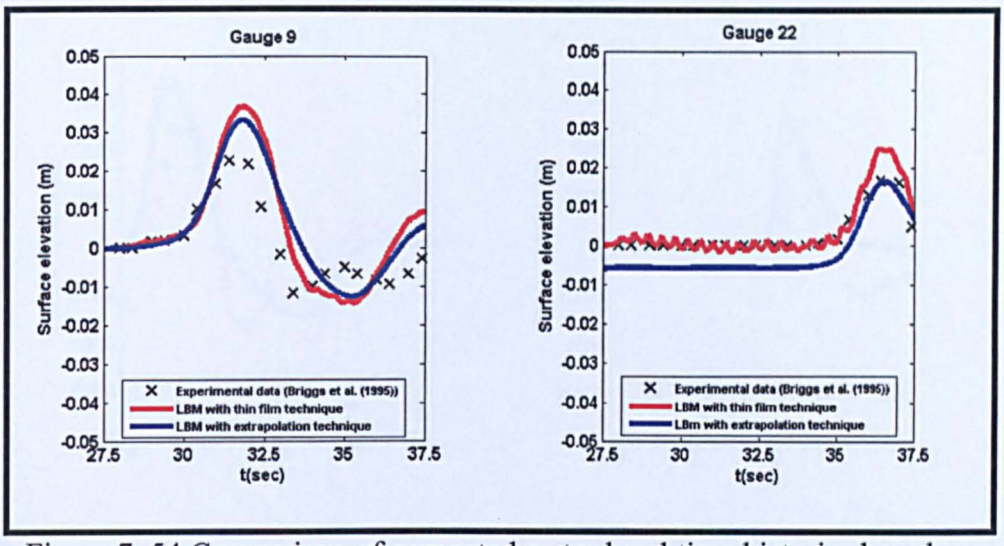

Figure 7. 54 Comparison of computed water level time histories based on the two moving shoreline techniques for $H/h_0 = 0.045$ at Gauge 9 and 22. Symbols indicate experimental data [15].

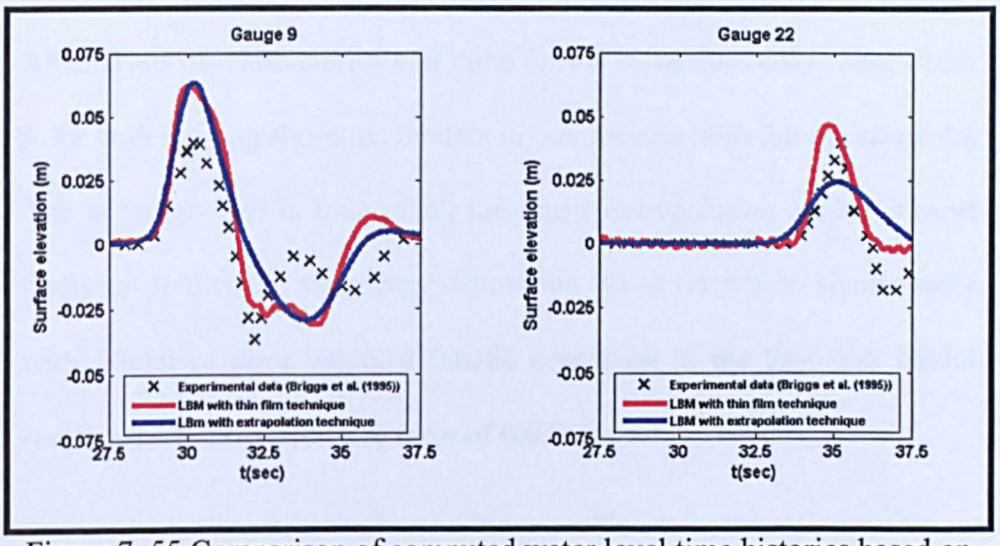

Figure 7. 55 Comparison of computed water level time histories based on the two moving shoreline techniques for $H/h_0 = 0.096$ at Gauge 9 and 22. Symbols indicate experimental data [15].

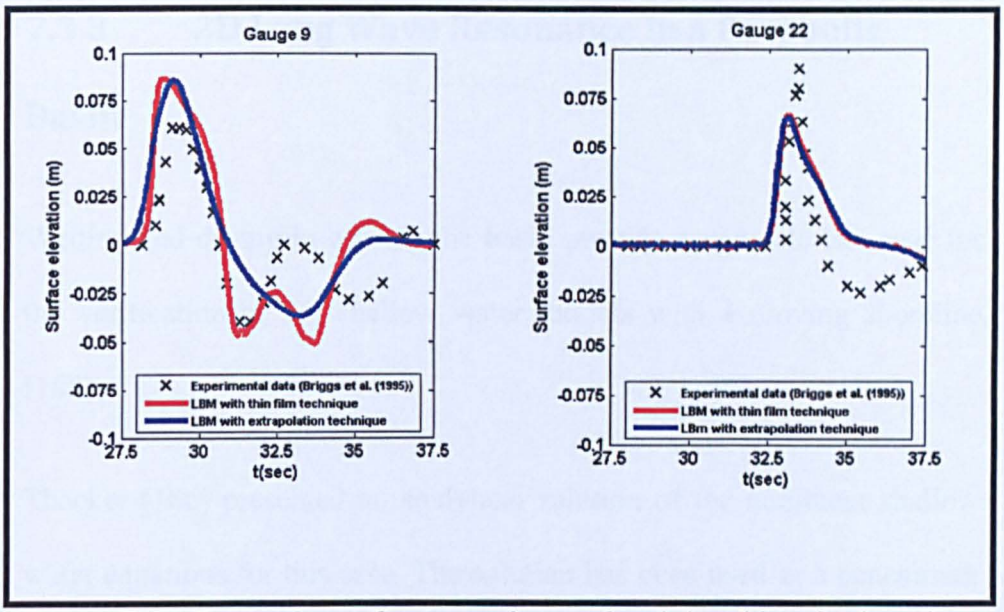

Figure 7. 56 Comparison of computed water level time histories based on the two moving shoreline techniques for $H/h_0 = 0.181$ at Gauge 9 and 22. Symbols indicate experimental data [15].

An analysis of relative error was done for the instantaneously water depth h for both moving shoreline models in comparison with the experimental data at gauge 9. It is found that, the linear extrapolation model is most likely to predict the secondary depression wave formation significantly with a relative error value of 0.0186 compared to the thin film model results which have a relative error of 0.0193.

7.3.3 2D Long Wave Resonance in a Parabolic Basin

Wetting and drying in a parabolic basin provide a valuable test case for the verification of 2D shallow water models with a moving shoreline [185].

Thacker [186] presented an analytical solution of the nonlinear shallow water equations for this case. The solution has been used as a benchmark case by other researchers [52,62,64,66-68] in validating their models. Therefore, this is a reliable test for the lattice Boltzmann model.

The initial water surface elevation and flow velocities are given as follows [186]:

$$\eta(r,t) = h_0\left[\frac{(1-A^2)^{1/2}}{1-A\cos(\omega t)} - 1 - \frac{r^2}{a^2}\left(\frac{(1-A^2)}{(1-A\cos(\omega t)^2)} - 1\right)\right], \tag{7.5}$$

$$u(r,t) = \frac{1}{1-A\cos(\omega t)}\left(\frac{1}{2}\omega x A\sin(\omega t)\right), \tag{7.6}$$

$$v(r,t) = \frac{1}{1-A\cos(\omega t)}\left(\frac{1}{2}\omega y A\sin(\omega t)\right), \tag{7.7}$$

where the frequency ω and coefficient A are given, respectively by:

$$\omega = \sqrt{8gh_0/a^2},$$

$$A = \frac{(a^2 - r_0^2)}{a^2 + r_0^2}, \tag{7.8}$$

and the basin shape is:

$$z_b(r) = h_0\left(1 - \frac{r^2}{a^2}\right), \tag{7.9}$$

in which $r = \sqrt{x^2 + y^2}$ is the distance from centre point; r_0 the distance from the centre point to the point where the shoreline initially located. The depth profile for the basin and the definition of $a, r_0 \, and \, h_0$ are shown in Figure 7.57. The values used for the numerical test are similar to that used by Marche et al. [68]; $a = 1$, $r_0 = 0.8m$, and $h_0 = 0.1m$.

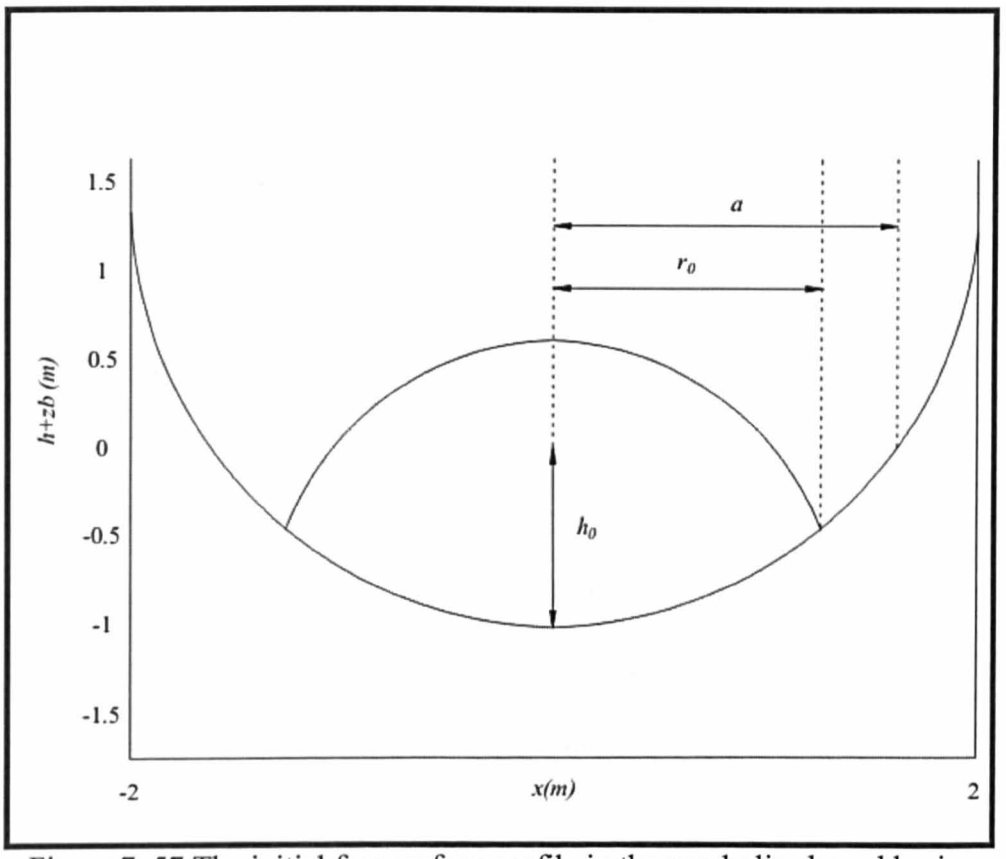

Figure 7. 57 The initial free surface profile in the parabolic shaped basin.

Initially, the simulation was carried out for the thin film and the linear extrapolation techniques layered with minimum water depth $h_{min} = 0.0005m$ and grid space of $\Delta x = \Delta y = 0.025m$ until $4\frac{1}{2}$ oscillation cycles of period T were completed. The wave profile results for both wetting and drying techniques were in poor agreement with the analytical solution, and began to deviate as early as $t = 2T$. This may be due to the omission of the dissipative term in the shallow water equation, which is consistent with the deviation effects noted by other researchers [14,52,64]. Grid convergence test is used in deciding the suitability of grid spacing in the model. In this test, grid spacing of $dx = 0.01m$ and

$0.005m$ with time step $dt = 0.001sec$ and relaxation time $\tau = 0.62$ were used for both wetting and drying algorithms. The results obtained by using the thin film model with the grid space of $dx = 0.005m$ were very good compared to those for $dx = 0.01m$.

However, for the linear extrapolation model, the combination of the grid space $dx = 0.005m$ with the time step $dt = 0.001sec$ and the relaxation time $\tau = 0.62$ caused the model to become unstable. Therefore, 601×601 lattice grids with $\Delta x = \Delta y = 0.005m$ were used for the linear extrapolation model computation. The time step was $\Delta t = 0.0005sec$ with $\tau = 0.65$ that satisfies the stability criteria.

7.3.3.1 Results using the thin film shoreline algorithm

A simulation is carried out using the thin film technique with $\tau = 0.62$ until $4\frac{1}{2}$ cycles of oscillation period T had elapsed. The water profiles at the middle of the basin (in y direction) and along the x direction at different cycles are plotted and compared in Figures 7.58 – 7.62.

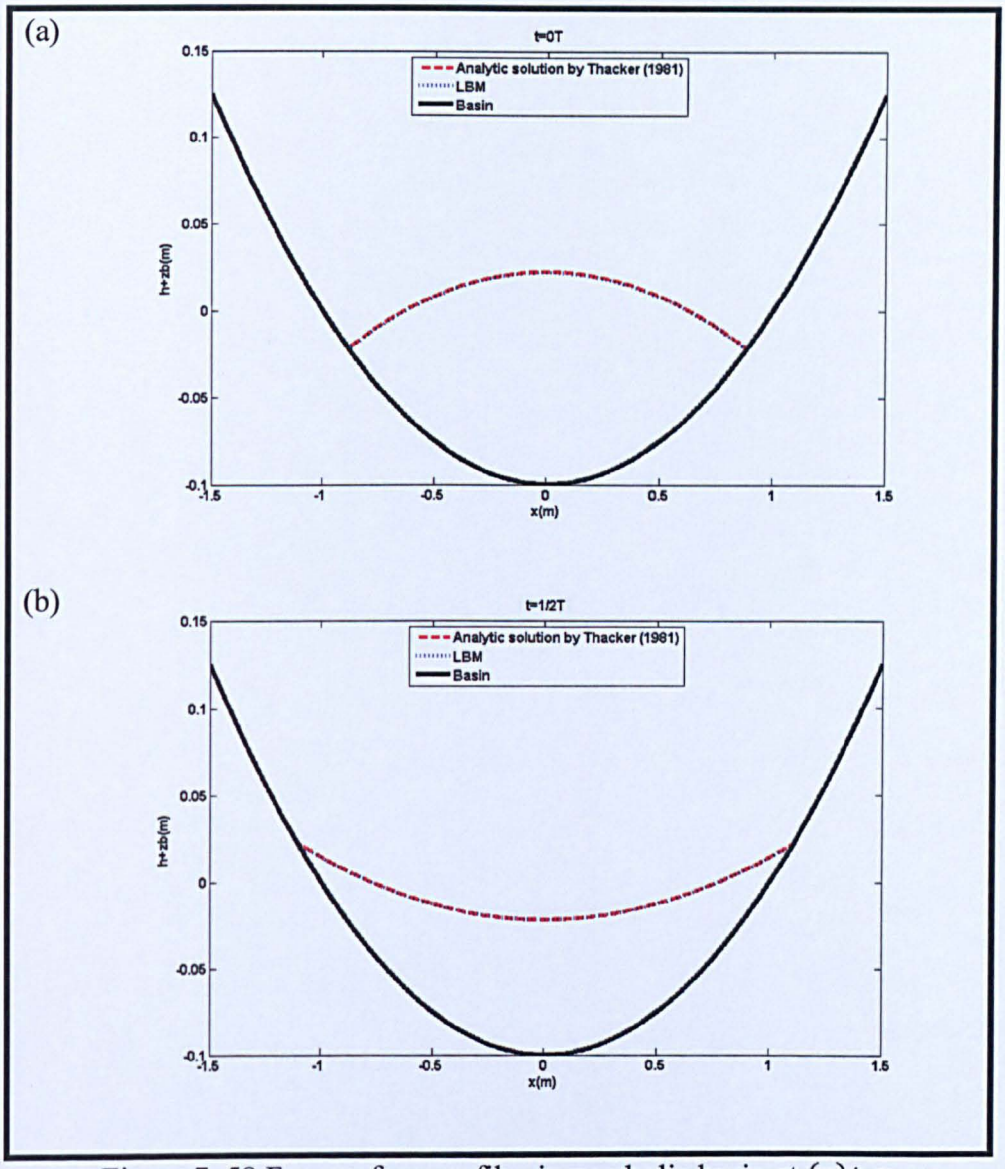

Figure 7. 58 Free surface profiles in parabolic basin at (a)$t = 0$, and (b)$t = 1/2T$.

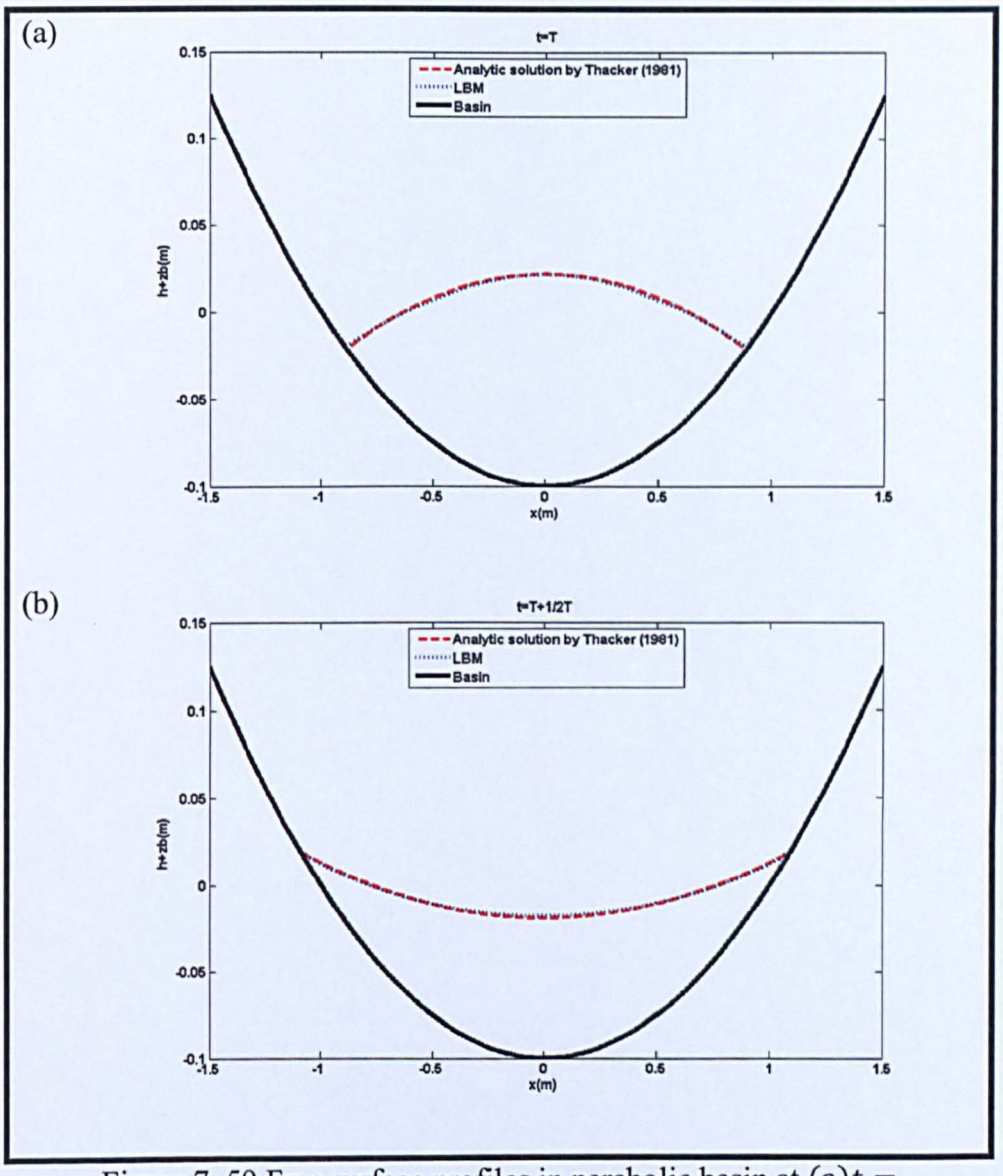

Figure 7. 59 Free surface profiles in parabolic basin at (a)$t =$

T, and (b)$t = T + 1/2T$.

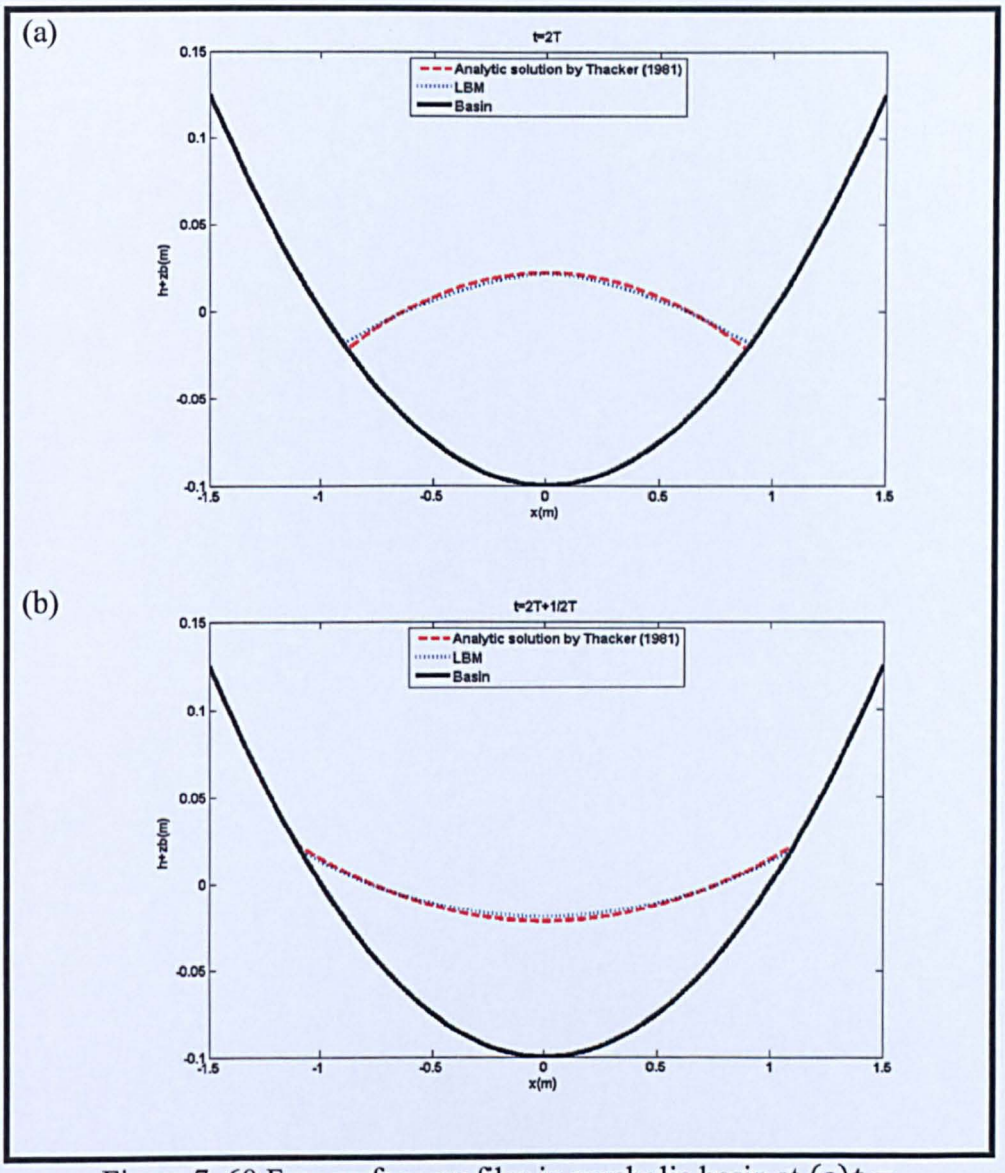

Figure 7. 60 Free surface profiles in parabolic basin at (a)$t = 2T$, and (b)$t = 2T + 1/2T$.

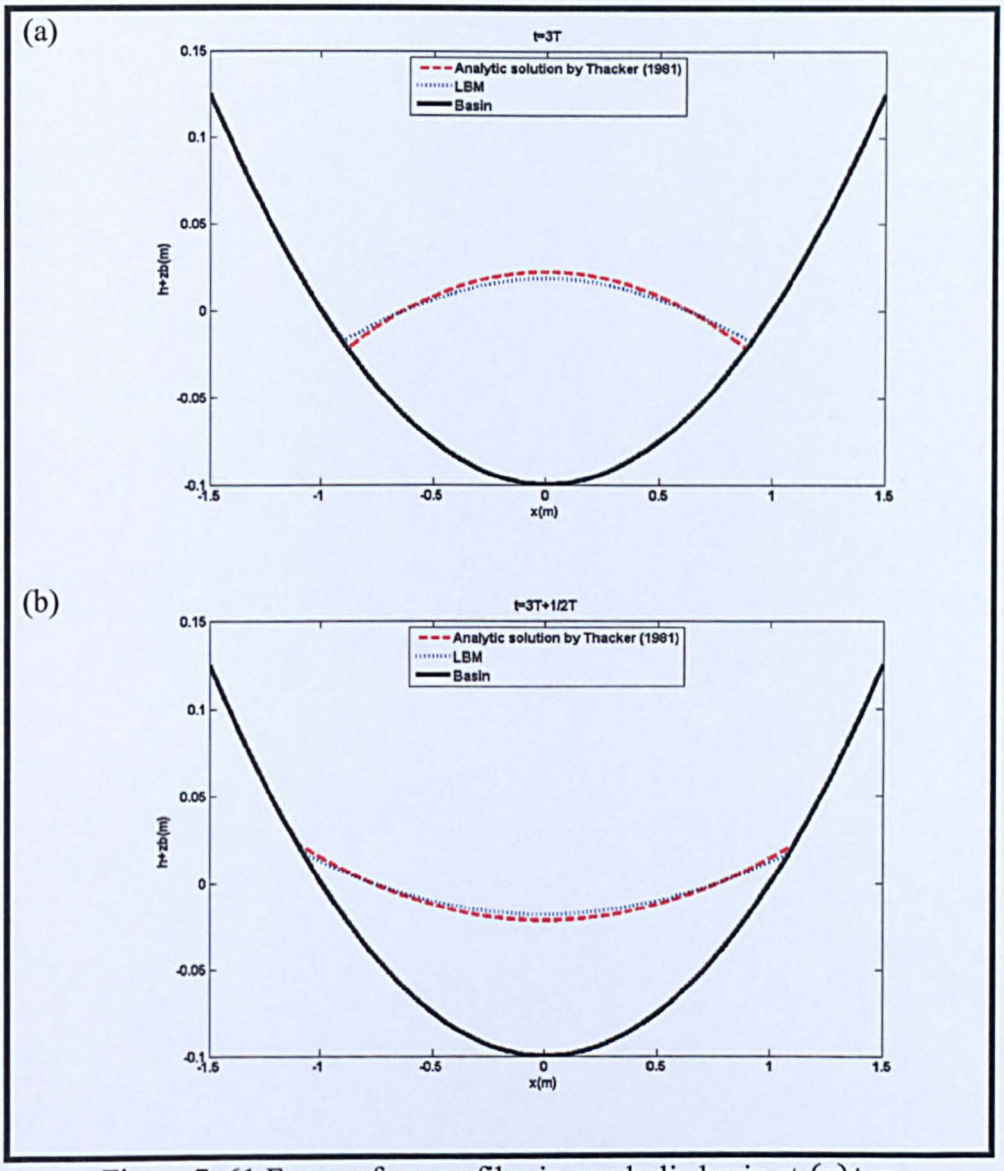

Figure 7. 61 Free surface profiles in parabolic basin at (a)$t = 3T$, and (b)$t = 3T + 1/2T$.

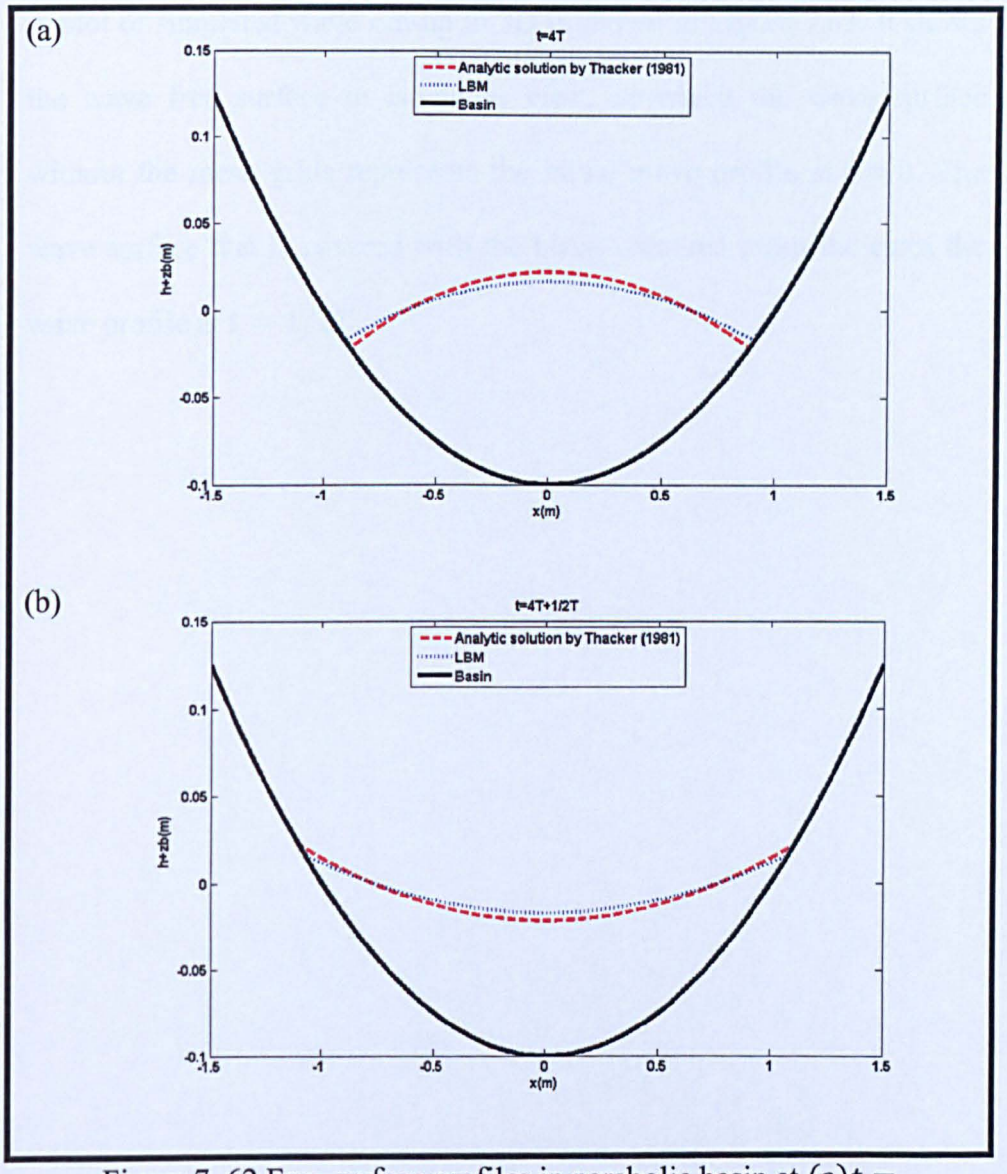

Figure 7. 62 Free surface profiles in parabolic basin at (a)$t = 4T$, and (b)$t = 4T + 1/2T$.

From the results shown in the above figures, the numerical results are in very good agreement with the analytical solutions [186] from $t = T$ until $t = 3T + 1/2T$. Deviation of the thin film model results begins at $t = 4T$ (see Figure 7.62 (a) and (b)).

A plot of simulated wave run-up in 3D is shown in Figure 7.63. It shows the wave free surface in isometric view, in which the wave surface without the mesh grids represents the initial wave profile at $t = 0$. The wave surface that is covered with the black coloured mesh indicates the wave profile at $t = 1/2T$.

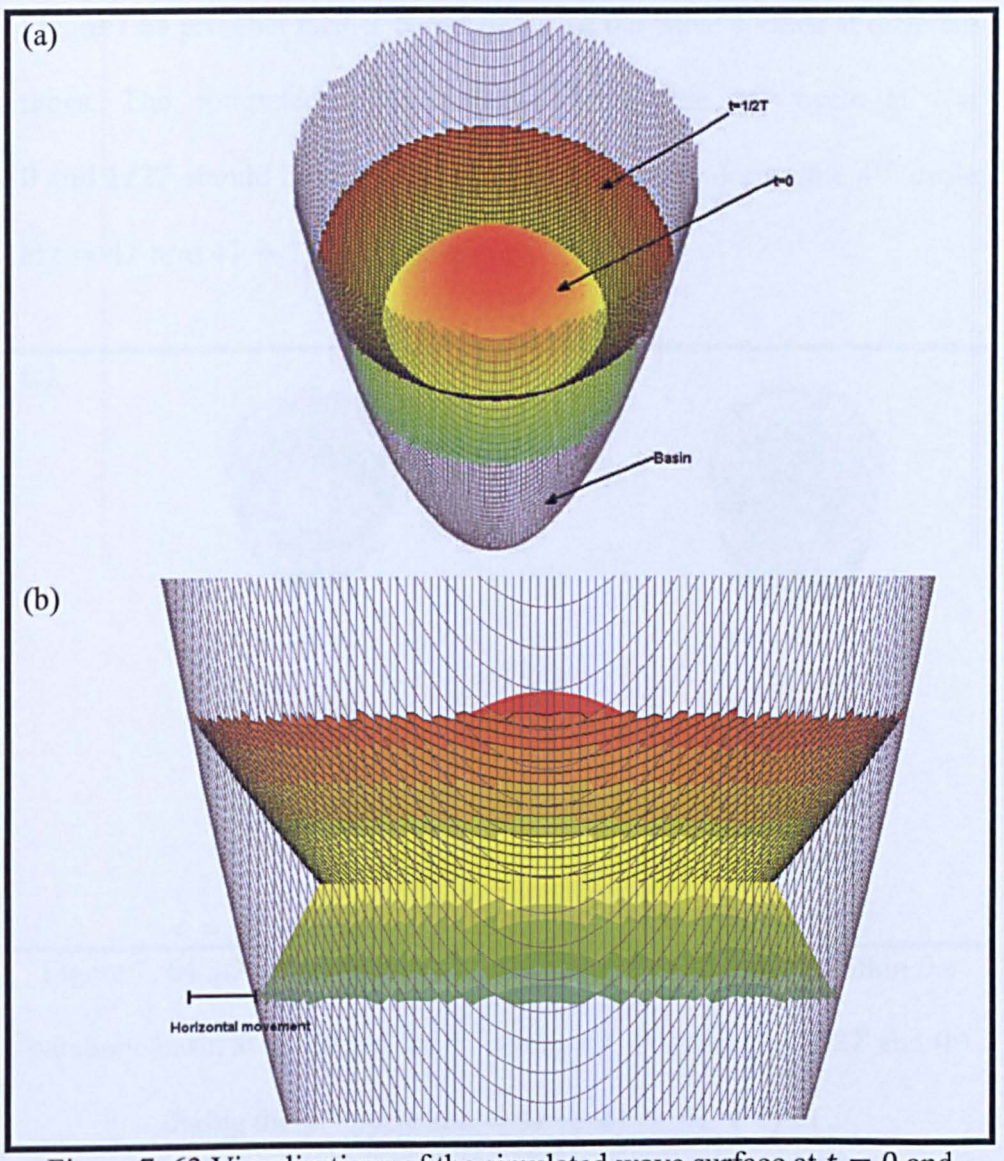

Figure 7. 63 Visualisations of the simulated wave surface at $t = 0$ and $t = 1/2T$, marked without the mesh grids and with the mesh grids, respectively. (a) The wave surfaces in isometric view and (b) wave profile surface in x direction.

As can be seen in Figure 7.63 (b), the shoreline moves to a new location during the computation (see the horizontal gap between both wave profiles). It should be noted that the jagging wave surface in Figure 7.63 (b) is due to plotting technique, which is different for real situation.

Figure 7.64 presents further comparisons of the wave surface at different times. The computed wave surfaces during the 1^{st} cycle at $t = 0$ and $1/2T$ should be compared against the surface during the 4^{th} cycle at $t = 4T$ and $4T + 1/2T$, respectively.

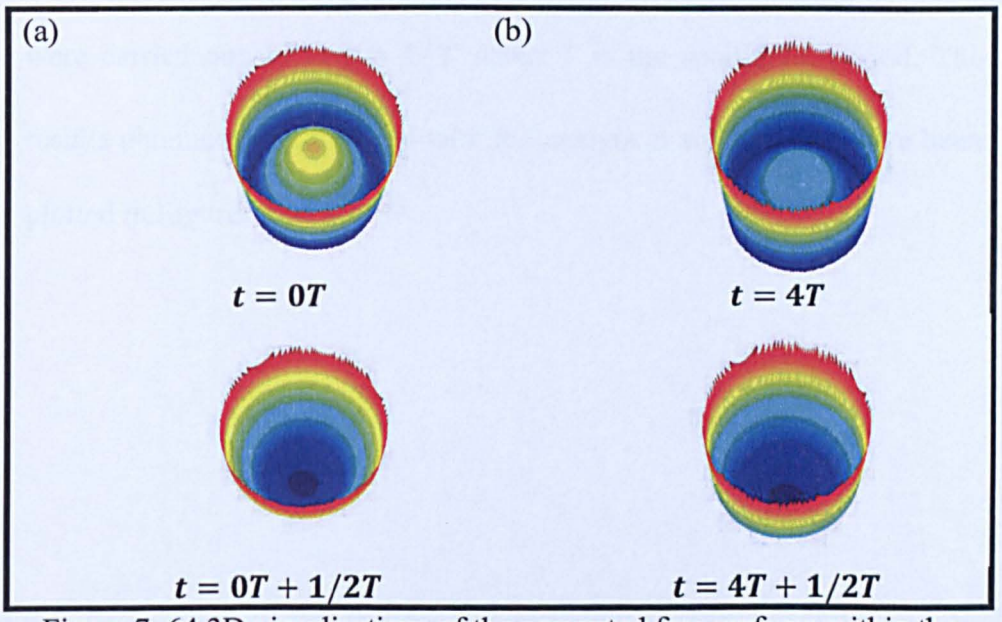

Figure 7. 64 3D visualisations of the computed free surfaces within the parabolic basin at (a) during the 1^{st} cycle at $t = 0$ and $t = 1/2T$ and (b) during the 4^{th} cycle at $t = 4T$ and t = $4T + 1/2T$.

The numerically predicted wave surfaces during the 4^{th} cycle under predict the wave profile, unlike the 1^{st}cycle. Despite the discrepancy, Figure 7.62 indicates that the thin film model simulated the long-wave run-up phenomenon in a parabolic shaped basin reasonably up to 4^{th} cycle of period.

7.3.3.2 Results using the linear extrapolation shoreline algorithm

Analysis of long-wave run-up in a parabolic shaped basin is continued with the linear extrapolation moving shoreline technique. Simulations were carried out up to $t = 4\frac{1}{2}T$ where T is the oscillation period. The results obtained are compared with the analytical solution and have been plotted in Figures 7.65 – 7.69.

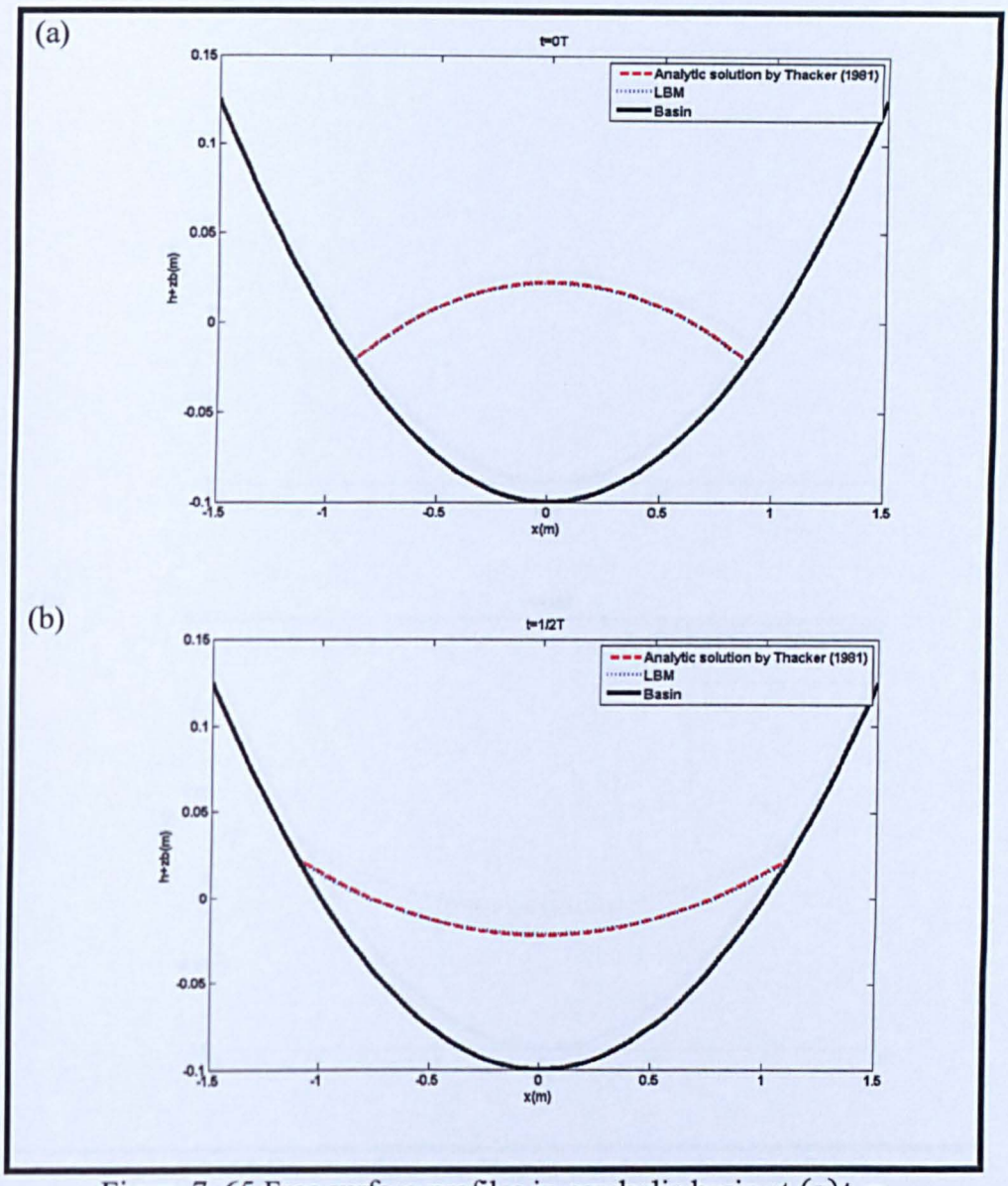

Figure 7. 65 Free surface profiles in parabolic basin at (a)$t = 0$, and (b)$t = 1/2T$.

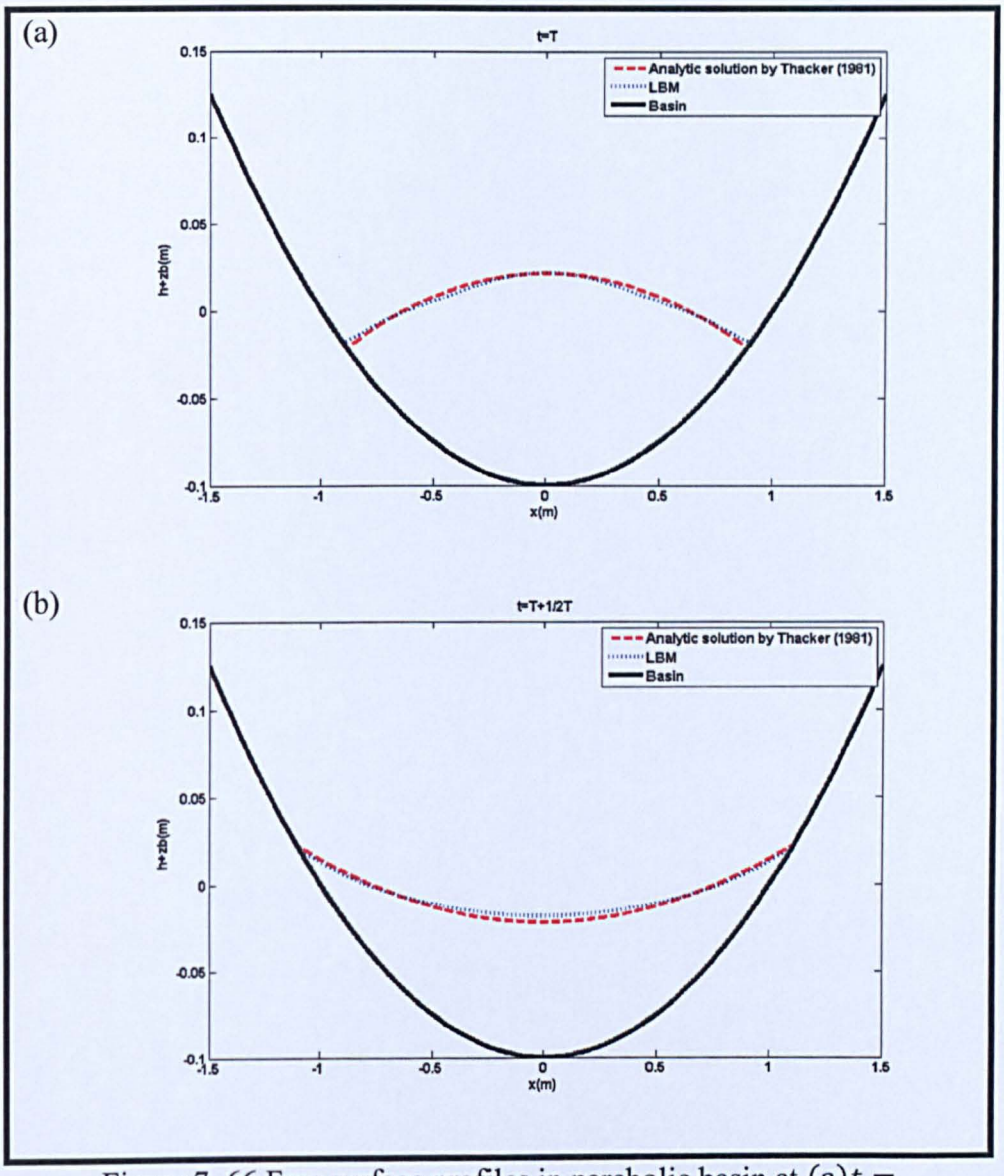

Figure 7. 66 Free surface profiles in parabolic basin at (a)$t =$

T, and (b)$t = T + 1/2T$.

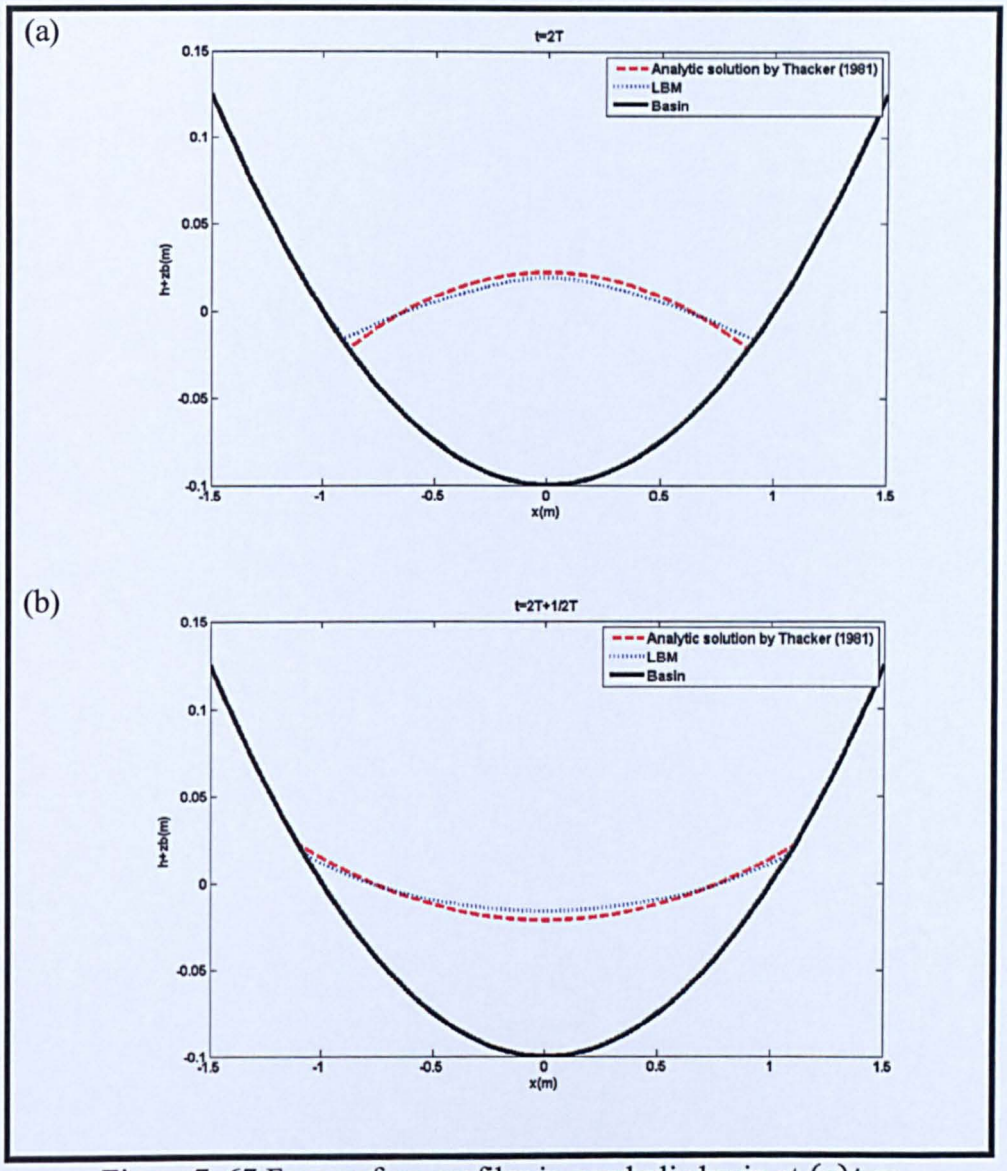

Figure 7. 67 Free surface profiles in parabolic basin at (a)$t = 2T$, and (b)$t = 2T + 1/2T$.

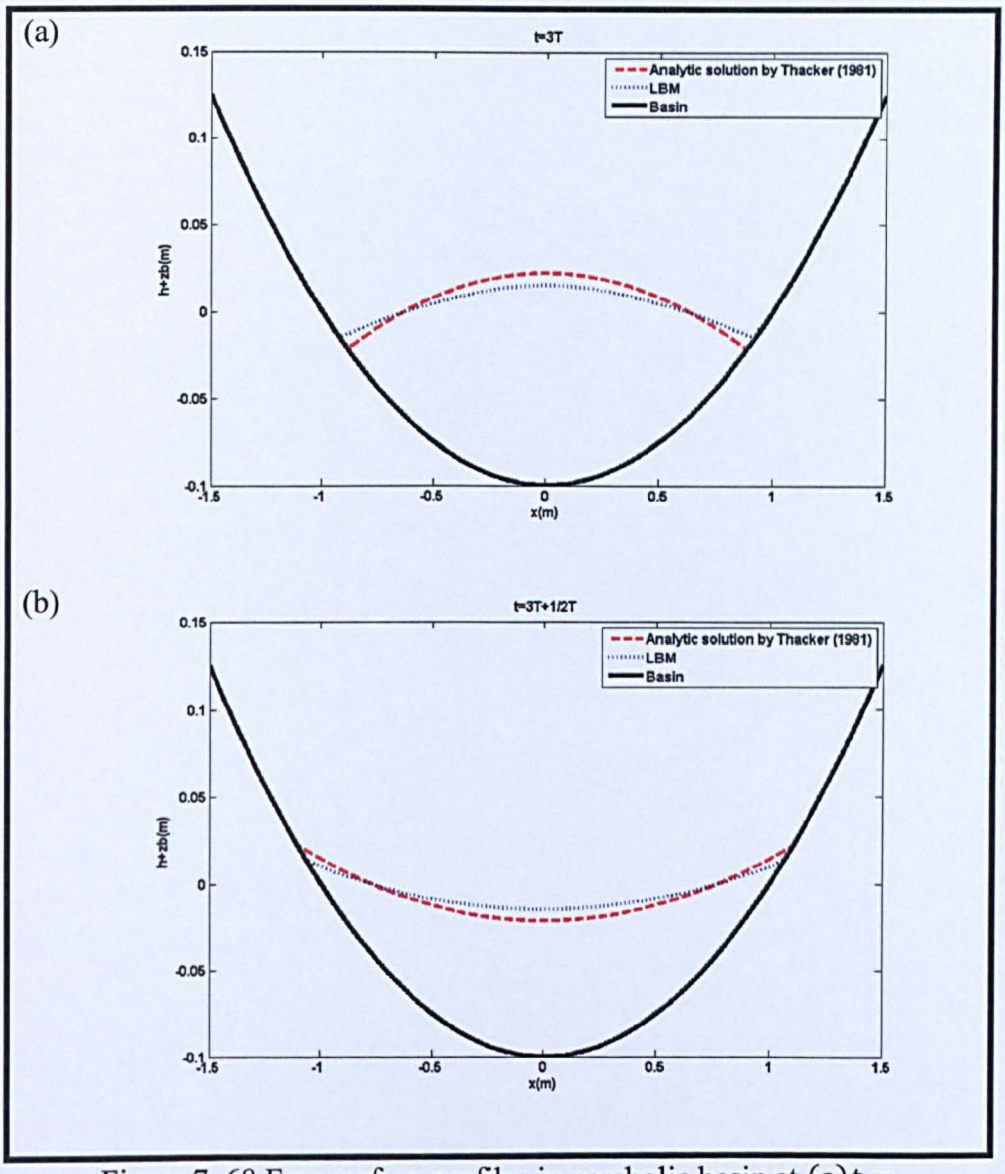

Figure 7. 68 Free surface profiles in parabolic basin at (a)$t = 3T$, and (b)$t = 3T + 1/2T$.

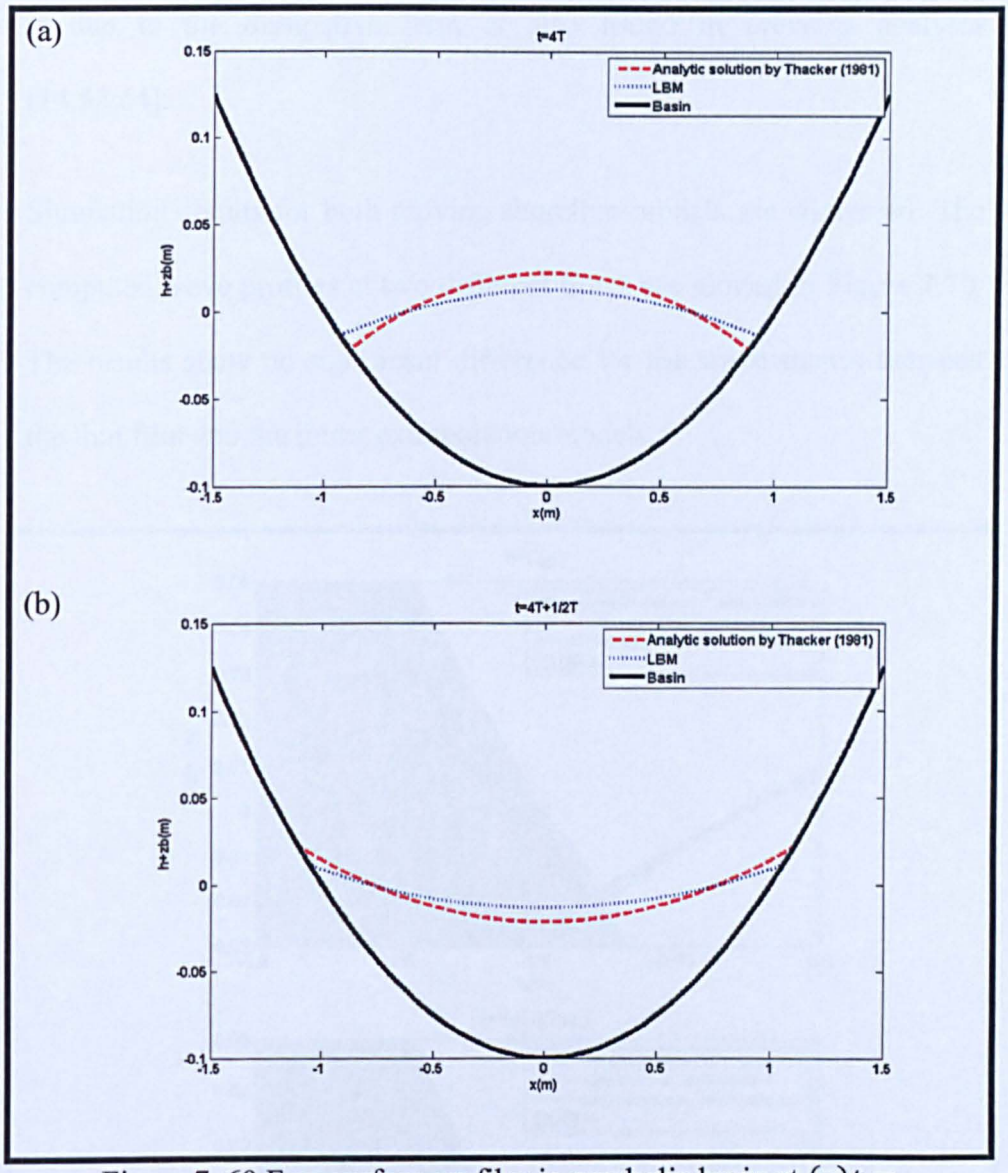

Figure 7. 69 Free surface profiles in parabolic basin at (a)$t = 4T$, and (b)$t = 4T + 1/2T$.

Acceptable results are achieved up to $t = T + 1/2T$. However, discrepancies occur from $2T$ onwards (see Figures 7.67 – 7.69), where the simulated wave profiles (parabolic curve) are slightly under predicted. It is believed that this happened due to the lack of a dissipative term in the shallow water equation. The effect of the water profile deviation that

is due to the dissipative term is also found in previous analyses [14,52,64].

Simulation results for both moving shoreline models are compared. The computed wave profiles at two different times are plotted in Figure 7.70. The results show no significant difference for the wave shapes between the thin film and the linear extrapolation models.

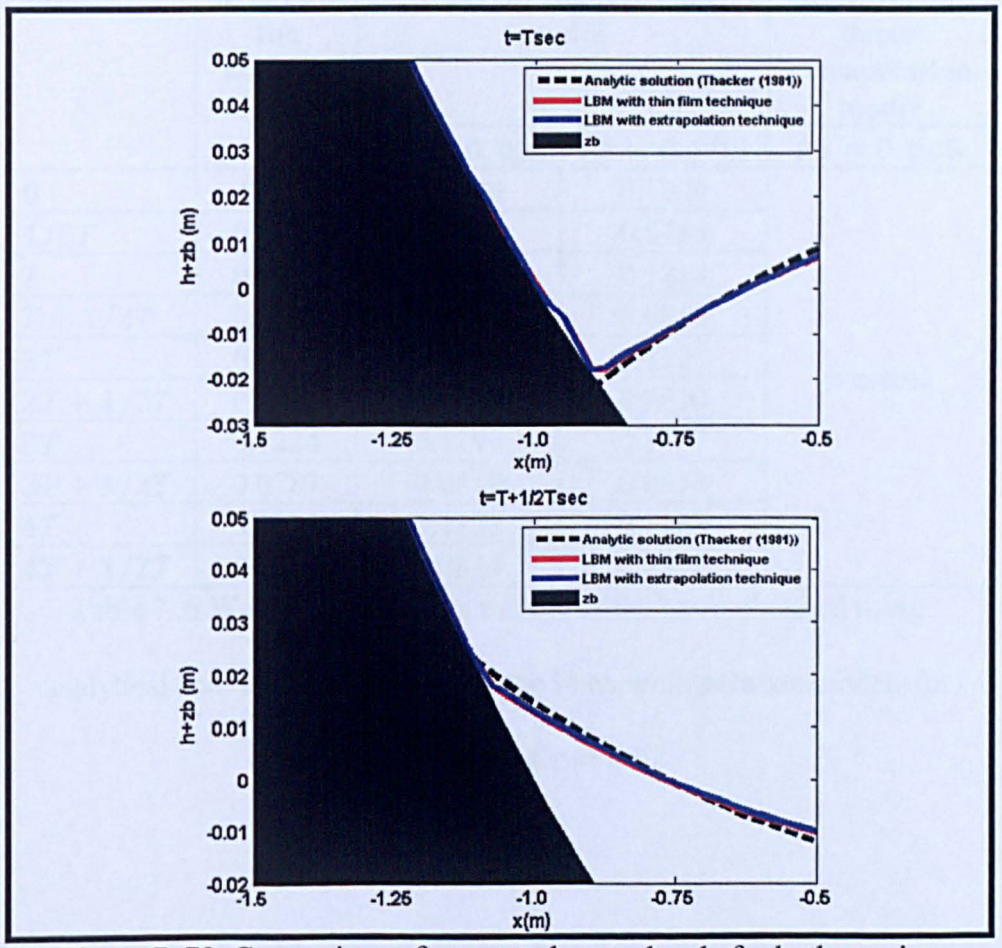

Figure 7. 70 Comparison of computed water levels for both moving shoreline techniques at $t = T$ and t = $T + 1/2T$ sec. The dashed-line indicates the analytic solution [186].

In order to evaluate the error for the two moving shoreline algorithms, analysis was carried out of the relative error for the water depth h at the middle of the basin. The water depth was compared for different selected sizes of lattice at each time cycle. Table 7.6 lists the results for $\Delta t = 0.001sec$ and $\tau = 0.62$. Table 7.7 lists the results for $\Delta t = 0.0005sec$ and $\tau = 0.65$.

Time	$h(m)$ **for the analytic solution**	$h(m)$ **for the thin film model**		$h(m)$ **for the linear extrapolation model**
		$\Delta x = 0.01$	$\Delta x = 0.005$	$\Delta x = 0.005$
0	0.122	0.1220	0.1220	unstable
$1/2T$	0.0786	0.0784	0.0785	
T	0.1221	0.1212	0.1218	
$T + 1/2T$	0.0811	0.0819	0.0814	
$2T$	0.1224	0.1226	0.1225	
$2T + 1/2T$	0.0788	0.0812	0.0810	
$3T$	0.1224	0.1190	0.1187	
$3T + 1/2T$	0.0787	0.0819	0.0818	
$4T$	0.1222	0.1176	0.1167	
$4T + 1/2T$	0.0788	0.0834	0.0830	

Table 7. 6 Water depth h at the middle of the basin obtained using analytical and for the thin film and the linear extrapolation models for $\Delta t = 0.001s$ and $\tau = 0.62$.

Time	$h(m)$ for the analytic solution	$h(m)$ for the thin film model	$h(m)$ for the linear extrapolation model
		$dx = 0.005$	$dx = 0.005$
0	0.1220	0.1220	0.1220
$1/2T$	0.0786	0.0792	0.0792
T	0.1221	0.1225	0.1222
$T + 1/2T$	0.0811	0.0820	0.0820
$2T$	0.1224	0.1199	0.1199
$2T + 1/2T$	0.0788	0.0822	0.0837
$3T$	0.1224	0.1157	0.1157
$3T + 1/2T$	0.0787	0.0850	0.0850
$4T$	0.1222	0.1131	0.1128
$4T + 1/2T$	0.0788	0.0866	0.0867

Table 7. 7 Water depth h at the middle of the basin obtained using analytical and the thin film and the linear extrapolation models for $\Delta t = 0.0005s$ and $\tau = 0.65$.

Tables 7.8 and 7.9 list the corresponding relative error values for both models for (a) $\Delta x = 0.005m, \Delta t = 0.001s$ with $\tau = 0.62$, and (b) $\Delta x = 0.005m, \Delta t = 0.0005s$ and $\tau = 0.65$.

Time	Relative error %	
	Thin film algorithm	
	$\Delta x = 0.01m$	$\Delta x = 0.005m$
0	0	0
$1/2T$	0.25	0.13
T	0.74	0.25
$T + 1/2T$	0.99	0.37
$2T$	0.16	0.08
$2T + 1/2T$	3.05	2.79
$3T$	2.78	3.02
$3T + 1/2T$	4.07	3.94
$4T$	3.76	3.27
$4T + 1/2T$	5.84	5.33
Average error	**2.16**	**2.04**

Table 7. 8 Relative error in water depth for the thin film model with $\Delta x = 0.01m$ and $0.005m$ at $\Delta t = 0.001s$ and $\tau = 0.62$.

Time	Relative error %	
	Thin film algorithm	Linear extrapolation algorithm
0	0.00	0
$1/2T$	0.76	0.76
T	0.33	0.33
$T + 1/2T$	1.11	1.11
$2T$	2.04	2.04
$2T + 1/2T$	4.31	6.22
$3T$	5.47	5.47
$3T + 1/2T$	8.01	8.01
$4T$	7.45	7.69
$4T + 1/2T$	9.90	10.03
Average error	**3.94**	**4.17**

Table 7. 9 Relative error in water depth for the thin film and the linear extrapolation models with $\Delta x = 0.005m, \Delta t = 0.0005s$ and $\tau = 0.65$.

As shown in Table 7.8, the smaller grid size produced smaller relative errors for the thin film model. From the analysis summarized in Table 7.9, the largest errors are obtained for the linear extrapolation model. Nevertheless, the average errors of results for both models are still under 5%.

The computed run-up and the run-down process can be carried on for a longer time without having any difficulties in terms of stability. The only thing to be considered before implementing this technique in the model is to make sure that the time step obeys the CFL criteria for minimum water depth value. Hence, the instability problems can be avoided.

Overall, the thin film and linear extrapolation models give satisfactory prediction of the long-wave run-up phenomenon in parabolic shaped basin up to $4T$ and $2T$ oscillation cycles, respectively. Despite the results that are not satisfactory, overall, the thin film and extrapolation techniques appear to have been successfully applied in the current lattice Boltzmann model for capturing moving shorelines.

Chapter 8 Conclusions and Recommendations

8.0 Conclusions

The evolution of the LBM including the history of cellular automata and the Boltzmann equation has been explained, followed by an elaboration of the N-S equations in relation to the shallow water equations. The derivation and implementation of the shallow water equations in the LBM have been presented.

The primary objective of this study is to investigate the capabilities of the LBM by utilizing the method in complicated practical situations such as those involving complex flow conditions and geometry. The model was validated against standard analytic solution and then calibrated and validated using the results of independent studies.

A simple wave run-up model using the LBM has been developed, as shown in Chapter 5. Two different types of moving shorelines were considered. The capability of the model in predicting the wave run-up was investigated by using appropriate experimental and numerical data from available literature.

8.1 Recirculating Flow

LABSWE^{TM} has been tested to predict hydraulic free surface flows in complicated channel domains. Five cases were considered:

a) Turbulent flow within a channel with a semi-circular sidewall cavity

b) Flow in a channel with a spur-dike

c) Turbulent flow within a single expansion channel

d) Turbulent flow within a double expansion channel

e) Turbulent jet-forced flow in symmetrical and asymmetrical circular basins.

For turbulent flows, the Smagorinsky constant C_s and the semi-slip boundary condition are used to produce an appropriate flow pattern downstream of the channel expansions, the spur-dike and within the circular shaped channel. The model predicts circulating flow patterns and lengths comparable to experimental results and analytical solutions, hence proving that it is capable of efficiently simulating complicated open-channel flow phenomena.

8.2 Sidewall Friction Effect

Analysis of the sidewall friction effect on complex flows in complicated open-channel geometries has been carried out. A semi-slip boundary condition is employed in the LABSWE^{TM} using a prescribed wall friction coefficient C_f. For verification purposes, a test case undertaken experimentally by Molls et al. [55] was selected. The simulated results are in good agreement with the experimental data and alternatives

numerical results, in that the flow velocity profile affected by sidewall friction is correctly predicted.

The effect of sidewall friction was then studied for velocity profiles across the channel width. Three different channel shapes and flow characteristics were chosen:

a) Turbulent flow in a single expansion channel with upstream $Q = 20.2l/s$ and downstream $h = 24.2m$.
b) Turbulent flow in a double expansion channel with upstream $u = 2.35m/s$ and downstream $h = 1.524m$.
c) Turbulent flow in a channel with a semi-circular sidewall cavity with upstream $u = 0.25m/s$ and downstream $h = 0.25m$.

The outcomes of the simulations show no significant effects of sidewall friction within the eddy zone. This is due to the dominant effect of vorticity. The very wide channel caused the flow velocity distribution to be asymmetric in the y-direction. Therefore, in order to obtain a realistic profile, a longer channel should be modelled. A stable velocity profile should be obtained far from the strong turbulence in the eddy. Overall, LABSWE™ has been proven capable of modelling the effect of sidewall and bed friction.

8.3 Wave Run-up and Moving Shoreline

A version of LABSWE^{TM} implemented with a moving shoreline algorithm has been built and tested. Thin film and linear extrapolation methods were employed for the moving shoreline phenomena. The model was verified by predicting 1D solitary long-wave run-up at a beach, 2D solitary wave interaction with a conical island and 2D oscillation wave in a parabolic basin.

The implementation of the thin layer of fluid in the whole computational domain resulted in a stable and simple model. The thin film technique appears to be both a straightforward and reasonably accurate method that can be implemented in the LBM.

The extrapolation technique also successfully produced reasonable simulations of wave run-up and run-down. Despite the tricky algorithm that has to be coded in 2D hydraulic problems, the simulation results obtained are good. However, there is an issue related to conservation of mass and momentum.

Thang et al. [187] revealed an important finding. The force term included in the current lattice Boltzmann model [45] solves the shallow water problems to machine accuracy. Unfortunately, it does not precisely satisfy the correct mass and momentum balances. Therefore, the

discrepancies obtained in the wave run-up analysis are strongly believed to have resulted from the inaccurate model system. The technique seems less accurate in preserving these two important physical elements that are essential to computational analysis in the field of CFD.

Despite the discrepancies, the simulated results are in overall agreement with available experimental data and analytical solutions.

8.4 Recommendations

Throughout the research, several ideas have come to light, that overcome problems arising in terms of modelling and validating the wave run-up lattice Boltzmann model.

In relation to the wave run-up studies, it was noticeable that at some points, the lattice Boltzmann model is unable to predict the breaking wave phenomenon. The predicted water profile differs from the expected profile at the time when the wave is breaking because of limitations in the depth-averaged shallow water equation. This remains an important but unresolved problem [183].

In addition, there is no dissipative term in the model. The effect of the dissipative term can also be seen in the 2D parabolic basin wave run-up study case. In the simulation, the water deviates after a few times of iteration. Despite the discrepancy, this particular case is actually an ideal test for the non-linear shallow water models with dissipation term due to its sensitivity to gravitational force [64]. A dissipative term should be therefore incorporated in the lattice Boltzmann model for the nonlinear shallow water equations. Thus the model should be able to predict the breaking wave activity more accurately.

A multi-relaxation time model (MRT) should be used in future to obtain results that are more accurate. It provides the maximum number of adjustable relaxation times and allows some freedom in the construction of equilibrium functions of non-conserved moments. Despite its considerable computational load, MRT is still a good computational fluid dynamic technique in terms of stability and accuracy [89].

Finally, as the velocity and fluid depth profile in the vertical direction have become central to various analyses and studies in the CFD field, it is desirable to have a 3D model, so that the model becomes more realistic.

8.5 Final Remarks

The Bhatnagar-Gross-Krook lattice Boltzmann model has been enhanced by considering a significant step in predicting complex shallow water hydraulic phenomena. Additionally, wall friction effects are also better appreciated and employed in the model. A practical wave run-up model has also been developed in connection with moving shoreline phenomena.

Appendix A A proof of second-order accuracy for the stationary case $u_i \equiv 0$ with source term or non-zero force term

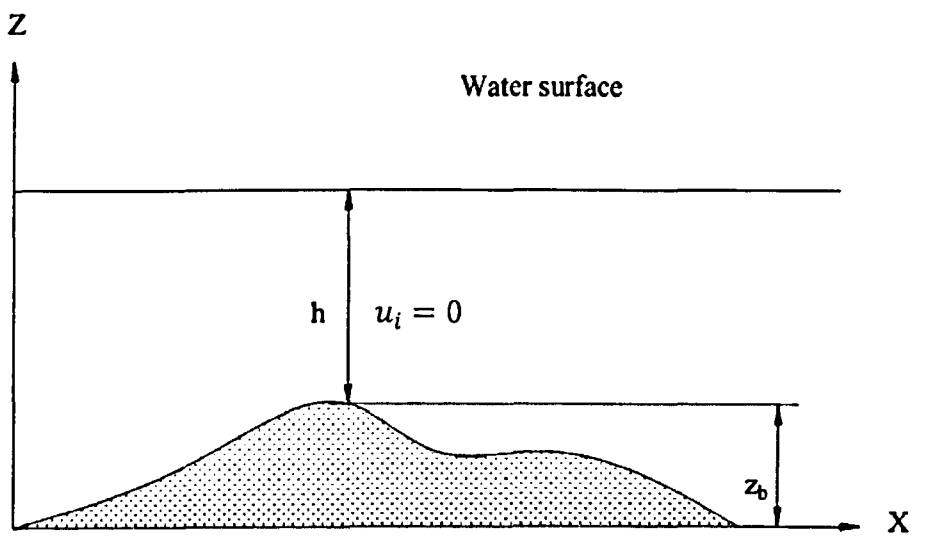

Figure 8. 1 Still water above an uneven bed.

There is a non-vanishing force term in the right hand side of the lattice Boltzmann equation for shallow water equations such as follows:

$$f_\alpha(x + e_\alpha \Delta t, t + \Delta t) - f_\alpha(x,t) = -\frac{1}{\tau}(f_\alpha - f_\alpha^{eq}) + \frac{\Delta t}{6e^2} e_{\alpha i} F_i. \quad (8.1)$$

where the force related to still water at $u_i \equiv 0$ above bed topography as in Figure 8.1 is given by:

$$F_i = -gh\frac{\partial z_b}{\partial x_i}. \tag{8.2}$$

Therefore, for the LBM to be correct, the force term must be cancelled.

To demonstrate the accuracy of the LBM, a Taylor expansion is taken to the first term on the left hand side of equation (8.1) such as

$$\begin{aligned} f_\alpha(\boldsymbol{x} + e_\alpha\varepsilon, t + \varepsilon) &= f_\alpha(\boldsymbol{x}, t) \\ &+ \varepsilon\left(\frac{\partial}{\partial t} + e_{\alpha j}\frac{\partial}{\partial x_j}\right) f_\alpha(\boldsymbol{x} + \beta e_\alpha\varepsilon, t + \beta\varepsilon), \end{aligned} \tag{8.3}$$

where

$$0 < \beta < 1. \tag{8.4}$$

Substitution of equation (8.4) into (8.1) gives:

$$\begin{aligned} &\varepsilon\left(\frac{\partial}{\partial t} + e_{\alpha j}\frac{\partial}{\partial x_j}\right) f_\alpha(\boldsymbol{x} + \beta\boldsymbol{e}_\alpha\varepsilon, t + \beta\varepsilon) \\ &= -\frac{1}{\tau}(f_\alpha - f_\alpha^{eq}) \\ &+ \frac{\varepsilon}{6e^2} e_{\alpha i} F_i\left(\boldsymbol{x} + \frac{1}{2}\boldsymbol{e}_\alpha\varepsilon, t + \frac{1}{2}\varepsilon\right). \end{aligned} \tag{8.5}$$

By taking $\sum e_{\alpha i}$. (8.5) we obtain

$$\frac{\partial}{\partial t}\sum_{\alpha} e_{\alpha i} f_{\alpha}(\boldsymbol{x}+\beta \boldsymbol{e}_{\alpha}\varepsilon, t+\beta\varepsilon) \tag{8.6}$$

$$+\frac{\partial}{\partial x_j}\sum_{\alpha} e_{\alpha i} e_{\alpha j} f_{\alpha}(\boldsymbol{x}+\beta \boldsymbol{e}_{\alpha}\varepsilon, t+\beta\varepsilon)$$

$$= F_i\left(\boldsymbol{x}+\frac{1}{2}\boldsymbol{e}_{\alpha}\varepsilon, t+\frac{1}{2}\varepsilon\right).$$

From

$$\sum_{\alpha} e_{\alpha i} f_{\alpha}(\boldsymbol{x}, t) = \sum_{\alpha} e_{\alpha i} f_{\alpha}^{(eq)}(\boldsymbol{x}, t), \tag{8.7}$$

in the LBM, we have

$$\sum_{\alpha} e_{\alpha i} f_{\alpha}(\boldsymbol{x}+\beta \boldsymbol{e}_{\alpha}\varepsilon, t+\beta\varepsilon) = \sum_{\alpha} e_{\alpha i} f_{\alpha}^{(eq)}(\boldsymbol{x}+\beta \boldsymbol{e}_{\alpha}\varepsilon, t+\beta\varepsilon), \tag{8.8}$$

and with reference to

$$f_{\alpha} = f_{\alpha}^{(0)} + \varepsilon f_{\alpha}^{(1)} + \varepsilon^2 f_{\alpha}^{(2)} + O(\varepsilon^3), \tag{8.9}$$

one can obtain

$$\sum_{\alpha} e_{\alpha i}\, e_{\alpha j} f_{\alpha}(\boldsymbol{x}+\beta \boldsymbol{e}_{\alpha}\varepsilon, t+\beta\varepsilon) \tag{8.10}$$

$$= \sum_{\alpha} e_{\alpha i} e_{\alpha j}\, f_{\alpha}^{(eq)}(\boldsymbol{x}+\beta \boldsymbol{e}_{\alpha}\varepsilon, t+\beta\varepsilon)$$

$$+ \varepsilon \sum_{\alpha} e_{\alpha i}\, e_{\alpha j} f_{\alpha}^{(1)}(\boldsymbol{x}+\beta \boldsymbol{e}_{\alpha}\varepsilon, t+\beta\varepsilon) + O(\varepsilon^2).$$

Therefore, by use of local equilibrium function,

$$f_{\alpha}^{eq} \tag{8.11}$$

$$= \begin{cases} h - \dfrac{5gh^2}{6e^2} - \dfrac{2h}{3e^2} u_i u_i, & \alpha = 0, \\ \dfrac{gh^2}{6e^2} + \dfrac{h}{3e^2} e_{\alpha i} u_i + \dfrac{h}{2e^4} e_{\alpha i} e_{\alpha j} u_i u_j - \dfrac{h}{6e^2} u_i u_i, & \alpha = 1,3,5,7, \\ \dfrac{gh^2}{24e^2} + \dfrac{h}{12e^2} e_{\alpha i} u_i + \dfrac{h}{8e^4} e_{\alpha i} e_{\alpha j} u_i u_j - \dfrac{h}{24e^2} u_i u_i, & \alpha = 2,4,6,8. \end{cases}$$

to evaluate the terms in (8.8) and (8.9), equation (8.7) becomes

$$\left[\frac{\partial}{\partial t}(hu_i) + \frac{\partial}{\partial x_j}\left(hu_i u_j + \frac{1}{2} gh^2 \delta_{ij}\right)\right]_{(\boldsymbol{x}+\beta \boldsymbol{e}_{\alpha}\varepsilon, t+\beta\varepsilon)} \tag{8.12}$$

$$= F_i\left(\boldsymbol{x} + \frac{1}{2}\boldsymbol{e}_{\alpha}\varepsilon, t + \frac{1}{2}\varepsilon\right) - \varepsilon \sum_{\alpha} e_{\alpha i}\, e_{\alpha j} f_{\alpha}^{(1)}$$

$$+ O(\varepsilon^2).$$

Combining

$$\Lambda_{ij} = \frac{\varepsilon}{2\tau}(2\tau - 1)\sum_{\alpha} e_{\alpha i} e_{\alpha j} f_{\alpha}^{(1)}. \tag{8. 13}$$

and

$$\Lambda_{ij} \approx -\frac{e^2\varepsilon}{6}(2\tau - 1)\left[\frac{\partial hu_i}{\partial x_j} + \frac{\partial (hu_j)}{\partial x_i}\right]. \tag{8. 14}$$

gives

$$\sum_{\alpha} e_{\alpha i} e_{\alpha j} f_{\alpha}^{(1)} = -\frac{e^2\tau}{3}\left[\frac{\partial (hu_i)}{\partial x_j} + \frac{\partial (hu_j)}{\partial x_i}\right]. \tag{8. 15}$$

By considering the initial condition, $u_i = 0$, equation (8.15) becomes

$$\sum_{\alpha} e_{\alpha i} e_{\alpha j} f_{\alpha}^{(1)} = 0, \tag{8. 16}$$

leading to equation (8.12) in the following second-order accurate form:

$$h(\boldsymbol{x} + \beta \boldsymbol{e}_{\alpha}\varepsilon, t + \beta\varepsilon)\frac{\partial}{\partial x_i} h(\boldsymbol{x} + \beta \boldsymbol{e}_{\alpha}\varepsilon, t + \beta\varepsilon) = F_i\left(\boldsymbol{x} + \frac{1}{2}\boldsymbol{e}_{\alpha}\varepsilon, t + \frac{1}{2}\varepsilon\right). \tag{8. 17}$$

Substitution of the force term related to be bed topography (8.2) into (8.16) results in

$$h(\boldsymbol{x}+\beta \boldsymbol{e}_{\alpha}\varepsilon, t+\beta\varepsilon)\frac{\partial}{\partial x_i}h(\boldsymbol{x}+\beta \boldsymbol{e}_{\alpha}\varepsilon, t+\beta\varepsilon) \tag{8. 18}$$

$$= -h\left(\boldsymbol{x}+\frac{1}{2}\boldsymbol{e}_{\alpha}\varepsilon, t+\frac{1}{2}\varepsilon\right)\frac{\partial}{\partial x_i}z_b\left(\boldsymbol{x}+\frac{1}{2}\boldsymbol{e}_{\alpha}\varepsilon, t+\frac{1}{2}\varepsilon\right).$$

After rearranging equation (8.18) and setting $\beta = 1/2$, we obtain:

$$\left[h\frac{\partial}{\partial x_i}(h+z_b)\right]_{\boldsymbol{x}+\frac{1}{2}\boldsymbol{e}_{\alpha}\varepsilon, t+\frac{1}{2}\varepsilon} = 0. \tag{8. 19}$$

For the stationary case,

$$h + z_b = \text{constant}, \tag{8. 20}$$

equation (8.19) holds true throughout the domain, as illustrated in Figure 8.1.

For $\beta \neq 1/2$, a Taylor expansion is taken to the term on the left hand side of equation (8.18) in time and space about point $\boldsymbol{x}+\frac{1}{2}\boldsymbol{e}_{\alpha}\varepsilon, t+\frac{1}{2}\varepsilon$ giving,

$$h(\boldsymbol{x}+\beta \boldsymbol{e}_{\alpha}\varepsilon, t+\beta\varepsilon)\frac{\partial}{\partial x_i}h(\boldsymbol{x}+\beta \boldsymbol{e}_{\alpha}\varepsilon, t+\beta\varepsilon) \tag{8.21}$$

$$= h\left(\boldsymbol{x}+\frac{1}{2}\boldsymbol{e}_{\alpha}\varepsilon, t+\frac{1}{2}\varepsilon\right)\frac{\partial}{\partial x_i}h\left(\boldsymbol{x}+\frac{1}{2}\boldsymbol{e}_{\alpha}\varepsilon, t\right.$$

$$\left.+\frac{1}{2}\varepsilon\right)+\mathcal{O}\left(\left[\beta-\frac{1}{2}\right]\varepsilon\right).$$

From equation (8.4),

$$\left|\beta-\frac{1}{2}\right|<\frac{1}{2}. \tag{8.22}$$

As β is obviously small, it can be assumed to be the same order as ε, because ε is the time step,

$$\mathcal{O}\left(\left[\beta-\frac{1}{2}\right]\varepsilon\right)\sim\mathcal{O}(\varepsilon^2) \tag{8.23}$$

Consequently, equation (8.21) can be replaced with the following second-order accurate expression,

$$h(\boldsymbol{x}+\beta \boldsymbol{e}_{\alpha}\varepsilon, t+\beta\varepsilon)\frac{\partial}{\partial x_i}h(\boldsymbol{x}+\beta \boldsymbol{e}_{\alpha}\varepsilon, t+\beta\varepsilon) \tag{8.24}$$

$$= h\left(\boldsymbol{x}+\frac{1}{2}\boldsymbol{e}_{\alpha}\varepsilon, t+\frac{1}{2}\varepsilon\right)\frac{\partial}{\partial x_i}h\left(\boldsymbol{x}+\frac{1}{2}\boldsymbol{e}_{\alpha}\varepsilon, t+\frac{1}{2}\varepsilon\right).$$

Substitution of equation (8.24) into (8.18) also leads to equation (8.19), indicating again that the centred scheme satisfies the $\mathcal{N}$ – property at second order accuracy.

References

[1] Meselhe E. A.and Sotiropoulos F. Numerical simulation of transcritical flow in open channels. *Journal of Hydraulic Engineering.* 1997, **123** (9):774.

[2] Teeter A. M., Johnson B. H., Berger C., Stelling G., Scheffner N. W., Garcia M. H., et al. Hydrodynamic and sediment transport modeling with emphasis on shallow-water, vegetated areas (lakes, reservoirs, estuaries and lagoons). Hydrobiologia 2001 **444** (1-3):1-24.

[3] Cao Z., Pender G., Wallis S., Carling P. Computational Dam-Break Hydraulics over Erodible Sediment Bed. *Journal of Hydraulic Engineering.* 2004, **130** (7):689-703.

[4] Zhou J. G. *Lattice Boltzmann methods for shallow water flows.* Berlin : Springer, 2004.

[5] Klar A., Seaid M., Thommes G. Lattice Boltzmann simulation of depth-averaged models in flow hydraulics. *International Journal of Computational Fluid Dynamics.* 2008, **22** (7):507-522.

[6] Al-Barwani H.and Purnama A. Simulating brine plumes discharged into the seawaters. *Desalination.* 2008, **221** (1-3):608-613.

[7] Banda M. K., Seaid M., Thommes G. Lattice Boltzmann simulation of dispersion in two-dimensional tidal flows. *Int J Numer Methods Eng* 2009 **77** (6):878-900.

[8] Huang W.and Spaulding M. 3D Model of Estuarine Circulation and Water Quality Induced by Surface Discharges. *Journal of Hydraulic Engineering.* 1995, **121** (4):300.

[9] García A., Revilla J. A., Medina R., Álvarez C., Juanes J. A. A model for predicting the temporal evolution of dissolved oxygen concentration in shallow estuaries. *Hydrobiologia.* 2002, **205**:47-476.

[10] Kowalik Z.and Bang I. Numerical computation of tsunami run-up by the upstream derivative method. *Sci. Tsunami Hazards.* 1987, **5** (2):77-84.

[11] Yeh H. The Flores Island tsunamis. EOS Trans.Am.Geophys.Union 1993, **74** (33; 33):369.

[12] Satake K. Tsunami field survey of the 1992 Nicaragua earthquake. EOS Trans.Am.Geophys.Union 1993, **74** (13):145.

[13] Yeh H. The 1994 Shikotan earthquake tsunamis. Pure Appl.Geophys. 1995, **144** (3-4):855-874.

[14] Cho,Y. S. *Numerical simulations of tsunami propagation and run-up.* United States, 1995.

[15] Briggs M. J., Synolakis C. E., Harkins G. S., Green D. R. Laboratory experiments of tsunami runup on a circular island. *Pure and Applied Geophysics,Earth and Environmental Science.* 1995, **144** (3):569-593.

[16] Kim D., Cho Y., Yi Y. Propagation and run-up of nearshore tsunamis with HLLC approximate Riemann solver. *Ocean Engineering.* 2007, **34** (8-9):1164-1173.

[17] Ghidaoui M. S., Deng J. Q., Gray W. G., Xu K. A Boltzmann based model for open channel flows. *Int.J.Numer.Methods Fluids* 2001 **35** (4):449-494.

[18] Harlow F. H.and Welch J. E. Numerical calculation of time-dependent viscous incompressible flow of fluid with free surface. *Physics of Fluids.* 1965, **8** (12):2182-2189.

[19] Grubert J. P. Numerical Computation of Two-dimensional Flows. *ASCE J Waterw Harbors Coastal Eng Div.* 1976, **102** (1):1-12.

[20] McGuirk J. J.and Rodi W. A depth-averaged mathematical model for the field of the near side discharges into open-channel flow. *J.Fluid Mech.* 1978, **86** :761-781.

[21] Tubbs,K. *Lattice Boltzmann Modeling for Shallow Water Equations Using High Performance Computing.* , Louisiana State University, 2010.

[22] Abbott M. B.and Ionescu F. On The Numerical Computation Of Nearly Horizontal Flows. *Journal of Hydraulic Research.* 1967, **5** (2):97.

[23] Falconer R. A. Numerical Modeling of Tidal Circulation in Harbors. *Journal of the Waterway, Port, Coastal and Ocean Division, Proceedings of the American Society of Civil Engineers.* 1980, **106** (1):31-48.

[24] Casulli V. Semi-implicit finite difference methods for the two-dimensional shallow water equations. *Journal of Computational Physics.* 1990, **86** (1):56-74.

[25] Glaister P. Approximate Riemann solutions of the two-dimensional shallow-water equations. *Journal of Engineering Mathematics.* 1990, **24** (1):45-53.

[26] Toro E. F. Riemann Problems and the Waf Method for Solving the 2-Dimensional Shallow-Water Equations. 1992 **338** (1649):43-68.

[27] Alcrudo F.andGarcia-Navarro P. A High-Resolution Godunov-Type Scheme in Finite Volumes for the 2d Shallow-Water Equations. Int.J.Numer.Methods Fluids 1993 **16** (6):489-505.

[28] Chippada S., Dawson C. N., Martinet M. L., Wheeler M. F. A Godunov-type finite volume method for the system of Shallow Water Equations. Comput.Methods Appl.Mech.Eng. 1998 **151** (1-2):105-129.

[29] Aizinger V.and Dawson C. A discontinuous Galerkin method for two-dimensional flow and transport in shallow water. *Advances in Water Resources.* 2002, **25** (1):67-84.

[30] Gunstensen A. K., Rothman D. H., Zaleski S., Zanetti G. Lattice Boltzmann Model of Immiscible Fluids. 1991 **43** (8):4320-4327.

[31] Chen H., Chen S., Matthaeus W. H. Recovery of the Navier-Stokes equations using a lattice-gas Boltzmann model. *Physical Review A.* 1992, **45** :5339-5342.

[32] Chen S.and Doolen G. D. Lattice boltzmann method for fluid flows. 1998 **30** :329-364.

[33] Lallemand P.and Luo L. -. Theory of the lattice Boltzmann method: Dispersion, dissipation, isotropy, Galilean invariance, and stability. *Physical Review E - Statistical Physics, Plasmas, Fluids, and Related Interdisciplinary Topics.* 2000, **61** (6 B):6546-6562.

[34] Wolf-Gladrow D. *Lattice gas cellular automata and lattice Boltzmann models: An introduction.* Berlin : Heidelberg, Springer, 2000.

[35] Ponce Dawson S., Chen S., Doolen G. D. Lattice Boltzmann computations for reaction-diffusion equations. *Journal of Chemical Physics.* 1993, **98** (2):1514.

[36] Martinez D. O., Chen S., Matthaeus W. H. Lattice Boltzmann magnetohydrodynamics. *Physics of Plasmas.* 1994, **1** (6):1850.

[37] Kang Q. J., Zhang D. X., Chen S. Y. Unified lattice Boltzmann method for flow in multiscale porous media. 2002 **66** (5).

[38] Succi S. *The lattice Boltzmann equation for fluid dynamics and beyond.* Oxford, Clarendon Press, 2001.

[39] Salmon R. The lattice Boltzmann method as a basis for ocean circulation modeling. J.Mar.Res. 1999 **57** (3):503-535.

[40] Zhong L., Feng S., Luo D., Gao S. Wind-driven, double-gyre, ocean circulation in a reduced-gravity, 2.5-layer, lattice boltzmann model. *Advances in Atmospheric Sciences.* 2006, **23** (4):561.

[41] Feng S. D., Mao J. Y., Zhang Q. Lattice Boltzmann equation model in the Coriolis field. 2001 **10** (12):1103-1105.

[42] Xu K., Martinelli L., Jameson A. Gas-Kinetic Finite Volume Methods, Flux-Vector Splitting, and Artificial Diffusion. *Journal of Computational Physics.* 1995, **120** (1):48.

[43] Xu K., Kim C., Martinelli L., Jameson A. BGK-based schemes for the simulation of compressible flow. 1996 **7** (3):213-234.

[44] Zhou J. G. A lattice Boltzmann model for the shallow water equations with turbulence modeling. *International Journal of Modern Physics C: Computational Physics & Physical Computation.* 2002, 10, **13** (8):1135.

[45] Zhou J. G. A lattice Boltzmann model for the shallow water equations. *Computer Methods in Applied Mechanics & Engineering.* 2002, **191** (32):3527.

[46] Zhou J. G. Comparison study of lattice Boltzmann method and Godunov method for shallow water flows. *Proceedings of the Congress-International Association for Hydraulic Research.* 2007, **2** (32):493.

[47] Bilgil A. Effect of wall shear stress distribution on manning coefficient of smooth open rectangular channel flows. *Turkish Journal of Engineering and Environmental Sciences.* 2003, **27** (5):305-313.

[48] Babarutsi S., Nassiri M., Chu V. H. Computation of shallow recirculating flow dominated by friction. *Journal of Hydraulic Engineering.* 1996, **122** (7):367-372.

[49] Kranenburg C. On the evolution of roll waves. *Journal of Fluid Mechanics.* 1992, **245** :249.

[50] Li Y., Jin Y., Yin Y., Shen H. Simulation of shallow-water waves in coastal region for marine simulator. 2008,.

[51] Titov V. V.and Synolakis C. E. Modeling of breaking and nonbreaking long-wave evolution and runup using VTCS-2. *Journal of Waterway, Port, Coastal & Ocean Engineering - ASCE.* 1995, **121** (6):308-316.

[52] Fuhrman D. R.and Madsen P. A. Simulation of nonlinear wave run-up with a high-order Boussinesq model. *Coastal Engineering.* 2008, **55** (2):139-154.

[53] Yamazaki Y., Kowalik Z., Cheung K. F. Depth-integrated, non-hydrostatic model for wave breaking and run-up. *International Journal for Numerical Methods in Fluids.* 2009, **61** (5):473-497.

[54] Mahdavi A.and Talebbeydokhti N. Modeling of non-breaking and breaking solitary wave run-up using FORCE-MUSCL scheme. *Journal of Hydraulic Research.* 2009, **47** (4):476-485.

[55] Molls T., Zhao G., Molls F. Friction slope in depth-averaged flow. *Journal of Hydraulic Engineering.* 1998, **124** (1):81.

[56] Brufau P.and Garcia-Navarro P. Two-dimensional dam break flow simulation. *International Journal for Numerical Methods in Fluids.* 2000, **33** (1):35-57.

[57] Brown J. E.and Bearman G. *Waves, tides and shallow-water processes / prepared by an Open University course team; (by) Joan Brown...(et al.) ; editor: Gerry Bearman.* Oxford, Pergamon in association with the Open University, 1989.

[58] Synolakis C. E. The runup of solitary waves. *Journal of Fluid Mechanics.* 1987, **185** :523-545.

[59] Zelt J. A. The run-up of nonbreaking and breaking solitary waves. *Coastal Engineering.* 1991, **15** (3):205-246.

[60] Lloyd P. M.and Stansby P. K. Shallow-water flow around model conical islands of small side slope. II: submerged. *Journal of Hydraulic Engineering.* 1997, **123** (12):1068-1077.

[61] Sobey R. J. Wetting and drying in coastal flows. *Coastal Engineering.* 2009, **56** (5):565-576.

[62] Balzano A. Evaluation of methods for numerical simulation of wetting and drying in shallow water flow models. *Coastal Engineering.* 1998, **34** (1-2):83-107.

[63] Rogers B., Fujihara M., Alistair G. L. B. Adaptive Q-tree Godunov-type scheme for shallow water equations. *International Journal for Numerical Methods in Fluids.* 2001, **35** (3):247.

[64] Lynett P. J., Wu T., Liu P. L. -. Modeling wave runup with depth-integrated equations. *Coastal Engineering.* 2002, **46** (2):89-107.

[65] Gross E. S., Bonaventura L., Rosatti G. Consistency with continuity in conservative advection schemes for free-surface models. *International Journal for Numerical Methods in Fluids.* 2002, **38** (4):307-327.

[66] Kim D. -., Cho Y. -., Kim W. -. Weighted averaged flux-type scheme for shallow-water equations with fractional step method. *Journal of Engineering Mechanics.* 2004, **130** (2):152-160.

[67] Wei Y., Mao X. -., Cheung K. F. Well-balanced finite-volume model for long-wave runup. *Journal of Waterway, Port, Coastal and Ocean Engineering.* 2006, **132** (2):114-124.

[68] Marche F., Bonneton P., Fabrie P., Seguin N. Evaluation of well-balanced bore-capturing schemes for 2D wetting and drying processes. *International Journal for Numerical Methods in Fluids.* 2007, **53** (5):867-894.

[69] Preissmann A.andCunge J. A. Calcul du intumescences sur machines électroniques. 1961, 656-664.

[70] Dodd N. Numerical model of wave run-up, overtopping, and regeneration. *Journal of Waterway, Port, Coastal and Ocean Engineering.* 1998, **124** (2):73-81.

[71] Oey L. -. A wetting and drying scheme for POM. *Ocean Modelling.* 2005, **9** (2):133-150.

[72] Hu K., Mingham C. G., Causon D. M. Numerical simulation of wave overtopping of coastal structures using the non-linear shallow water equations. *Coastal Engineering.* 2000, **41** (4):433-465.

[73] Sielecki A.and Wurtele M. G. The numerical integration of the nonlinear shallow-water equations with sloping boundaries. *Journal of Computational Physics.* 1970, **6** (2):219-236.

[74] Shyy W. Moving-Boundary Problems. In: Minkowycz W. J., Sparrow E. M., Murthy J. Y., editors. *Handbook of numerical heat transfer* . 2nd ed. Hoboken, New Jersey, John Wiley and Sons, 2006, 559-592.

[75] van Leer B. Towards the ultimate conservative difference scheme. V. A second-order sequel to Godunov's method. *Journal of Computational Physics.* 1979, **32** (1):101-136.

[76] Frandsen J. B. A simple LBE wave runup model. *Progress in Computational Fluid Dynamics.* 2008, **8** (1-4):222-232.

[77] Ulam S. Random processes and transformations. 1952, 264-275.

[78] Neumann N. J. *The theory of self-reproducing automata.* Urbana, University of Illinois Press, 1966.

[79] Signorini J. Complex computing with cellular automata. In: Manneville P., Boccara N., Vichniac G. Y., Bidaux R., editors. *Cellular Automata and Modeling of Complex Physical Systems* Berlin, Springler, 1989, 57-72.

[80] Zuse K. Calculating Space. 1970 **AZT-70-164-GEMIT** .

[81] Sukop M. C.andThorne D. T. *Lattice Boltzmann modeling : an introduction for geoscientists and engineers.* Berlin, Springer, 2006.

[82] Rothman D. H. Lattice-gas cellular automata; simple models of complex hydrodynamics. 1997, **[5]** .

[83] Gavrilova M., Gervasi O., Kumar V., Tan C. J. K., Taniar D., Laganà A., et al. Modelling of Complex Cryptographic Systems in Terms of Simple Cellular Automata. 2006, 577.

[84] Hutchison D., Kanade T., Kittler J., Kleinberg J. M., Mattern F., Mitchell J. C., et al. Cellular Automata Models for Complex Matter. 2007, 385.

[85] Liu X., Li X., Shi X., Wu S., Liu T. Simulating complex urban development using kernel-based non-linear cellular automata. *Ecological Modelling.* 2008, **211** (1-2):169-181.

[86] Gardner M. Mathematical games: The fantastic combinations of John Conway's new solitaire game "life". *Scientific American.* 1970, **223** :120-123.

[87] Frisch U., Hasslacher B., Pomeau Y. Lattice-gas automata for the Navier-Stokes equation. *Physical Review Letters.* 1986, **56** (14):1505-1508.

[88] Raabe D. Overview of the lattice Boltzmann method for nano and microscale fluid dynamics in materials science and engineering. *Modelling and Simulation in Materials Science and Engineering.* 2004, **12** (6):R13-R46.

[89] Liu H. Lattice Boltzmann simulations for complex shallow water flows. 2009 .

[90] Chopard B.andDroz M. *Cellular automata modeling of physical systems.* UK, Cambridge University Press, 1998.

[91] Dreweke A. *Lattice Boltzmann method for DSM systems : implementation and optimization with JAVA.* Saarbrücken, Germany, VDM Verlag, 2008.

[92] Sterling J. D.and Chen S. Stability Analysis of Lattice Boltzmann Methods. *Journal of Computational Physics.* 1996, **123** (1):196.

[93] Durst F. *Fluid mechanics : an introduction to the theory of fluid flows.* Berlin, Springer, 2008.

[94] Janna W. S. *Introduction to fluid mechanics.* Boca Raton, CRC Press, 2010.

[95] P.K. Stansbyand J.G. Zhou. Shallow-water flow solver with non-hydrostatic pressure: 2D vertical plane problems. *International Journal for Numerical Methods in Fluids.* 1998, **28** (3):541.

[96] Falcanor R. A. An introduction to nearly-horizontal flows. In: Abbot M. B.andPrice W. A., editors. *Coastal, Estuarial and Harbour Engineer's Reference Book* London, Chapman and Hall, 1993, 27-36.

[97] Kuipers J.and Vreugdenhil C. B. Calculations of two-dimensional horizontal flow. *Delft Hydraulics Laboratory Report.* 1973, **S163** (1).

[98] Borthwick A. G. L.and Akponasa G. A. Reservoir flow prediction by contravariant shallow water equations. *Journal of Hydraulic Engineering.* 1997, **123** (5):432-439.

[99] Featherstone R. E.andNalluri C. *Civil engineering hydraulics: essential theory with worked examples.* Oxford, Blackwell Science, 1995.

[100] Piomelli U. High Reynolds number calculations using the dynamic subgrid-scale sress model. *Physics of Fluids A.* 1993, **5** (6):1484-1490.

[101] Germano M., Piomelli U., Moin P., Cabot W. H. A dynamic subgrid-scale eddy viscosity model. *Physics of Fluids A.* 1991, **3** (7):1760.

[102] Aidun C. K.and Clausen J. R. Lattice-Boltzmann method for complex flows. *Annual Review of Fluid Mechanics.* 2010, **42** (1):439-472.

[103] Nawachukwu B. A. Flow and erosion near groyne-like structures. 1979 .

[104] Xu K. BGK-based scheme for multicomponent flow calculations. 1997 **134** (1):122-133.

[105] Higuera F. J.and Jimenez J. Boltzmann approach to lattice gas simulations. *Europhysics Letters.* 1989, **9** (7):663.

[106] Noble D. R., Chen S., Georgiadis J. G., Buckius R. O. A consistent hyrodynamic boundary condition for the lattice Boltzmann method. *Physics of Fluids.* 1995, **7** (1):203.

[107] Zhou J. G. An elastic-collision scheme for lattice Boltzmann methods. *International Journal of Modern Physics C.* 2001, **12** (3):387-401.

[108] Skordos P. A. Initial and boundary conditions for the lattice Boltzmann method. *Physical Review E.* 1993, **48** (6):4823-4842.

[109] Guangwu Y. A lattice Boltzmann equation for waves. *Journal of Computational Physics.* 2000, **161** (1):61.

[110] Feynman R. P., Leighton R. B., Sands M. *The Feynman lectures on physics.* Redwood City, CA, Addison-Wesley, 1989.

[111] Lutsko J. F. Chapman-Enskog expansion about nonequilibrium states with application to the sheared granular fluid. *Physical Review.E, Statistical, Nonlinear, And Soft Matter Physics.* 2006, **73** (2):021302-021302.

[112] Davidson P. A. *Turbulence : an introduction for scientists and engineers.* Oxford, Oxford University Press, 2004.

[113] Belotserkovskii O. M., Oparin A. M., Chechetkin V. M. *New approaches.* Cambridge, Cambridge International Science Publishing, 2005.

[114] Pappetti F.andSucci S. *An introduction to parallel computational fluid dynamics.* New York, Nova Science Publishers, 1996.

[115] Barth T. J., Griebel M., Keyes D. E., Nieminen R. M., Roose D., Schlick T., et al. On the relation between subgrid-scale modeling and numerical discretization in large-eddy simulation. 2007, 15.

[116] Hou S., Sterling J., Chen S., Doolen G. D. A lattice Boltzmann subgrid model for high Reynolds number flows. *Fields Institute Communications.* 1996, **6** :151-166.

[117] Martys N. S., Shan X., Chen H. Evaluation of the external force term in the discrete Boltzmann equation. *Physical Review.E.* 1998, **58** (5):6855-6857.

[118] Hayashi H. Lattice Boltzmann method and its application to flow analysis in porous media. *R&D Review of Toyota CRDL.* 2003, **38** (1):17-25.

[119] Buick J. M.and Greated C. A. Gravity in a lattice Boltzmann model. *Physical Review.E.* 2000, **61** :5307-5320.

[120] Guo Z. L., Zheng C. G., Shi B. C. Discrete lattice effects on the forcing term in the lattice Boltzmann method. 2002 **65** (4).

[121] Batchelor G. K. *An introduction to fluid dynamics.* London, Cambridge University Press, 1967.

[122] He X.and Luo L. -. A priori derivation of the lattice Boltzmann equation. *Physical Review.E.* 1997, **55** (6):R6333-R6336.

[123] Abe T. Derivation of the lattice Boltzmann method by means of the discrete ordinate method for the Boltzmann equation. *Journal of Computational Physics.* 1997, **131** (1):241-246.

[124] Bhatnagar P. L., Gross E. P., Krook M. A model for collision processes in gases. I. Small amplitude processes in charged and neutral one-component systems. *Physical Review.* 1954, **94** (3):511-525.

[125] Koelman J. M. V. A. A simple lattice Boltzmann scheme for Navier-Stokes fluid flow. *Europhysics Letters.* 1991, **15** (6):603.

[126] Ziegler D. P. Boundary conditions for lattice Boltzmann simulations. *Journal of Statistical Physics.* 1993, **71** (5-6):1171.

[127] Zou Q.and He Z. On pressure and velocity boundary conditions for the lattice Boltzmann BGK model. *Physics of Fluids.* 1997, **9** (6):1591.

[128] Chen H. Volumetric formulation of the lattice Boltzmann method for fluid dynamics: Basic concept. *Phys.Rev.E.* 1998, **58** (3):3955.

[129] Zhou Y., Zhang R., Staroselsky I., Chen H. Numerical simulation of laminar and turbulent buoyancy-driven flows using a lattice Boltzmann based algorithm. *International Journal of Heat & Mass Transfer.* 2004, **47** (22):4869-4879.

[130] Yu D., Mei R., Shyy W. A multi-block lattice Boltzmann method for viscous fluid flows. *International Journal for Numerical Methods in Fluids.* 2002, **39** (2):99.

[131] Liu H., Zhou G. J., Burrows R. Lattice Boltzmann model for shallow water flows in curved and meandering channels. *International Journal of Computational Fluid Dynamics.* 2009, **23** (3):209-220.

[132] Yu D., Mei R., Luo L., Shyy W. Viscous flow computations with the method of lattice Boltzmann equation. *Progress in Aerospace Sciences.* 2003, **39** (5):329.

[133] Pan C., Luo L., Miller C. T. An evaluation of lattice Boltzmann schemes for porous medium flow simulation. *Computers & Fluids.* 2006, **35** (8):898-909.

[134] Ladd A. J. C. Numerical simulation of particular suspensions via a discretized Boltzmann equation. Part 2. Numerical results. *J.Fluid Mech.* 1994, **271** :311-339.

[135] Douglas J. F., Gasiorek J. M., Swaffield J. A. *Fluid mechanics.* Harlow, Longmans Scientific, 1995.

[136] Zhou J. G.and Goodwill I. M. A finite volume method for steady state 2D shallow water flows. *International Journal of Numerical Methods for Heat and Fluid Flow.* 1997, **7** (1):4-23.

[137] Fox R. F. Nonlinear dynamics and chaos: With applications to physics, biology, chemistry and engineering. *Physics Today.* 1995, **48** (3):93-94.

[138] Schueler G. J.andSchueler B. J. The chaos of Jung's psyche. 1997 .

[139] Lorenzo-Trueba J., Voller V. R., Muto T., Kim W., Paola C., Swenson J. B. A similarity solution for a dual moving boundary problem associated with a coastal-plain depositional system. *Journal of Fluid Mechanics.* 2009, **628** (1):427-443.

[140] Calvo N., Durany J., Toja R., Vázquez C. Numerical methods for a fixed domain formulation of the glacier profile problem with alternative boundary conditions. *Journal of Computational and Applied Mathematics.* 2011, **235** (5):1394-1411.

[141] Vrankar L., Kansa E. J., Ling L., Runovc F., Turk G. Moving-boundary problems solved by adaptive radial basis functions. *Computers & Fluids.* 2010, **39** (9):1480-1490.

[142] Sheu T. W. H.and Chen H. Y. H. A transient analysis of incompressible fluid flow in vessels with moving boundaries. *International Journal of Numerical Methods for Heat and Fluid Flow.* 1999, **9** (8):833.

[143] Pontillo M., Schmocker L., Greco M., Hager W. H. 1D numerical evaluation of dike erosion due to overtopping. *Journal of Hydraulic Research.* 2010, **48** (5):573.

[144] Sierra J. P., González-Marco D., Mestres M., Gironella X., Oliveira T. C. A., Cáceres I., et al. Numerical model for wave overtopping and transmission through permeable coastal structures. *Environmental Modelling & Software.* 2010, **25** (12):1897-1904.

[145] Tuan T. Q.and Oumeraci H. A numerical model of wave overtopping on seadikes. *Coastal Engineering.* 2010,**57** (8):757-772.

[146] Ebersole B. A., Westerink J. J., Resio D. T., Dean R. G. Performance evaluation of the New Orleans and Southeast Louisiana Hurricane Protection System, Volume IV — the storm . 2007 .

[147] Madsen P. A., Soerensen O. R., Schaeffer H. A. Surf zone dynamics simulated by a Boussinesq type model. Part I. Model description and cross-shore motion of regular waves. 1997 **32** (4):255-288.

[148] Johnson B. H. *Development and verification of a three-dimensional numerical hydrodynamic, salinity, and temperature model of Chesapeake Bay [microform].* Vicksburg, Miss. : US Army Corps of Engineers, Hydraulics Laboratory ; [Springfield, VA : National Technical Information Service, distributor, 1991-, 1991.

[149] Zienkiewicz O. C.andOrtiz P. A Split-Characteristic Based Finite-Element Model for the Shallow-Water Equations. Int.J.Numer.Methods Fluids 1995 **20** (8-9):1061-1080.

[150] Junk M.and Wen-An Y.
Weighted L^2-stability of the lattice Boltzmann method. *SIAM Journal on Numerical Analysis.* 2009, **47** (4):1651-1665.

[151] Cao N., Chen S., Jin S., Martinez D. Physical symmetry and lattice symmetry in the lattice Boltzmann method. *Physical Review.E.* 1997, **55** (1):R21-R24.

[152] Worthing R. A., Mozer J., Seeley G. Stability of lattice Boltzmann methods in hydrodynamic regimes. *Physical Review.E.* 1997, **56** (2):2243-2253.

[153] Courant R., Friedrichs K., Lewy H. On the partial difference equations of mathematical physics. IBM Journal of Research and Development 1967 **11** (2):215-234.

[154] Sunderam V. S., Albada G. D. v., Sloot P. M. A., Dongarra J. J., Sunder C. S., Babu V. Entropic lattice Boltzmann method on non-uniform grids. 2005, 72.

[155] Niu X. D., Shu C., Chew V. T., Wang T. G. Investigation of stability and hydrodynamics of different lattice Boltzmann models. *Journal of Statistical Physics.* 2004, 11, **117** (3):665-680.

[156] Aaltosalmi,U. *Fluid flow in porous media with the lattice-Boltzmann method.* , University of Jyvaskyla, 2005.

[157] Noble D., Georgiadis J., Buckius R. Direct assessment of lattice Boltzmann hydrodynamics and boundary conditions for recirculating flows. *Journal of Statistical Physics.* 1995, **81** (1-2):17.

[158] Maier R. S., Bernard R. S., Grunau D. W. Boundary conditions for the lattice Boltzmann method. *Physics of Fluids.* 1996, **8** (7):1788.

[159] Autar K.andEgwu E. K. Introduction, approximation and errors. In: Autar K.andEgwu E. K., editors. *Numerical Methods with Applications: Abridged* . second edition ed. http://www.autarkaw.com, 2010, 1.03.1-1.03.6.

[160] Llewellin E. W. LBflow: An extensible lattice Boltzmann framework for the simulation of geophysical flows. Part II: usage and validation. *Computers & Geosciences.* 2010, **36** (2):123-132.

[161] Katherine H., Jon F., Tamzin P. Sediment management and dredging in lakes. 2002 .

[162] Molls T.and Chaudhry M. H. Depth-averaged open-channel flow model. *Journal of Hydraulic Engineering.* 1995,**121** (6):453.

[163] Yazdi J., Sarkardeh H., Azamathulla H. M., Ghani A. A. 3D simulation of flow around a single spur dike with free-surface flow. *International Journal of River Basin Management.* 2010, **8** (1):55-62.

[164] Tingsanchali T.and Maheswaran S. 2-D depth-averaged flow computation near groyne. *Journal of Hydraulic Engineering.* 1990, **116** (1):71.

[165] Oveisy A.and Banihashemi M. A. The process of the energy loss in supercritical flow at abrupt expansion due to flow pattern. *Proceedings of the Congress- International Association for Hydraulic Research.* 2001, **D/1** :455-461.

[166] Fe J., Navarrina F., Puertas J., Vellando P., Ruiz D. Experimental validation of two depth-averaged turbulence models. *International Journal for Numerical Methods in Fluids.* 2009, **60** (2):177-202.

[167] Ruiz D. Ensayos experimentales y simulación numérica de problemas de dinámica de fluidos. 2006 .

[168] Novák P. *Hydraulic structures.* York, Taylor & Francis, 2007.

[169] Moss W. D., Baker S., Bradbury L. J. S. Measurements of mean velocity and reynolds stresses in some regions of recirculating flow. 1977, :13. 1-13. 7.

[170] Chapman R. S.and Kuo C. Y. Application of the two-equation k-ε turbulence model to a two-dimensional, steady, free surface flow problem with separation. *Int.J.Numer.Methods Fluids.* 1985, **5** :257-268.

[171] Vreugdenhil C. B. Computation of flow patterns in rivers. 1982, **108** :1296-1310.

[172] Borthwick A. G. L.and Barber R. W. River and reservoir flow modelling using the transformed shallow water equations. *International Journal for Numerical Methods in Fluids.* 1992, **14** (10):1193-1217.

[173] Borthwick A. G. L.and Barber R. W. Numerical simulation of jet-forced flow in a circular reservoir using discrete and random vortex methods. *International Journal for Numerical Methods in Fluids.* 1992, **14** (12):1453-1472.

[174] Anastasiou K.and C.T. Chan. Solution of the 2D shallow water equations using the finite volume method on unstructured triangular meshes. *International Journal for Numerical Methods in Fluids.* 1997, **24** (11):1225.

[175] Wang J.and Liu R. Combined finite volume–finite element method for shallow water equations. *Computers & Fluids.* 2005, 12, **34** (10):1199-1222.

[176] Li Y., Ya-li Duan, Guo Y., Ru-xun Liu. Numerical simulation of laminar jet-forced flow using lattice Boltzmann method. *Applied Mathematics & Mechanics.* 2009, **30** (4):445-453.

[177] Shilton A.and Harrison J. Development of guidelines for improved hydraulic design of waste stabilisation ponds. *Water Science and Technology.* 2003, **48** (2):173-180.

[178] Mironer A. *Engineering fluid mechanics.* New York, McGraw-Hill, 1979.

[179] Lansford W. M.andMitchell W. D. *An investigation of the backwater profile for steady flow in prismatic channels. A report of an investigation conducted by the Engineering Experiment Station,*

University of Illinois in cooperation with the United States Geological Survey, Urbana, University of Illinois, 1949.

[180] Synolakis C. E. The runup of long waves. 1986 .

[181] Borthwick A. G. L., Ford M., Weston B. P., Taylor P. H., Stansby P. K. Solitary wave transformation, breaking and run-up at a beach. 2006 **159** (3):97-105.

[182] Peregrine D. H. Solitary waves in trapezoidal channels. *Journal of Fluid Mechanics.* 1969, **35** :1-6.

[183] Liu P. L. F., Cho Y. S., Briggs M. J., Kanoglu U., Synolakis C. E. Runup of Solitary Waves on a Circular Island. J.Fluid Mech. 1995 **302** :259-285.

[184] Madsen P. A.and Sørensen O. R. A new form of the Boussinesq equations with improved linear dispersion characteristics. Part 2. A slowly-varying bathymetry. *Coastal Engineering.* 1992, **18** (3-4):183-204.

[185] Marche F. A simple hybrid well-balanced method for a 2D viscous shallow water model. In: Deconinck H.andDick E., editors. *Computational Fluid Dynamics* Springer Berlin Heidelberg, 2006, 261-266.

[186] Thacker W. C. Some exact solutions to the nonlinear shallow-water wave equations. *Journal of Fluid Mechanics.* 1981, **107** :499-508.

[187] van Thang P., Chopard B., Lefèvre L., Ondo D. A., Mendes E. Study of the 1D lattice Boltzmann shallow water equation and its coupling to build a canal network. *Journal of Computational Physics.* 2010, **229** (19):7373-7400.